Developing a Hierarchical Digital Core Analysis Workflow for Petro-Physical Characterisation of Cross-laminated Reservoir Rocks at Pore Scales

Chen Jin

Submitted for the degree of Doctor of Philosophy

Heriot-Watt University

School of Energy, Geoscience, Infrastructure & Society

January 2018

ABSTRACT

The study presented in this thesis addresses a critical shortfall of Digital Core Analysis (DCA) in the petro-physical characterisation of natural rock samples that exhibit complex and spatially non-separable multi-scale arrangements of mineral grains of variable sizes and chemical compositions. Since those multi-scale arrangements define non-stationary (heterogeneous) grain-pore distributions, they must be characterised on sufficiently large sample volumes for sample reconstruction at pore and grain scales, to simulate the fluid flow processes for predicting petro-physical properties. Such characterisations can only be done in a multi-stage manner at multi-scales and multi-locations on a sample, due to the mutual constraints of the imaging field of view and resolution. Typical multi-scale approaches fuse images from various sources based on shared features (e.g. disproportionately large grains) as cross-scale references, but have limited application when the shared features are less obvious (non-separable) across multi-scale images. For common cross-lamination in sandstone rocks that exhibit hierarchical structures controlling grain-pore distribution and are demarcated by physical features such as inter-/intra-lamina (set) bounding surfaces, a multi-scale DCA workflow would be ideally suited for the petro-physical characterisation but would be challenging to apply when the visibility of cross-scale shared features (bounding surfaces) is weak.

This work argues that the workflow needs to have the following elements: 1) a multi-scale spatial sampling/characterisation procedure; 2) a way to maintain correct cross-scale spatial correlation among individual sampled datasets through shared features, as reference to the same sample, and 3) a stochastic reconstruction procedure that honours the multiscale structures identified in 1) and correlated in 2), and reconstructs the pore-grain-scale non-stationarity they expressed across the correlated datasets. The work presented in this thesis focuses on cross-lamination in sandstone rocks to identify challenges arising to multi-scale characterisation and to develop a suitable hierarchical DCA workflow. For this purpose, an outcrop tight Aeolian cross-laminated sandstone sample of 6x6x6 cm^3 that includes representative hierarchical structures was chosen.

The key achievements are: 1) a suitable imaging-based exploratory and recursive sampling and characterisation procedure to maximise correlation between datasets. Analysis on the resultant multi-scale datasets showed that sharp and gradual grain compositions change between adjacent laminasets (inter-laminaset) and laminae (intra-laminaset), respectively, to form thin but finite-thickness bounding surfaces, which are

ideally suited as shared physical features. However, challenges are identified including a) the inter-laminaset bounding surfaces are obscured by “artefacts” and cannot be enhanced by existing techniques and b) intra-laminaset bounding surfaces are hard to be even observed because of gradual composition variation. 2) To identify the two types of bounding surfaces as shared features to help registration, two new techniques were developed by exploring geological knowledge on structural morphology and mineral compositions, respectively, and were shown to be able to successfully identify and extract shared inter- and intra-laminaset bounding surfaces. 3) For a pair of realisations of sampled inter- and intra-laminaset bounding surfaces and estimated grain-pore distribution information, a non-stationary index map of grain texture (size and orientation) on the whole sample domain can be constructed to define the mean of affinity transformations for stochastically populating stationary (homogeneous) grain and pore structures by a reconstruction method which is implemented based on Multiple Points Statistics (MPS). One reconstructed pore-grain model was obtained in this work and contains 11900x11900x11900 voxels at a voxel resolution of 4 μm. This model was verified to capture key pore-grain variations associated with the characterised lamination structures.

ACKNOWLEDGMENTS

I am incredibly grateful to my main supervisor Doctor Jingsheng Ma. I cannot find enough words in expressing how instrumental Jingsheng has been in my development as a researcher as well as a person. I met Jingsheng for the first time while I was doing my master in Petroleum Engineering. I can never begin my journey in research without Jingsheng's recommendation and his continuous support during my PhD study. He has been always optimistic, encouraging, and supportive, making me feel enthusiastic after every meeting we had. He has spent uncountable hours helping me take my paper and presentation to a higher level. He read every sentence of my job market paper and gave me a detailed feedback. I am also very fortunate to have Doctor Zeyun Jiang as my second supervisor. Zeyun has been very helpful throughout this thesis. His remarkable suggestions improved many findings of my paper to new levels. Both Jingsheng and Zeyun were also generous with me in many other ways, supporting my research by putting me in connection with his own network from both research and industry community, by inviting me to present my work at conferences in Avignon, and London, and by funding me through Industry projects. It is my hope that this thesis marks the beginning of a new journey of interaction, collaboration, and learning.

I would also like to thank Professor Steve McDougall and Doctor Xiaoxian Zhang for their dedicated examinations and reviewing on my work, which improved my understanding to a new level. I would also like to thank Professor Sebastian Geiger, Doctor Rink van Dijke and Professor Patrick Corbett for their help on the examination.

I also want to express my sincere gratitude to other researchers of IPE for their help and support throughout this thesis. I am very fortunate to have Dr Andy Gardiner and Professor Patrick Corbett for their advice on geology. I would like to thank Professor Gary Couples and Doctor Helen Lewis who introduced me to the access to experimental facilities in the institute. There is countless appreciates for Dr Jim Buckman, Sally Hamilton and Dr James M. Somerville for continues help on using lab facilities. Without their assistance, this work would not have been completed.

Finally, I would also like to extend my gratitude to my family, without your full support this thesis could never be done.

DECLARATION STATEMENT

(Research Thesis Submission Form should be placed here)

TABLE OF CONTENTS

LISTS OF TABLES

LISTS OF FIGURES

GLOSSARY

DCA	Digital Core Analysis
SE	Secondary Electrons
SEM	Scanning Electron Microscope
BSE	Back Scattered Electrons
BSEM	Back Scattered Electrons Microscope
EDS	Energy Dispersive X-ray Spectroscopy
XRT/CT	X-Ray Computed Tomography
μ-XRT	Micro X-Ray Computed Tomography
MXRT	Macro/industrial X-Ray Computed Tomography
MCMC	Markov Chain Monte-Carlo
MPS	Multiple Point Statistics
FoV	Field of view
ROI	Region of Interests
REV	Representative Elementary Volume
LBS	Laminaset Bounding Surface
CV	Coefficient of Variation
SNR	Single-to-Noise Ratio
AD	Anisotropic Diffusion
SNESIM	Single Normal Equation Simulation
Stationarity	Stationarity is an assumption that is often reasonable for spatial data. There are two types of stationarity. One is mean stationarity, where it's assumed that the mean is constant between samples and is independent of location. Second-order stationarity is the assumption that the covariance between two points is the same for a given distance and direction, regardless of which two points are chosen.

Texture	Lithology texture refers here to both grain texture and composition in a lamina, and it controls the heterogeneity of porosity and the anisotropy of local permeability. The key grain textures of concern in this work include grain size, orientation and shape.
Grading Gradient	The rate of grain size increase/ decrease over distance at a direction perpendicular to depositional surface.
Intersection Angle	The sharp angle between lamina and the underlying stratification plane of laminaset.
Register	Spatially correlate two or more datasets in one coordinate system

LIST OF PUBLICATIONS BY THE CANDIDATE

C. Jin and J. Ma, (2014) "An automated machine-learning procedure for robust classification of SEM images of cross-laminated sandstones for digital rock analysis," Society of Core Analysis Symposium, September 2014.

C. Jin and J. Ma, (2016) "Advanced fracture segmentation from X-ray tomography (XRT) images of reservoir core samples by machine learning-based centreline extraction," EAGE-SCA International Symposium, March 2016.

C. Jin, J. Ma, J. Buckman, P. Zhang, and G. Couples, (2017) "Registering Scanning Electron Microscopy (SEM) and X-Ray Tomography (XRT) images for pore-grain characterisation of cross-laminated siliciclastic rock samples", The Geological Society Symposium, February 2017.

C. Jin, C. Lv, R. Wang, A. Zhu and J. Ma, "Challenges in Ultra-tight Rock Characterisation for Fluid Flow Modelling in Digital Core Analysis", 9th International Conference on Porous Media, May 2017.

C. Jin and J. Ma, "Connectivity-enhanced segmentation of linear structures from noisy grey-scale images by supervised classification: Part 1: Insights into connectivity-enhancing nature and influential factors", in preparations draft (70% finish).

CHAPTER 1 - INTRODUCTION

Digital Core Analysis (DCA) (or Digital Rock Physics (DRP)) refers generally in the literature to an approach or a technology for analysing and predicting the physical properties of rock samples; it applies a chain of modelling operations on a given sample from sample imaging, image-based characterisation, to tomographic reconstruction, to be followed by high-fidelity numerical simulations of physicochemical processes on the reconstructed models. The simulated physical properties of rocks could be applied to a wider scientific community, for example upscaling into field-scale reservoir simulation to assist hydrocarbon recovery and CO2 storage in the petroleum industry (Blunt et al., 2013) or monitoring and predicting water resources and pollution in environmental science ((Schnaar and Brusseau, 2006)). DCA possesses many advantages over traditional laboratory-based testing techniques; it is low-cost, efficient, repeatable and capable of performing numerical experiments under conditions that cannot be achieved in lab-based testing to answer 'what-if' questions and apply the answers to wider research communities to predict production or prevent hazards in different scenarios. In past decades, DCA has evolved to become an indispensable tool, especially to study the controls exerted by pore structures of a sample on fluid flow and to predict sample flow properties for sub-surface engineering such as greenhouse sequestration and geo-energy resource extraction (see Blunt et al. (2013) for a review).

However, the use of DCA in fluid flow study is limited primarily to small rock samples with homogeneous pore structures (i.e. properties like porosity and pore size), referred to as stationary in this work by having a constant mean and covariance between any two points of the same distance within the sampled domain. This is because a single high-resolution imaging acquisition on such a sample is adequate to construct a representative stationary pore-scale model accurately enough to model the essence of the flow. For conventional clastic reservoir rocks with an average pore diameter of tens of microns, the best X-ray tomographic imaging instrument can resolve pores of that average size but only on a sample whose volume is about 2x2x2 cm^3, due to the mutual constraint between Field of View (FoV) and the image resolution. Progress has been made to resolve smaller pores below that average by utilising additional higher resolution images. This leads to a multiscale DCA approach in which different imaging techniques are applied on the same or different FoVs of the same sample at different resolutions; those datasets must be spatially correlated with one another to reconstruct models for that sample for numerical

simulation of fluid flow at the pore scale. Multiscale DCA has been applied for the multi-scale characterisation of carbonate rock samples, using disproportionally large individual grains and/or pores as shared references for registering (spatially correlating two or more datasets in one coordinate system) coarse and fine datasets where the maximum-to-minimum resolution ratio of any two datasets to be integrated is about 10. Within such a scale range, the smallest intra-grain-pore properties are assumed to be stationary, and stochastically "decorated" into resolved larger inter-grain-pore structures. Sok et al. (2010) characterised a carbonate rock sample in this way by integrating different imaging techniques, including micro X-ray computed tomography (XRT), backscattered SEM (BSEM), and focused ion beam SEM (FIB-SEM). This approach, however, has not been applied to geologically complex samples. A cross-lamination in sandstones may contain non-separable hierarchical structures at an overall length scale of more than tens of cm, but they constrain the non-stationarity (the antonym of defined stationarity, representing heterogeneous properties) of grain-pore properties distributions where grains size variations may be relatively gentle, ranging from a few tens to hundreds of microns. This makes it impossible to find disproportionally large grains or pores as references for registration. But how to expand DCA to characterise such large structures and associated non-stationarity has not be considered, except for a few very simple cases (e.g. planar lamination, studied by (McDougall and Sorbie, 1993)). Therefore, the work of this thesis is designed to investigate and develop an appropriate approach to expand DCA for generic cross-lamination in sandstones.

In sandstones, the cross-lamination is the most commonly observable smallest structure. It is composed of a sequence of layers of sand-rich sediments that contains a variable proportion of silts and clays in a hierarchical manner. Each layer is about millimetres to centimetres thick and is called a lamina. Due to the cyclic nature of deposition and transportation, cyclic grain texture (e.g. size, orientation and shape) variation, referred to as grading, appears in each lamina and a lamina typically belongs to a conformable set of the successive laminae, referred to as a laminaset. Each laminaset has thickness varying from centimetres to decimetres, and in it, each lamina may appear to be parallel to the overall stratification plane, referred to as planar laminae, or locally at an angle (intersection angle) to that plane, referred to as curved laminae. The curved lamina is often due to changes in the topography of the depositional surface, referred to as the bedform. In a cross-lamination, the separation between two adjacent laminasets or

laminae is marked by a physical inter-laminaset bounding surface (inter-LBS) or intra-laminaset bounding surface (intra-LBS) of a finite thickness, respectively. An inter-LBS is often associated with a dramatic geological event of erosion, nondeposition, or abrupt change in lithology, and therefore, is often associated with a rather large contrast in grain texture and composition between the inter-LBS and respective main bodies it separates. That contrast is likely to be enhanced, as it induces preferential change to inter-LBS grain-pore structures and grain-pore surface properties in subsequent diagenetic processes, making it possible to identify an inter-LBS by a suitable imaging means, with high certainty. On the other hand, cyclic and gradual transitions result in only a subtle contrast in grain texture and composition between the laminae an intra-LBS separates; this makes it difficult to observe an intra-LBS by any imaging means, let alone to measure it with any high certainty (Ghous et al., 2005).

The hierarchical depositional structures in cross-lamination typify the spatial non-stationary variation of the topology and geometry of the pore space and pore surface properties, and therefore control pore-scale fluid flow. For a representative cross-lamination sample of tens of centimetres in dimension, laboratory experiments enable the manifestation of pore-scale multiple fluids flows to be observed as heterogeneous and anisotropic flow fields at the sample scale and thus the volume fraction of different phases can be estimated (Huang et al., 1995). Because of the hierarchical nature of cross-lamination, it is important to understand its collective controls on single and multiphase fluid flow in order to gain knowledge about the relative importance of different geological features at respective scales in a hierarchy. Such understanding is needed to design a field sampling scheme and to make a prediction of flow properties of samples using the most appropriate approaches (Corbett et al., 1992, Ringrose et al., 1993).

DCA has been employed to establish links between the observed flow patterns and the underlying pore structures; however, only for a planar lamination or a few laminae on small samples so far (McDougall and Sorbie, 1993, Ghous et al., 2005). The challenges that cross-lamination poses to DCA arise from the complexity of its internal hierarchical structures and gradual transition in grain properties across its sub-structures. These two factors mean that the smallest substructures, laminae, in a cross-lamination, are not distinguishable from one another at pore scale, and may not be separated reliably at the lamina scale either. Therefore, a cross-lamination needs to be treated as a non-separable representative elementary volume (REV) to capture the integrity of its pore space. To

reconstruct such a REV, one may apply the concept of the "geo-pseudo" approach that was originally devised for top-down sampling and characterisation of complex cross-bedding and modelling of fluid flow behaviours (Corbett et al., 1992; Ringrose et al., 1996). The concept of the "geo-pseudo" approach was adopted to develope a top-down exploratory and recursive hierarchical sampling scheme by considering problems of "where, at what scale and how many samples should be taken" in order to capture spatial arrangements. This scheme utilises industrial X-ray computerised tomography (XCT), scanning electron microscopy (SEM) and micro-XCT to capture inter- and intra-laminaset structures and inter- and intra-lamina lithology texture (i.e. grain texture + composition) variation, respectively, which together control non-stationary spatial distribution of grains and pores in terms of their properties for the sample, while the latter also captures local representative stationary (homogeneous) grain-pore distributions.

The overall objective of this thesis is to expand the multiscale DCA on representative cross-lamination by developing a suitable hierarchical DCA workflow that incorporates the "geo-pseudo" concept and enabling techniques for reconstructing cross-laminated samples at pore-grain scales. It is argued that, given the hierarchical nature of cross-lamination, a suitable hierarchical DCA workflow needs to have the following sequence of elements: 1) a multi-scale spatial sampling and characterisation scheme; 2) a mechanism to register individual datasets that are obtained by sampling through identified shared features; and 3) a stochastic reconstruction procedure that honours the multiscale structures identified in 1) and correlated in 2), and the pore-grain-scale non-stationarity they express.

A suitable imaging-based sampling and characterisation scheme needs to ensure that the key structural characteristics, which express the non-stationarity of pores and grains, can be estimated on individual sub-samples, in a manner consistent with their spatial relationships at localities and scales appropriate to each structure, reliably, from a number of sub-samples on each structure. However, to characterise spatially correlated distributions among datasets yielded through sampling, a suitable mechanism must be established to register them onto the same coordinates, to ensure correctly cross-scale spatial correlation. Shared physical references for any pair of datasets are needed for this purpose. The best candidates are inter-LBS and intra-LBS, and therefore the sampling scheme must be designed so that some LBSs can be revealed and identified in all datasets. With spatially correlated datasets, a procedure is needed to 'fuse' derived spatial

information for pore-grain-scale reconstruction of a sample. This procedure must deal with the local stationarity, together with consideration of the randomness and global non-stationarity of pore and grain distributions associated with hierarchical structures. The procedure must be implemented for parallel reconstruction, given the sheer size of the reconstruction domain. Clearly, the interrelation among the three elements means that any solution to address one issue that exists in one element influences the options available to address another.

For a cross-laminated sample, key research questions/issues related to each of the elements in a workflow may be identified as follows:

Sub-sampling and characterisation

- What hierarchical structures of cross-lamination are observable? and how do they spatially relate to one another at corresponding scales? and how could they be explored consistently? The geology of cross-lamination determines what structures can exist but does not guarantee that they are observable, collectively, by imaging techniques. This means an exploratory analysis is always a necessary component of this workflow, at each sub-sampling scale. Based on the geo-pseodo concept, a top-down exploratory and recursive sampling approach is the most appropriate because: 1) a larger structure is likely to influence the fluid flow more strongly than the smaller one does and to be observed with a higher level of certainty; 2) the challenge in identifying non-separable structure and representative subsample volume could be decreased by employing "where, what scale and how many" questions at each sub-sampling scale; and 3) typical sampling approaches like those of Sok et al. (2010) or De Boever et al. (2015), where the sampling was designed without exploratory analysis and recursively collecting information, have limited application in studying complex cross-lamination with non-separable hierarchical structures.
- What parameters are appropriate and geologically meaningful to describe the structures individually and collectively, and how may they be best estimated using what imaging techniques? The geologists have identified appropriate parameters in the geological context and the real question of concern here is to come up with a design of image acquisition and characterisation to maximise the ability to estimate them by the most cost-effective means, reliably and robustly.

- What are the geologically meaningful characteristics shared across acquired images that are useful as spatial references for registration? Identifying such characteristics at the right scales is the critical requirement for a multiscale DCA.
- What would be the most appropriate scheme to carry out image acquisition so that a sample of concern can be subsequently characterised sufficiently on datasets to provide quantitative information about that sample?

Identification of shared features and image registration

- Does any geological feature express itself in such way across image datasets that it can be observed and extracted with high confidence at a comparable image resolution? As will be reviewed in Chapter 2 of this thesis, inter-LBSs and/or intra-LBSs are the best candidates with the most expressive grain properties being not the grain texture, as in the case of vuggy carbonate rocks (Sok et al., 2010), but the grain composition.
- Does any existing enhancement and extraction technique apply well on all datasets? And if not, how may new techniques be devised by maximising compositional information in the datasets that are consistent with geological knowledge about LBSs, while accounting for uncertainty? These questions arise because the compositional expression of an inter-LBS or intra-LBS would differ in datasets acquired by different imaging techniques at different FoVs, resolution and locations, and is thus subject to variable degrees of uncertainty.

Stochastic Pore-grain reconstruction

Supposing all the necessary datasets have been registered in the same coordinate system and been characterised individually and collectively, the following questions need to be considered for stochastic reconstruction:

- How could grain-pore non-stationarity that is expressed by the spatial relationships of structures be represented and modelled in stochastic reconstruction procedures? Conceptually, the non-stationarity may be represented as a volumetric index map on the sample domain, where each index links to a set of parameters that define the grain-pore non-stationarity at a point in space with respect to a local stationary distribution. For the cross-lamination of concern in this work, such an index map may be constructed from the characterisations of sample global structures and local pore-grain distributions, in accordance with

geological knowledge. Note that an index map can only be considered at best as a realisation of unknown truth with variable degrees of uncertainty associated.

- What geostatistical modelling techniques and procedures are suitable for reconstruction? As will be reviewed in Chapter 2, not all stochastic reconstruction techniques are designed to handle an index map such as described above, while some of them can do so, to some degree.
- Given a suitable procedure, how can it be implemented to perform reconstruction efficiently? For the sheer size of the targeted model, reconstruction needs to be conducted by parallel processing.

What issues remain as obstacles to such tasks and what technique needs to be developed are all due to be answered in the review.

The work of this thesis is designed to address research questions and key challenges and to develop a generic multiscale DCA workflow. By doing so, this work develops 1) a top-down sampling scheme based on the key concept of "geo-pseudo" to address non-separable hierarchical structures of lamination; 2) enabling techniques to reveal shared features from multi-scale images for registration, and 3) a stochastic procedure to reconstruct the non-stationarity associated with cross-laminated samples at pore scales. The workflow being developed ensures that structure-constrained grain-pore variations of a sample can be captured adequately and consistently by hierarchical sub-sampling for multiscale correlative characterisation and pore-scale stochastic reconstruction of that sample. To meet the objective and to demonstrate the workflow, a tight aeolian cross-laminated sandstone sample is used throughout this work. A preliminary exploratory analysis on this sample, to be given in Chapter 3, confirms that the sample contains a mixture of hierarchical structures of curved or planar laminasets, lamina and inter- and intra-lamina grading, and is large enough to be considered as a representative volume of cross-lamination.

The thesis is organised as follows.

Chapter 1, the present chapter, has outlined the objective of this thesis work and its importance.

Chapter 2 presents a literature review into the background in the subject fields of this research. It covers the following aspects:

1) The geometric, topological and topographic characteristics of geological hierarchical structures, with respect to laminasets, laminae in a laminaset and grain grading in and across laminae, in typical wind ripple (Aeolian) cross-lamination. Parameters that geologists use to measure the characteristics of individual structures and the relationships between structures, in relation to the bedform, paleo-flow direction, sedimentary direction and other factors, are summarised. Characteristic lithology texture variations prior to diagenesis are reviewed, along with significant changes to them during diagenesis. Potential issues that may arise in identification of inter-LBSs and intra-LBS are considered as: a) inter-LBSs may be distracted by unconnected cementation, a mixture of different minerals that may appear similar on images, and erosion and bioturbation b) intra-LBS may less observable because of gradual grain texture variation. The review of the nature of cross-lamination also implies that all laminae appear to be similar geometrically, down to the grain scale, across a set of neighbouring laminasets that are accumulated on the same bedform surface, and therefore, have similar parameters such as laminaset/ lamina thickness, intersection angle and grading gradient (the rate of increase/ decrease of grain size over distance at a direction perpendicular to the depositional surface) according to Reading (2009) or Allen (1982)).

2) DCA is reviewed along with key categories of DCA techniques: imaging, characterisation, reconstruction and numerical simulation. Essential imaging techniques (XCT, SEM/ Energy Dispersive X-ray Spectroscopy (EDS)) are reviewed by emphasising their individual strengths for specific rock characterisations and their properties in terms of the size of their FoV and their resolutions, with a view on establishing how they may fit multiscale DCA collectively for top-down sampling. Commonly applied characterisation techniques in DCA, which are also applicable to lamination, are highlighted and so are stochastic reconstruction techniques.

3) The limitations of current DCA techniques for cross-lamination characterisation are identified and analysed, and these are: a) a representative element volume of cross-lamination is often too large to permit a single image acquisition to sample the full hierarchical structures at a pore-grain resolution, due to the mutual constraints of FoV and image resolution; one must design a systematic multiple sub-sampling scheme first; b) in the case of multiscale image datasets obtained from sampling, some of them may not resolve any pores or grains at all, and therefore characterisations must be expanded to analyse not only those datasets individually, but also all datasets, collectively. One

particular requirement to meet for a collective analysis is that all datasets of concern must be registered on the same coordinates through shared geological features. Inter- LBSs and intra-LBSs are the best candidate as shared features, but may not appear prominent in some datasets, due to the distraction in connectivity and weak contrasts in lithology texture variations. Characterisation must be equipped with tools for enhancing Inter-LBSs and intra-LBSs in respective images and extracting them for image registration. 3) after extracting information about a sample from characterisations of subsamples, that sample may only be sensibly reconstructed by a stochastic process. In traditional DCA reconstruction, the occurrence of a pore or grain in space is assumed to follow a stationary process with a homogeneous lithology texture in the reconstruction domain. For a representative domain of cross-lamination, its grain-pore distribution is non-stationary across the sub-domains of the hierarchical structures, and non-stationarity must be represented, as a volumetric index map, and incorporated in a stochastic reconstruction process, by applying affinity transformation to a non-stationary process. The foreseen large pore-scale model makes reconstruction less trackable and it must be done in parallel.

Chapter 3 reports the development of a top-down subsampling scheme for the tight Aeolian cross-laminated sandstone sample with an average grain size between a few tens to hundreds of microns in a representative volume of 6x6x6cm^3. For generic application to other samples, although the scale difference between average grain sizes and representative volume may vary for different depositional environments, the general idea of the developed top-down sampling scheme could apply. The geology of the sample is first described, followed by a report of a preliminary exploratory analysis on the sample that was designed to reveal the geological characteristics for any cross-laminated sample using rather traditional petrographic techniques. The analysis reveals 1) the sample contains upper curved and bottom planar laminasets and all expected geological structures, including grain grading and lithology variations; and 2) the sample forms a representative element volume; and 3) key parameters can be estimated on images obtained by specific imaging techniques. The results of the analysis conclude that the best candidates as shared geological features are inter-LBSs, and a suitable top-down sampling scheme should make use of 1) low-resolution XRT (MXCT) to image the whole sample to capture global distributions of inter-LBSs; 2) high-resolution SEM/EDS to image a large area of a sample surface to characterise intra-LBSs with respect to the corresponding base inter-LBSs and lithology textures; and 3) high-resolution XRT (μXRT) to capture

grain grading within and across laminae and local stationary pore-grain distributions. The results also include the estimates of lamina curvature and lamina intersection angle to the corresponding base inter-LBS.

The top-down sampling was carried out to yield three datasets. The analysis through macro/industrial X-Ray Computed Tomography (MXRT) confirmed that the structures of inter-laminasets were constant across the domain for curved and planar laminasets on the top and bottom of the sample, respectively. Inter-LBSs were captured with high certainty regarding their exact positions but lower certainty in their individual thickness, continuity and their connectivity, and are the best candidates as shared features for registration. On a large surface area perpendicular to the paleo-flow direction, SEM/EDS images were taken at a high resolution (1 μm^2/pixel), to resolve lithology texture variations within and across the structures that are also present in MXRT. The analysis on SEM/EDS images showed that even inter-LBSs are severely obscured in BSEM images due to high grain lithology variation. However, from corresponding EDS images, the lithology variation is confirmed to be associated with Haematite (Fe_2O_3) and Dolomite ($CaMg(CO_3)_2$) grains that appear along inter-LBSs, and can then be explored to extract inter-LBSs for registering SEM/EDS with MXRT. It is confirmed that most intra-LBSs cannot be identified with great confidence, although they may be inferred from measurable parameters, including lamina thickness and intersection angle. µXRT contains images obtained on several core plugs of 3-5 mm in diameter, to augment SEM/EDS with 3D pore-grain distributions within and across laminae. These plugs were taken at physical locations sufficiently close to a thin-section and were ensured to intersect inter-LBSs. Parameters estimated include grain size, grading gradient and grain orientation variation during grading. It is argued that some of the images are good for training local stationary processes that are needed for reconstruction. Operational details relating to each dataset are documented and summarised, along with important lessons learnt during the design of the sampling procedure of optimising the drilling location and condition of sub-core plugs.

Chapter 4 reports the development of two solutions to address the issues concerning the extraction of 'well-behaved' Inter-LBSs from MXRT and SEM/EDS, respectively, as shared features to register them so that they can be used to define a non-stationary index map for reconstruction. The first solution overcomes the inter-LBS discontinuity by removing high-frequency grey-scale variations in MXRT which correspond to small 'fake'

gaps, but retaining the low-frequency ones, large 'true' gaps. This is done by a special supervised classification scheme for piece-wise linear features, through a sequence of 2D image slices, one by one. In this scheme, classifiers for linear features are trained using training images in which ground-truth linear features are defined, so that their continuity with respect to the small and large gaps in the ground-truth can be learned by a machine-learning algorithm in a suitable image feature space.

Note that the solution is only described and discussed here in such details that a technical appreciation can be made, with additional technical details given in an Appendix. The continuity-enhanced inter-LBSs from MXRT extracted by this solution are analysed to reveal their connectivity and associated holes likely relating to discrete geological cementing events, such as erosion and bioturbation.

The second solution explores grain lithological variations associated with inter-LBSs in SEM/EDS, in order to enhance their extraction. It overcomes the issue that, when a SEM image is rescaled or upscaled by either linear or nonlinear (cubic) scaling, the resultant images may not retain even weak information on the inter-LBSs useful for registration. Inspired by the fact that X-ray imaging can retain the inter-LBSs on a 2D slice in a low-resolution image like MXRT, the idea behind this solution is to treat an EDS image as a sample where each pixel possesses the mass of one or more chemical elements, and to calculate an effective mass attenuation coefficient for each coarse grid pixel using a weighted average of elemental mass attenuation coefficients using filtered chemical elements respecting its geological nature. For each coarse pixel, a weighting factor for each element is calculated from the sum of its atomic mass overall, underlining fine pixels normalised by summing them over all elements. This solution is demonstrated to retain some inter-LBSs at the same resolution to MXRT, because of the presence of the heavier iron element along them. With matching inter-LBSs identified in both MXRT and SEM/EDS, both datasets are registered for defining a trend map of grain variation for reconstruction.

Chapter 5 reports the development of a stochastic reconstruction procedure based on Multiple-Point Statistics (MPS) for reconstructing a full 3D grain-pore model for the sample, considering the grain non-stationarity associated with hierarchical structures. A non-stationary index map is defined using information and data obtained in previous chapters as follows: 1) take a realisation of inter-LBSs to define the inter-laminasets; 2) distribute intra-LBSs with respect to inter-LBSs, according to estimated parameters to

define laminae in each laminaset; 3) populate the grain grading gradient within and grain orientation for each and every lamina; 4) choose a sub-domain of the μXRT to serve training datasets of the local stationary grain-pore distribution. Such a non-stationary index map represents non-stationarity as a discrete volumetric trend map, and its indexes are converted in the forms of affinity transformation to the local stationary grain-pore distribution. The single normal equation simulation (SNESIM) (Strebelle, 2002) is employed to implement MPS reconstruction. To reconstruct the sample at the pore scale at a resolution of 4 μm, the reconstruction domain is 11900x11900x11900 voxels. To speed up reconstruction, a parallel processing reconstruction procedure is implemented based on an efficient domain decomposition and an ordering scheme to minimise the latency of synchronisation. This model is verified to capture, qualitatively and quantitatively, key pore-grain variations associated with the characterised lamination structures.

Chapter 6 draws conclusions, identifies limitations and suggests further developments of the work.

CHAPTER 2 - LITERATURE REVIEW AND IDENTIFICATION OF RESEARCH CHALLENGES

This chapter presents a literature review into the background of the subject of this research. It covers the following aspects: 1) the nature of the geological hierarchical structures of cross-lamination with respect to non-stationary pore-grain spatial distributions and identifying potential markers of hierarchical structures that would serve multiscale sampling and reconstruction; 2) the state of the art of Digital Core Analysis (DCA) for multiscale imaging, pore-scale characterisation and reconstruction of the internal structures of porous media in a generic view; and 3) examining and identifying limitations of multiple-scale DCA for a representative sample, and reviewing potential solutions that would serve in top-down sampling and characterisation, identification of shared features and non-stationary stochastic reconstruction. A summary leading to a conceptual design of a hierarchical DCA workflow is presented at the end of this chapter.

2.1 Lamination

The aim of this section is to review the characteristics of lamination, focusing on what hierarchical structures there are, how they are related to each other spatially at respective scales and in terms of lithology texture variations. It also aims to review what parameters are used to characterise individual structures and their relationships, spatial relationship and how those parameters imply non-stationarity or stationarity of grain-pore character. As lithology variation creates a potential marker of hierarchical structures, its physical nature needs to be understood through the literature and potential issues that could distract the identification of such markers need to be discussed.

In sedimentary rocks, lamination is a small scale sequence of fine layers of preserved sediments, called laminae. A lamina contains grains whose orientations, sizes and compositions occur in cyclic and gradual transitions, and due to the cyclic nature of deposition, it usually belongs to a conformable set of successive laminae, called a laminaset. Each laminaset is separated from its adjacent one by an inter-LBS that marks a sudden change due to a different geological event, such as erosion, non-deposition or abrupt sediments in lithology and perhaps more significant compositional change by diagenesis. Within a laminaset, a lamina is separated from its adjacent lamina by an intra-LBS, potentially highlighted by grain texture changes. The simplest form of lamination is planar lamination, also called horizontal, parallel, and flat lamination (as illustrated in Figure 2.1), in which flat laminae and laminasets are stacked parallel to each other. More

complicated is cross-lamination, in which laminae and laminasets are inclined and intersect with each other; this could be developed when the flow (paleocurrent) has shaped the depositional surface, referred to as the bedform, in sedimentary environments such as alluvial fans, and aeolian, fluvial, deltaic, shallow marine and deep-water clastic deposits. For the purpose of developing a multiscale DCA workflow for characterising general cross-lamination, this work takes an aeolian cross-laminated sandstone sample as an example, and therefore, the following discussion is focused on aeolian lamination.

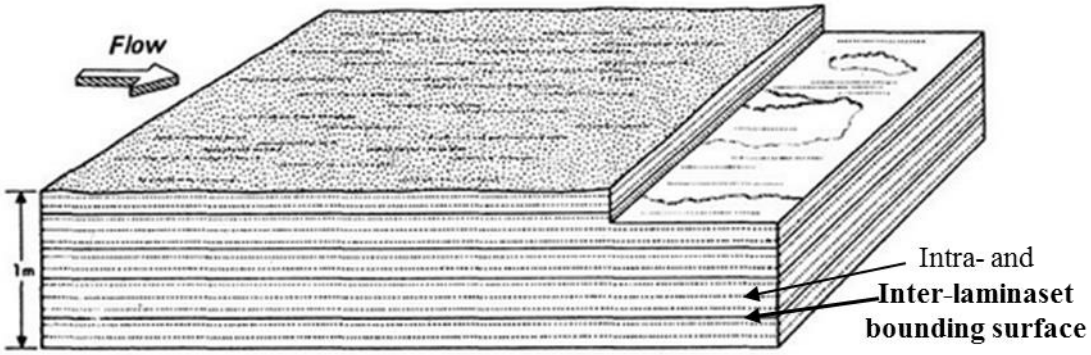

Figure 2.1 Example of planar lamination and corresponding terminologies: Harms et al. (1982)

2.1.1 Hierarchical structure of cross-lamination in aeolian environment

Laminasets

Aeolian lamination is a result of sequential deposition of sediments whose hierarchical structures and grain textures vary with the energy of the wind that transported the sediments. A dedicated introduction to the formation of hierarchical structures of aeolian lamination can be found in books such as those by Reading (2009) or Allen (1982) and the key elements are summarised here. According to Makse (2000), "Subject to the effects of wind, a flat sandy surface is unstable and evolves into a regular periodic pattern of wavelength of the order of 10 cm and height of a few centimetres" (see Figure 2.2(A) for an example of aeolian ripple and Figure 2.2(B) for typical wavelengths and corresponding grain size associated with aeolian ripple). The ripple waves are typically formed along the wind (paleocurrent) direction, which is the first important parameter that should be estimated, and based on which the 3D waveform can be described by wavelength and wave height at 2D cross-sections perpendicular to or parallel to the paleocurrent direction respectively. On a piece of a rock sample, the estimation of paleocurrent direction can be performed based on observing the geometry of the preserved laminations at different cross-sections. Typically, distinctive straight-crested

and curved-crested forms (see Figure 2.3(A-B)) of a laminaset can be observed from cross-sections perpendicular to the paleocurrent direction, with the former corresponding to lower wind velocities and the latter to higher velocities, and thus, the paleocurrent direction can be estimated. As shown in Figure 2.3(A-B) both straight-crested and curved-crested forms have elongated laminasets observable from the cross-section parallel to the paleocurrent direction and each laminaset contains a set of parallel laminae intersecting with the laminaset, while at cross-section perpendicular to the paleocurrent direction, laminae are parallel to the erosion surface of the laminaset they belong to. The wave height can be measured in a cross-section perpendicular to the paleocurrent, which is equivalent to the laminaset's thickness, and the wavelength can be estimated between two neighbouring wave peaks or valley points based on the laminaset's erosion surface observed in a cross-section parallel to the paleocurrent.

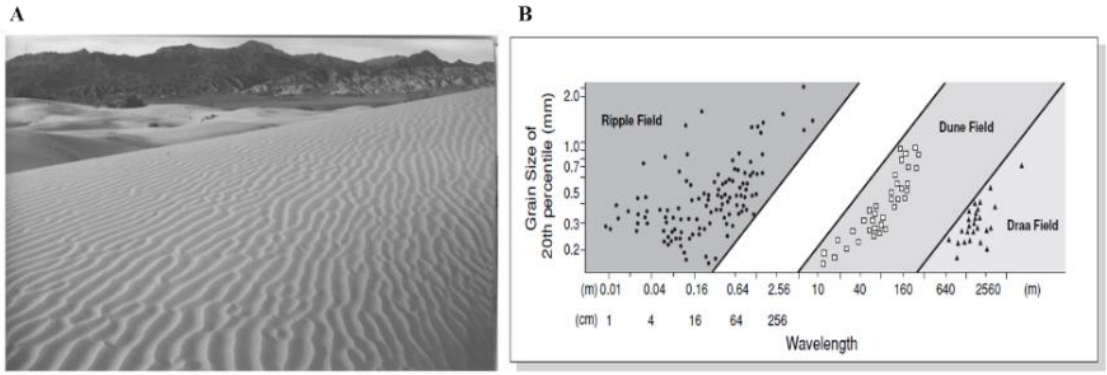

Figure 2.2 (A) Wind sand ripples on a sandy surface in Death Valley National Park, California Makse (2000) and (B) Sediment grain size versus wavelength in wind-generated bedforms: Corbett et al. (2005) after Wilson (1972).

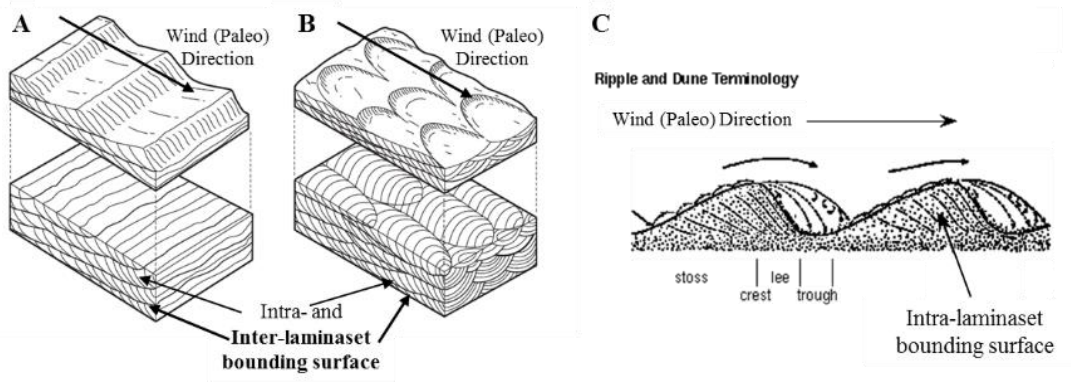

Figure 2.3; (A) Straight-crested horizontal planar cross-lamination/bedding; (B) curved-crested trough cross-lamination/bedding: Allen (1982); and (C) profile and internal structure of a well-developed ripple: Corbett et al. (2005) after Allen (1973).

Lamina

When the wind current passes over, grains roll over the crest from upwind of the wave, referred to as the stoss side, to downwind, referred to as the lee side, causing the ripple to migrate in the direction of wind (see Figure 2.3(C) for an explanation of this terminology on a 2D cross-section parallel to the paleocurrent direction). As a ripple migrates downwind, the accumulation of grains on the lee side is preserved in the form of planar or upwardly concave layers. Due to the periodic changes of wind energy, the size of grains being transported varies gradually and periodically and the process is referred to as grading. Periodic grading leaves a set of successive accumulated layers parallel to the lee side; each layer with a cycle of grading is referred to as a lamina. The thickness of a lamina is one important geometrical parameter that can be estimated between intra-LBSs that separate laminae. However, due to gradual grain size change, an intra-LBS is often hard to identify directly, but it is possible to infer lamina thickness based on the circulated variation of grain size. As the ripple migrates in the downwind direction the stoss sides are continuously eroded. If the sediment supply is less than the rate of erosion, very few laminae will be preserved. However, if the rate of sediment supply is more than the rate of sediment removal, a set of laminae, i.e. a laminaset, will be preserved. When depositional conditions like wind direction change, the preserved laminaset will be "cut off" and leaves an erosion surface. New laminasets are then formed on the erosion surface, leaving the laminae within a laminaset parallel to each other and intersecting with the erosive sedimentary surfaces that separate laminasets. Therefore, the other important parameter describing laminae is the preserved apparent intersecting angle observable at cross-section parallel to the paleocurrent. According to Allen (1982) and Reading (2009), laminae typically have the same or similar intra-lamina grain-pore texture, lamina thickness and intersecting angle, typically between 20°-30°, across several neighbouring laminasets.

Grading

Grain sorting falls into a spectrum between two extreme forms where grains either become finer or coarser as they move upwards in a lamina, referred to as normal grading and inverse grading respectively, and these differences are known to relate to transport mechanisms, grainflow and grainfall, respectively (Allen, 1982, Reading, 2009).

Normal grading starts with a new flow which erodes the underlying layer with larger grains to be deposited at high wind energy first and successively smaller grains as the energy gets lower. Inverse grading is commonly associated with wind ripple lamination

where low wind energy tends only to cause grains to fall down from the crests on the concave-upward slip faces by siltation, resulting in smaller grains to jumping further down toward the lower-impact-energy trough. Grading appears in a stack of ~1-2 grains thick layers parallel to the lee side of a ripple; however, according to Hunter (1977), layers would stack on the stoss side if the wind reverses its direction or on both sides if the wind blows in an oblique direction. Given a sample, the grading direction can be determined from a cross-section parallel to the paleocurrent direction, while grading gradient and lamina thickness may be estimated on a cross-section perpendicular to the paleocurrent (see Figure 2.3(A-B) for illustration).

2.1.2 Lithology texture of a lamina and impact on flow:

Lithology texture refers here to both grain texture and composition in a lamina, and it controls the heterogeneity of porosity and the anisotropy of local permeability. Variation in lithology texture is closely associated with every structure in lamination, as that variation gives rise to observable patterns and therefore the structures collectively control fluid flow within and across the lamination. Key grain textures of concern are grain size, orientation and shape, which are explained as follows.

1) Grain size is typically characterised by a pair of long and short axes of a non-spherical grain or the diameter of a spherical grain. Grain size in fine aeolian sandstone is around 100s μm in diameter (Allen, 1982, Reading, 2009). It is well-known that the permeability of sandstone tends to positively correlate with grain sizes (Beard and Weyl, 1973, Corbett et al., 2005), which positively correlates with the size of pores and pore throats. Therefore, the variation in grain size and sorting in lamination may significantly alter flow direction.

2) Non-spherical grains may be deposited with a preferred orientation, with their long axes either parallel or perpendicular to the paleo-current direction. In lamination, Rees (1968) pointed out that the longest grain axes are approximately aligned in the direction of paleocurrent along the lee side surface, for a curved ripple system, as a result of grain interaction during deposition from grain flow (Taira, 1989). Therefore, the preferred orientation may be characterised by both visual observations or quantifying the spatial variation of grain orientations in relation to inclined ripple laminae. The orientation of long axes can be estimated according to the measured intersection angle of the laminae. According to Baas et al. (2007) grain orientation is likely to affect the anisotropy of permeability, as the fluid flows more easily along the preferred orientation than across.

3) Grain shape is usually described by the circularity of a grain correlated to the ratio of its area and the square of the perimeter. Characterising the spatial variation of grain shape in relationship to a lamina could be taken as additional evidence of preferred orientation, because preferred orientation only occurs for non-spherical grains, which can be distinguished from spherical grains by shape.

4) Apart from grain texture variations, grain composition variations are often strongly correlated with LBSs in a lamination layer, which often has preferred cementation during diagenesis, depending on the depositional environment. In an aeolian lamination in a desert environment, Authigenic dolomite ($CaMg(CO_3)_2$) along with haematite (Fe_2O_3) are preferentially cemented at the finely laminated bounding surface layer and mark LBS in distinctive reddish or brownish colour under natural light (Walker, 1967, Glennie et al., 1978). Using Gibbs Free Energy theory or the "ageing" process, Van Houten (1961) explained this phenomenon as due to the fact that ferric hydroxides stay longer in the low permeability bounding surface layer and will transform into red coloured haematite pigment with time. According to Walker and Waugh (1973) and Walker (1976), the erosional inter-LBS is often subject to more significant diagenesis than intra-LBS, due to the more abrupt permeability change.

The complex hierarchy of lamina and laminasets in a lamination as expressed as lithology texture variation gives rise to the variable anisotropy of fluid flow and flow properties, and thus affects, as stated in: "in which direction the rock is most permeable, and also to what degree fluids will be trapped within a reservoir" (Corbett et al., 2005). According to Baas et al. (2007), the permeability is generally higher parallel to the paleo flow direction, and lower perpendicular to the paleo flow direction. In a laboratory experiment of water injection at low flow rates into a water-wet, cross-laminated heterogeneous aeolian sandstone slab with inter-lamina permeability contrast of up to 1 order of magnitude, Huang et al. (1995) monitored the water and oil interface when water was injected to displace oil by computerized-tomography (CT) and observed oil being trapped in high permeability laminae, because in low permeability laminae, capillary action traps more oil, by as much as 30% to 50%. This shows the importance of the structures of lamination on fluid flow.

2.1.3 Features that mark or hide hierarchical structures

As explained in the above discussion, in a rock sample, lamina and laminasets are marked by the surfaces separating them. In an inverse grading system, which is more common

for an aeolian ripple developed lamination, the inter- or intra-LBS is a fine-grained layer with grains as thin as ~1-2 grains thick and with grain sizes coarsening up across layers stacking sequentially on the inter- or intra-LBS, according to De Boever et al. (2015). A surface that separates a pair of laminae and is expressed as grain texture changes is often referred to as an intra-LBS. The more significant lithology change between two laminasets is associated with the erosional surface and is referred to as an inter-LBS (see labelled example in Figure 2.3(B-C)). Inter- and intra-LBSs, as the markers of preserved laminaset structures, are of critical elements of concern in the characterisation and modelling process (Rubin and Carter, 1987) and can serve as a cross-scale reference for developing a multiscale DCA workflow. The observability of bounding surfaces, may be affected by a set of factors, as follows:

1) the degree of compositional variability: inter-LBSs are often more readily observed than intra-LBSs because the former contain compositionally more distinctive deposits within rather than around them, than Intra-LBSs do. However, the compositional variation at the bounding surface may not always provide enough contrasting information to make lamination visible, according to Campbell (1967). In his study on a homogeneous sandstone samples by X-ray imaging, Hamblin (1965) demonstrated that the lamination with little texture and composition variation leads to a less visible hierarchical structure.

2) the style of cementation: cementation tends to enhance the compositional variations across a bounding surface and to make the surface to appear "continuous" with grain particles transformed as a result of diagenesis. Those particles appear to "insert" themselves between the original deposited fine layers of grains in an evenly distributed way. Physical structures may appear in observation as noises waiting to be identified.

3) co-diagenesis process: lamination may favour another set of diagenesis processes and when different diagenesis processes work simultaneously, they may lead to distractions in the identification of bounding surface. For example, feldspars would present similarly to the previously discussed haematite and dolomite that potentially highlight inter-LBS in a density-sensitive image, because of their similar density. Feldspar is one of the most commonly occurring diagenetic phases in aeolian sandstone (Waugh, 1978) and, according to De Boever et al. (2015), is often evenly distributed within a sample. Therefore, feldspar may create evenly distributed noises and its impact on the identification of inter-LBS needs to be identified.

4) Disturbance to the continuing bounding surface: both erosion and bioturbation may create "discontinuities" on individual bounding surfaces and across a set of laminae or laminasets, as tunnels, respectively. According to Johnson (1990), the effects of bioturbation change grain texture and sorting.

As discussed in this section, the key to characterising lamination is characterisation of hierarchical structures to estimate a set of parameters, as summarised in Table 2.1. The process of measuring, estimating and inferring parameters depends on features which mark of hierarchical structures, i.e. inter- and intra-LBS. Two factors that potentially contribute to characterisation of LBSs are: sudden variation of grain-pore geometry texture and compositional variation of haematite, together with dolomite, preferentially occurring at inter-LBS. Although bounding surfaces have been identified the best candidates indicating hierarchical structures, potential challenges exist, due to texture variation or distractions, as discussed. This section has identified appropriate parameters in the geological context and the real question of concern here is to come up with a design of image acquisition and characterisation to maximise the ability to estimate them by the most cost-effective means, reliably and robustly, which is to be studied in next section.

Table 2-1 Anticipated parameters to describe hierarchical lamination structures.

Laminaset	Estimate paleocurrent direction, wavelength parallel to and wave height at cross-section perpendicular to paleocurrent
Lamina	Estimate intersection angle parallel to paleo face and lamina thickness at cross-section perpendicular to paleocurrent
Grading	Estimate grading direction parallel to and grading gradient at cross-section perpendicular to paleocurrent

2.2 DCA

Digital core analysis (DCA) characterises the pore structures of a sample by imaging, image processing, and grain-pore reconstruction. A reconstructed grain and pore model can then be 'transformed' into a simpler model (e.g. a pore network model, (Jiang et al., 2007) on which multi-phase fluid flow processes and others can be simulated to predict properties of that sample (e.g. van Dijke and Sorbie (2003), McDougall and Sorbie (1993) or McDougall and Sorbie (1999)). This section reviews what existing characterisation techniques are commonly used in DCA and how they may be best used to image geological features of lamination, to identify and measure those features, and to reconstruct grain-pore models for a sample. It also identifies the limitations of those

techniques when they are extended for multi-scale characterisation with respect to lamination.

2.2.1 Imaging techniques

A wide range of imaging techniques are used in DCA characterisation. As the intention of this work is to demonstrate how to make use of the most cost-effective techniques to perform multiscale grain-pore characterisation for cross-lamination, only those techniques to be used in this work are reviewed briefly here, and their advantages and disadvantages will be summarised at the end.

2.2.1.1 Optical microscopy

Optical microscopy has long been used in petrographic analysis (e.g. (Chisholm, 1911, Andriani and Walsh, 2002). It is a type of microscope which uses visible light and a system of lenses to magnify images of transmitted light through a thin-section of a sample. A standard thin-section is about 2-4 cm wide and long with a thickness of 30 μm. According to Heintzmann and Ficz (2006), an optical microscope can provide resolution down to 0.23 μm, thus covering most grain-pore features of a fine clastic sandstone whose grains are typically over 0.1mm in diameter. An optical microscope enables a sample to be imaged at high resolution but low cost, and is, therefore, ideal for an exploratory study on grain-pore features.

Optical microscopes can be used with different light sources. Fluorescent and polarized lights are the two most popular light sources, especially for rock and mineral studies, among the many others, and can help distinguish mineral types associated with hierarchical structures of lamination for basic compositional analysis. Therefore a microscopy that supports these two types of lights is an important candidate for exploring compositional variations. Nishiyama and Kusuda (1994) claim that fluorescent microscopy appears to provide more distinguishability in pore spaces. Bultreys et al. (2016) note that when a sample is embedded in a blue coloured dye before making a thin section it can colour pores into brighter blue colour and yield higher contrast with the mostly greyscale minerals, to help analyse pores. However, an optical microscope tends to have a too small field of view (typically several thousand pixels at each dimension) to achieve high resolution for making statistical quantitative measurements over a large representative area or volume. This can be overcome by applying modern scanning optical microscopy.

Petrographic analysis is often combined with visual characterisation on a larger sample by exploring the differences of mineral grains in their reflection index and the differences in capillary force of variable pores. For iron and dolomite cemented LBSs, red or dark brown coloured LBSs would be observable under natural light. Although the smallest particle visible to the human eye is around 0.5um according to Curcio et al. (1990), the human eye can recognise a structure geometry as small as 100um (roughly the diameter of human hair), which is about a thickness of ~1-2 grains in a LBS in aeolian sandstone. To identify LBSs one may wet the surface of the sample with a wetting fluid, water for sandstones, to explore differential wet marks due to capillary force variation (Reading, 2009). Visual characterisation can provide a rich set of information about the lamination, and is a good exploratory technique.

2.2.1.2 Scanning Electron Microscopy (SEM) with energy-dispersive X-ray spectroscopy (EDS)

A SEM is a type of electron microscope that produces 2D images of a thin section sample by scanning it with a focused beam of electrons. An incident beam electron may pass through the sample without colliding with any atom in the sample atom, or may collide with an atom or the nucleus of the atom. In the latter two cases, the collisions lead to the emission of an electron, called a secondary electron, or the reflection of the incident electron, now referred to the backscattered electron, to be captured by dedicated detectors. Since a depression on the surface tends to trap secondary electrons and prevent them from being detected, the spatial variation in its counts taken during a period reflects the surface topography. On the other hand, since a low atomic weight element reflects fewer backscattered electrons than a high atomic weight element does during the same period, the count of backscattered electrons correlates mainly to density variation, and surface topography variation to a much less degree, as only a small number of backscattered electrons may be trapped by the surface topography. The electron beam position is combined with the detected signal to produce one dot on a phosphor screen, a pixel on a respective Secondary Electron (SE) image or Back Scattered Electron (BSE or BSEM) image. For each pixel, it is associated with an intensity value determined from accounts of detected signal, and the SE image value reflects the degree of depression while the BSE value is a BSE coefficient determined based on the work of Müller (1954), so that in terms of the atomic number, heavy (high atomic number) elements appear brighter in the image than lighter ones.

Furthermore, X-rays may be released along with the secondary electron emission, if an electron collides with an inner shell of an atom, which is forced to stabilise itself by allowing an outer electron to drop into that inner shell by releasing the extra energy of that outer shell electron. That extra energy is released in the form of X-ray. The emitted X-ray can be detected by Energy Dispersive Spectroscopy (EDS) to allow observers to identify what those particular elements are and their relative proportions in terms of atomic % at an emission spot area of around 1 μm in diameter. Reviews of SEM have been provided by Lloyd (1987) and Goldstein (2003).

An SE image is very useful for analysing the topography of a sample, as the image provides a 3D-like surface appearance (Reed, 2005), while a BSE image is used for analysing the variation of the atomic number (Z) element of the sample (Lawes, 1987). An EDS image provides information on chemical elements and proportions for more accurate composition characterisation. BSE and EDS images would be important sources of data for this work, to identify inter-LBSs, if they are preferentially cemented with relative heavier iron and dolomite, as demonstrated by De Boever et al. (2015), with a BSE image. As discussed, iron and dolomite are a result of diagenesis, which is one of the foundational reasons for the lithology variations in lamination. Therefore, EDS is important because the mineral elementary distribution in EDS is associated with the diagenesis process, as shown by Almarzooq et al. (2014).

Depending on the size of the phosphor screen, SEM can only scan a small area less than 10 mm^2 at a resolution of about 1 μm^2/ pixel. For a standard thin section, multiple scans can be performed to cover the whole area of the sample to yield a set of tiled images. Those images can then be stitched together to form an image at a submicron resolution on a large cm-scale FoV of a sample. Such SEM images are crucial for this work, as they can provide data about both grain and pore structures in the context of the hierarchical structures of lamination, including laminasets and their laminae, and serve as intermediate datasets to link with both high and low-resolution datasets for multiscale DCA characterisation.

Imaging artefacts may be induced in several ways but one of the key causes is the charging effect. The charging effect takes place on non-conductive materials as a result of the accumulation of static electric charges on the specimen's surface. This static charge influences the electron signals and thus image information. Several methods are adopted during the sample preparation and imaging in order to reduce the charging effect,

including coating non-conducting samples, geomaterials, with a thin conductive film (Robinson and Nickel, 1979). Carbon has been used as a coating element, as it has a relatively small effect on the X-ray spectrum and is good for EDS imaging (Reed, 2005). However carbon coating still has limitation, because it does not help increase the secondary electrons and therefore reduce artefacts due to the low secondary-electron yield like gold (Bultreys et al., 2016).

2.2.1.3 X-ray computed tomography (XRT)

X-ray Computed Tomography (X-Ray CT or XRT) is a type of non-destructive 3D imaging technique. In tomographic imaging, X-rays are directed at a sample from many orientations and the decrease in X-ray intensity is measured along a series of linear paths. The intensity reduction is described as a function of X-ray energy, path length, and material linear attenuation coefficient. From the acquired data of intensity reduction, computer algorithms can be used to reconstruct the distribution of X-ray attenuation coefficients in the sample volume being imaged for calculating normalised attenuation, called Hounsfield number or CT number, (Hounsfield, 1973), which is saved as intensity in a 3D grey-scale image. The image intensity is positively related to the atomic number (Z) of material at a voxel, and appears brighter for denser than for lighter materials (Herman, 2009).

High-resolution X-ray imaging has long been used to study smaller scale internal grains of rock samples (Dunsmuir et al., 1991). The resolution achieved by X-ray CT is directly related to the sample size, and the ratio of sample size to resolution is of the order of 10^3 (see Table 2.2 of Ketcham and Carlson (2001). According to Cnudde and Boone (2013), the applications of X-ray CT can be classified based on the sample size of the study. For typical centimetre to decimetre scale core samples, industrial CT or Macro X-ray CT (MXRT) with high-energy X-rays could be applied to achieve a voxel resolution of over 100 microns. At such resolution, most of the pores or grains cannot be resolved, but the pattern of closely arranged grains of similar composition may be apparent, because the intensity at each voxel reflects the average atomic numbers in the corresponding small sample volume. X-ray CT instruments have been developed to achieve a high voxel resolution around 1 micron down to 0.5 micron, and are here referred to as micro-X-ray CT (μXRT).

Table 2-2 General relationship between scale of observation and resolution (Ketcham and Carlson, 2001)

Scale of observation	Scale of resolution
m	mm
dm	100 μm
cm	10 μm
mm	μm

X-ray CT imaging has a wide range of applications in geoscience (see the survey of Ketcham and Carlson (2001)). According to Cnudde and Boone (2013): "when one is performing X-ray CT on core samples, the surface, as well as the internal features, including bedding features, sedimentary structures, natural and coring-induced fractures, cement distribution, small-scale grain size variation and density variation, can now be analysed" (summarised from Coles et al. (1991). This study attempts to make use of both Macro-XRT (MXRT) and micro-XRT instruments to identify structural patterns at mm to cm scales and grains and pores at μm scale, respectively, in conjunction with SEM and optical microscopy.

Several imaging artefacts may occur in XRT imaging and affect accurate characterisation of a sample. Among them, the common artefacts are ring and hardening effects. Ring artefacts are due to the mis-calibration of the detector or a defective detector, such as a sensitivity difference in the pixels of the detector. This results in rings centred on the centre of rotation. The ring artefacts appear as complete or partial circular strikes in the image. Figure 2.4(A) shows an example of the ring effect. Turpeinen (2015) noted that "ring artefacts are dominant scanner-based artefacts that can disturb the segmentation". Typically, ring artefacts can be reduced by applying filters, according to Herman (2009). To characterise lamination in this work, one must also consider the distortion caused by the ring artefacts to the continuity of bounding surfaces.

The hardening effect is a common artefact in XRT imaging using polychromatic x-ray beams. According to Herman (2009) the attenuation, μ, at a fixed point will always be greater for photons with lower energy. However, the energy spectrum of the x-ray beam changes (hardens) as it passes through the object. X-ray beams reaching a particular point inside the body from different directions are likely to have different spectra and thus will be attenuated differently. This makes it difficult to assign a single value to the attenuation coefficient at that point. Hardening effects could occur globally for a homogeneous sample and locally for an inhomogeneous sample. The global hardening effect leads to

the edges of an object appearing brighter than the centre, a cupping effect (see Figure 2.4(B) for an example). The local hardening effect leads to streaks and dark bands that appear around dense objects. Achterhold et al. (2013) explain that the presence of streaks and dark bands occurs because local absorption depends on the neighbouring material. The global hardening effect can be corrected by removing the background or simply cutting off the edge. On the other hand, the local hardening effect is much harder to mitigate and calls for application of a range of techniques, such as normalising the image by the average of beam hardening, dual energy scans to derive a virtual monochromatic image, and installing an anti-scatter grid in front the detector to deal with local scattering associated with heavy elements.

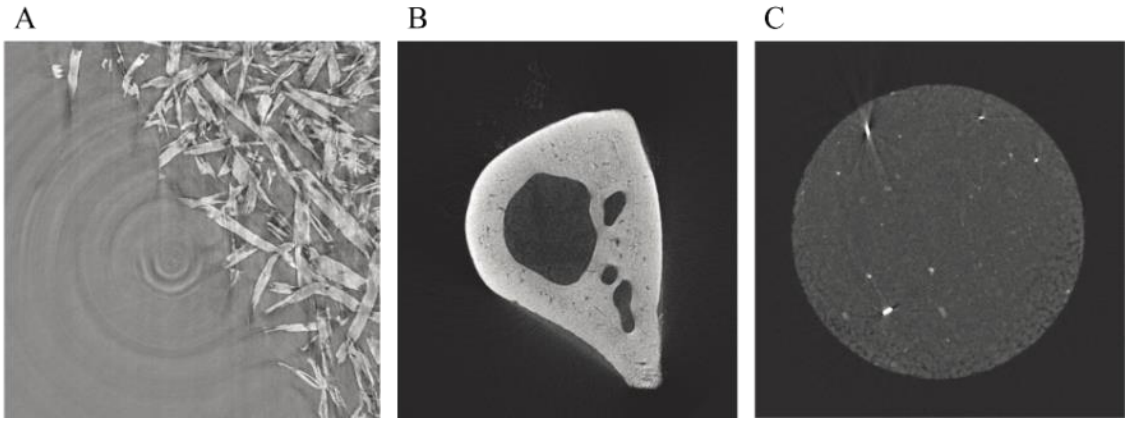

Figure 2.4 Examples of artefacts: (A) Ring artefacts on a paper sample; (B) The effect of beam hardening on a bone sample, in which the edges of the bone appear brighter than the inner material; (C) Streaks and shadows around metal inside a bentonite sample: Turpeinen (2015).

Local hardening effects can make it difficult to interpret images for particular features in lamination, such as an iron-concentrated bounding surface. In an MXRT image, the brighter spot of a heavier iron particle may appear larger than its true physical size, due to the scattering, and those iron particles that are actually scattered along the surface collectively appear as a continuous surface in the image. See Damcı and Çağatay (2016) for an example, where they imaged brighter iron particles in MXRT on a core sample at 60 μm voxel resolution and inferred the existence of continuous bounding surfaces by visual observation. On a laminated sandstone containing a plausible planar finite-thickness surface between laminae visualised from its side wall, De Boever et al. (2015) found that, due to grain-pore composition variation at the surface, a low-resolution XRT image contained useful signals on the existence of that surface in 3D which could not be confirmed based on grain texture analysis on a high-resolution image. This effect could be a useful indicator of the possible existence of a true bounding surface and its

approximate location, but must be accounted for when making an interpretation. In other words, the existence of a bounding surface must be confirmed by other techniques. On the other hand, for some heavier minerals that happen to be distributed evenly across the space, like feldspars, in some cases, they can induce local hardening, and for those close to a bounding surface, they induce scatters that overshadow the signals of other particles in the surface, leading to incorrect interpretation. Therefore, the role of mineral compositions needs to be investigated by other means to reveal true information on an image.

Furthermore, local hardening can cause a strong "blurring" effect at the interface of two grains when the acquisition is made at a low resolution, and this can introduce uncertainty if that interface is to be used as a reference. Figure 2.5 illustrates one example from Latham et al. (2008) where the author intends to register a µXRT image and a BSEM image acquired on the same sample at their respective resolutions. For the interest of this work, Figure 2.5 is further explained with iron and feldspar distinguished and labelled based on the geometric appearance that iron appears as cementation while feldspar appears as an elongated particle. For the registered Micro X-Ray Computed Tomography (µ-XRT) image on the right, the brighter part has mixed highlighted iron and feldspar as a result of the "blurring" effect, which can, however, be distinguished from the BSEM image on the left. One should note that in Figure 2.5 µ-XRT is applied; therefore, the resolution of the XRT image is still relatively high (2.69 μm^3/voxel) while the distraction of feldspar could be more significant for the MXRT image whose resolution is lower and has enlarged the local hardening "blurring" effect.

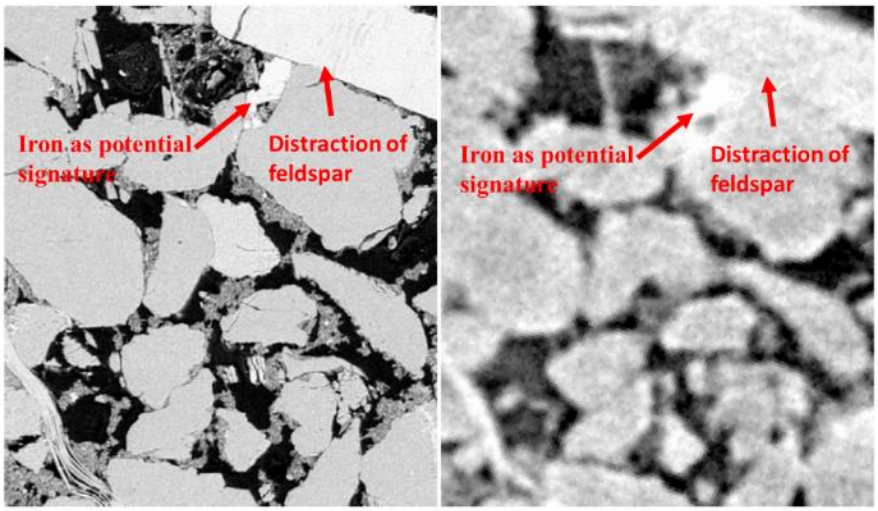

Figure 2.5 High-resolution BSEM image region at 0.1 μm^2/voxel (left) and registered region of micro-XRT 3D image at (right) at 2.69 μm^3/voxel: Latham et al. (2008)

The above-discussed artefacts are caused by the physical nature of imaging: the average imaging nature of the limited size of pixels also induces artefacts that infect the characterisation of porous media. When the resolution is low, and for porous media, an uncaptured pore below pixel size will partially fill the pixel and the obtained intensity would be averaged and thus smaller than the true material density; such an impact is referred to as the partial-volume effect. The averaging also means neighbouring pixels do not represent the true material density, and these are referred to as finite resolution induced blurring effects.

2.2.1.4 Summary

Table 2.3 summarises imaging techniques commonly used in DCA with respect to the following aspects: field of view, resolution, possible uses for lamination characterisation, sensitivity on dolomite and haematite or grain-pore geometry, advantages and disadvantages. Some of these aspects will be elaborated with the analysis in a later section.

Table 2-3 Summary of DCA imaging techniques (Dolomite and Haematite: D&H; Grain-Pore geometry: G-P geo)

Techniques	Sample field of view	Resolution	Interests of observation in lamination	Sensitivity on D&H or G-P geo	Advantages	Disadvantages
Visual observation	Hand-specimen sample at any size	> 100 Micro pixels	Surface view of inter- and intra-LBS	D&H present red colour	Large field of view to identify structure	Coarse surface view only
Optical microscope (Fluorescence and polarized light)	Thin section at 2-4 cm with thickness= 30 µm	Down to 0.23 μm^2/ voxel	G-P and mineral variation associated with lamina	D&H by composition sensitive feature	Cheap, quick fine-scale 2D observation	Limited FoV, lack 3D
SE	Non-polished sample clastic	Down to 1 nm^2/ voxel	G-P 3D surface	G-P geo 3D-like surface look	Quick fine-scale 3D surface topology	Small FoV
BSEM	Coated thin section at 2-4 cm with thickness =30 µm	Down to 100 nm^2/ voxel	G-P 2D surface	G-P geo 2D quantitative	Large FoV potential for registration, 2D G-P observation	Lack 3D, coating may distract true distribution
EDS	Thin section at 2-4 cm with thickness =30 µm	Down to 100 nm^2/ voxel	G-P 2D surface	D&H in colour map	Extend BSEM with compositional distribution and improve correlation	Lack 3D
Macro X-RT	Centimetre to decimetre scale core sample	> 100 μm^3/ voxel	Internal 3D of Hierarchical structures: Inter- and intra-LBS	D&H brighter intensity	Internal 3D of structure; Density sensitive nature on D&H	Artefacts may alter presentation of mineral distribution
Micro X-RT	Millimetre-scale core plug	Several μm^3/ voxel	G-P 3D	G-P geo 3D	Internal 3D of G-P	Small FoV

2.2.2 Image characterisation

In the previous section, common techniques for imaging acquisition have been reviewed. The focus of this section is on how to analyse them for the purpose of pore-scale characterisation by image processing. Such characterisation is concerned with exploring grains and pores in term of their structures and measuring their morphology in terms of shape, geometry and topology. In order to review this sub-field concisely and point to this study, all images are considered to be grey-scale intensity images and at each pixel or voxel, the intensity value is related to the physical properties of a material, such as reflection index (optical), depth of depression (secondary electron), backscattered electrons (BSEM), chemical element composition (EDS), absolute or normalised attenuation (XRT). The common process in image characterisation is 1) to pre-process images to enhance the features of interest; 2) to segment interesting features from the rest; 3) to measure features' morphology to quantify them. Many image processing techniques exist in general-purpose or dedicated image processing packages and can be used for this purpose (e.g. Avizo (www.Avizo.com); Fiji, or imageJ, (www.Fiji.sc) (Schindelin et al., 2012).

In the sub-sections that follow, key technical approaches which have been developed for each of these three elements, and are also relevant to this work, are reviewed. For recent dedicated reviews on digital image characterisation, the reader is referred to Andrä et al. (2013) or Turpeinen (2015).

2.2.2.1 Pre-processing

Images acquired on a sample typically contain noise and the aim of the pre-processing is to improve the signal-to-noise ratio (SNR) of an image so that features of concern, such as grains and pores, can subsequently be segmented correctly, with high certainty. Since many types of noises can arise in a typical rock image, it is difficult to filter out all types of noises by a single filter. Many filters have been tested in the past, but two of these turn out to be applicable to a wide range of rock images, and they are median filter and anisotropic diffusion (AD) filter (Andrä et al., 2013). The median filter replaces each original intensity at a point in an image by the median value of its neighbouring intensities (Francus, 1998, Van Den Berg et al., 2003) and can effectively reduce the random noise at each point with an abnormal intensity with respect to those at its surroundings, but is not so effective to preserve thin features like boundary contact between grains (Ghous et al., 2005). An AD filter has been applied to rock images (Ghous et al., 2005, Ismail et al.,

2013, Botha et al., 2015) to overcome the limitation of the median filter. Unlike the median filter, an AD filter diffuses the intensity at one point to its surroundings in an anisotropic manner, to avoid diffusing across the edge of objects, and so it ensures robust noise removal inside grains and grain edge contacts to be preserved. Figure 2.6 shows an example of an X-ray image before and after an AD filter is applied, to illustrate enhancement in contrast and preservation of edge contacts. For a recent review of digital rock image feature enhancing techniques, the reader is referred to Andrä et al. (2013).

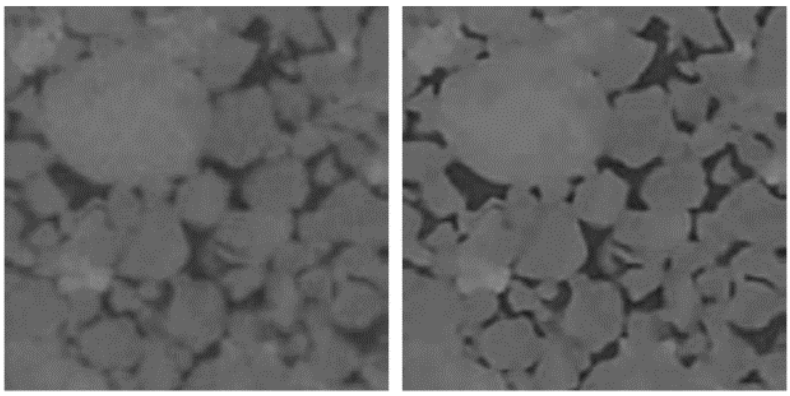

Figure 2.6 Left: original data set. Right: after anisotropic diffusion filters: Ghous et al. (2005).

2.2.2.2 Segmentation

The image segmentation is concerned with separating a feature or features of the same type from one another and from the rest in a pre-processed image. The simplest assumption to be made here is that there is a threshold intensity that separates the intensities of some features from the rest. This assumption may work only in the case where there is a contrast between the intensity of a feature and that of the others. For an XRT or BSEM image, segmentation is concerned with separating grains and pores. Because pores and grains have very different intensities, relating to the atomic number, a threshold may be easily identified from an intensity history of an image, if there is a single lowest frequency between two higher frequency intervals corresponding to low-pore and high grain-intensities. In this case, methods that can calculate the optimal threshold in a bi-modal histogram, such as the Otsu method (Otsu, 1975), are widely used for grain-pore segmentation (Blunt et al., 2013, Wildenschild and Sheppard, 2013). However, the intensity histogram of a rock image is multi-modal, due to the sample's composition variation, noises, the partial-volume effects occurring in the mixture of under-resolved pores and grains, and finite resolution induced blurring effects. This means that segmentation must consider multiple local thresholds. The watershed segmentation (see

Barnes et al. (2014) for a recent review) has found its use in this case. In watershed segmentation, an intensity map is treated as a topographic map including high point peaks and low point valleys, on which water can flow down towards valleys, and with the accumulation of water, the separation between accumulated water and air is defined as the waterline. Many watershed algorithms have been devised to deal with topography of different complexities. A basic watershed algorithm evenly fills (from the "sky") water on the topographic map, and to determine a boundary each time, the waterline in neighbouring valleys meet, so as to separate features. In grain and pore segmentation, the watershed algorithm can be applied on a distance map of the grey scale image, where pixel values are lowest (valley) at the centre of grains or pores, but highest (mountain peak) at the edge between grains and pores. The typical watershed algorithm identifies each and every peak in the topographic map, which may generate unwanted boundaries. The marker-based watershed algorithm proposed by Beucher and Meyer (1992) can deal with such a situation by subjectively selecting valley points as seed points, referred to as markers, for each feature, and then the watershed algorithm pushes the waterline on the intensity map from selected markers and only defines a boundary when meeting with the waterline from neighbouring markers.

When a segmentation method does not guarantee to segment grains from one another, other methods for separating grains needs to be applied before accurate measurements regarding grains can be made (Ismail et al., 2013). A typical method is based on cycles of erosion and dilation operations proposed by Russ and Woods (1995). However, Van Den Berg et al. (2003) claims the erosion of the grain phase may lead to over-segmented pores. Andrä et al. (2013) suggest another separation method, implemented in Avizo software, can more efficiently separate grains. The approach first calculates, on a segmented grain-pore image, the distance of each pixel to the closest centre of a grain, referred to as a distance map. Then the watershed algorithm is applied on a distance map to define boundaries between grains to separate grain particles.

Recently, Andrä et al. (2013) compared a watershed segmentation with grain separation on images after applying an AD filter, implemented in Avizo software, and the Otsu thresholding on the same images after applying the median filter, implemented in Fiji software, and claimed both approaches would work efficiently on grain-pore segmentation. In this work, it is believed that the former is more efficient for grain segmentation purposes because it separate grains which are connected to one another at

local touching points. However, the latter is more appropriate for pore segmentation because it is efficient from a computer simulation point of view and more accurate in segmenting pore space by avoiding an increase in porosity when removing touching points during separation. Therefore, in this work, both approaches are used, for grain and pore segmentation respectively.

2.2.2.3 Grain-pore measurements

When features of interest such as grains or pores have been segmented out from an image, morphologic properties can be measured from a segmented image for quantitative characterisation. A number of quantitative measurements may be made for grains and pores, as summarised in Turpeinen (2015). Only a few measurements relevant to this work are summarised in Table 2.4 for 2D and 3D images. For a segmented grain-pore image, area/volume can be calculated for each separated individual particle of grain or pore, reflecting their size. The area/ volume fraction can be calculated for either the grain or pore phase in an image or selected area and reflects the porosity of each phase. Orientation and circularity are measurements only to characterise the grain phase. Orientation is the preferred orientation of each individual grain, characterised by the major and minor axes of a fitted ellipse (see Figure 2.7 (left) for illustration). 3D measurements of orientation are defined as spherical coordinates (see Figure 2.7 (right) for illustration). Circularity is defined as dimensionless measurements correlated to the ratio of the area over perimeter square, and with a value of 1 indicating a perfect circle and 0 indicating an increasingly elongated shape. Circularity reflects elongated grains as secondary evidence of preferred orientation.

Table 2-4 2/3D measurements and associated features

Dimension	Size	Orientation	Shape	Size in porosity
2D	Area	Orientation	Circularity	Area Fraction
3D	Volume	Orientation phi	Circularity	Volume Fraction

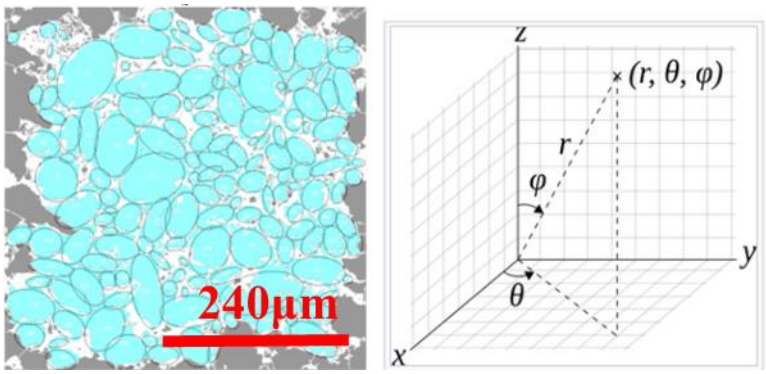

Figure 2.7 left: an illustration of measurement in an 800x800 pixels^2 sampling window with overlay mask and ellipses filled; right: Spherical coordinates (r, θ, φ) are often used in mathematics: radial distance r, azimuthal angle θ, and polar angle φ. The meanings of θ and φ have been swapped compared to the physics convention (see (Moon and Spencer, 2012).

Techniques for making grain measurements have been well-established for segmented images and implemented in software packages like Avizo and Fiji. However, when the statistics of those measurements of grains are of interest, special care must be taken to ensure the statistics for specific measurements are meaningful and representative. With respect to estimating preferred grain orientation, researchers (Baas 2000, Baas et al. 2007) have considered the case where a sample contains a mixture of large and small grain particles. Since large grains tend to function as load-bearing framework grains while small grain particles tend to fill between the large grains, the orientations of the large grains should be representative, and tend to be much less random than those of the small grains (Pettijohn, 1987, Branney and Kokelaar, 2002). Therefore, in this case only large grains should be considered, although there is no guidance for setting a threshold to divide large and small grains (Baas et al., 2007). For the preferred orientation, it is noted that the arithmetic means of all large grain orientations is not useful but a quadrant-based average orientation should be used, as suggested by Baas (2000).

2.2.2.4 Trend of grain textures by sampling

In a sample where the grain textures exhibit spatial, non-stationary (heterogeneous) distribution, there is a need to characterise the spatial trend for each grain texture measurement from a segmented image. A spatial trend may be used to register this image and others that are acquired at low resolutions. Given an image, a spatial trend may be evaluated over a set of sampling windows that together cover that image. To define those windows, the following parameters must be considered: sampling window size and interval.

A sampling window must be not only large enough so that statistics estimated on that window become meaningful and stable from noises (Anguy et al., 1994, Buchter et al.,

1994) but also small enough so that the measured statistics estimate local stationary distributions. With respect to determining the trend of grain grading in lamination, both (Van Den Berg et al., 2003, Ghous et al., 2005) set their sampling window size to the thickness of the thinnest lamina. To determine a representative window size, a heuristic procedure may be derived to calculate some statistics on windows of a certain size while adjusting that size until given criteria are satisfied. Such criteria may be defined as the inequality of the coefficient of variation (Cv) and the ratio of standard deviation to mean, for selected measurement(s) in windows.

The sampling interval determines how far one window should be away from another during sampling, and how safely the quantities derived on the two windows can be interpreted as a smooth variation in the window size. For sampling structures in laminations, Naruse and Masuda (2006) suggest that a sampling interval should be as large as possible, to reduce computation cost, as long as it is no larger than the thickness of a structure, to ensure its true smooth variation is captured seamlessly. Ghous et al. (2005) use an extreme interval of one pixel on the μXRT image to capture the detailed variation of the sampling window size at a cost of high computation.

For hierarchical structures like cross-lamination, sampling needs to be performed for each specific structural feature. The principles for determining window size and interval given above must be applied with respect to the distributions of each corresponding feature. This means that the windows go along the feature. For a given feature observable at a coarser scale than grains, such as an LBS or lamina, the exploratory analysis may be applied to identify them (see Chapter 3 for elaboration).

2.2.3 Pore structure reconstruction

Pore structure reconstruction is concerned with generating one or more sets of image realisations that honour information about a sample obtained from the image characterisation summarised above, so as to perform sensitivity analyses at different scenarios and reduce the cost of taking additional samples and images. Due to the complexity of a real rock sample, a reconstructed volume is a simplified version of that sample, in the best manner that is practical. For modelling fluid flow through the pore space of a sample, most reconstruction techniques generate a model that resembles the observed pore space of a sample only in terms of statistical geometry properties. All reconstruction methods are stochastic in nature, as statistical geometry properties about a sample are incomplete, and obtained only in its subdomain. It is worth noting that many

other important flow-influencing factors, such as the mineralogy of the pore space and thus the wettability of pore surfaces, are not considered in the reconstruction and thus will not be discussed in this work, although their effects may be explored through sensitivity analysis in flow modelling, in a manner that does not reflect their true spatial distributions.

Stochastic simulation techniques have been developed for grain-pore reconstruction by matching statistical correlation functions, low-order microstructural descriptors, such as autocorrelation function, two-point probability function and lineal-path function for pores and grains (Liang et al., 1998, Yeong and Torquato, 1998, Torquato, 2002). When statistical correlation functions may be estimated from segmented images acquired on a sample, a stochastic simulation, like simulated annealing, is performed to match multiple functions simultaneously. This approach may fail to reproduce the long-range connectivity of pore space, in particular for a low-porosity system (Okabe and Blunt, 2004).

Process-based reconstruction stochastically simulates grain deposition, compaction and cementation (Bryant and Blunt, 1992, Bryant et al., 1993, Øren and Bakke, 2002) sequentially for each specific depositional environment. For a sample, imaging and image characterisation are utilised to derive information on grain textures and lithology, grain correlation, and styles of compaction and cementation, to set up a stochastic simulation. The outcome of this reconstruction is a set of contacting grains that may be cemented. These results can be discretised into image volume. For an actual sandstone, it has been shown that this approach reproduces adequately important intrinsic properties, such as the degree of connectivity, the specific internal surface, and the two-point correlation function (Øren and Bakke, 2002). This approach is dependent on the depositional process.

Pattern-based reconstruction attempts to reproduce the grain-pore structures for a sample to match grain-pore patterns, on a fixed-sized window, observed in segmented images for that sample, referred to as training images. A stochastic simulation is then performed to assign a label of pore or grain to each voxel in the simulation domain, so as to maximize the reproduction of the 'most likely pattern' at that location with respect to all other labels in the window. The 'most likely pattern' is defined as specific to each scheme and determined from the training images. (Wu et al., 2004, Wu et al., 2006) developed an efficient Markov Chain Monte Carlo (MCMC) simulation scheme in which pores are assumed as a Markov random field and the 'most likely pattern' is determined to reach

the highest transition probability from one pattern to another. Multiple-Point Simulations (MPS) were applied by (Okabe and Blunt, 2004, Hajizadeh et al., 2011) and the 'most likely pattern' is determined by the highest probability of all possible patterns. Both schemes have been shown to be able to reproduce observed grain-pore patterns, connectivity and correlation functions.

All the methods mentioned above are designed to deal with stationary spatial distributions in the domain, based on the given sample and can, therefore, reproduce grain and pore structures well for homogeneous samples. However, they cannot handle non-stationary grain textures across a set of sub-domains and must be adapted if they are to be used to reproduce grain and pore structures for strongly heterogeneous samples, such as the laminated sandstones of concern in this work.

2.3 DCA for multiscale characterisation: key challenges and approaches for solutions

The DCA characterisation techniques reviewed above have limited use in characterising samples that contain multiscale geological structures, like cross-lamination. In this section, DCA's limitations for multiscale characterisation are examined to identify key challenges faced in DCA and to propose plausible approaches to develop the needed solutions. This is done according to the three categories of research questions given in Chapter 1.

2.3.1 Sub-sampling and characterisation

As summarised in section 1.2.1, standard DCA imaging techniques are devised mainly for the purpose of capturing internal structures of grains (their compositions and pores). If a tomogram of a laminated sandstone sample is to be acquired, a µ-XRT would be the most suitable tool. However, if resolving shapes of pores of 1 µm in diameter is sought, a sample must be smaller than around 1 mm in diameter (estimated based on an imaging field of view of 1000x1000x1000 voxels^3 in typical µ-XRT facilities). On a sample of such size imaged at that resolution, individual features can be studied in detail, as demonstrated in previous work (Van Den Berg et al., 2003, Ghous et al., 2005), with respect to the laminae. However, it is not possible to tell what hierarchical structures exist and are observed, let alone how they spatially relate to one another at corresponding scales and how they could be explored consistently. To answer these questions, it would be ideal if a tomogram could be acquired on a sample large enough to encapsulate a full set of plausible structures of interest. An MXRT is capable of making an acquisition on a

large sample but at much lower resolution, insufficient to resolve a thin feature of a few grains thick, such as LBSs. Nevertheless, if a LBS does contain a high proportion of a high atomic number heavy element (e.g. iron) in grain particles along with it, the thin feature may stand out on an acquired tomogram, because the heavy particles influence the average attenuation disproportionately and the X-ray scattering effect induced by heavy elements, as mentioned in 1.2.2.

What has been argued above is that there is no single imaging technique that can meet the needs of characterising a laminated sample and thus, multiple imaging techniques must also be applied at different scales and resolutions collaboratively to achieve the goals stated in the research questions in relation to sub-sampling and characterisation. The principle considerations should take place at three levels as follows.

Methodology

The research questions range from being exploratory (e.g. what features are there?) to quantitative (e.g. how thick are laminae on average?) in nature, and exploratory ones must be answered first. For a new sample, the sub-sampling and characterisation must be carried out by a combination of exploratory analysis and quantitative analysis. An exploratory analysis is always needed to reveal what may exist in what forms, to define what is needed next – quantitative or exploratory analysis.

Procedure

Given the hierarchical structures anticipated in a laminated sample, what structures should be considered, and in what order? Based on the geo-pseudo concept, a top-down sampling approach is the most appropriate, as a larger structure is likely to influence the fluid flow more strongly than the smaller one does and to be observed with a higher level of certainty. A top-down sampling needs to be carried out overlapping sub-domains, so that all resultant image datasets can be registered onto the same coordinate system, if shared features can be identified among them.

Techniques

In order to investigate what hierarchical structures there are in a sample, an exploratory analysis must be carried out on a sample large enough to encapsulate a set of possible structures of interest. From a cost-effectiveness point of view, one should consider applying visual inspection and classical petrographic techniques, as reviewed previously, to explore a sample for signs of geological features and relationships before applying

more sophisticated and more costly techniques when needed to progress. The exact sequence of techniques to be applied should be decided interactively for each specific sample. Based on the previous work of De Boever et al. (2015) (they focus on single bounding surface only; also see discussion later), for any quantitative characterisation of a cross-laminated sample, a minimum set of imaging tools would need to include SEM/EDS and M/μXRT.

2.3.2 Identification of shared features and image registration

Sub-sampling and characterisation result in a set of enhanced and characterised image datasets, and these must be registered to characterise the whole sample. A critical question of concern is whether shared geological features can actually be identified from those image datasets with high certainty.

For vuggy carbonate rocks, it has been demonstrated that grain textures are a good shared feature. Sok et al. (2010) imaged a carbonate rock sample using a micro X-ray tomogram, BSEM, and focused ion beam SEM (FIB-SEM), at the maximum-to-minimum resolution ratio of about 10, and integrated them using a disproportionally large grain as the reference. As reviewed above, in a laminated aeolian sandstone sample, grain textures are not suitable candidates as shared features because grain textures are rather homogeneous, with weakly non- stationarity within each structure. However, grain composition variation along thin inter-LBSs makes these the best-shared features, as they can be observed and identified in low-resolution MXRT images as ‘trends’.

This situation is well illustrated using the SEM and μXRT images obtained by De Boever et al. (2015). Figure 2.8 shows those images, all acquired from the same sample with a likely planar bounding surface between two vertically-stacked laminae. Figure 2.8(A-B) shows BSEM and EDS images on a vertical face cutting through the surface with respect to the sample orientation, given in Figure 2.8(F), in which the strong planar cloud of unevenly distributed brighter light-grey ‘dots’ suggests the existence of a surface. Note that in Figure 2.8(A), there is no indication of the existence of that surface, but in Figure 2.8(B) there is a linear pattern of higher concentration of scattered red pixels of iron-rich elements that suggest that a surface may be located here, in consistency with geological understanding. The same observations can be made in Figure 2.8(C-E).

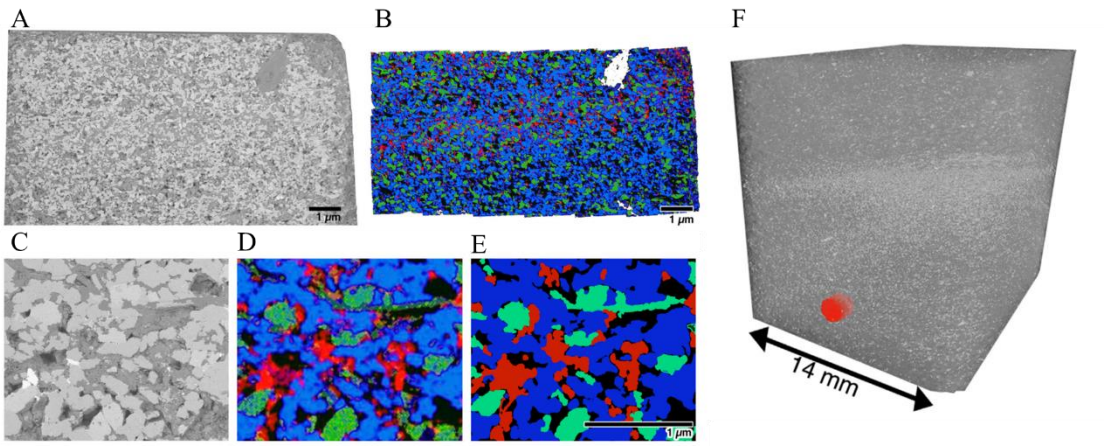

Figure 2.8 SEM images and the µXRT image acquired with respect to a bounding surface (De Boever et al., 2015). (A-B) BSEM image and corresponding EDS map at 1.08 µm^2/voxel. Blue = quartz, green = clays and feldspars, red = iron oxides; (C) zoomed-in view of BSEM image; (D) zoomed-in view of EDS map; (E) simplified EDS map so that grains can be identified individually as different minerals; (F) µXRT with a resolution of 8.9 µm^3/voxel. Note that the partially transparent full sample view reveals that dense minerals, represented in lighter grey, are unevenly distributed throughout the sample

For the image datasets of De Boever et al. (2015), the tasks of identifying inter-LBSs can be defined as to reconstruct a bounding surface from the planar cloud of bright dots in µXRT image and SEM images, respectively, where the reconstructed bounding surface and curve are defined on respective images with the same resolution as the µXRT image. The identified bounding surface can then serve as a reference to register high- and low-resolution images to fuse grain-pore structures into structured lamination. So far, neither of these two tasks has been considered for image registration. The major challenges are due to the scarcity and irregularity of 'good' signals, as consequences of the complex geology associated with inter-LBSs and induced artefacts in imaging and image processing.

In the sections that follow, the issues relating to the reconstruction of bounding surfaces and curves from XRT and SEM images, respectively, are elucidated first, followed by a brief summary of relevant techniques that may be adopted for reconstruction.

2.3.2.1 Challenge-1: Reconstructing a bounding surface from XRT

In a low-resolution XRT image in which a bounding surface appears as a surface-like cloud of bright 'dots', those "dots" can appear scarce and/or irregular for a number of reasons. As reviewed previously, the scarcity of 'dots' may reflect the true geological distribution of a small number of heavier grain elements that occur along the surface and across the surface within a finite band. Those elements are likely to induce artefacts during imaging, such as local hardening effects and scattering effects, which make the cloud appear thicker than the LBS should be. The scarcity gives rise to 'fake' gaps in the

image. The irregularity of 'dots', on the other hand, may reflect geological processes such as the change in supplied sediments, erosion that took place and bioturbation, and it gives rise to large 'true' gaps in the image.

The challenge is how to reconstruct a continuous thin surface to fit through the middle of an unknown true surface.

2.3.2.2 Challenge-2: Reconstructing a bounding surface from SEM images

A bounding surface may not be recognisable on SEM images at a very high resolution when the discrete objects are all observed, unless the images are upscaled. An optimal upscaling ratio of a high over a low resolution must be chosen appropriately to bring the bounding surface out as a trend. However, in order to register an XRT and SEM images, the SEM images must be upscaled to an image at the resolution of the XRT to transform features to the same physical scale before applying for image registration. If that upscaling ratio is much larger than the optimal upscaling, less information about the bounding surface (e.g. heavy grain elements) will be retained, if any, after upscaling. In practice, an upscaling ratio is a factor of about 10 when only one bounding surface is considered alone (e.g., De Boever et al. (2015) but that ratio can reach up to 100 when multiple bounding surfaces are considered together, as the sample has to be much larger. As to be illustrated later in Chapter 4, the classical rescaling techniques by either linear or nonlinear (cubic) scaling on a BSE image fails to retain any information on a bounding surface. The challenge is how to retain information on a bounding surface after upscaling to enable reconstruction of one bounding curve for registration.

2.3.2.3 Relevant techniques for reconstructing a bounding surface from XRT

The challenges of reconstructing a continuous thin surface to fit through the middle of an unknown true surface, while respecting information obtained regarding the various gaps are rarely discussed in DCA. It is, however, similar to the problem of segmenting a piece-wise linear or planar structure with connectivity preserved, and have been discussed in relation to many other subjects, like the segmentation of cracks in mechanical parts (Abdel-Qader et al., 2003, Fujita and Hamamoto, 2011) or human bones (Kang et al., 2003, Descoteaux et al., 2006). One of the common characters across those studies is applying multiple filters to characterise small neighbouring areas, thus segmenting a pixel based on multiple local features rather than the pixel intensity itself, so that the thin un-obvious bounding surface can be recognized from the complicated noisy background.

A filter as referred to here is often a small window at a certain size with a specific designed mathematical operation on pixel values within the window to describe different aspects of neighbouring structure features around the centre pixel. Considering each filter describes different aspects of the structure, a set of filters are often applied together to capture different aspects and enhance recognition of the structure. Two ways of using a set of filters generally apply: 1) the set of filters could be applied sequentially to yield a grey-scale image with structures enhanced. On the outcome image, typical segmentation approaches may be applied to segment the targeted structures (Lesage et al., 2009, Balafar et al., 2010); 2) The other way is to use a set of filters describing different aspects of structure in parallel on the original image to yield a set of descriptors of local features around each pixel, referred to as feature vectors. The pixels in the image can, therefore, be seen as data points distributed (described) in a multidimensional feature vector field. Those data points can then be fed into more sophisticated classification methods to classify those data points in the multidimensional feature vector field into different groups, and thus the image is segmented.

The sequential filtering approach has so far achieved limited success in overcoming the challenge, because sequentially applying filters to render information in the intensity may lose important aspects of structures in the process that capture the true connectivity. For the parallel filtering approach, sophisticated classification methods including unsupervised and supervised classification could apply. The unsupervised method groups data in the high-dimensional feature field directly, based on mathematical operations, for example, the long-developed K-mean method by MacQueen (1967) groups data based on spatial clustering of data in the feature vector field. Supervised classification, in contrast, learns a classifier in the feature vector field from a subset of data with known group belongings, referred to as ground truth (Buhmann et al., 1999, Mohri et al., 2012) from one or more example image, referred to as a training image, and to predict group belongings on a new images, referred to as a testing image. The supervised approach naturally fits this work, because human knowledge about various gaps can be introduced, together with a wide range of readily available classification algorithms and is also generic, as long as a suitable set of image filters can be established.

The set of filters, termed a filter-bank, naturally fits the introduced supervised classification approach and has been proven to work efficiently on piece-wise linear structure segmentation (Xu et al., 2006, Rigamonti et al., 2011b, Becker et al., 2013).

This leads to a class of filter-bank based supervised piece-wise linear/planar segmentation methods (with a typical workflow shown in Figure 2.9) that share the following common characteristics: 1) using a bank of filters to extract features of concern; 2) using training images to bring in additional information by given ground truth of pixels whose original intensity is less obvious on connectivity in the original images; 3) employing machine-learning algorithms to learn relationships between features and the ground truth in the training images and to construct a classifier to segment the testing image.

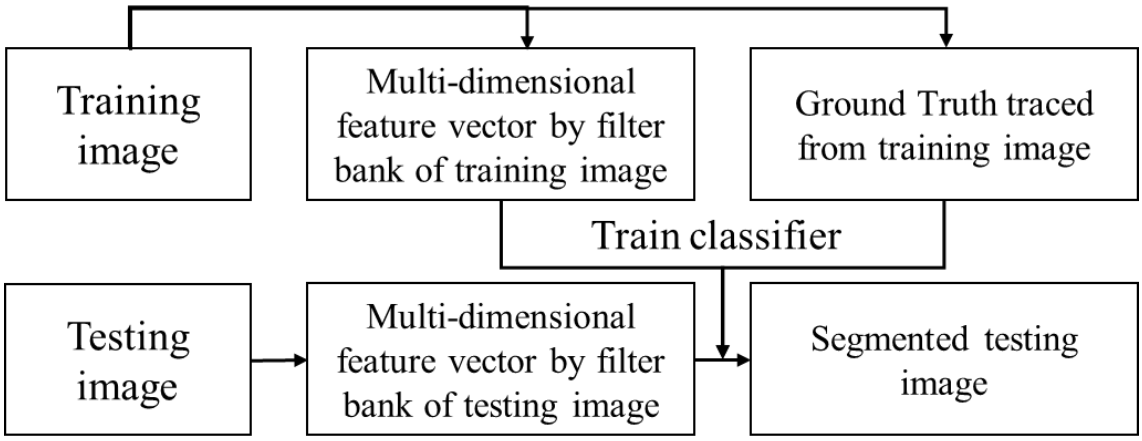

Figure 2.9 Typical procedure of supervised classification with filter bank

Although segmenting a piece-wise linear/planar structure from a noise background by a filter bank-based supervised classification has been discussed in many subject areas, systematic investigation into why, how and to what extent the approach could be applied to improving segmented connectivity in relation to the construction of training images and the selection of suitable banks of filters is required. Clearly, a good understanding of these is crucial to develop optimal methods to ultimately overcome the challenge. This work will discuss how a set of controlling factors related to the nature of the challenge of segmenting a bounding surface can be used to segment it in a way that will reflect the true nature of its connectivity.

2.3.2.4 Relevant techniques for reconstructing a bounding surface from BSEM

To retain the trend of a bounding surface, based on the previous review of the nature of bounding surfaces, the composition must be considered. What has been proposed here and is to be explored in this work is to identify the controlling factors that highlight a bounding surface through geological characterisation. With the assistance of the compositional map provided by EDS that can be obtained at identical resolution and FoV as BSEM, the composition distribution can be taken into account during upscaling, to retain the key patterns of bounding for registration purposes.

2.3.3 Non-stationary reconstruction

Supposing all the necessary datasets are registered at the same coordinate system and characterised individually and collectively, the following subsections discuss how the pore-grain non-stationarity that is expressed by the spatial relationships of structures can be represented and modelled in a stochastic reconstruction procedure.

2.3.3.1 Geological non-stationary nature and characterisation

Stationarity is an assumption that is often reasonable for spatial data and commonly used in geostatistics (Olea, 2012). In mathematical terms, there are two types of stationarity, according to Deutsch and Journel (1998). One is mean stationarity, where it is assumed that the mean is constant between samples and is independent of location. Second-order stationarity is the assumption that the covariance between two points is the same for a given distance and direction, regardless of which two points are chosen within the sample. As reviewed above, the multi-scale arrangements of hierarchical structures define the heterogeneity (thus non-stationarity) of grain-pore lithology distributions, including grain texture and composition. It is, therefore, necessary to develop multiscale DCA to characterise and reconstruct the local non-stationary grain-pore lithology associated with hierarchical lamination structures, to study the combined impact on fluid flow. Given that laminations are formed layer by layer, it can be seen that each ~1-2 grains thick layer has homogeneous grain-pore lithology and is the smallest stationary unit. Among the previously reviewed lithology features, as a result of grading, grain textures including grain size and orientation vary over layers within laminae and laminasets and can be characterised to define non-stationary grain texture variation (Reading, 2009). Grain shape can also be characterised but only as additional evidence of variation in orientation. In aeolian lamination, grain composition variations tend to be more prominent than grain texture variations between laiminasets, and composition variations can thus be used to characterise inter-LBSs and are of use to characterise the pattern of the structures, as discussed in 2.1.3. Although, according to van Dijke et al. (2007), composition distribution also affects fluid flow in a more sophisticated way (e.g. pore surface wettability), this work will only focus on estimating the variation of grain texture parameters to seek simplicity in an initial multiscale characterisation and reconstruction workflow, and use the compositional feature only as a signature highlighting hierarchical structures.

To serve later reconstruction, the non-stationarity may be represented conceptually as a volumetric index map on the sample domain, where each index links to a set of parameters that define the local mean (stationarity) of the grain-pore textures to instruct stochastic reconstruction at a point in space with respect to non-stationary distribution across points. For the cross-lamination of concern in this work, such an index map could be constructed from characterisations of sample hierarchical laminaset and lamina structures and local pore-grain distributions, in accordance with layered grading. Based on the review, it has been established that the inter-LBSs is more likely to be reconstructed directly with relatively high certainty in a MXRT image, based on compositional variation. The reconstructed inter-LBSs represent one realisation of laminaset structure distribution in contrast to the probability map based approach used by Mohebi et al. (2009), where a set of realisations could be reconstructed. Intra-LBSs may be more difficult to reconstruct directly but may be indirectly reconstructed based on measurable parameters, including intersection angle and thickness, to infer lamina structure distribution. In this way, inter- and intra-LBSs, as the markers of preserved structures, can be taken as the basis of a non-stationary trend map of hierarchical structures. The non-stationary variations within each lamina can be estimated by assuming each ~1-2 grains-thick layer as the smallest stationary unit; with grading direction characterised, conceptual layers can be reconstructed stacking over inter- or intra-LBS. A volumetric index map can, therefore, be defined by assigning non-stationary parameters based on the measured trend of grain texture variations, including size variation, by grading gradient and preferred orientations. The parameters required to define an index map are summarised in Table 2.5. The key to characterisation is, therefore, a data-driven statistical parameter collection to estimate the stationary and non-stationary grain-pore texture distribution associated with hierarchical structures.

Table 2-5 Parameters for describing hierarchical lamination structures.

Laminaset	Directly reconstructed from MXRT
Lamina	Indirectly reconstructed by intersecting angle and thickness
Grading	Indirectly reconstructed by grading direction, grain size grading gradient and preferred orientation distribution

2.3.3.2 Reconstruction: MPS for grain-pore

Not all stochastic reconstruction techniques are designed to handle an index map as described above, although some of them do so to some degree. With an index map, each stationary unit can be seen as a sub-domain, and a stochastic method is expected to have

the following characteristics: 1) reconstructing complex but rather stationary grain-pore topology and morphology with given examples from a sub-sample, respecting means and variograms; 2) transforming a given grain-pore structure based on a set of grain and pore geometrical means and variograms assigned to the specific spatial domain; 3) personalised regional reconstruction based on defined sub-domains honouring boundary connectivity (thus the reconstructed grain-pore-space in different neighbouring regions are connected naturally).

Based on the review in 2.2.3, it was found that the statistical approach has been weak in revealing the complex grain-pore structure and the processed approach been lacking in generalisability, while the pattern-based approach is worth consideration, as it borrows statistics from the patterns of training images directly, rather than 2-point variograms or kriging statistics, thus reducing the risk of exporting details irrelevant to target heterogeneity by the simplified statistical method (Strebelle, 2002). Two pattern-based approaches, referred to as MCMC (Wu et al., 2004) and MPS by single normal equation simulation (SNESIM), developed by Strebelle (2002) have been compared, with full details provided in Appendix A.1. The key conclusions related to this work are: 1) typical MCMC does not apply regional sub-domain-based reconstruction with transformation while MPS does; 2) MPS regional reconstruction also respects pre-reconstructed grain-pore structure from neighbouring pre-simulated regions as hard data and therefore, connectivity is retained at the boundary between regions. The regional reconstruction advantage of MPS makes it naturally fit for modelling non-stationary grain-pore variation associated with hierarchical lamination structures. Therefore, in this work, MPS is employed in the workflow for full 3D pore-space reconstruction.

A detailed mathematical expression of the MPS reconstruction procedure is given in Appendix A.2. The key steps of MPS are as follows: 1) a fixed size template goes though every pixel of the training image to collect image patterns around the central pixel to build a patterns library; 2) for each pattern in the library, the probability of the central pixel in the state of “1” or “0” can be calculated; 3) on a new canvas, the template visits every pixel, in a random path, to establish the state of each visited pixel, condition to the neighbouring pattern and the corresponding probability is saved in the library. It is pointed out by both Strebelle (2002) and (Okabe and Blunt, 2004) that the mean and variogram of the training image could be reproduced with MPS, thus ensuring the stationarity is reproduced in a simulated sub-domain. Beyond basic MPS, the key

regional sub-domain reconstruction features of MPS specific to the interests of this work, are as follows: 1) to simulate non-stationarity, regional reconstruction transforms a given training image according to the grading nature of the lamination by scaling and rotating it correlated to the given index, to give new training images and stochastically reconstruct them over the regions; 2) to ensure the transformed structure still connects naturally at the boundary between regions, the reconstruction is performed sequentially for the regions. The reconstructed image for one region would be taken as hard data to condition the reconstruction of pixels at the boundary of the next region, by extending the domain of next region to include hard data from the previous region. Figure 2.10(A) illustrates a training image scaled at three scales, in which the largest pore-space is assigned to the bottom region and the smallest to the top region. A rotation feature rotates the training image so that the reconstructed image is also rotated for different regions. Figure 2.10(B) illustrates a training image rotated -30^{o}, 0 ^{o} and 30 ^{o} to reconstruct the rotated channel pattern to the green, blue and red regions respectively.

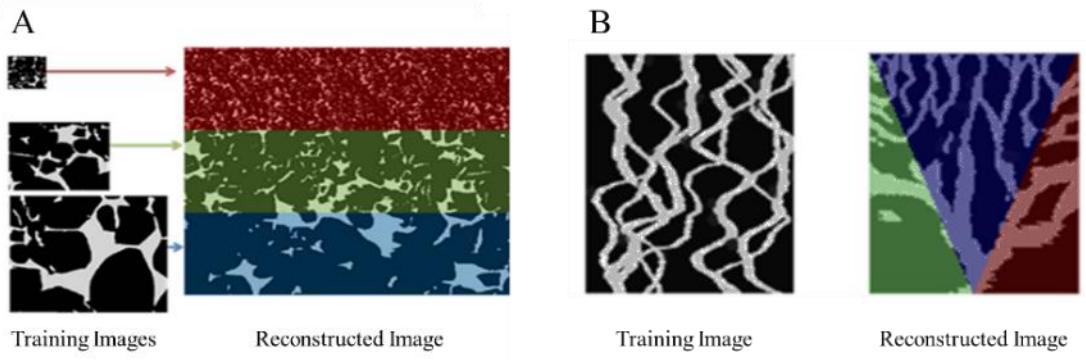

Figure 2.10 Key features of MPS respecting layered grading nature: A) regional reconstruction with training image at different scaling factor; regions are reconstructed sequentially each taking the previous reconstructed region as hard data to keep boundary connectivity; B) Training image assigned rotation of -30^{o}, 0 ^{o}, 30 ^{o} to green, blue and red regions respectively. Scaling factor of 3 was also applied to all three regions.

Key features of MPS which contribute to grain-pore-space reconstruction of a grading system are summarised in Table 2.6 (based on the SNESIM function built in the SGeMS software package (Remy et al., 2009)), which are the template features dealing with its potentially heterogeneous grain-pore nature; regional scaling and rotation simulate the variation in grain size and orientation associated with grading. The hard data constrained regional simulation ensures connectivity between regionally simulated grading for laminae and laminasets.

Table 2-6 Summary of key features of the contribution of MPS to pore-space reconstruction of layered grading system

Feature	Template scan through training image	Hard data honoured reconstruction	Regional scaling	Regional rotation
Advantage	Handles complex structures	Preserves Connectivity	Simulates grading size	Simulates grading orientation

When using the discussed MPS method to address the challenge of non-stationary grain-pore reconstruction, another challenge is that the reconstruction of the full 3D pore space model could require significant computational power. Given the multiscale nature of lamina sandstone, a microscale model is required for a centimetre scale domain to cover representation of the inter-laminasets. The microscale resolution for a typical fine sandstone could be less than 4um^3/voxel to capture pore-space. For a representative cross lamina structure, a model of at least 5cm^3 is required. Therefore, a full 3D pore-space model with dimensions of 12500^3 voxels is required. As a single CPU simulator is not practical in solving such a problem, a strategy needs to be developed to perform the simulation in parallel.

2.4 Design of workflow

This chapter reviewed the literature in general to establish 1) the non-stationary grain-pore variation associated with hierarchical structures and their features; 2) imaging, characterisation and reconstruction methods used in DCA and 3) it has reviewed the application of DCA in characterisation of multiscale features of lamination and identified potential limitations and challenges that could occur in a general sense along with potential solutions. Because of the complexity of hierarchical structures and their case-specific relationship with DCA characterisation techniques, for an unknown sample to be studied, any generically applicable workflow must also be sample specific. The workflow must be designed as a combination of exploratory analysis and quantitative analysis to confirm structural features of interest, followed by their correlation to appropriate DCA techniques, to design a workflow and confirm challenges so as to develop solutions. Such a workflow/methodology can be: 1) carry out an exploratory analysis (i.e. preliminary analysis) to find out the geological background and coarsest structural information at least cost, and then carry out subsampling by a combination of exploratory analysis and quantitative analysis, targeting each type of feature anticipated respecting general geological knowledge; 2) extract shared features from quantitative

datasets, and carry out registration; 3) define a non-stationary index map and perform the reconstruction. A workflow specific to an aeolian sandstone sample has been selected in this work, each proposed step can be explained as follows:

Step I: The workflow starts with exploratory analysis by traditional petrography and preliminary lithology and compositional analysis using SE, BSEM and EDS to estimate the scale range and build an understanding of the spatial distribution of structures and identify the potential cross-scale reference. To characterise the hierarchical structures of lamination according to scales of structure in relation to the resolution range of each imaging technique, as summarised in Figure 2.11, it is necessary to image the inter-laminaset of a sample by MXRT and to characterise the inter-laminaset structure. The laminaset structure is potentially highlighted by the preferred cemented iron in inter-LBS, which could be identifed in the MXRT image. The identification of the bounding surface allows one to determine how many subsamples are needed for imaging local lithology spatial variation, where their sites should be and at what scale each sub-scale of imaging should be taken. According to Figure 2.11, further application of digital BSEM and EDS analysis is anticipated to give quantitative measurements covering hierarchical structures from laminaset level down to grain-pore in 2D, in order to analyse their spatial correlation, together with MXRT images. These analyses would together determine the further sampling configuration of a smaller core plug for 3D μ-XRT analysis. The analysis is again anticipated to correlate with the knowledge of the hierarchical structure identified previously. To assist the spatial correlation of the obtained multiscale datasets though registration, the nature of the bounding surface as a potential cross-scale reference should also be examined though BSEM and EDS analysis, to idenitify the key challenges and suggest solutions in the next step.

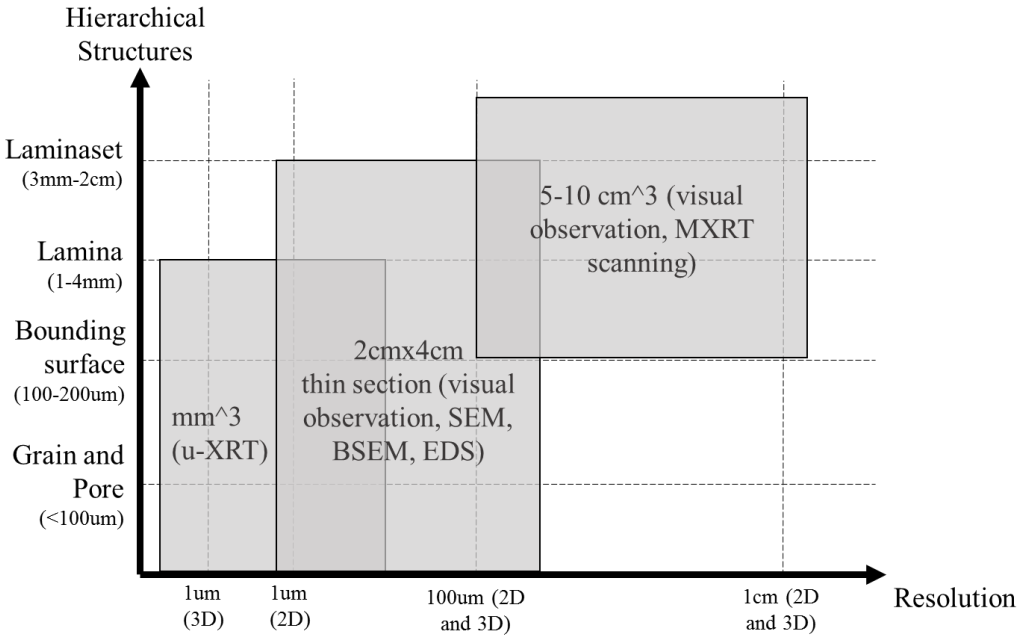

Figure 2.11 Potential ranges of hierarchical structures that could be covered by each reviewed digital imaging technique

Step II: The morphology and compositional nature of a bounding surface should have been confirmed through the analysis in Step I From this data, the key challenges of identifying bounding surfaces in corresponding datasets (MXRT and BSEM) can be identified. In this step image processing techniques need to be developed to extract the bounding surface, respecting the morphology and compositional nature, and how they will be presented in a different source of images.

Step III: when bounding surfaces as cross-scale references have been extracted, the multiscale datasets need to be spatially integrated. Before integration, there should be a review, to establish if all the information necessary for reconstruction has been obtained. The missing information, if any, needs to be defined and supplemented. An index map could be therefore be built respecting the integrated and supplemented information. The index in the map should be correlated to the characterised non-stationary lithology variation associated with grading in the hierarchical structures of lamination. Stochastic reconstruction respecting the index map should then be implemented using the discussed MPS algorithm, by defining sub-domains and transformation parameters according to the index map, as a non-stationary control. Practically, an appropriate parallel processing method needs to be developed to ensure the simulation can be done in a realistic time frame.

After conducting a thorough and comprehensive literature review on DCA, it is concluded that there is no existing framework that can lead to successful multiscale characterisation when hierarchical structures do not appear to be obvious. The proposed workflow extends typical multiscale DCA by integrating the "geo-pseudo" concept to enhance identification of non-obvious hierarchical structures to better spatially correlate multiscale data. The workflow was illustrated on an aeolian fine cross-laminated sandstone sample. It has pushed multiscale study on lamination to a new level and points out a new direction to deal with pore-scale geological structures which have not been considered previously. This framework goes beyond those to include local heterogeneity with measured permeability at mm scale, but those below millimetres at the pore scale. It provides an opportunity to study for the first time the combinational impact of intra- and inter-laminaset characterisations at different scales. The workflow integrates images gained from different scales and sources, which instruct a reconstruction of the full pore-scale model corresponding to heterogeneity and anisotropy at different scales. The idea proposed as a workflow here will be invaluable for the study of non-stationary pore systems associated with multiscale spatially non-separable structures.

CHAPTER 3 - DEVELOPMENT OF RECURSIVE SUB-SAMPLING PROCEDURE

This chapter reports the development of a recursive, imaging-based subsampling procedure for hierarchical characterisation of cross-laminations for a given sample. The resultant datasets are intended to contain information sufficient to reconstruct pore and grain structures of the sample stochastically. In this work, the concept of a 'geo-pseudo approach' is employed to sample critical structures in a top-down fashion. This implies that, for a given sample, the sub-sampling and characterisation must be carried out by a combination of exploratory analysis and quantitate analysis. The locations and geometries of one or more structures at one level of the hierarchy must be estimated under the constraints of the structures at the previous level of hierarchy (i.e. the one above the current level of hierarchy) and together they collectively determine one or more suitable imaging instruments to be selected to further subsample those structures at the right FoVs and resolutions.

To explore the nature of cross-lamination and what it imposes on the development of the sampling procedure, an Aeolian outcrop sample of Permian-Triassic fine-grained red sandstone slab was chosen and was found to be representative, in a preliminary analysis (to be summarised below), in that it: 1) encapsulates all common hierarchical structures of cross-laminated sandstones; 2) is large enough to capture the distribution of laminasets but compact enough to acquire data using 'standard' DCA imaging techniques. This representative sample was used through this study to develop a hierarchical DCA workflow.

In what follows, a geological description of that sample is provided first, to be followed by the results of a preliminary analysis to highlight the geological characteristics of the sample in terms of hierarchical lamination structures, structure geometry, and the spatial variations of mineral grains associated with the structures. This preliminary analysis provides initial information necessary to design the recursive sub-sampling procedure for the sample. How to apply the procedure appropriately is discussed in detail and argued with justifications. From the three datasets obtained following the sampling procedure, a conceptual model of the sample is developed to highlight the critical importance of finding commonly-shared features for dataset registration, to be considered in the following chapter.

3.1 Sample description and preliminary analysis

The preliminary analysis described in this section identified key generic elements to be considered for multiscale characterisation and reconstruction by analysis of the geometry and composition. The geometric analysis determined the representative sub-sampling volume for multiscale characterisation by investigating generic geometries and scales of representative hierarchical structures: interwoven curved and planar laminasets, laminae within each set, grading within laminae, and grains and pores within them. The composition analysis determined cross-scale linkage by identifying inter- and intra-LBSs that separate hierarchical structures as references. Based on the preliminary analysis, a multiscale top-down characterisation workflow could be designed to obtain three scales of recursive sub-sampling, capturing centimetre-scale laminasets, millimetre scale intra-laminaset laminae, micrometre scale grading within lamina and the grain-pore features within them, all with shared parts of bounding surfaces.

A brownish to reddish fine-grained cross-laminated sandstone slab, about 23 cm high (x-axis), 6 cm thick (y-axis) and 10 cm wide (z-axis), as shown in Figure 3.1(A), was obtained from a quarry at Lochabriggs in southern Scotland. Based on the geology of the region, described by Shotton (1956) and Waugh (1970), the sandstone slab comes from the Permian-Triassic geological sequence (see a detailed description in Appendix B.1). The fine-grained red sandstone with bed/ layered geometry is typically from a hot and arid Aeolian environment. The reddish colour of the sample suggests its iron-rich compositional nature, consistent with findings on similar Aeolian sandstones widely found in a similar region by Huang et al. (1995) and other places around the world, (Walker, 1967). The dark red, thin laminated structure observed is typically a result of authigenic dolomite, along with iron ions (as a result of magnesium in dolomite crystals ($CaMg(CO_3)_2$), often replaced by iron ions) preferentially cemented at the finely laminated bounding surface layer. Since this work is to develop the workflow, this generic fine-grained sample was chosen to ensure 3D XRT imaging could be acquired using commonly available instruments, without the loss of generality.

By visual inspection under natural light, it could be seen that the sample contained horizontal planar laminasets at its lower part of the x-axis and curved laminasets at the upper part of x-axis, separated by a boundary between both types of laminasets, which could not, however, be clearly identified on the surface of the dry sample. Over 20 horizontal planar laminasets or laminae could be observed, separated by inter- or intra-

LBSs of a few millimetres thickness. Planar inter- or intra-laminaset structures did not appear to be distinguishable, because they have the same geometry. More than 20 curved laminasets could be observed on either the sample's xy or xz faces in the upper part, as they were clearly demarcated by the intersecting and darker reddish inter-LBSs that appeared with a thickness (<1mm) thinner than the horizontal part (Figure 3.1(B-C)). Some intra-LBSs between laminae could be observed, but with a much weaker contrast in colour on the sample's xz face, each lamina was about a few millimetres thick, intersecting the inter-LBS at acute angles. Paleocurrent direction could be determined as perpendicular to the xy surface that has upward curved laminasets (Figure 3.1(B)) and inverse to the acute angle between the intersecting intra- and inter-LBSs at the xz surface (see paleocurrent direction labelled in Figure 3.1(C)). Each curved laminaset was about a few centimetres thick at xy surface that perpendicular to paleocurrent direction (see (Figure 3.1(B)), with wavelength of over 10 centimetres elongated at the xz surface that parallel to paleocurrent direction (see Figure 3.1(C))).

Given the visual structural information above, it is safe to conclude that a sub-volume of over 4 cm in height (in the x-axis) and the same thickness (in the y-axis) and width (in the z-axis) in the upper part of x-axis of the sample would catch three stacks of curved laminasets at different heights, where each stack contains more than one curved laminaset. The width of the sample in the z-axis direction captures a half-wavelength of lateral 'cycling' laminasets observed on the xz faces, while the thickness is a full curve length on the xy faces. A sub-volume of over 2 cm high (in the x-axis) in the lower part of the sample contains a stack of several planar laminasets. For the purpose of this study, i.e. to characterise inter- and intra-laminaset structures and their flow impact, a sub-volume of 6x6x10cm^3 (at the x, t, and z-axis) was taken to contain both curved and planar lamiasets, with a 4-to-2 split in height (x-axis) for the upper and lower parts. This volume was further split into two, with 6-to-4 splits in width (z-axis), to yield a 6x6x6 cm^3 sub-volume, L1, highlighted in red in Figure 3.1(A). A thin volume (Tp) has also been taken from the counterpart sub-volume of L1 from the xz face, highlighted in yellow in Figure 3.1(A). Both sub-volumes contain dozens of planar laminasets and at least 3 stacks of curved laminasets of half of their average wavelength, laterally. The reasoning for collecting Tp at xz face is to find potential preferred orientation feature under the microscope which in 2D might only be identifiable at cross-section parallel to paleocurrent direction. For a non-spherical grain preferentially lie along paleo current

direction, its cross-section would only present differently with non-preferentially laid grains at cross-section parallel to paleocurrent direction (this point has been discussed in section 2.1.2). The cross section perpendicular to paleocurrent direction would only reveal a nearly circular cross section (low aspect ratio close to 1) for either grains with or without preferred orientation feature and make it impossible to observe the variation in orientation on the surface.

L1 and its counterpart sub-volume are considered as 'identical' and equally representative for developing the workflow, given their generic characteristics. In what follows, L1 and its counterpart sub-volume were then used in the preliminary analysis. In this analysis, L1 was used intact to estimate more quantitatively the ranges of geometrical parameters for hierarchical structures, including laminasets and laminae. The counterpart sub-volume of L1 was cut into several thin volumes at different depths, to obtain a small chip and the top (yellow) volume, Tp, as shown in Figure 3.1(A) to perform the following procedure. The small chip was used to estimate an average grain size and the proportion of dominant mineral grains. An impregnated thin section (about 2x4 cm^2 with thickness of 30 μm) with blue-stained epoxy resin was made from Tp (also referred to as Tp) and imaged using an SEM instrument to first acquire preliminary SE image to estimate grain size, and to infer resolutions to perform BSEM and EDS images. Apart from visual manual observation on hierarchical structures, including laminae and layered grading within laminae, quantitative estimates on the ranges of pore/ grain sizes, orientation, and distribution were derived from the BSEM image. The trends of compositional characteristics in relation to bounding surfaces were revealed from the EDS image. The collective results from this analysis enabled the design of a suitable recursive top-down sampling and characterisation for L1, to investigate the REV of hierarchical structures, with shared identifiable parts (bounding surfaces) as references of correlation.

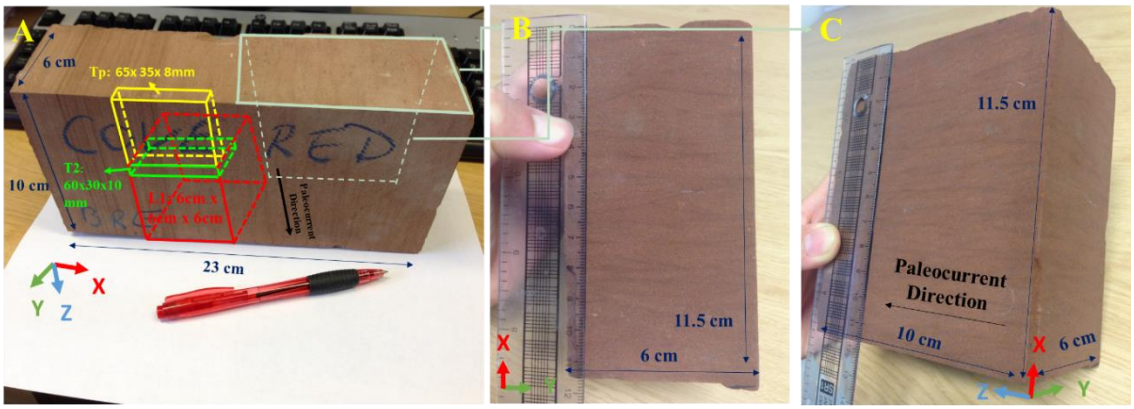

Figure 3.1 A) 6x10x23 cm^3 whole sample and sub-volumes resulting from REV selection and recursive sampling; B) an xy view of the sample face perpendicular to the paleocurrent direction and C) an xz view of the sample face parallel to the paleocurrent direction.

3.1.1 Geometry of bounding surfaces from L1

Early in this stage of the research, the scales of laminaset to lamina and their associated bounding surfaces were visually assessed. Here a classical technique was employed to investigate their geometry and estimate more quantitatively the range of each scale. A small amount of water was applied on each surface of L1. Since the water is expected to be the wetting fluid with respect to the air, the water tends to be sucked in faster by smaller pores, to give differentially wetted surfaces and therefore optical reflection properties. This enhances visual inter- and intra-LBS contrast to the other materials of the sample. Figure 3.2 (B-C) shows two side surface views of L1 (Figure 3.2 (A)) to identify and measure the geometry of the bounding surface. Inter-LBS are clearly observed as darker reddish transition zones at thicknesses around 1mm or less. Apart from horizontal planar bounding surfaces, inter-LBS geometry is observed as an up-curved shape in the xy face perpendicular to paleocurrent direction, (as labelled in Figure 3.2(B)) and a long inclined surface in the xz face parallel to paleocurrent direction, (as labelled in Figure 3.2(C)). The different geometries observed on each face confirmed the curved-crested trough cross-lamination geometry, as reviewed in section 2.1.1. A small number of intra-LBSs were observed with less clear presentation and only observed on the xz face parallel to the paleocurrent direction (as labelled in Figure 3.2(C)). These observations and interpretations are consistent with what is typically believed about the geometrical nature of laminated sandstone (Reading, 2009). Precise measurements on the ranges of their respective scales and orientation were made using a ruler and protractor on the wetting-enhanced sample surfaces and the results are given in Table 3.1.

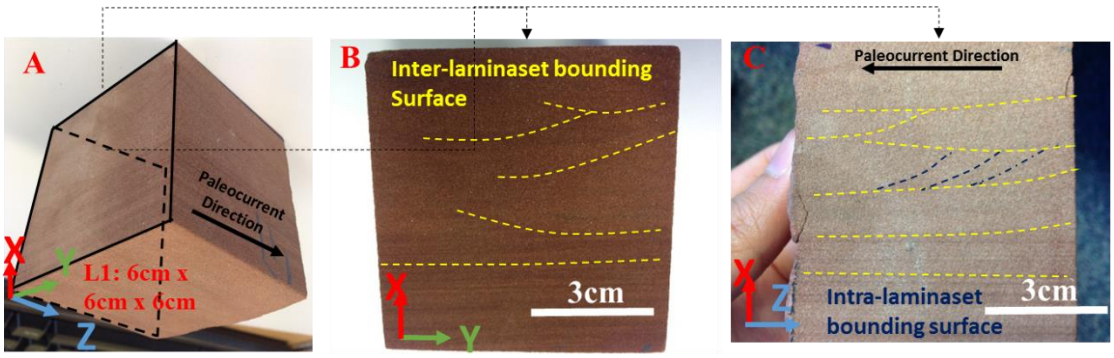

Figure 3.2 (A) L1 with the xy face perpendicular to the paleocurrent direction phottted in front; (B) a photo taken on the water wetted xy face, perpendicular to the labelled paleocurrent direction in (A), with interpreted inter-LBS in yellow dashed lines; (C) a photo taken on wetted xz face parallel to the labelled paleocurrent direction in (A) with interpreted inter-LBS in yellow dashed lines and intra-LBS in dark blue dashed lines;

3.1.2 Grain-pore size analysis

The small chip was taken from the counter-volume of L1 and scanned using the secondary electrons (SE) mode of a Zeiss SEM. The SE image, Figure 3.3, was interpreted by a professional petrography analyst, with following results: 1) the overview in Figure 3.3(A) suggests clastic grain particles appear to be around 100 μm in diameter with low roundness and a sub-angular shape suggesting a potential short distance of transportation. The linear-point contact between particles suggests mid-compaction; 2) the overview in Figure 3.3(A) suggests the top three mineral grains by proportion are quartz (65%), feldspar (25%), and lithic (15%); 3) irregular overgrowth appears on some quartz grains (for example, Figure 3.3(B)) suggesting occurrence of diagenesis; 4) intergranular fillings appear to be brown clay (2-3%), and patchy calcite (3%) components (for example, Figure 3.3(C)), suggesting potential occurrence of bioturbation.

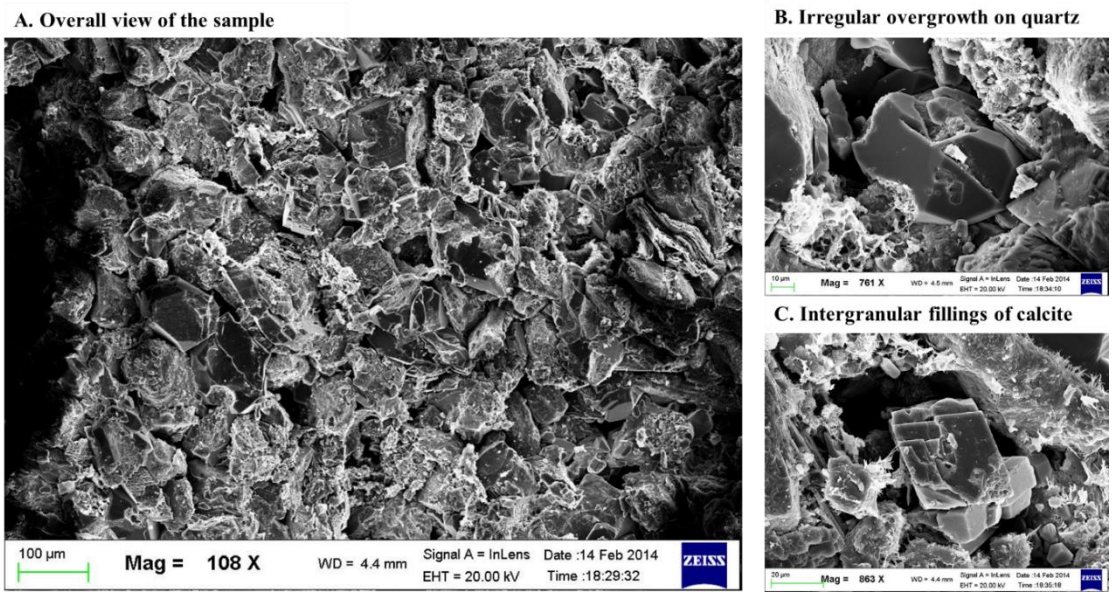

Figure 3.3 An SEM SE image of a small sample chip A) Sample overview; B) Zoomed in view of irregular overgrowth on quartz and C) Zoomed in view of intergranular fillings of calcite

A high-resolution SEM image obtained for a blue-stained epoxy resin impregnated thin section, Tp (Figure 3.4(A)) was used to investigate hierarchical structures of lamina and grain and pore variation associated with grading by: 1) manually observing grain-pore character variation to identify potential grading and preferred orientation; 2) quantitative investigation of grain-pore size and 2D spatial and statistical distribution. A SEM instrument (Quanta FEG 650 SEM) at the Institute of Petroleum Engineering, Heriot-Watt University, was used to perform multi-scans on an array of marginally overlapping sub-areas covering Tp, to produce a set of SEM BSEM images. Those images were registered and stitched together to form a single high-resolution SEM BSEM image (Figure 3.4(B)) with the size of 33098x49119 pixels^2. All BSEM images were taken at the same resolution of 0.6x0.6 µm^2/pixel, capable of fully resolving grains as small as 6 µm in diameter, or 10 pixels across.

Manual evaluation

The BSEM image was firstly evaluated manually by looking at grain-pore size variation to identify laminae and layers. Inter- and intra-LBSs are labelled in Figure 3.4(B) manually, with brownish to reddish thin layers observed in image of the thin section under natural light in Figure 3.4(A) as references. The labelling of the bounding surface was also based on zooming in and subjectively searching the fine grain-pore layer separating laminae or laminasets with distinctively different grain-pore sizes. The intersection angles between the manually plotted inter- and intra-LBS were measured, whose average

is 21.70°. Three 6188x3508 pixels across FoV at locations from either curved or horizontal planar laminasets containing intersection of inter- and intra-LBSs (Views-1 to 3 in Figure 3.4(B)) have been selected to verify manually labelled bounding surfaces with more detailed observation on 1) grain size contrast between laminae; 2) potential preferred orientation close to bounding surface; 3) the direction of layered grading above the bounding surface.

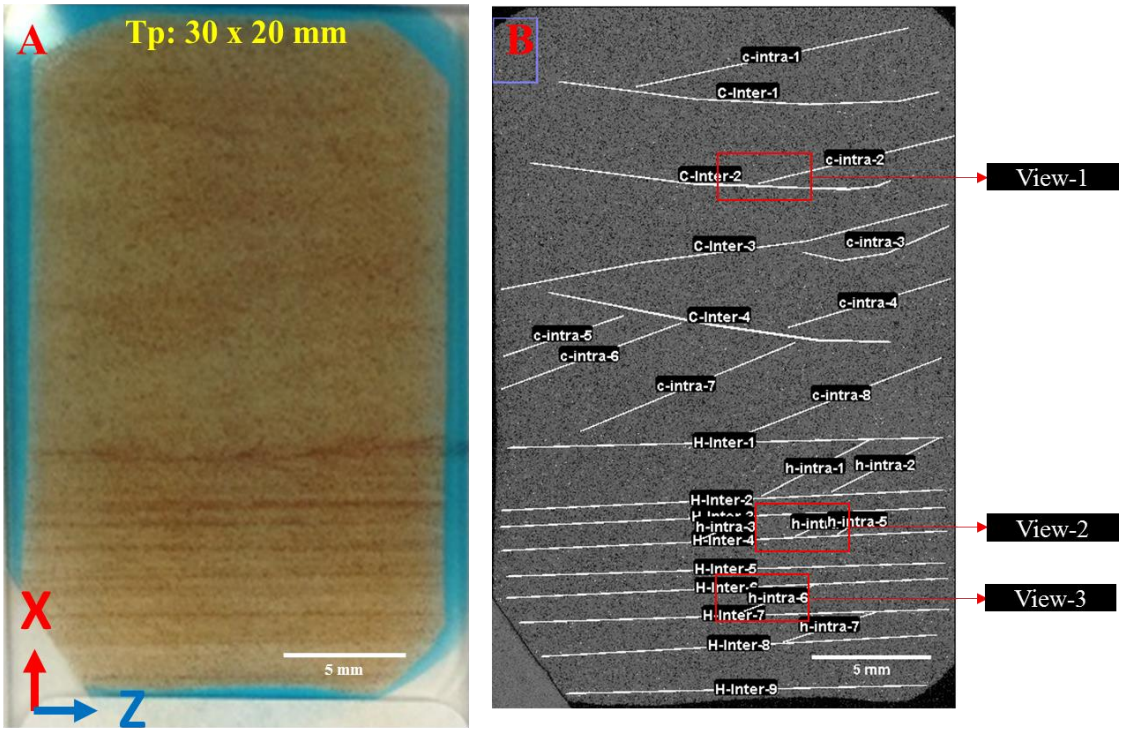

Figure 3.4 (A) 2x3 cm^2 blue-stained epoxy resin impregnated thin section containing dozens of horizontal planar laminasets at the bottom and 3 curved laminasets at top of the sample; (B) BSEM image with a resolution of 0.6x0.6 μm^2/ pixel for 33098x49119 pixels^2. Bounding surfaces are interpreted visually from the photo (A) in combination with subjectively searching the fine grain-pore layer separating laminae or laminasets with distinctively different grain-pore size. Inter-LBSs are labelled for the horizontal planar and curved part, as H-Inter- and C-Inter- respectively. Intra-LBSs are labelled for the horizontal planar and curved part as h-intra- and c-intra- respectively.

The three FoVs from both curved and horizontal planar laminasets are illustrated in Figure 3.5 (A-C); finer grain-pore layers are observed close to the labelled bounding surface which separates adjacent regions into laminae with coarser grain-pore space. Coarsening-up of grains and pores is observed in the direction further away from the labelled fine layer above the intersecting intra- and inter- laminaset bounding in Figure 3.5 (A-C). The thin layer and associated coarsening-up grading occurred above both inter- and intra-LBSs simultaneously. This is possible because of the change in direction of the wind, which leads to grading on both lee and stoss side, corresponding to intra- and inter-LBS respectively. Figure 3.5 (D-E) gives a further zoomed-in view, centred at the intersection

between intra- and inter-LBS, aiming to investigate the potentially preferred orientation. A minor degree of preferred orientation is observed above or below the inclined intra-LBS, but with low confidence.

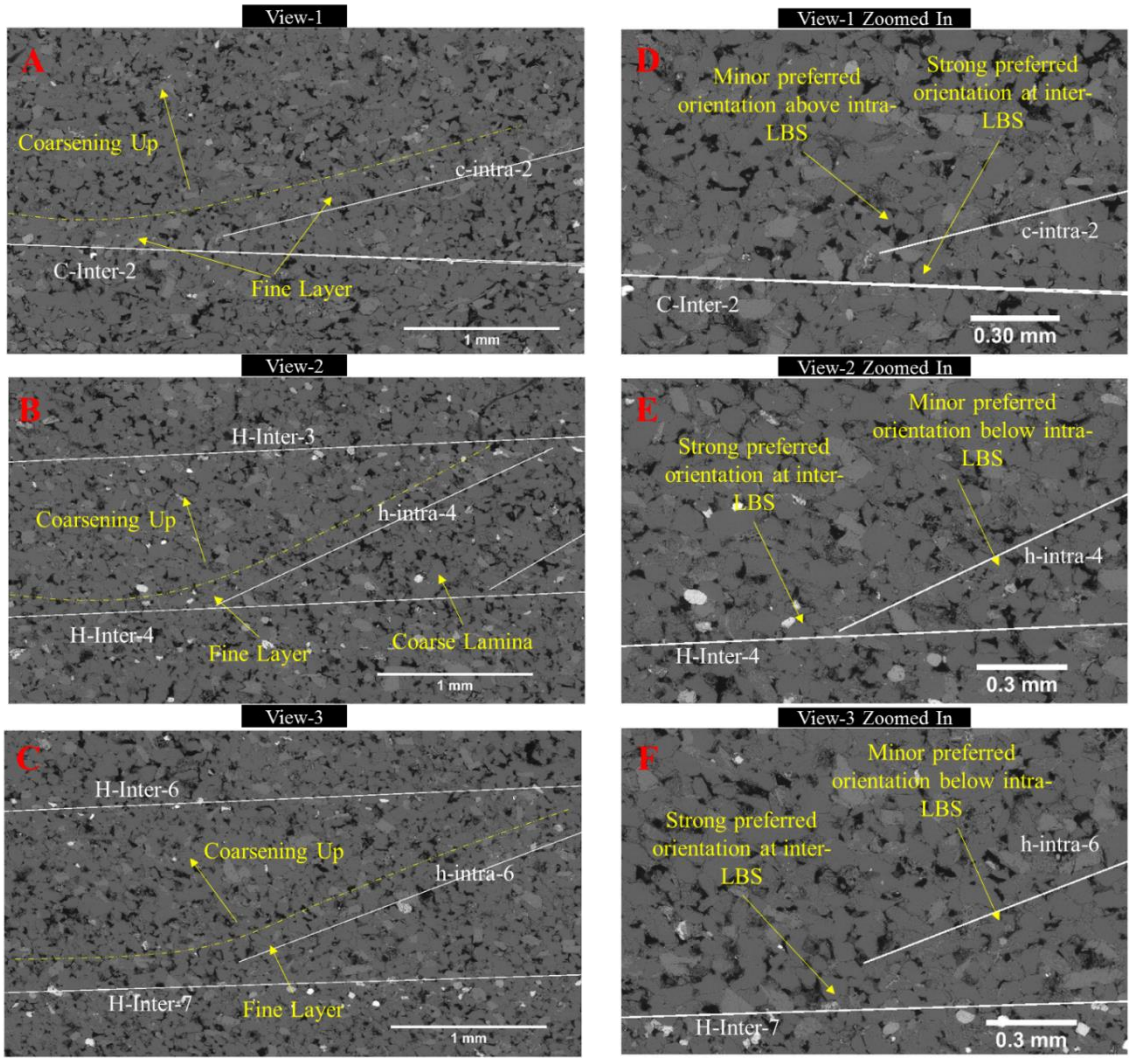

Figure 3.5 A-C gives Views-1 to 3 highlighted in Figure 3.4(B) of BSEM image with a resolution of 0.6x0.6 μm^2/ pixel for 6188x3508 pixels^2. Manually-defined bounding surfaces labelled as white line named in Figure 3.4(B). The suspected fine layer above the bounding surface is highlighted in yellow dashed line. D-F gives further zoomed-in view for 2802x1776 pixels^2 of A-C, centred at the intersection between intra- and inter-LBS (termed as BS for short in the label in the image) aiming to further investigate potentially preferred orientation.

Quantitative measurement

The manual observation gives a qualitative suggestion of structure; however, the certainty is low because it has introduced too much subjectivity. For further quantitative measurement, the BSEM image was preprocessed using filters, as reviewed in section 2.3.2, based on the imaging processing software Avizo and Fiji to remove noise resulting from image artefacts and to improve the signal-to-noise ratio. The grains are segmented from the pore regions in the processed image using the watershed-based method and then

into separate grain particles to be measured (as reviewed in the Avizo approach in section 2.2.2.2). Pores are segmented using the Otsu thresholding method, without separation, and each separate individual pore-space is measured. Figure 3.6(A-C) illustrates the processed image of a small sub-region of the BSEM image (Figure 3.6(A)) and segmented grain particles Figure 3.6(B) and pores Figure 3.6(C). This detailed analysis is documented in Appendix B.2 . The first threshold of 10 pixels in the area is applied for both grain and pore quantification, to exclude artificial noises with small area. The second threshold is chosen for the segmented grains to exclude small grains, as suggested by Baas et al. (2007) for more representative grain feature quantification (especially orientation). The inflection point of the grain size histogram has been selected as the second threshold, as highlighted in Figure 3.6(D). Three quantitative measurements were performed to investigate: 1) grain size distribution; 2) preferred orientation close to bounding surface and 3) overall statistics of grain and pore character on Tp.

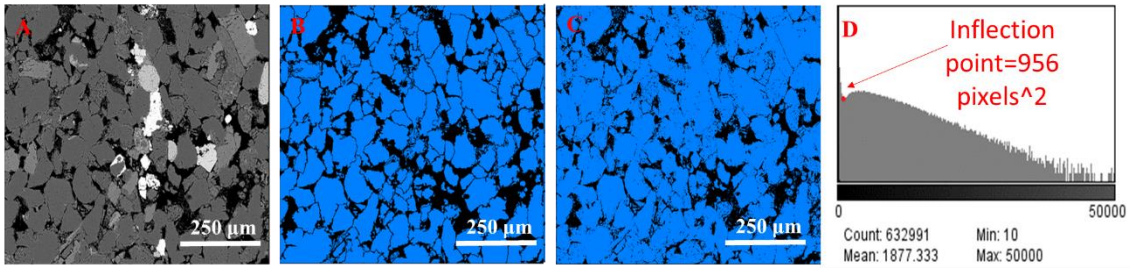

Figure 3.6 (A) Zooming in on a grey scale BSEM image (grains in grey and brighter colour and pores in black);; (B) segmented grains to be measured (grains in blue and pores in black); (C) segmented pores to be measured (grains in blue and pores in black);; (E) Histogram of grain area in pixels^2, part of the range (10-50000) is zoomed-in to highlight inflection point by red spot.

A first quantitative measurement was performed to investigate the spatial distribution of grain size in relation to lamina structure to verify the visually plotted bounding surfaces. Average grain sizes were measured in 26 sub-regions manually plotted previously, representing laminae between the manually determined bounding surfaces in Figure 3.4(B). The full details of this measurement are given and discussed in Appendix B.2 and the main conclusions are summarised as follows: 1) Generally, regions from the horizontal planar part have smaller grain size than the curved part; 2) Grain size across manually labelled regions appears to be similar within curved and horizontal laminasets, suggesting either the lamina feature is similar within each type of laminaset or possible inaccuracy of manually labelled regions; 3) The boundary between horizontal and curved laminasets appears not clear, because inclined laminae potentially occurred in the horizontal laminaset, with low certainty, though.

A second quantitative grain orientation measurement was performed to investigate the potential preferred alignment of grains along the lamina bounding surface. Grain orientations were measured within lamina regions separated by manually identified bounding surfaces at small FoVs (three selected FoVs, as illustrated in Figure 3.4(B)). The reason for not applying quantitative measurements to the large FoVs was to reduce the possibility of distraction by unidentified laminae with the discussed manual approach (see full discussion in Appendix B.2). With the grains' long axis orientation calculated, the grains for each lamina region were then filtered by orientations of the selected range, and the area fraction of filtered grains occupying each corresponding region was calculated. By comparing the grain area fraction for each orientation range over different lamina regions, the existence of a preferred orientation could be verified. Based on the full measurement results and discussion in Appendix B.2, for View-1 from the curved laminaset, regions close to the inclined LBS are preferentially occupied by grains with orientation close to the inclination angle of the inclined LBS. Therefore, the preferred occupation in line with the bounding surface inclination provided evidence of the existence of a preferred orientation. This also suggested the manually identified lamina regions were with relatively high certainty. However, there is not such a clear preferred occupation observed in View-2 and View-3 which suggests either a preferred orientation is less likely to occur or the manually labelled regions may not reflect the true intra-laminaset geometries for the horizontal laminaset.

Apart from regional measurements, the overall quantitative measurement of grain and pore sizes of Tp is calculated and summarised in Table 3.1 with average grain and pore sizes being 76.9 μm and 8.1 μm, identified by the long axes, respectively. The low grain circularity of 0.25 verified the SEM observation of sub-angular shaped grains. The remaining measured grain and pore characters are kept as reference to compare with the further measurements from datasets at different direction and resolution. The geometry and scales measured on the hierarchical structures of the laminaset, laminae, and layers within the laminae are also summarised in Table 3.1.

Table 3-1 Summary of structures observed from analysis (as mentioned in previous section/paragraphs)

Hierarchical Structures	Laminaset			Lamina			Layer within lamina
	Curved		Horizontal planar	Curved		Horizontal planar	Curved and Horizontal planar
Measurement / Sample	Set thickness	Set length at paleo direction	Set thickness	Lamina thickness	Intersect angle b.t. 3rd and 2nd surface	Lamina thickness	Bounding Surface thickness
L1 (Surface)	1-2 cm	10 cm	1-3mm	1-4 mm	25-30°	1-3mm	<1 mm

Hierarchical Structures	Laminaset	Lamina	Layer within lamina		Grain and Pore (BSEM overall)							
Measurement / Sample	Thickness of Curved (Cuv) and Horizontal Planar (Hor)	Intersect angle, thickness and grading	Thickness	Geometry		Count	Average Size in area	%Area	Long axes	Short axes	Angle	Circularity
Tp	Cuv: 2cm Hor: 1-3 mm	Intersect angle= 21.7°	100-200µm	Parallel BS	Grains	1.36E+05	3102.4 µm^2	72.1	76.9 µm	46.4 µm	92.8°	0.25
					Pores	1.07E+06	71.8 µm^2	13.1	8.2 µm	3.7 µm	N/A	N/A

The SE analysis implied relatively complex sub-angular geometry of the grains, thus suggesting potential anisotropic geometry, therefore, further investigation needed to be performed in the perpendicular direction. The occurrence of diagenesis and bioturbation suggested further compositional analysis to look at the spatial distribution of related minerals. BSEM offers manual observation and suggestions on the geometry of laminae and direction of grading within laminae in cross-section parallel to paleocurrent direction. Generally, the manual observation confirmed the existence of inclined laminae within the curved laminaset, with relatively higher certainty, whereas the inclined laminae identified manually within the horizontal laminaset, close to the boundary between both types of laminaset, are doubted, because they failed to show good agreement with quantitative orientation measurement. This suggests there might be a transitional zone between both types of laminaset, where a curved laminaset feature also occurs within the last part of horizontal laminaset, but with lower certainty. The inverse grading for the laminae of the curved laminaset observed manually in the cross-section parallel to the paleocurrent direction suggests grading layers stacking on both inter- and intra-LBS, because of changes in wind direction. However, grading within the different curved lamina features needs further investigation to be performed in the cross-section perpendicular to paleocurrent direction. Manual observation also suggested the bounding surface could be as thin as ~1-2 grains thick. Quantitative investigation of grain-pore size suggested relatively similar lamina features within either curved or horizontal laminasets. The preferred orientations are observed based on the manually identified intra- and inter-LBSs

for curved laminasets. An intersecting angle of 21.7° between the manually identified intra- and inter-LBSs is measured and smaller than that obtained by the visual observation on the L1 surface of 25-30°. It is therefore suggested that the manually identified bounding surface may be less accurate and that more accurate identification of the bounding surface is required. Overall grain and pore size have been quantified to suggest 0.8 μm is required to cover pore analysis (1/10 pore size is usually used to estimate resolution requests).

The main challenge suggested by this section is to accurately identify the bounding surface. The reason is the boundary between laminae or laminasets is a transitional region; therefore, the bounding surface, by definition the layer of finest grain, is hard to identify manually based on variation in grain geometry. It is therefore suggested to carry out compositional analysis, as described in the next section.

3.1.3 Composition Analysis on Tp

The thin-section Tp was scanned using a SEM with an EDS detector, to characterise spatial trends of mineral compositions of grains, with a specific focus on the spatial correlation of heavier minerals and bounding surfaces. For this purpose, a low-resolution EDS image of Tp is firstly taken with a resolution of 124x124 μm^2/pixel (~1-2 grains in diameter across) over the whole sample and yielded a 154x277 pixels square image, as shown in Figure 3.7(A).

In Figure 3.7(A), iron ions, highlighted in green are observed to concentrate at inter-LBS, especially for the bottom horizontal planar part in a pattern consistent with the thin, dark red layers observed under natural light for Tp (Figure 3.4(A)). The poorer observation for the curved part with low-resolution EDS suggests higher resolution EDS is required during recursive sampling and imaging to observe the thinner curved inter-LBS. This confirms the findings in the geological review that iron ions, which form haematite by reacting with dolomite during diagenesis, is preferentially cemented at the bounding surface and should thus be considered as potential shared features to be included during recursive sampling and identified as a cross-scale linkage reference.

In addition, bioturbations, highlighted by concentration of the randomly occurring clusters of Ca ions are observed. Figure 3.7(B) is a zoomed-in BSEM view, at a similar location to the Ca ions cluster identified in EDS, with the area highlighted by the yellow

box containing bioturbation. The pattern of bioturbation observed by EDS is consistent with that observed patchily by BSEM. In BSEM, quantitative measures were performed within the labelled area of bioturbation, as well as one neighbouring area with identical size, for comparison. The results proved the arrangement of grains is more coherent for the bioturbation area with smaller grain and pore size and lower porosity than surrounding areas. The random occurrence of bioturbation may lead to disturbance on the lamination structure, and therefore an impact on fluid flow, and should be considered especially during reconstruction and simulation.

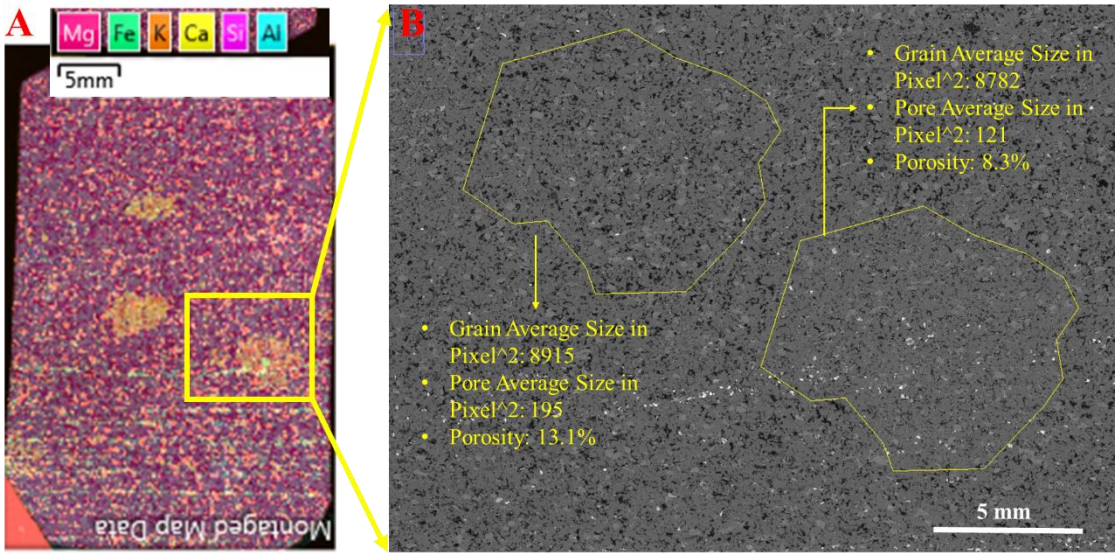

Figure 3.7 (A) Coarse EDS overall scanning of TP with a resolution about 124x124 μm^2/pixel for 154x277 pixels^2.

3.1.4 Conclusions of the preliminary analysis

Centimetre-scale inter-LBSs were identified visually from the sample surface and summarised in Table 3.1. The geometry of curved laminasets at centimetre scale is distinctively different at surface perpendicular to and parallel with the paleocurrent direction, which is consistent with the geological expectation of a curved crest tough cross-lamination. Therefore, 3D MXRT imaging is suggested to obtain the internal complex structure of curved lamination of L1, especially, to further identify representative geometry and recursively design sub-sampling size and location.

Similarly, Tp offered representative geometric analysis at a cross-section parallel to the paleocurrent direction for laminae at millimetre scale and grading within laminae at hundreds of micrometres scale and grain-pores at the micrometre scale. The BSEM was found to struggle in identifying the thin inter- and intra-LBS (~1-2 grains thick)

accurately. Low-resolution EDS confirmed the preferred cementation of iron ions at a bounding surface could be a potential indicator for identifying the bounding surface layer accurately, but higher resolution EDS is required. The confirmation of preferred cementation of iron ions also verified density sensitive MXRT would be helpful to identify inter-LBS. Based on visually identified LBS, grading stacking direction and intersection angle are estimated.

The quantitative measurements based on subjectively defined regions suggested that inclined intra-laminaset laminae is more likely to appear in curved laminasets than horizontal laminasets and that a transitional zone may exist close to the boundary between both types of laminasets. The existence of a transitional zone is inferred by the fact that the inclined laminae feature, which is supposed to be observed in curved laminasets only, has also been observed within a horizontal laminaset, at the location close to the curved laminaset. The grain-pore sizes were measured as larger in the curved laminaset than the horizontal laminaset, based on manually defined laminae regions, but were relatively similar within each type of laminaset. It is therefore suggested laminae and grain-pore features are similar within each laminaset but different across, and a transitional zone may exist in between where both types of features mix.

The geometry of the laminae is expected to be different at cross-section perpendicular to paleocurrent from that parallel to the paleocurrent; this therefore suggests that further investigation should be performed on the cross-section perpendicular to the paleocurrent direction to investigate grading. The complex 2D sub-angular grain geometry implies a complex 3D geometry of grains, which could also be investigated in combination with further 2D analysis of thin section perpendicular to paleocurrent direction. Thus, to obtain the 3D grain-pore space geometry for the purpose of 3D pore-space reconstruction, further sub-sampling of micro core plugs is required..

To implement these suggestions, a recursive top-down subsampling is required. REV of the laminasets, laminae, layers and grain pores should be considered during sampling at each scale, according to the measured structure range in Table 3.1. In addition, the multi-scale sampling should contain shared parts of the bounding surface as references for top-down characterisation and multiscale integration.

3.2 Process of recursive sub-sampling

The preliminary analysis resulted in a set of geometrical estimates about the hierarchical structures (see Table 3.1) that are needed for designing and implementing a recursive sampling procedure appropriate to the sample. The two key design principles of a recursive sampling procedure, according to the concept of top-down "geo-pseudo", are: 1) sampling representative identified hierarchical structures at a coarse scale to further identify smaller hierarchical structures at the next finer scale: each sampling is designed according to recursively collected hierarchical structure information; and 2) a sub-sample taken at a scale must overlap partially with one or more other sub-samples in space taken at the same and different scales to capture shared structures of interest and to register them.

By applying these principles to the sample, the recursive sub-sampling procedure starts from the sub-volume L1, as the preliminary analysis justifies its representativeness, and further subsampling and characterisation to collect hierarchical structures recursively, down to the pore and grain scales. In what follows, the design process is reported here to answer the generic questions: Where should one take samples? How many samples should one take? At which sample sizes should one take samples? Since the process is iterative in nature, involving taking and analysing samples at one scale and making the decision for the next scale, consideration is given to not showing details of all analyses, in order to avoid distracting the understanding of the process. For this reason, some detailed analyses will be reported in the Appendices.

3.2.1 Sampling on L1

6cmx6cmx6cm L1 was introduced, taken to contain both curved and planar laminasets with a 4-to-2 split in height (x-axis) on the upper curved and lower planar parts. L1 has been argued to contain the REV of laminaset structures (dozens of planar laminasets and 3 stacks of curved ones) based on the preliminary surface analysis. The quantified surface measurement summarised in Table 3.1 supports the REV argument, as the 1-2 cm and 1-4mm laminaset thicknesses measured for the curved and planar laminasets respectively are much thinner than the 6cm of the sample height. From L1, different geometries of inter- and intra-LBS were observed at two perpendicular surfaces; 3D XRT imaging is therefore suggested to implement the understanding of the internal 3D geometry of the

laminaset or its bounding surface and provide suggestions on further subsampling size and locations.

3.2.1.1 Physical sampling and imaging procedure

L1 is the largest sub-volume involved in this design. At this scale, the goal is to characterise the internal laminaset structures by identifying the inter-LBS, which cannot be achieved in the preliminary analysis on the surface or from 2D datasets. Given the volume of L1, a full-size 3D XRT imaging was performed using an industrial MXRT machine, nanoVoxel-4000 (by a collaborator at the lab of Beijing Normal University). L1 has been scanned by low resolution, at 100x100x100 μm^3/voxel, to scan a 562x550x525 volume (note this resolution is the highest achievable for the industrial CT to image the whole sample), but with sufficient resolution to retain a potential identified cross-scale linkage: the ~1-2 grains thin (100-200 μm according to Table 3.1) bounding surface. The energy of the XRT imaging is based on "trial and error", with peak X-ray energy level of 0.2 MeV, so that the energy is high enough to penetrate the 6 cm cubic sample. Figure 3.8(A) and Figure 3.9(A) show a reconstructed grey-scale xy slice and the whole 3D MXRT volume of L1. The thin bounding surface is presented in a slightly brighter colour (higher X-ray attenuation that implies a heavy mineral) but its contrast has been decreased by brighter parts at the boundary of the sample caused by global hardening effect. The global hardening effect can be effectively removed based on the concept of the 'rolling ball' algorithm described by Sternberg (1983), in which a ball of given radius is rolled over the bottom side of the intensity surface (Figure 3.8(A)) to remove the uneven background (Figure 3.8(C)) (see Appendix B.3 for a detailed discussion). After the removal of the global hardening effect, bounding surface are presented with higher contrast whose intensity surface as in Figure 3.8(B) having a more even base (background).

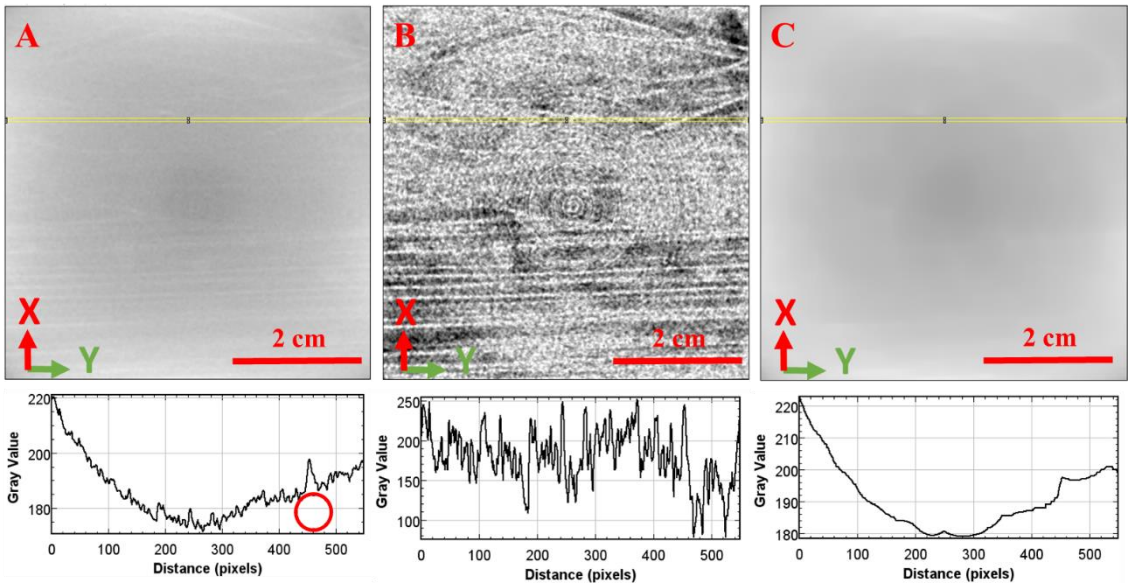

Figure 3.8 (A) one 2D raw MXRT image slice of the stack slices obtained by industrial MXRT, where pixel values represent attenuation at each point; (B) processed image of A, with global hardening effect background removed and presenting clearer bounding surface features in bright curvilinear region; (C) the global hardening effect background has been removed from A. Below each image is a pixel intensity plot along the selected line, as highlighted by yellow 1-pixel wide rectangle. The horizontal-axis of each intensity plot represents distance along the rectangular long axis and the vertical-axis of the intensity plot is the pixel intensity. The red circle in the intensity plot of (A) represents the ball with a diameter of 50 pixels rolling below the intensity plot, to remove the background.

3.2.1.2 Image analysis and results, implication on sub-sampling decision

Figure 3.9(B) shows the 3D XRT image of L1 after hardening was removed from original, shown as Figure 3.9(A), and the bounding surface is more obvious. A simple image analysis method ("segmentation editor" plugin in ImageJ) was applied for a preliminary visual exploration of the internal laminaset structures. The method to segment the 3D bounding surface starts with the manually traced bounding surface on 10 xy slices evenly distributed along z-axis and automatically connects missing bounding surfaces on the remaining xy slices by propagation in the Z axis direction, based on similarity of 3D local intensity. Figure 3.9(C) shows the segmented 3D bounding surface, with each separated surface labelled in a different colour. 17 horizontal planar surfaces and 9 curved surfaces are labelled, which verifies the representativeness of L1. From Figure 3.9(B-C) 3D it can be seen that the bounding surface in the upper curved part presents a clear curved-crested trough as a cross-lamination feature, which is consistent with the surface observation. Figure 3.10 displays the segmented curved bounding surfaces, one by one, to visually analyse their geometry and to infer their sedimentary character. Because every sample is different, the inference and evaluation of the sedimentary character could only be correlated to the characteristics reported in the literature in section 2.1. From Figure 3.10 only one lunar up-curved surface (pink, on the right) and one almost planar (yellow, on

the left) are observed with relatively complete surface geometry, which could be seen as the bottom part of an up-curved ripple, while others appear like halves of lunar curved bounding surfaces. The curved surfaces appear to have the same elongation in the paleocurrent (Z) direction, as labelled. The geometry of the segmented bounding surfaces confirms the extracted bounding surfaces are mainly inter-LBSs, based on their geometry, because intra-LBSs will occur as a set parallel surfaces intersecting at an inter-LBS. The geometry of the laminaset is believed to have similar features within the sample because the majority of up-curved crest surfaces are elongated in the same Z direction, and less than one wavelength has been captured for all surfaces within the sample.

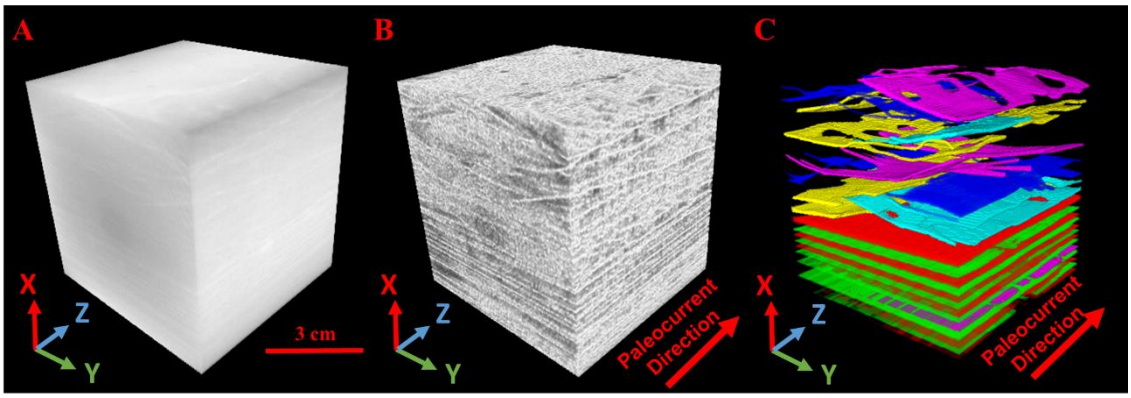

Figure 3.9(A) 3D XRT of L1 with size 562x550x525 at 100um^3/voxel; (B) Same volume of A after global hardening effect has been removed by rolling ball method illustrated in Figure 3.8; (C) sub-automatically segmented 1st and inter-laminaset bounding surfaces from (A (27 connected surfaces are segmented); separate surfaces are labelled in different colours for better illustration.

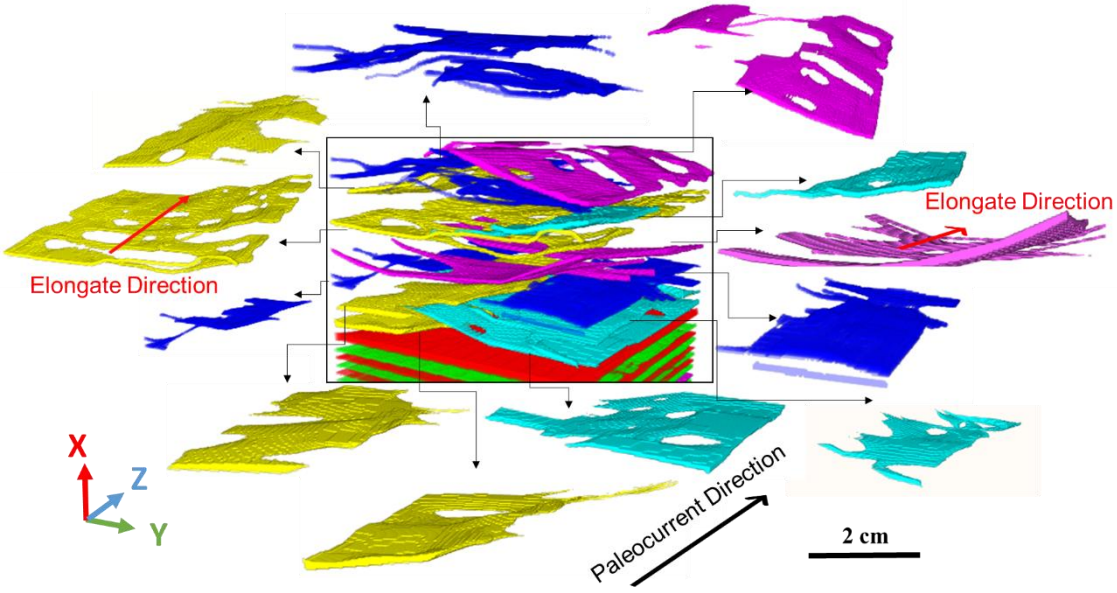

Figure 3.10 Curved bounding surfaces displayed separately to analyse the geometry and formation of the curved laminaset

The scales of the laminasets are measured based on segmented inter-LBS (Figure 3.9(C)) (see detailed discussion in Appendix B.3) and summarised in the extended Table 3.3. The curved laminaset thickness of 3-11 mm is measured between segmented inter-LBS, which are slightly thinner than appeared from surface observation. The measured thickness suggests MXRT imaging provides more internal observation and provides insights regarding internal bounding surfaces that the surface view could not identify. The half wavelength of 5cm which is estimated verifies the preliminary surface observation and no full wave of bounding surface was observed in L1. Horizontal set thickness is consistent with the surface view but could still not distinguish inter- or intra-LBS; therefore, the measurement is applied to both laminaset and lamina thickness in Table 3.3.

The thickness of the bounding surface was measured as <1 mm from the processed image (Figure 3.9(B)) and < 2mm from the segmented image (Figure 3.9(C)). Considering that the previous BSEM manual observation estimated the thickness could be as thin as 100-200 μm, the segmented bounding surface in MXRT is effective to study the laminaset geometry because of its larger FoV, but it may lack accuracy in identifying the thickness of the thin layer of the bounding surface. This limitation is mainly caused by low resolution and the set of imaging artefacts (e.g. the blurring effect) of XRT, as reviewed in section 2.2.1.3. Apart from increasing resolution, further compositional analysis is required, because the imaging artefacts are related to the complex composition and need to be studied. The less accurate identification of the bounding surface layer as the initial bottom layer of a lamina may be an obstacle to characterising layered grading within those laminae in which the layers have thicknesses less than a thinnest lamina of 1 mm, based on previous measurements. The presentation of bounding surfaces in density-sensitive XRT verified the concentration of heavier minerals (presented as lower X-ray attenuation). However, the limitation in segmenting the bounding surfaces of LI suggested further compositional analysis is needed at a higher resolution to investigate the fundamental constitution of the bounding surface and to help develop a more accurate segmentation method.

Simple segmentation is also limited in its ability to keep the connectivity of bounding surface in the Z direction (see Figure 3.11 for a comparison of two perpendicular slices). The reason is that the simple segmentation method is based on a given traced xy slice and auto-propagates in the Z direction, and therefore lacks connectivity examples in the Z

direction. Moreover, intra-laminaset surfaces appear not to be successfully segmented with the simple segmentation method in Figure 3.9(C), because of lack of contrast in the MXRT image.

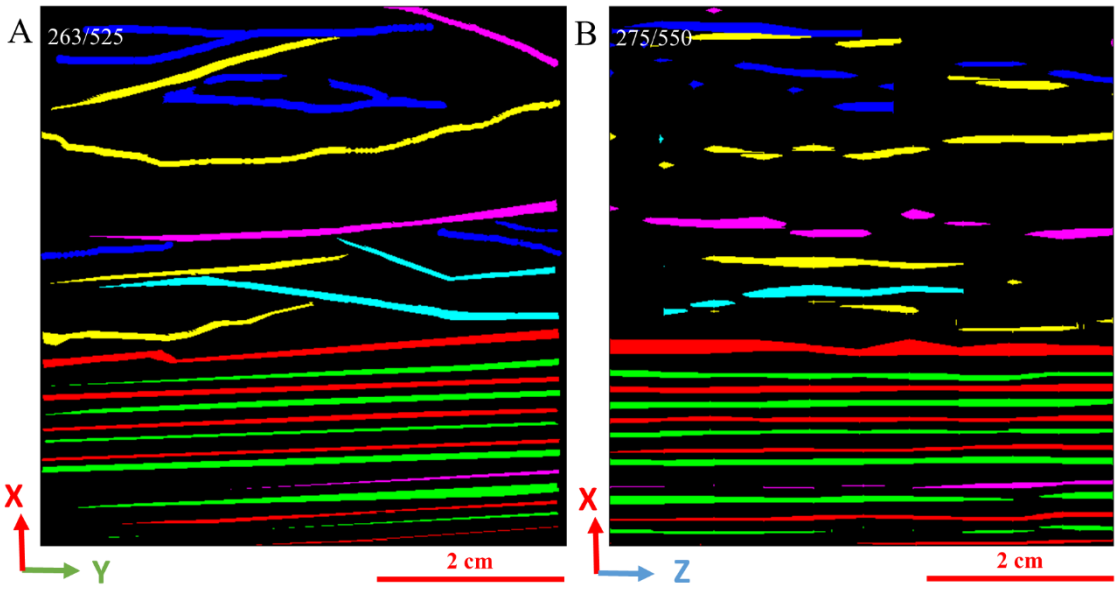

Figure 3.11 Two perpendicular side views of the segmented bounding surface of L1 obtained by simple segmentation method: A) 263/525 slice of segmented bounding surface in xy direction; B) 275/550 slice of segmented bounding surface in xz direction.

With the internal structure presented in this section, the sample appears to have an up-curved laminaset deposited after the horizontal laminaset; therefore, the +X direction perpendicular to the planar surfaces could be assumed as the sedimentary direction. The analysis of the internal geometry also verified that each curved laminaset has a similarly up-curved geometry, elongated in the paleocurrent direction, of about half a wavelength within the sample size of L1. This suggests that lamina geometrical features within the laminasets could potentially be similar, but further quantitative verification, for example, by lamina thickness, is required. Considering the thickness of a laminaset measured is typically less than 2cm, one thin section sub-sample perpendicular to the paleocurrent direction would include a representative number of up-curved cross-sections of the laminasets involved in L1. The REV and resolution could be determined based on extended Table 3.3. The identification of inter-LBS with uncertainty low in their exact positions but high in their individual thickness, continuity and their connectivity suggests further compositional analysis should be performed on subsamples which have a higher resolution. Thus, the potential challenge in segmenting thin bounding surfaces implied in this section should be further verified after compositional analysis on subsamples.

3.2.2 Sampling on T2

One piece of chip, referred to as T2, has been cut off from one of the six surfaces of the cube L1, which is perpendicular to the paleocurrent direction, as the xy surface contains up-curved bounding surfaces, as illustrated in Figure 3.12(A) and also in the original sample in Figure 3.1, to illustrate its relative location. This was done because: 1) the top-down sampling principle requires taking shared parts of the structure between T2 and L1, which could be confirmed from the segmented MXRT of L1; and 2) both L1's MXRT and Tp analysis suggested further investigation is required perpendicular to the paleocurrent direction, to capture the different geometries of representative hierarchical structures from the laminaset down to grain-pore grading. A 60x30x10 mm^3 chip was collected perpendicular to the paleocurrent direction from the xy surface, where bounding surfaces were observed from both the L1 surface and MXRT images. A standard, blue-stained epoxy resin impregnated thin section of size 2x4cm^2 and 30um thick was prepared as T2 (Figure 3.12(B)), which included REV of laminasets and laminae, according to the geometric scales updated after L1 MXRT analysis, as summarised in Table 3.3.

High-resolution compositional analysis was performed first, because: 1) both low-resolution EDS on Tp and MXRT on L1 observed inter-LBS to be sensitive to the heavier iron ions cementation, but the fundamental grain-pore scale nature is hard to reveal accurately, because the resolution is too low; 2) the intra-laminaset thin bounding surface is even harder to observe by both MXRT of L1 and BSEM of Tp. High-resolution compositional analysis of the bounding surface was performed by 1) an optical microscope using fluorescence and polarized lights, using a Zeiss AxioCam MRc5, at four selected FoVs, to contain inter-LBSs as labelled P1-P4 in Figure 3.12(B), with different magnifications; and 2) a high-resolution EDS image at 1.1x1.1 μm^2/pixel, with a dimension of 19845x38074 pixels square on T2, shown in Figure 3.12(C) (using Quanta FEG 650 SEM at Institute of Petroleum Engineering, Heriot-Watt University, in the same way as constructing the single BSEM image of Tp, as shown in Figure 3.4). After compositional analysis, BSEM (Figure 3.12(D)) was then performed at identical resolution and dimension on the same equipment with EDS, to investigate the geometries of hierarchical structures from laminar to grain-pore, as an implementation of Tp measurements but perpendicular to the paleocurrent direction.

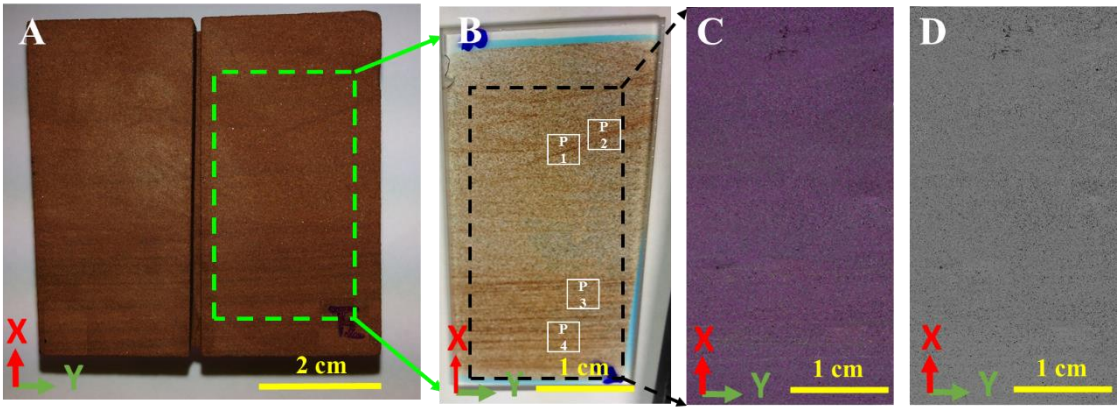

Figure 3.12 (A) Thin chip cut from L1 for T2; (B) Thin section T2 cropped at green dashed line box highlighted as FoV in A, with four FoVs labelled in white boxes for optical microscope analysis;(C) EDS scanned at black dashed line as boxed FoV highlighted in B, with resolution of 1.1x1.1 μm^2 /pixel with dimensions of 19845x38074 $pixels^2$; (D) BSEM scanned at identical FoV and resolution as for EDS;

To have a consistent understanding of how each dominant composition presents across the applied imaging techniques, one optical microscope image using polarized light and one using fluorescence light, one EDS image and one BSEM image are taken at the same FoV, P2, and manually registered to be compared in Figure 3.13. The dominant minerals are labelled in different colours in each image. Potential transitional bands of inter-LBS are highlighted between yellow dashes, based on manual observation, by identifying a fine grain layer with heavy mineral concentration and taking the natural light thin section photo at P2 in Figure 3.12(B) as a reference. The main observations include: 1) on the polarized light image (Figure 3.13(A)), darker coloured minerals proved to be haematite and dolomite-rich, based on the registered EDS, and are clearly cemented at inter-LBS. In contrast, the fluorescence light image (Figure 3.13(B)) enhanced the contrast of quartz and K-rich feldspars, that present in bright colours, but their distribution does not relate to specific structures of cross-lamination; 2) high-resolution EDS provides a robust approach to study the spatial distribution of minerals, therefore, the geometry of the bounding surfaces could be studied by looking at haematite and dolomite which proved to be preferentially cemented at bounding surfaces; 3) BSEM is less useful in compositional study but gives smooth presentation of grain particles (because it is less sensitive to elements within the grains) and shows a clearer edge in between; it is therefore good for grain-pore geometry analysis; 4) the optical polarized light image appears superior to others for identifying bounding surfaces because it reveals more concentrations of heavy minerals. This is because the optical polarized light image is a projected image of light transition through the thin-section rather than a reflection on the surface, as used by other methods, and therefore, would have a similar advantage in

identifying bounding surface as that obtained by radiographs (with 2D projection effect) as in the previously discussed example by Damcı and Çağatay (2016) in Chapter 2. Although fluorescent light is claimed to have an advantage in identifying pores, according to the literature reviewed in Chapter 2, it is, however, not the primary interest in this work. Therefore, in the next stages optical polarized light images are used to analyse the compositional and geometric characteristics of bounding surfaces, with EDS used to provide a more quantitative analysis of the overall geometry of bounding surfaces, by highlighting the presence of haematite and dolomite, and BSEM is used at the end to implement the grain-pore geometry quantitative measurements.

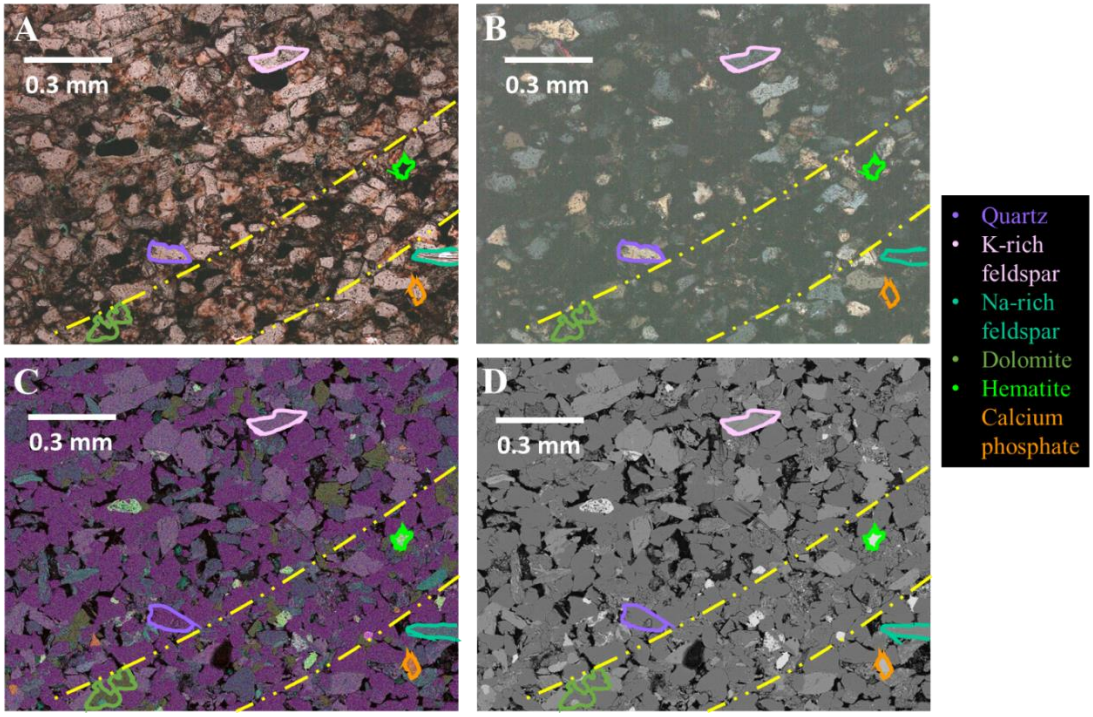

Figure 3.13 Comparison of four images taken at the same location: dominant minerals labelled in different colours; manually identified fine bounding surface layer, based on natural light photo as reference, is highlighted between yellow dashed lines. :(A) P2 under polarized light at 10X magnification; (B) P2 under fluorescent light at 10X magnification; (C) P2 with EDS at resolution of 1.1x1.1 μm^2 /pixel with dimensions 1266x1047 $pixel^2$; (D) P2 with BSEM at resolution of 1.1x1.1 μm^2/ pixel, with dimensions 1266x1047 $pixel^2$;

3.2.2.1 Optical microscope analysis for compositional study

Optical analysis using polarized light was performed at each of the four locations labelled as P1-P4 in Figure 3.12(B), at three magnifications. The full results and discussion are given in Appendix B.4 and the main conclusions are summarised here. 1) The bounding surface layer could be as thin as ~2-3 grains thick for the horizontal part; 2) The bounding surface appears to be a transitional band, where a distinctive boundary is still hard to identify; 3) Layered coarsening up (with average grain size increasing layer by layer as

stacking occurs over the bounding surface layer, with each layer having same thickness as the bounding surface layer), and thus inverse grading, is observed in the vertical (+X) direction, which is consistent with and confirms the previous assumption of a sedimentary direction; 4) For both horizontal and curved laminasets, the layered inverse grading is parallel to the manually defined bounding surfaces; 5) The intra-LBS is still hard to identify. The estimations are included in Table 3.3.

3.2.2.2 EDS analysis

High-resolution EDS imaging was performed over T2 to study the geometry of bounding surfaces at REV, highlighted by preferentially cemented haematite and dolomite. The 1x1 μm^2/pixel resolution of the EDS image covered average grain and pore long axes measured in Tp (Table 3.1). The top row of Figure 3.14(A) illustrates two zoomed-in views of haematite clustered with dolomite and cemented between quartz. The star shape is consistent with the geological claim that authigenic dolomite occurs surrounded by haematite, which is preferentially cemented between fine quartz grains. The cohesion of dolomite and haematite is also consistent with the geological claim that the Mg ions of dolomite ($CaMg(CO_3)_2$) is typically replaced by iron ions as a result of diagenesis. Dominant minerals are segmented by colour thresholds (see Figure 3.14(A): the bottom row shows an example of a zoomed-in view of dolomite segmented from an EDS image). The dominant minerals are segmented separately, with dolomite and haematite presented together as Figure 3.14(B), to highlight the bounding surface. Both K-rich and Na-rich feldspar are presented together in Figure 3.14(C) as feldspar, which is the second most important mineral in typical Aeolian sandstone, but also a potential distraction to identifying the bounding surface because of its high density, as noted in the review in Chapter 2. Figure 3.14(D) also shows the distribution of calcite, as indicator of bioturbation. Quartz is not discussed, as it is typically known as the main constituent of sandstone, and is expected to be distributed evenly over the sample.

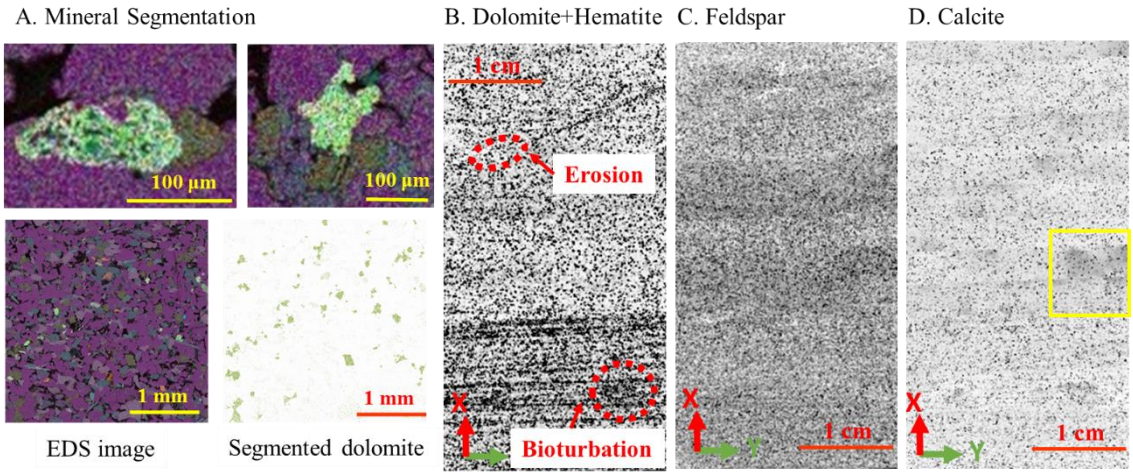

Figure 3.14; (A) Zoomed-in EDS image (same colour map with Figure 3.13(C) applied): top row shows two zoomed-in views of iron ions clustered with dolomite cemented between quartz and bottom row shows an example of dolomite segmented by colour threshold; (B-C) segmented binary element map shown with selected combinations: (B) Dolomite and haematite distribution maps on T2, both shown in black; (C) Feldspar (Black) distribution map on T2 and (D) Calcite (Black) distribution map on T2, indicating bioturbation.

From Figure 3.14(B), the dolomite and haematite distribution appear scattered but the general pattern is related closely to the inter-LBS that was observed from the thin section under natural light (Figure 3.12(B)), while intra-LBSs are still not observed clearly. However the dolomite and haematite related inter-LBS appears not to yield a continuous surface, because 1) haematite and dolomites have a scattered distributed on the bounding surface, as a result of cementation between quartz particles and naturally create small diameter "fake holes"; 2) the continuity of the bounding surface would also be interrupted by erosion, which creates "real holes" with a larger diameter than "fake holes" (see highlighted example in Figure 3.12(B)); 3) The occurrence of bioturbation would also create interruptions on the bounding surface, with even larger radius "real holes"(see highlighted example in Figure 3.12(B), corresponding to segmented calcite, indicating bioturbation, in Figure 3.14(D)). Bioturbation in Figure 3.14(D) presents as several randomly occurring clusters and the largest one is highlighted in the yellow box which appears close to the boundary between the curved and horizontal laminaset. The spatial location of the identified bioturbation is consistent with Tp, according to their spatial location. The relative locations of T2 and Tp are illustrated in Figure 3.15, the yellow box highlights that bioturbation in both T2 and Tp is spatially correlated; 4) Apart from "fake holes" and "real holes", however, the scattered distribution of feldspar potentially distracts the identification of bounding surface highlighted by haematite and dolomite as a result of the local hardening effect. The reason for the distraction is feldspar having a similar density (2.56 gm/cc) to dolomite (2.87 gm/cc). The distribution of feldspar (as

the second major constituent) in Figure 3.14(C) is very scattered over the map, apart from two wide bands in the middle, which might be correlated with the occurrence of a different lamina or laminaset. Therefore, its close similarity in density with dolomite may decrease the contrast and distract the identification of bounding surfaces, when occurring in a neighbouring location, of bounding surfaces presented in low-resolution density-sensitive MXRT images.

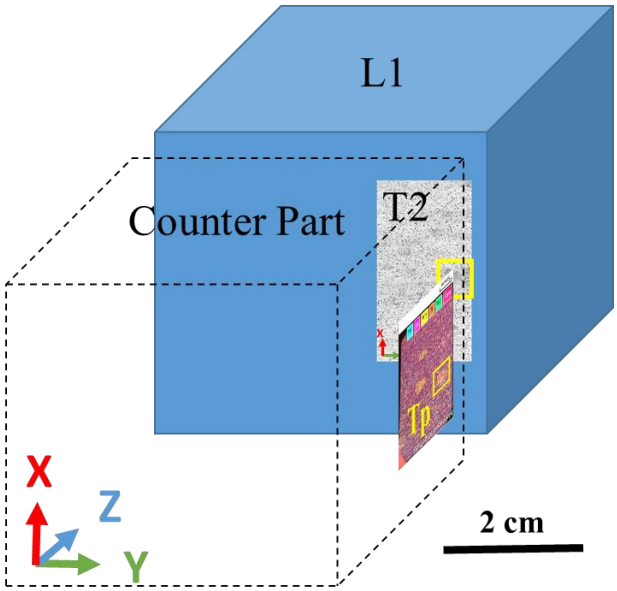

Figure 3.15 Comparison of bioturbation, highlighted by calcite distribution map in EDS of T2 and Ca ions distribution map in Tp, shown in the spatial location relative to L1.

As identification of bounding surfaces is critical to this work (to be taken as the cross-scale reference between multi-scale images) the four potential issues that could disconnect the true continuous bounding surface have been discussed above. To estimate the potential scale of the length of each type of discontinuity in the bounding surface, subjective measurements were performed, with details given in Appendix B.4 , and the results summarised in Table 3.2. In short, the "fake holes" were identified from the dolomite and haematite map by looking for regularly occurring small gaps with stable diameters following the trend of the bounding surface. On the dolomite and haematite map, erosion caused by "true holes" was also estimated by searching for abnormal and randomly occurred gaps with larger diameters. The size of the "true hole" caused by bioturbation could be estimated by measuring the diameter of the cluster in the calcite map. The distraction due to feldspar should be estimated with a slightly different logic, by searching for the average distance between small clusters of feldspar, because the distraction on identification of bounding surface is caused by the local hardening effect

and would be more significant when it is closer to a bounding surface. Therefore, the average distance between the scattered feldspar clusters needs to be known, so as to obtain an idea about the size of the neighbouring area within which the identification of bounding surface may be distracted by feldspar. The challenges of identifying a bounding surface, as discussed in chapter 2 are verified here, the length scales of dis-connectivity summarised here are important to instruct the development of a connectivity enhancing method in chapter 4.

Table 3-2 Discontinuity of bounding surface

Discontinuity reason	"fake hole" of scattered haematite and dolomite cementation	Distraction by feldspar	"true hole" of erosion	"true hole" of bioturbation
Length scale	< 2mm	~2.4 mm	> 5mm	> 6mm

Based on the EDS dolomite and haematite distribution map, the horizontal laminaset thickness could be updated with more accurate measurements, because the high-resolution EDS captured the fine ~1-2 haematite and dolomite grain cemented inter-LBS layer. The thickness of the horizontal part is clearly identifiable, however, where the thinnest part is observed to be < 1mm, and a thickness range of 0-3mm is estimated, as shown in Table 3.3. The thickness of the curved laminaset is, however, not clear, because of the limited FoV, and only two curved inter-laminaset bounding surfaces are observed to intersect with each other.

3.2.2.3 BSEM quantitative measurement

The zoomed-in view of Figure 3.14(A) demonstrates that high-resolution EDS is good at providing an accurate elementary distribution map, but each grain particle would be full of the noise of different colours, as a result of the mixture of different elements. Therefore, the BSEM of T2 was segmented, following the same method as in Tp, as illustrated in Figure 3.6 (with details in Appendix B.5), and overall quantitative statistics of grain-pore geometries were measured, as summarised in extended Table 3.3.

A comparison of grain and pore measurements of Tp and T2 is summarised in Table 3.3. The overall number of grains and pores (count) measured in T2 is larger than in Tp, which could be a result of the larger sample size of T2 (4x2 cm^2) than that of Tp (3x2 cm^2). The average grain and pore size in terms of their surface areas, and long and short axes are roughly in agreement between Tp and T2 (note that the slight difference may be also caused by the number of decimal places set). However, the circularity of grains in T2 is

higher than in Tp, in which the cross-sections of elongated grains would present more elliptical shapes from cross-section parallel to paleocurrent direction, Tp, and present more circular shapes from cross-section perpendicular to paleocurrent direction, T2. The different circularity observed for grains from cross-section at two perpendicular direction provided indirect evidence of preferred orientation. The average angle (orientation) of grains measured in Tp is about 3° deviation from the values obtained in T2. The 3° deviation in T2 is considered significant, as the second piece of evidence of orientation inclined parallel to the paleocurrent direction. The 3° deviation is significant because the larger numbers of grains that were counted with arbitrary orientation would average the relatively small number of grains with the preferred orientation.

Table 3-3 Summary of Updated Measurements

Hierarchical Structures	Laminaset			Lamina			Layer within lamina	
	Curved		Horizontal planar	Curved		Horizontal planar	Curved and Horizontal planar	
Measurement / Sample	Set thickness	Set half wave length	Set thickness	Lamina thickness	Intersect angle b.t. 3rd and 2nd surface	Lamina thickness	Bounding Surface thickness	
L1 (Surface)	1-2 cm	5 cm	1-3mm	1-4 mm	25-30°	1-3mm	<1 mm	
L1 (XRT)	3-11 mm	5 cm	3.43 mm	N/A			<1mm*	<2mm

Hierarchical Structures	Laminaset	Lamina	Layer within lamina		Grain and Pore (BSEM overall)							
Measurement / Sample	Thickness of Curved (Cuv) and Horizontal Planar (Hor)	Intersect angle, thickness and grading	Thickness	Geometry		Count	Average Size in area (μm^2)/ volume(mm^3)	% Area	Long axes (2D/3D) μm	Short axes (2D/3D) μm	Angle	Circularity (2D)/ Shape_VA3d (3D)
Tp (0.6μm^2)	Cuv: 2cm Hor: 1-3 mm	Intersect angle= 21.7°	100-200 μm	Parallel BS	Grains	1.36E+5	3102.4	72.1	76.9	46.4	92.8°	0.25
					Pores	1.07E+6	71.8	13.1	8.2	3.7	N/A	N/A
T2 (1.1μm^2)	Cuv : N/A Hor: 0-3mm	Thickness ~ 400-800μm	100-200 μm	Parallel BS	Grains	1.99E+5	3392.5	73.8	77.2	48.2	89.8°	0.35
					Pores	1.35E+6	111.1	16.4	9.3	4.2	N/A	N/A

* : measurement from processed but not segmented XRT image of L1

This section has described how thin sections of T2 were measured by the optical microscope, EDS and BSEM. Based on these measurements, the main conclusions and suggestions are: 1) heavy haematite and dolomite are confirmed as the signature of the bounding surface and responsible for the brighter presentation of bounding surface in MXRT because of their higher density. The thin, fine grain layer in the bounding surface could be as thin as ~1-2 grains thick; therefore, the need for more accurate segmentation than simple segmentation on L1 is suggested; 2) intra-LBSs are still hard to observe, even

with high-resolution EDS images; so the laminae and layers within them still require investigation; 3) preferred orientation and grading are measured with limited confidence because a continuous bounding surface and 3D orientation could not be accurately identified from either 2D Tp or T2 images. Therefore, further investigation is suggested to be performed in 3D μ-XRT, where the bounding surface is expected to be better identified by a 3D projection view (similar to radiographs, as previously discussed in Chapter 2) and 3D orientation could also be studied; 4) the different circularity between T2 and Tp perpendicular to and parallel to the paleocurrent directions verified the 3D complex geometry of grains and pores, apart from the preferred orientation. Therefore, 3D μ-XRT is suggested to further characterise grains and pores.

3.2.3 Sampling on selected plugs

3D imaging on small plugs was performed in this stage of the research, to investigate the geometry of laminae, layers and the grain-pore space within them. The investigation of lamina features of grading and preferred orientation is limited in 2D images, because continuous bounding surfaces are hard to identify. Further investigation is expected to be possible by use of 3D μ-XRT images, which are potentially capable of providing clear identification of bounding surfaces by looking at a projected view of a stack of xy slices in 3D, where the scattered distribution of heavy minerals on a yz planar or curved surface is concentrated into a straight or curved line.

Apart from including 3D small-scale laminar structures for investigation, the sampling of small plugs needs to include parts shared between L1 and T2, to correlate the finer scale images for reconstruction purposes. Correlating plug images with L1 MXRT could be a challenge with large scale difference, but the 2D images of T2 intentionally covered a large area on one L1 surface at the pore-grain resolvable resolution, to serve as intermediate for correlation. Therefore, the next sub-sample was chosen to target selective small volumes of core plugs, each of which penetrates through one laminaset, and at the closest practical location to T2, to acquire 3D μXRT image of them at a resolution equivalent to that of the T2 2D images. Based on previous discussion, it appears that horizontal planar and curved laminasets have different geometries of laminae and grading layers; therefore, at least one plug needed to be prepared to investigate each type of laminaset.

Seven small cylindrical plugs of 3-5 mm in diameter and 4mm long were taken from the remaining volume of L1 (all are from a selected location containing part of the bounding surface), as shown in Figure 3.16. Of these, four were located in the curved laminaset region, while the remaining three were in the horizontal planar region. Figure 3.16(B) shows the locations of the plugs, named as S1 to S7, and Figure 3.16(C) shows plugs drilled at the closest practical distance (< 3mm) to the surface to avoid collapsing. The first set of μ-XRT images was acquired for 3 plugs S1, S3 and S4, (using XRadia/Zeiss VersaXRM 410 at the School of Engineering & Computing Sciences, University of Durham to achieve high resolution (< 5x5x5 μm^3/voxel) to capture the grain-pore structures). Among them S1 and S4 were selected to be analysed. This was because 1) the scanned μ-XRT contained relative clear patterns of bounding surfaces; 2) S4 and S1 fall within the horizontal planar and curved laminasets, respectively, and 3) they are located behind T2 and could relate to T2 through shared bounding surfaces. The analysis of these images (see below) indicated that taking additional μ-XRT images besides those of S4 and S1 would be unlikely to obtain further information. The grain and pore geometry of S1 and S4 were firstly quantitatively measured to extend the information in Table 3.3. The bounding surface was then further investigated on both images, followed by a quantitative study on the preferred orientation and layered grading.

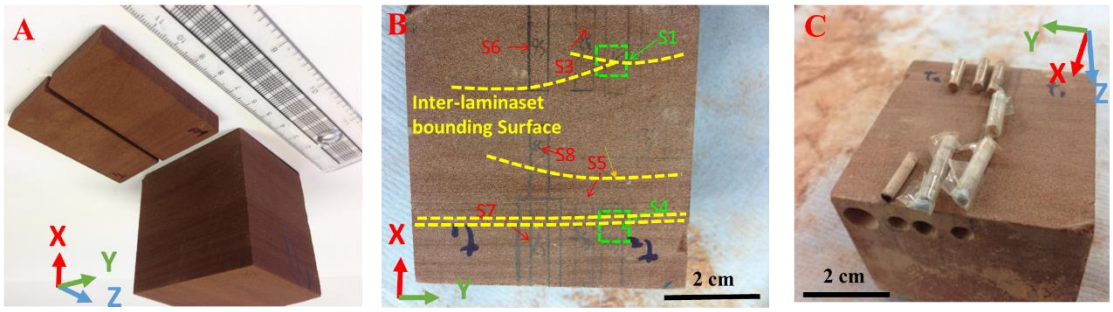

Figure 3.16 (A) Illustration of the rest of L1 after T2 had been cut off from surface (image put upside down to display curved laminaset in upper sample, to be consistent with previous images); (B) xy surface locations of 7 plugs with example inter-LBS labelled; (C) Illustration of 3-5mm diameter cylinder plugs drilled close to the surface after T2 had been taken off.

3.2.3.1 Overall geometry and quantitative measurements

Both S4 and S1 were scanned using μXRT at two voxel resolutions, 1 μm^3/voxel and 3.1x3.1x3.1 um^3/voxel for S4, and 1x1x1 um^3/voxel and 4.3x4.3x4.3 um^3/voxel for S1. At the higher resolution, only the centre part of S4 and S1 was imaged instead of the whole. Figure 3.17(A) and Figure 3.18(A) show the renderings of 3D images of S1 and S4 respectively, with half volume of a low-resolution image and full volume of a high-

resolution image registered manually in the centre. Figure 3.17(B) and Figure 3.18(B) show the green box highlighting a middle slice of the xy cross-section stack, also with a high-resolution image registered manually in the middle. It can be observed that the bounding surfaces of no more than 5 grains thick on both samples can be traced safely following the high-intensity bright voxels in both high- and low-resolution µ-XRT images (note the bounding surface observed in µ-XRT is considered as an inter-LBS reference to the sample photo taken under natural light in Figure 3.16); the bright voxels are known to be associated with grains composed of a high proportion of heavy metal components, as identified from the SEM images and optical microscopy images in the previous section. Given that the purpose of the sampling is to estimate lamina thickness and grading character, a larger FoV is preferred to achieve more representative measurement. A decision was made to use low-resolution images only in the following discussion.

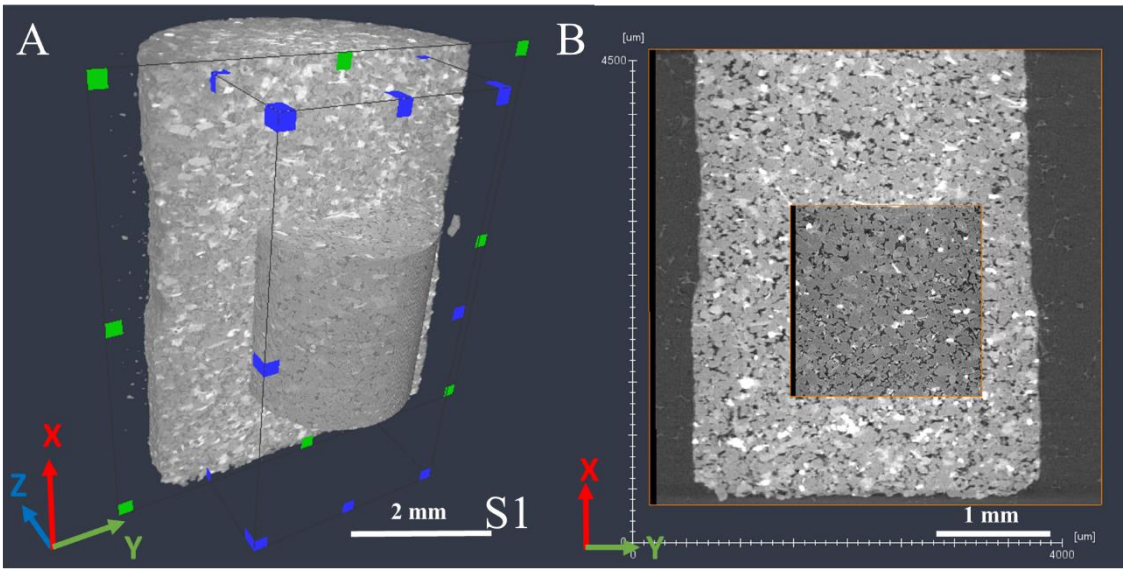

Figure 3.17 (A) Renders of S1 imaged at resolution of 4.3x4.3x4.3 µm^3/voxel (the outer larger cylinder volume) and resolution of 1x1x1 µm^3/voxel FoV in the centre (the inner smaller cylinder volume); blue boxed volumes of image with resolution of 1x1x1 µm^3/voxel are cropped for full quantification measurements; (B) Green boxed xy cross-section of A.

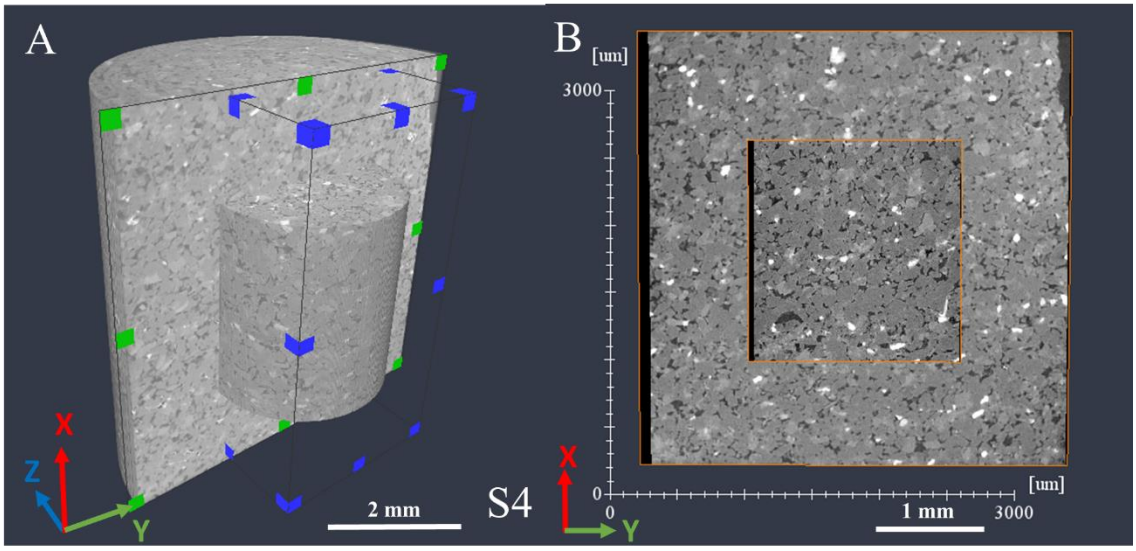

Figure 3.18 (A): renders of S4 imaged at resolution of 3.1x3.1x3.1 μm^3/voxel (the outer larger cylinder volume) and resolution of 1x1x1 μm^3/voxel FoV in the centre (the inner smaller cylinder volume), blue boxed volumes of image with resolution of 1x1x1 μm^3/voxel are cropped for full quantification measurements; (B) Green boxed xy cross-section of A.

As discussed in section 2.2.2.3, because of the different strengths of different segmentation methods, typical watershed-based segmentation approaches were applied for grain segmentation, while the Otsu thresholding approach was applied for pore segmentation (the same as with 2D BSEM segmentation). The overall grain-pore character was again measured (see Appendix B.6 for details of segmentation and measurements on μ-XRT) to implement quantitative measurements of grain-pore geometries in 3D. The measurements were performed for the volumes highlighted in the centre blue box, as in Figure 3.17(A) and Figure 3.18(A), to exclude edge artefacts. The results were incorporated into the quantitative measurements in Table 3.4. The percentages of grain and pore volumes from S1 and S4 agreed with both Tp and T2 measurements. The long axes and short axes measured in the 3D images of S1 and S4 are clearly larger than in the 2D measurements, because in 3D each grain and pore are fully imaged rather than one cross-section. The differences in the measured long and short axes between 3D and 2D proved that it was necessary to use the 3D image to capture the 3D complex geometry of grains and pores. The 3D shape factor measured for both S1 and S4 deviated from "1" (standing for a perfect sphere), which is further evidence of the 3D complex geometry of grain particles. The long axes and short axes measured in 3D S1 were larger than those in S4, suggesting larger grain size from the curved part than from the planar part. Therefore, grain-pore reconstruction between curved and planar parts needs to be treated differently. Grain orientation is measured by calculating the

polar angle formed with the –X axis in spherical coordinates (see section 2.2.2.3) and varies in the range [0, 90] degrees. The average overall grain orientation of S1 was found to be similar to that in S4.

Table 3-4 Summary of Quantification Measurements after update of S1 and S4

Hierarchical Structures	Laminaset			Lamina			Layer within lamina	
	Curved		Horizontal planar	Curved		Horizontal planar	Curved and Horizontal planar	
Measurement / Sample	Set thickness	Set half wave length	Set thickness	Lamina thickness	Intersect angle b.t. 3rd and 2nd surface	Lamina thickness	Bounding Surface thickness	
L1 (Surface)	1-2 cm	5 cm	1-3mm	1-4 mm	25-30°	1-3mm	<1 mm	
L1 (XRT)	3-11 mm	5 cm	3.43 mm	N/A			<1mm*	<2mm

Hierarchical Structures	Laminaset	Lamina	Layer within lamina		Grain and Pore (BSEM overall)							
Measurement / Sample	Thickness of Curved (Cuv) and Horizontal Planar (Hor)	Intersect angle, thickness and grading	Thickness	Geometry		Count	Average Size in area (μm^2)/ volume(mm^3)	% Area	Long axes (2D/3D) μm	Short axes (2D/3D) μm	Angle	Circularity (2D)/ Shape_VA3d (3D)
Tp (0.6μm^2)	Cuv: 2cm Hor: 1-3 mm	Intersect angle= 21.7°	100-200 μm	Parallel BS	Grains	1.36E+5	3102.4	72.1	76.9	46.4	92.8°	0.25
					Pores	1.07E+6	71.8	13.1	8.2	3.7	N/A	N/A
T2 (1μm^2)	Cuv : N/A Hor: 0-3mm	Thickness ~ 400-800μm	100-200 μm	Parallel BS	Grains	1.99E+5	3392.5	73.8	77.2	48.2	89.8°	0.35
					Pores	1.35E+6	111.1	16.4	9.3	4.2	N/A	N/A
S1 (4.30μm^3)	Cuv : 600 μm Hor: N/A	Thickness = 753 μm SF_{rate1D}=0.021	100-200 μm	Parallel BS	Grains	1.62E+4	8.0E-4	74.1	173.0	71.6	62.4°	5.06
					Heavy	1.20E+4	2.6E-3	0.45	196.8	101.7	69.4°	1.47
					Pores	3.60E+4	7.6E-5	15.8	75.5	38.2	N/A	N/A
S4 (3.07μm^3)	Cuv : N/A Hor: 500 μm	Thickness = 760 μm SF_{rate1D}=0.023	100-200 μm	Parallel BS	Grains	1.53E+4	3.2E-4	75.8	126.5	73.3	61.3°	4.96
					Heavy	1.33E+4	5.7E-4	0.8	116.9	63.3	62.7°	1.55
					Pores	8.93E+4	1.2E-5	16.3	24.0	13.2	N/A	N/A

* : measurement from processed but not segmented XRT image of L1

3.2.3.2 Preferred orientation of heavy mineral highlighted bounding surface

To further quantify preferred orientation, the previously confirmed heavier iron minerals as markers of the bounding surface were segmented by setting a threshold for the brighter intensity particles (see Appendix B.6 for details of segmentation) which are masked in blue colour in Figure 3.19 (A) and Figure 3.20 (A) for S4 and S1 respectively. Segmented heavy minerals from both S4 and S1 were viewed from xy projection (in the perpendicular paleocurrent direction) as in Figure 3.19(B) and Figure 3.20(B). The heavy grain particles are concentrated and presented as two horizontal planar bounding surfaces for S4 and one horizontal and two inclined bounding surfaces about to intersect with each other for S1. The geometry of the heavy bounding surfaces is consistent with the sampling location illustrated in Figure 3.16(B), which were identified as inter-LBSs.

Quantitative grain orientation measurements were performed on segmented heavy particles and are summarised in Table 3.4. Heavy particles appear to have a larger size (in terms of volume, long and short axes) than the overall average. The 3D circularity of

heavy particles is closer to "1", suggesting a more circular shape as a result of formation by diagenesis cementation. S1 has an orientation of heavy minerals which deviates more from the overall average than S4, implying that S1 may have a more significant preferred orientation. The histogram distributions of grain orientation for S4 and S1 were also plotted in circular format, often referred to as polar histogram or rose map, to characterise directions (Baas, 2000), as shown in Figure 3.19(D) and Figure 3.20(D) respectively. The rose map plots the anticlockwise bin data (histogram of orientation between 0-90°, here) with their abundance values proportional to the radius of the rose map. For better visualisation, the rose map also implements the remaining quadrants (180-360°) by copying and adding 180° over the original data. The rose map of the heavy minerals is compared with overall particle distribution for S4 and S1 in Figure 3.19(C) and Figure 3.20(C) respectively. The rose maps for S4 overall and S4's heavy minerals are very similar, suggesting the horizontal planar surface did not introduce a distinctively different orientation to the overall average. The rose map for S1 heavy particles deviates from S1 overall and is more inclined along the horizontal direction (like the upper locally horizontal bounding surface in S1) thus implying a stronger preferred orientation. The S1 overall rose map is also similar to those of S4, because overall distribution has been averaged by particles away from the bounding surface without preferred orientations.

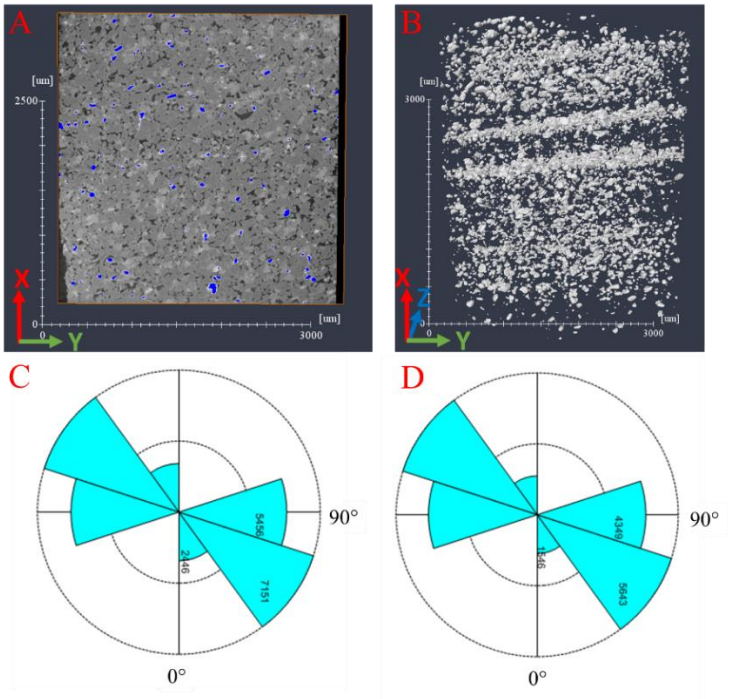

Figure 3.19 (A) xy cross-section of S4, illustrating brighter heavier particles (iron) segmented in blue mask; (B) segmented heavier mineral viewed from xy projection demonstrating clear concentration at horizontal planar bounding surface; (C) grain orientation distribution in rose map for overall S4

measurements (performed on centre boxed volume as in Figure 3.17(A)); (D) grain orientation distribution rose map for segmented heavier particles in B.

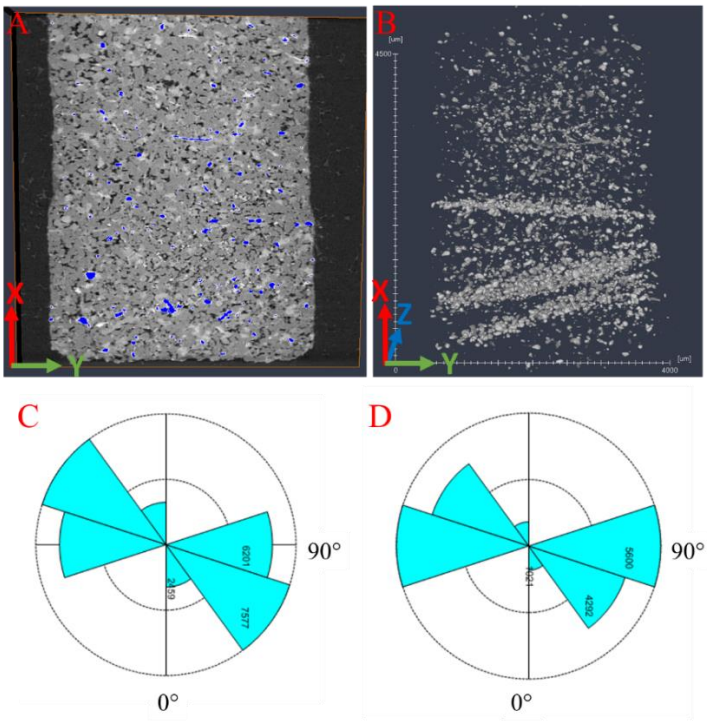

Figure 3.20 (A) xy cross-section of S1, illustrating brighter heavier particles (iron) segmented in blue mask; (B) segmented heavier mineral viewed from xy projection demonstrating clear concentration at inclined bounding surface; (C) grain orientation distribution in rose map for overall S1 measurements (performed on centre boxed volume as in Figure 3.17(A)); (D) grain orientation distribution rose map for segmented heavier particles in B.

This section has identified inter-LBSs by a heavy mineral projection view in 3D μ-XRT and confirmed strong preferred orientation along the inclined bounding surface from a curved laminaset. The thickness between identified inter-LBSs is estimated as 0.6mm and 0.5mm for S1 and S4 respectively, to represent laminaset thickness. Further grading measurements could be performed on the identified bounding surfaces.

3.2.3.3 Grading measurement

Inverse grading has been observed manually on 2D images of Tp and T2; however, it has not been quantitatively measured because the layered grading within laminae or laminasets could not be measured without identifying the continuous bounding surface. The viewing of concentrated heavy minerals at the bounding surface (inter-LBS) in 3D μ-XRT provided an opportunity to measure grading. In this section, it is explained how the sampling window was designed by subjectively tracing a 3D bounding surface visually identified by heavy minerals. Average grain volume was measured within the sampling window and by moving the window in a vertical direction, which is assumed as the sedimentary direction, based on previous laminaset geometry characterisation in

sections 3.1.1 and 3.2.1, and a log plot of the measured grain volume along the sedimentary direction would be expected to reflect potential grading.

For plug S4 that was taken from the horizontal part, the sampling window was designed as a planar box parallel to the visually identified horizontal planar bounding surface of the yz plane, as shown in Figure 3.21(A). The box had Y and Z dimensions reach the maximum of the sample (480 voxels). A thickness of 50 voxels (200 μm) was selected to be: 1) thin enough to represent a thin layer of 200 μm thick that potentially includes 2-4 grains, consistent with previous measurements (see Table 3.4) and 2) thick enough to include a representative volume (REV determined by the Coefficient of Variation (CV) plot, with same procedure as discussed for T2 in Appendix B.6). The sampling box moves from the bottom (X minimum end) up, with a 50-voxel moving interval each time (same to the thickness of sampling box so sampling does not overlap). 19 measurements were calculated for a distance of 2.9 mm up, from the bottom through the sample (the measurements are discussed and summarised in Appendix B.6). The log plot was masked onto one xy slice in Figure 3.21(C), to correlate with the visually observed brighter bounding surface and two inverse grading circles were observed, starting from the labelled yellow square and ending at the labelled yellow triangle. The main observations include: 1) finer grain size at two inter-laminaset bounding surfaces, as clearly identified in Figure 3.19(B); 2) the distance between the two inter-LBS appears very thin (about 600um); 3) the log grain sizes have two main rise trends with small turbulence between the labelled square and triangle icon, which are identified as inverse grading. The sudden decrease at the bottom of the visually identified inter-LBSs are treated as a disturbance, because the grain size rises again quickly after passing this point.

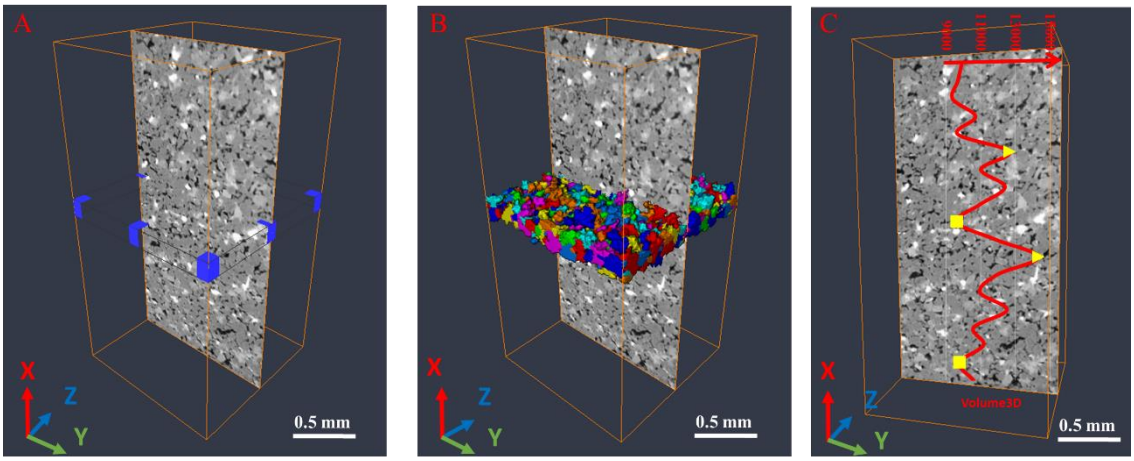

Figure 3.21 Illustration of grading measurement on plug S4 (3.07x3.07x3.07 um^3/voxel) from horizontal part (cropped volume illustrated in Figure 3.17(A) and shown as orange coloured bounding box), one xy slice is illustrated in the middle for reference: (A) A 480x480x50 sampling box at 500 voxels depth from bottom; (B) Segmented grains fall into the sampling box in A, labelled in different colours for measurements; (C) Measured grain volume in voxels versus depth plot and masked on one xy slice of cropped S4.

For plug S1 taken from the curved laminaset, Figure 3.22(A) illustrates one horizontal surface (referred to as H6) and one inclined surface (referred to as Sur1), which are traced from bounding surfaces identified by heavy minerals (Figure 3.20(B)). Sampling windows were defined by inclined and horizontal boxes marked by Y and Z dimensions reaching the maximum (480 voxels) and a thickness of 50 voxels (for the same reason given for S4) were designed (see Figure 3.22(B) and Figure 3.22(C) for grains measured in an inclined and horizontal sampling box). The same 50-voxel moving interval as for S4 were applied. Three measurements were made, starting from Sur1, and nine measurements were made starting from H0 in the vertical +X direction (the measurements are discussed and summarised in Appendix B.6). The log plot is masked in Figure 3.22(C) and the main observations include: 1) two inverse grading circles starting from the labelled yellow square and ending at the labelled yellow triangle are observed; 2) the fine grain volume layer appears at Sur1 (lower yellow square in Figure 3.22(C)); 3) strong inverse grading was observed from inclined Sur1 upwards; 4) a fine grain layer followed by inverse grading of 860um thickness occurred, starting at 645um above (3 moves) the traced horizontal bounding surface H6, which appears as a valley (upper labelled yellow square) in the log plot. The small delay of the valley point after tracing the bounding surface on log plot could potentially be caused by a set of reasons, for instance, an unidentified intra-LBS, assuming the vertical moving direction did not match the true sedimentary direction or was caused by disturbance by an artefact.

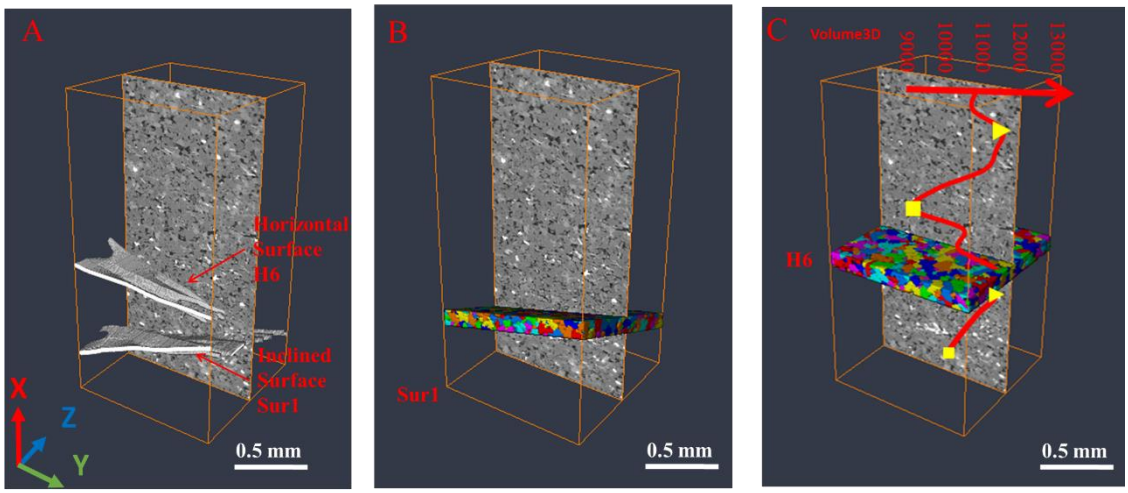

Figure 3.22 Illustration of grading measurement on plug S1 (4.3x4.3x4.3 um^3/voxel) from curved part (cropped volume illustrated in Figure 3.18(A) and shown as an orange bounding box), one xy slice is illustrated in the middle for reference: (A) One horizontal and one inclined surface traced with semi-automated method (see Appendix B.6 for detail); (B) segmented grains fall into a sampling box, Sur1 created for inclined surface in A, and are labelled in different colours for measurements; (C) segmented grains fall into a sampling box, H0, created for horizontal surface in A and are labelled in different colours for measurement; measured grain volume in voxels versus depth plot and masked on one xy slice of cropped S1.

It has been discussed that the heterogeneity of grain-pore textures in lamination could be seen as layers stacking over each other, with stationary (homogeneous) grain-pore textures within each layer but varying grain-pore textures across layers (coarsening-up of grain size in this work), and thus, non-stationarity. To reconstruct the coarsening-up inverse grading character as measured, an index (*l)* is required for each layer, indicating the variation of the mean of grain-pore textures (grain size (GS) and orientation). With index l corresponding to each layer to form an index map, MPS as reviewed in section 2.2.3, could be applied to stochastically reconstruct grain-pore spaces in each layer with grain-pore shape respecting the given training image and with the transformation corresponding to each index respecting the measured grain-pore texture variation. Therefore, the crucial step is to identify the correlation between the transformation and each index. For the grading of grain size discussed in this section, the correlation is about finding the function $f(\cdot)$ that $GS_l = f(l)$, where GS_l is the average grain size of layer l within a lamina containing N layers ($l \in [1,\ N]$). For the grading system discussed in this work, the average grain size of layer l can be seen as a proportion of average grain size of the base bounding surface layer (l=1). Thus $f(\cdot)$ could be expressed as $f(l) = SF_l \times GS_1$, in which GS_1 is the average GS of the base bounding surface layer l=1 (training image for MPS) and SF_l is a scaling factor (SF_l) defined for each layer l in a lamina. A function $f_{SF}(\cdot)$, where $SF_l = f_{SF}(l)$, should ideally be represented by a

probability map reflecting the variation of grain size over the layers, taking into account all kinds of uncertainties. However considering that 1) this work is focused on developing the overall subsampling and reconstruction workflow and 2) the sample has a rather homogeneous grain-pore texture and stable geometry of the lamination structure within curved or horizontal laminaset, this work simplifies the function $f_{SF}(\cdot)$ by assuming a linear relationship between the average grain size of each layer *l* over the base bounding surface layer *l=1*, thus $SF_l = SF_{rate} \times l + B$, in which SF_{rate} is a constant representing the slope (gradient) of the increasing grain size, and B is constant 1 representing the scaling relative to the base layer ($l = 1$).

Based on the above definition, for an inversely graded lamina containing N layers, SF_{rate} could be estimated by equation (3.1) for each lamina identified in the log plot. The SF_l for the layer *l* in an inversely graded lamina could then be calculated using equation (3.2). The SF_{rate} estimated in equation (3.1) is based on grain size measured in 3D volume, and therefore is a 3D volume gradient. The reconstruction to be introduced in the later section, however, needs a gradient in 1D in each of the three dimension. A simple estimation to calculate a 1D gradient from the 3D SF_{rate} by assuming cubic volume is given in equation (3.3) and the corresponding $SF_{l\,1D}$ is estimated by equation (3.4).

$$SF_{rate} = \frac{\frac{GS_N}{GS_1} - 1}{N} \tag{3.1}$$

$$SF_l = 1 + SF_{rate} * l \tag{3.2}$$

$$SF_{rate\,1D} = \sqrt[3]{1 + SF_{rate}} - 1 \tag{3.3}$$

$$SF_{l\,1D} = 1 + SF_{rate\,1D} * l \tag{3.4}$$

The $SF_{rate}s$ are measured for 2 laminae with monotonically increasing grain size for either S4 or S1. In Figure 3.21(C) and Figure 3.22(C) the starting bounding surface layer of each lamina is highlighted by a yellow square and ends at the following yellow triangle. The average SF_{rate} for the two laminae in S4 and S1 are added into Table 3.4, with an average SF_{rate} of 0.078 and 0.0648 in the 3D volume and SF_{rate1D} of 0.025 and 0.021 in the 1D axes for S4 and S1 respectively. Note that gradients are calculated per layer thickness of 200 μm. Lamina thickness can also be estimated by calculating the distance between the highlighted starting and end point of grading. An average thickness of

0.76mm and 0.75mm has been measured for the two laminae highlighted, for both S4 and S1.

This section has established that 3D μ-XRT projection has advantages in helping to identify the bounding surface; therefore, quantified measurements could be designed and bounding surface related preferred orientation and grading could be measured. The main conclusions and suggestions include: 1) based on the verified advantage that a 3D image may better represent a bounding surface, the bounding surface would be expected to be segmented from L1 more accurately if a method could be developed to address the previously discussed connectivity issues; 2) the brighter iron particles segmented along the bounding surface have orientations deviating further away from the overall average in S1 than in S4, thus implying a stronger preferred orientation for S1 along the orientation of the curved bounding surface; 3) log measurements proved capable of identifying layered grading and the measured gradient could be applied in pore-space reconstruction; 4) thickness of laminae could also be measured from log but μXRT only measured 2 laminae for either a horizontal planar or curved laminaset; therefore, further measurements are suggested to be performed on a larger FoV, to be representative; 5) from the thickness identified up to now, it appears horizontal laminae and laminasets have similar thicknesses and this suggests the two may not be distinguishable; 6) S1 and S4 are expected to register with L1 according to the identified bounding surface; therefore, the measurements could be implemented into 3D reconstruction.

3.3 Discussions on key observations and inferences about the structure hierarchy

The application of the recursive sub-sampling procedure above yielded three datasets, MXRT, SEM and μXRT. Analysis of those datasets has revealed that the laminar structures at the top of the hierarchy, i.e. laminasets, can be observed and measured directly from MXRT, whereas the positions of laminae and their geometry within each laminaset can only be inferred from auxiliary information extracted from the datasets by applying geological knowledge. Intra-lamina structures are thus inferred to exist based on grain grading (grain size variation in the log plot) obtained by μXRT. Although it is possible to measure the thickness of laminae from log plot, the geometry of individual laminae could only be inferred by manual observation in SEM and μXRT because intra-LBS could not be segmented from the image directly. In the following stage, direct observations from the datasets and inferences that have been made, based on evidence

obtained from the datasets about the structure hierarchy are discussed. This leads to a conceptual model of the structure hierarchy to be used in the reconstruction.

3.3.1 Summary of information obtained

Figure 3.23(A-H) summarises the data obtained through the developed top-down recursive sampling and characterisation, and illustrates how they contribute a full 3D pore space model, shown in the centre. Among them, apart from the MXRT of L1 which provided observation of the laminaset structure in Figure 3.23(A) and the μ-XRT of grain-pore in Figure 3.23(G-H) which would directly apply to the final model, the rest provide information at different levels of certainty to provide inferences on the structure of laminae and grading. Table 3.5 summarises the information regarding the hierarchical structures and corresponding certainty. Accurate identification of spatial distribution of inter-LBS and structural information of lamina and grading is a key issue to be addressed in next chapter. The contribution of key issues in constructing a full 3D pore space model are also illustrated in Figure 3.23 and highlighted with red background. The remainder of this chapter summarises and discusses how each observation and inference contributes to the final model, together with the nature of the remaining challenges.

Table 3-5 Summary of known and unknown geometric characters of hierarchical structures by Observation-OB or inference- IF after top-down recursive sampling and characterisation

Hierarchical Structures	**Known (OB- Observation/ IF- inference)**	**OB/IF**	**Certainty**	**Unknown (Anticipated measure)**
Laminaset	•Group of curved laminasets over a group of horizontal laminasets from MXRT. •Curved crest tough cross-lamina geometry	OB	•Low	•Thin 3D planar inter-LBS represents ~1-2 grains thick layer.
Lamina	•Parallel or intersecting geometry •Intersect angle	IF	•Low	•Intra-laminaset bounding surface •Representative measure of thickness of lamina
Layered grading within lamina	•Parallel to inter- or intra-laminaset for curved bounding surface, or intersection of both •Inverse grading feature •Preferred orientation	IF	•Low	•Representative measure of grading gradient
Grain and Pore	•Anisotropy geometry •μm scale	OB	•High	•N/A

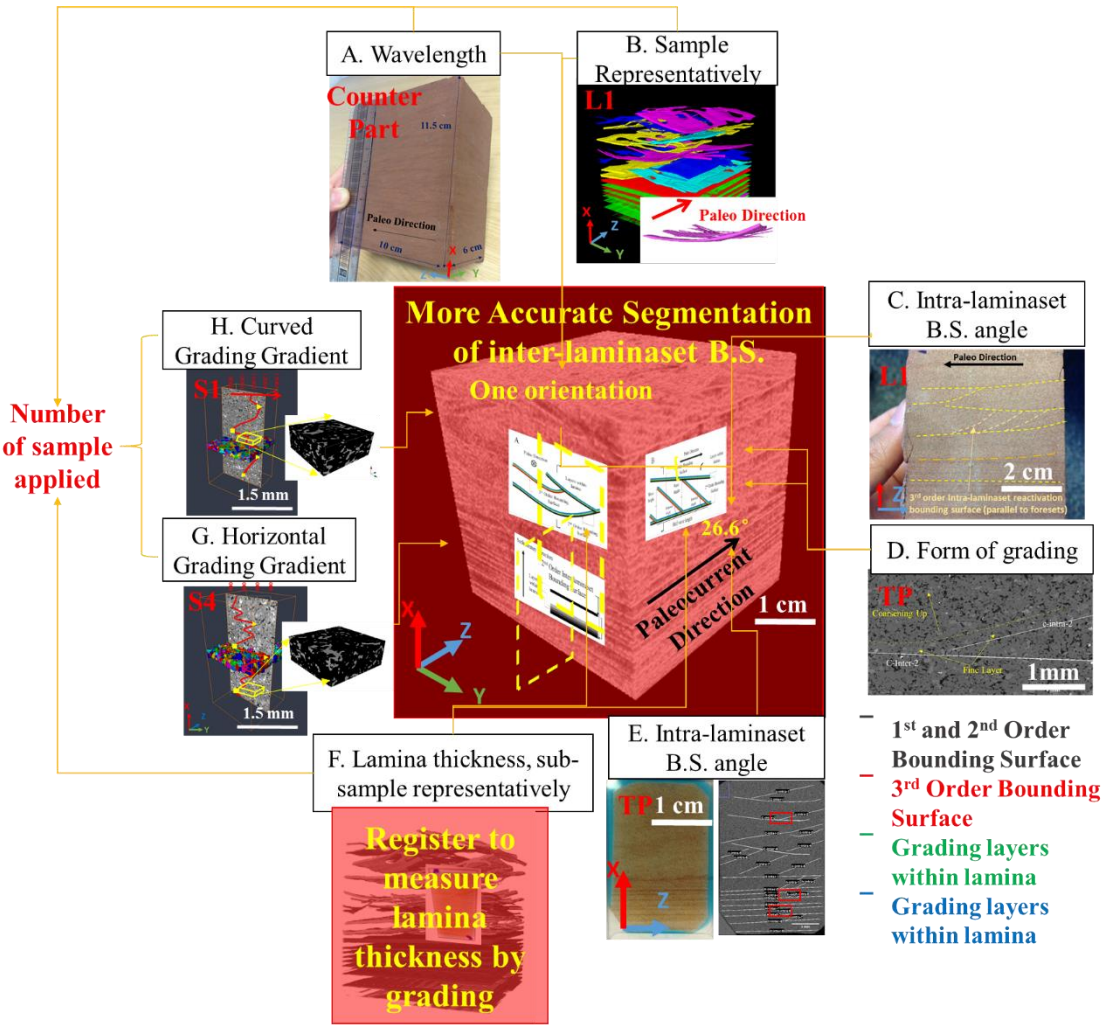

Figure 3.23 Information obtained by developed workflow of top-down recursive sampling and imaging, multiscale characterisation and proposed conceptual model of integration with registration and 3D pore-space reconstruction

3.3.2 Discussion of hierarchical structures and proposed conceptual model

In the following sections the obtained data are discussed to describe the generic nature of the hierarchical structures of the studied Aeolian fine cross-laminated sandstone sample. Based on observation, a conceptual model is proposed for each hierarchical structure, which by integration should yield a full hierarchical structure domain and sub-domains, and within which the grain-pore could be populated based on measurements.

1) Laminaset:

The surface geometries of two groups (horizontal and curved) of laminasets were preliminarily studied from the sample surface (Figure 3.23(A and C)) and its 3D geometries were further investigated by segmented inter-LBS from MXRT of L1 (Figure 3.23(B)). The geometric scales of the laminaset are summarised in Table 3.4, with a

thickness of mm to 2 cm; therefore, the 6x6x6 cm^3 L1 contained a representative number of stacked laminaset structures. Relatively stable laminaset structures were observed within each group, considering the similar geometry of horizontal planar laminasets and curved laminasets (because within the sample size of half a wavelength, most curved laminasets are following the same direction). Inter-LBS was expected to be segmented more accurately (it is thinner and has better connectivity) and to be treated as the base of the spatial domain constraint of the hierarchies' structures, as well as grain-pore variation (as shown in the middle of Figure 3.23).

2) Lamina:

At cross-section perpendicular to the paleocurrent direction, T2 intra-LBSs were hard to distinguish from inter-LBSs but were proved to exist by inverse grading and manually identified between and parallel bounding surfaces. Laminae were hard to identify by composition from MXRT in the 3D space directly, but assuming that the laminaset structures do not vary much within the selected sample, which is smaller than half the wavelength in each direction, one simple conceptual model of the lamina could be applied when explicit segmentation of the intra-LBS is not available. Intra-LBS separate laminae could be conceptually defined with single geometry properties as a sub-domain to extend the segmented inter-LBS from MXRT. Lamina geometries were investigated by fine resolution thin section images from two perpendicular surfaces (Figure 3.23(D-F)). Laminae appeared more likely to be parallel to the horizontal planar inter-LBS, whilst for the curved part, laminae appeared to be parallel to the inter-LBS at cross-section perpendicular to the paleocurrent direction and intersecting in a narrow range of acute angle with inter-LBS parallel to the paleocurrent direction. The separation of horizontal planar and curved laminaset could, however, be non-distinctive because transitional zone between two laminasets was observed in Tp. A transitional zone was identified because it was observed that inclined laminae could potentially exist in the horizontal laminaset when close to the boundary with the curved laminaset. However, the certainty of the exact location of the transitional zone was low because it was inferred from manually observed laminae. The intersection angle of the lamina was measured from the L1 surface and Tp in the range of 20-30^o , while the thickness of laminae was hard to identify because intra-LBS could not be accurately identified through images from different techniques. The thickness of a lamina measured from finer scale SEM by manual observation and small FoV plugs μ-XRT based on the circulation of grading gave an estimation of less

than 1mm for both the curved and horizontal part, which slightly deviates from the 1-4mm estimated from the L1 surface. Therefore, relatively higher uncertainty exists for lamina thickness and suggests that more representative measurement of circulation is needed from a larger FoV SEM image of T2 (Figure 3.23(F)). T2 was selected because from surface perpendicular to paleocurrent direction lamina and grading appear parallel to the inter-LBS, thus moving the sampling window measurements is easier.

3) Grading

Within laminae, inverse grading was observed parallel to the inter-LBS for the horizontal part or the intersection of intra- and inter-LBS for the curved part, based on manual estimation from 2D thin section images of Tp and T2 in two perpendicular directions. The preferred orientation was observed close to an inclined intra-LBS from Tp. Grain size with an increasing gradient of inverse grading was measured quantitatively through 3D μ-XRT measurements, based on conceptual layered grading assumed in a vertical direction. Therefore, conceptual inverse grading layers could be defined as an extension over inter- and intra-LBSs to construct a full set of sub-domain constraints. Non-stationary values of size and orientation property could be assigned within each sub-domain to reflect measured grain-pore variation over the inverse grading laminaset. Given that stable laminar features are assumed within the curved or horizontal part, S1 and S4 are potentially representative examples for reconstructing the pore-grain system for each type of laminaset (Figure 3.23(G-H)). Nevertheless, representativeness of grain-pore features in S1 and S4 could be further confirmed with larger FoV measurements on grading.

4) Conceptual model of laminae

A conceptual geological representation of hierarchical structures, referred to as a conceptual model, is proposed to classify the laminated sandstone into different regional sub-domains, to assign the associated grain-pore character variations representing hierarchical structures. The model treats horizontal planar and curved laminasets differently according to their different anisotropic geometry characters. Given the isotropic character of horizontal planar laminasets, this model gives the same geometry of horizontal planar structures on both cross-sections parallel to and perpendicular to the paleocurrent directions. As illustrated in Figure 3.24, horizontal planar laminasets are separated by black horizontal planar inter-LBSs. In this model intra-LBSs are not

specially distinguished from inter-LBSs for the horizontal part, because: 1) an intra-LBS has not been clearly identified for the horizontal part; 2) the thickness of the laminaset measured at the horizontal part appears similar to the lamina thickness inferred from grading; therefore, it could be meaningless to distinguish these. Thus layers reflecting grading are proposed as sediment on the inter-LBS, directly along the sedimentary direction, with same parallel planar geometry, as illustrated in the decreasing grey layers in Figure 3.24.

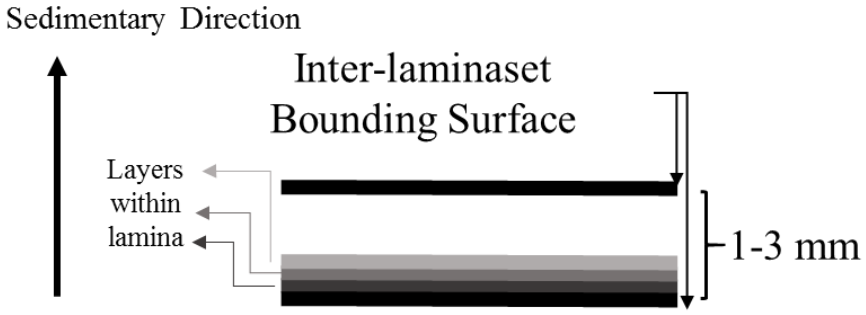

Figure 3.24 Illustration of horizontal planar geometry structure at cross-section in perpendicular or parallel direction

The model of a curved laminaset has different geometry at cross-section parallel and perpendicular to the paleocurrent directions, as illustrated in Figure 3.25. At cross-section parallel to the paleocurrent direction, as shown in Figure 3.25(B), inter-LBS (in black) separating laminasets are presented as a horizontal or an inclined straight line, as a result of a cross-section being taken of the elongated surface along the paleocurrent direction. Intra-LBSs (in red) within a laminaset separate a set of parallel laminae and intersect at an angle with inter-LBSs. The half wavelength between two intra-LBSs along the paleocurrent direction, together with the intersect angle determine the thickness of lamina that could be inferred by measuring grading at a cross-section perpendicular to paleocurrent direction. Based on the inverse grading observed parallel to both the lee side (intra-LBS) and stoss side (inter-LBS) from Tp by manual observation (low certainty) it is concluded that no segmentation of the intra-LBS (supposed to have higher certainty) would be available to provide more accurate information about the geometry of intra-LBS. The conceptual model in this work has been designed based on the observation in Tp to provide the information about the geometry of intra-LBS. A conceptual model has been developed in which grading could be seen as conceptual layers stacked upon the surface created by the intersection of (black) inter- and (red) intra-LBSs with same geometry in the sedimentary direction, as labelled in green and blue in Figure 3.25(B).

The geometries of hierarchical structures at cross-section perpendicular to the paleocurrent direction, as shown in Figure 3.25(A) are a result of Figure 3.25(B). In Figure 3.25(A) intra-LBS are parallel to black inter-LBS, and the conceptual layers are a stack over inter- or intra-LBS with the same geometry, in parallel.

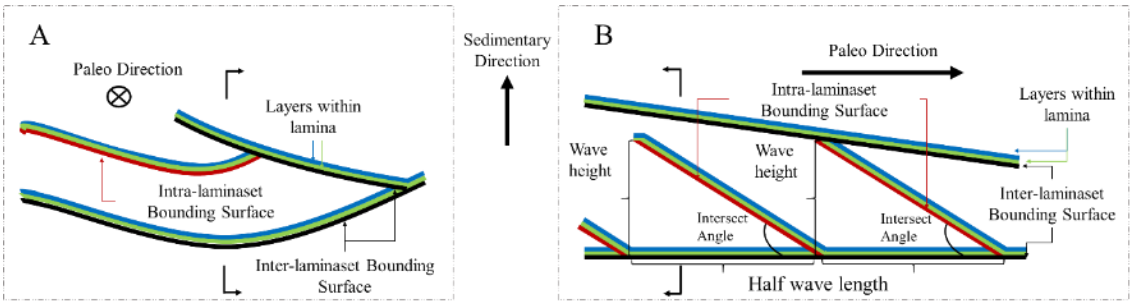

Figure 3.25 Illustration of curved laminaset geometry structure at a cross-section (A) perpendicular or (B) parallel to the paleocurrent direction, with inter-LBS plotted in black, intra-laminaset in red and layers within laminae in green and blue.

5) Discussion of uncertainty

To reconstruct the proposed model, apart from measurements summarised in Table 3.3, the missing information includes 1) accurate extraction of the thin, 3D inter-laminaset bounding surface from the MXRT image of L1, because the simple segmentation appears too thick for a bounding surface that could be as thin as ~1-2 grains thick. Moreover, simple segmentation also appears to struggle to retain 3D surface connectivity; 2) the thickness of the laminae needs to be identified at a more representative volume/area, based on the statistics for circulation of grain size between intra-LBSs as a result of grading; 3) the representativeness of the grain-size inverse grading gradient needs to be verified from a more representative image, because the μ-XRT image appears to be too small compared to the whole volume of L1. The uncertainty resulting from identifying the lamination structure by LBS and grain-pore variation would significantly alter the simulated flow path, as a result of the combination of the heterogeneity of the lamination structure and pore space topology and distribution (McDougall and Sorbie, 1993). In the next chapter it is therefore necessary to develop techniques and methods of investigation to address those uncertainties.

3.3.3 Remaining challenges

Three challenges are faced in identifying the unknown geometry; the first two would be based on the same principle: revealing bounding surfaces from MXRT and BSEM

respectively. Therefore, before discussing the challenge, the nature of bounding surfaces is summarised.

The nature of a bounding surface can be illustrated by Figure 3.26(A): a thin finer bounding surface scattering cemented by haematite and dolomite (~1-2 grains thick) causes smaller "fake holes" on a continuous bounding surface, which are also interrupted by larger "true holes" caused by erosion and bioturbation. This caused the challenges experienced with MXRT and BSEM. In MXRT, as shown in Figure 3.26(C), heavier haematite and dolomite together with the hardening effect, would present as brighter and highlight the bounding surface as a thin, brighter, linear (2D)/ planar (3D) pattern, but identifying them would involve the following challenges: 1) "fake holes" create small unconnected gaps that need to be bridged; 2) larger "true holes" create large unconnected gaps that should not be bridged; 3) the hardening effect of feldspar distract the identification of true linear bounding surface highlighted by haematite and dolomite, this verifies the prediction given in Figure 2.8 of Chapter 2. In high-resolution BSEM as shown in Figure 3.26(B), the bounding surface is much less obvious than in MXRT, because of both 1) the large scale of the difference without averaging and the local hardening effect on BSEM that improved contrast of the heavier mineral signature and 2) different imaging principles between BSEM and MXRT lead to different correlations between pixel intensity with the material. This observation verifies the predicted challenge proposed in Chapter 2, in Figure 2.8.

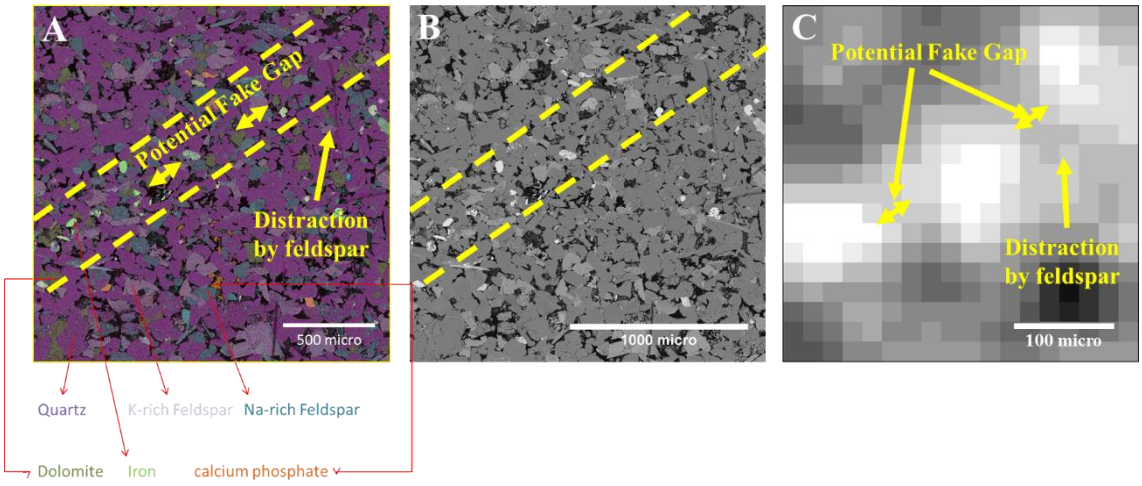

Figure 3.26 Manually registered EDS, BSEM and MXRT to highlight the nature of the bounding surface and its presentation in BSEM and MXRT, which implies a potential challenge in identifying shared bounding surfaces for registration: (A) EDS as in Figure 3.14(A) at 1x1 μm2/pixel resolution, with each

main mineral labelled; potential bounding surface layers are also highlighted; (B) registered BSEM at the same location and resolution as EDS in (A); (C) registered MXRT at resolution of 100x100 μm2/pixel.

Therefore, the three main challenges anticipated to be addressed in the remainder of this work can be summarised as:

1) Accurate identification of the inter-LBS from the MXRT of L1 respecting identified "fake holes", "true holes" and distractions.

2) Identifying inter-LBSs from the BSEM of T2, so as to design a sampling window as I did for S1 and S4 to measure grading. Apart from challenges of the different natures of imaging, identifying a continuous bounding surface from BSEM could still be challenging because of high grain lithology variation. Given that the inter-LBS are easier to identify from the MXRT of L1 and have shared parts with T2, registering BSEM onto the MXRT of L1 would provide the missing surface information to enable the statistical investigation of lamina thickness.

The registration is expected to help determining the geometry of the grading layer and determining the direction of grading by the registered bounding surface. An accurate registration is, however, less important, because the direction of grading is assumed beforehand, rather than being perpendicular to the accurately registered bounding surface; therefore, the determining grading direction benefits of registration has been lost and thus rendered accurate registration less important. However, the pre-determined vertical grading direction also brings uncertainty, both in measurement and reconstruction, which will be further analysed in later chapters.

3) Ideally, an index map to assist reconstruction requires the intra-LBS and grain sorting to be accurately identified to correlate the local grain texture transformation to the spatial hierarchical structure of lamination. However, as discussed these are hard to segment and measure with high certainty, and therefore, the uncertainty needs ideally to be considered as a soft probability map to represent the correlation between the spatial index and local transformation during reconstruction. In this work, however, taking into account the representativeness of the sample and relatively stable laminaset and lamina structures within two types of the laminaset, the decision has been made to define intra-LBSs and laminae deterministically, with conceptually layered sub-domains with one set of parameters, as measured. The non-stationary setting (grading gradient) of the grain sorting across sub-domains for reconstruction to be performed in Chapter 5 could be confirmed after grading measurements on a larger FoV in Chapter 4. The random

occurrence of bioturbation may lead to disturbing the hierarchical grading, and therefore needs to be considered as potential uncertainty in Chapter 5. This could be further discussed with the segmented bounding surface in Chapter 4 by analysis of surface geometries to identify the potential occurrence of bioturbation.

The first two challenges are to be addressed in Chapters 4, as highlighted in the red box in Figure 3.23. An integration of the obtained information as the task of Chapter 5, to address the third challenge, is conceptually illustrated in the centre of Figure 3.23. The integration implements the missing hierarchical structure as a set of sub-domain constraints to assign measured parameters for full 3D grain-pore space reconstruction.

3.4 Conclusions

This chapter reports the development of a top-down subsampling scheme for the tight Aeolian cross-laminated sandstone sample of the volume of 6x6x6cm^3. A preliminary exploratory analysis has been reported, first on the structural and compositional aspects of the sample, using a sub-dataset, Tp and a set of standard techniques for petrographic analysis. A recursive sub-sampling and characterisation procedure was then developed for the sample used in this work, to investigate the hierarchical nature of the sample structures and chemical composition. The combination of exploratory and quantitative analysis leads to a recursive sub-sampling and yielded three sets of image datasets: the 3D MXRT image on L1, 2D SEM BSEM and EDS images on Tp and T2 and 3D μXRT images on small plugs. From these, the hierarchical structures of the sample were observed and inferred at three length-scales, as follows:

1) Two groups of laminasets stacked one on top of another have been distinguished, in which the upper group contains a set of interwoven curved laminasets at half wavelength, with elongated axes following the same direction, while the lower is a vertical stacking of horizontal planar laminasets parallel to each other. Within each group, structures of inter-laminasets were constant across the domain and laminasets are demarcated by the inter-LBS, each of which could be characterised by a thin layer of grains with a higher concentration of haematite and dolomite compounds. Inter-LBS proved could be captured in MXRT with high certainty regarding their exact positions but lower certainty in their individual thickness, continuity and their connectivity, and are the best candidates as shared features for registration. However, the analysis conducted on SEM/EDS images showed

that even inter-LBSs are severely obscured in BSEM images and hard to segment directly, due to high grain lithology variation.

2) In each laminaset of either group, the intra-LBSs, which are supposed to exist in theory, to separate laminae from other adjacent ones, are suggested to be more likely to be distinguishable in the curved part than in the horizontal part, based on the inclined geometry. Intra-LBSs cannot be segmented as layers from grain compositions directly, but may be inferred from grain grading (see the next point).
3) Directional grain variation has been observed and shows a cyclic nature of grading, which can be explained by stacking laminae. The discrepancy in grain-size variation has been observed to appear at an isolated location only, which is attributed to localized bioturbations. μXRT argued SEM/EDS with 3D pore-grain distributions within and across laminae.

CHAPTER 4 - DATASET REGISTRATION

In Chapter 3, it was described how a fully-developed recursive sub-sampling and characterisation procedure yielded three image datasets: MXRT, SEM, and μ-XRT (see Figure 3-30) from which key structures of several hierarchical levels have been identified and analysed in the respective datasets. To reconstruct the sample, it is necessary to register all the datasets via one or more shared inter-LBS. However, as discussed, none of the simple characterisation techniques applied so far are capable of identifying features from BSEM and MXRT, respectively, which can be considered to correspond to the same bounding surface with any degree of certainty within the resolution required to position laminae. In fact, the scattered distribution of heavier mineral grains along each inter-LBS is attributed as the ultimate cause of this situation. The manifestations of that scattering in the two datasets acquired using different imaging techniques on different FoVs at different resolutions take very different forms. As discussed in the previous chapter, in MXRT, thin bounding surfaces are defined, presenting higher intensity, brighter voxels interrupted by holes of various size and create discontinuity, with the larger holes considered as the 'true holes' of bioturbation and erosion, while the smaller ones are considered as 'fake holes,' due to unconnected cementation of heavier minerals. The higher density and scatter distributed feldspar also cause distractions when they are close enough to a bounding surface. The challenge is to pick out those bounding surfaces from small local neighbours, to leave aside the distractions and at the same time to fill the 'fake holes' but to retain the 'true holes'. In SEM, heavier mineral grains appear as discontinuous brighter grain particles and they do not accurately re-assemble the topography of the bounding surfaces when they are simply connected at the high resolution of the dataset. The challenge is to pick one or more bounding surfaces that fit those dots in space. These challenges have been summarised from the literature review in Chapter 2, without any previous work being found that pointed to their fundamental nature, and verified through the three datasets obtained in the work reported in Chapter 3. So far no reported work exists which has considered the nature of this situation, let alone developing techniques to address it.

This chapter elaborates the nature of the hidden features in MXRT and SEM and the limitations of existing techniques and presents two new solutions that have been developed in this thesis to address specific challenges associated with each of the respective datasets.

4.1 Hidden features in MXRT

The bounding surfaces hidden in MXRT have been discussed, stemming from the nature of the distribution of minerals with various densities, associated or not associated with the physical bounding surfaces. The presentation of those distribution signatures and the disturbance of the bounding surface in MXRT are first discussed here, to reflect on how they fundamentally affect the task of identifying the bounding surface from the MXRT image.

1) Bounding surfaces are presented as thin brighter planar surfaces with 3D or linear structure in the 2D cross-section in the MXRT image, as shown in Figure 4.1(A), in which the brighter pixel intensity is a result of heavier iron and dolomite minerals that proved to be preferentially cemented in bounding surfaces. The bounding surface could be as thin as ~1-2 grains and presented as ~1-2 pixels thick, according to the zoomed-in view in Figure 4.1Figure 4.1(B), and the corresponding registered EDS is shown in Figure 4.1(C). The heavy mineral grains that are highlighting the bounding surfaces in MXRT, however, do not form a closely-spaced, dense layer, but their distribution is rather discrete. This is because the iron and dolomite are the results of diagenesis and appear to "insert" them between the original deposited fine layers of grains as evenly distributed, as shown in Figure 4.1(C). As a result, the bounding surface is presented in the MXRT image as higher intensity brighter pixels, interrupted by small "fake holes" and creating a discontinuity of less than 2mm in diameter, according to the measurement in Chapter 3.
2) Erosion also creates relatively larger middle-sized holes (diameter>5mm) by disrupting the originally formed bounding surface and leaving unconnected darker "true holes" on the bounding surface and causing a larger disconnected gap, as highlighted in Figure 4.1(A). "True holes" could also be a result of bioturbation, which was found to create the largest sized (diameter >6mm) disconnectivity in this study. Bioturbation has been confirmed in Chapter 3, and it was found that the calcium left in the penetrated large hole would present a large, brighter cluster in the MXRT image as a result of the relatively high density of calcium, as highlighted in Figure 4.1(A).
3) Feldspar creates a distraction by also having a higher density and a local hardening effect, as discussed in Chapter 3. In the work reported in Chapter 3, feldspar

particles were found to be scattered and distributed over the sample. When feldspar particles present close to a bounding surface, they will create brighter spots and distract the identification of the true bounding surface as Figure 4.1(B). The average distance between feldspar particles of about 2.4 mm, which was measured to help the development of the method in the present chapter.

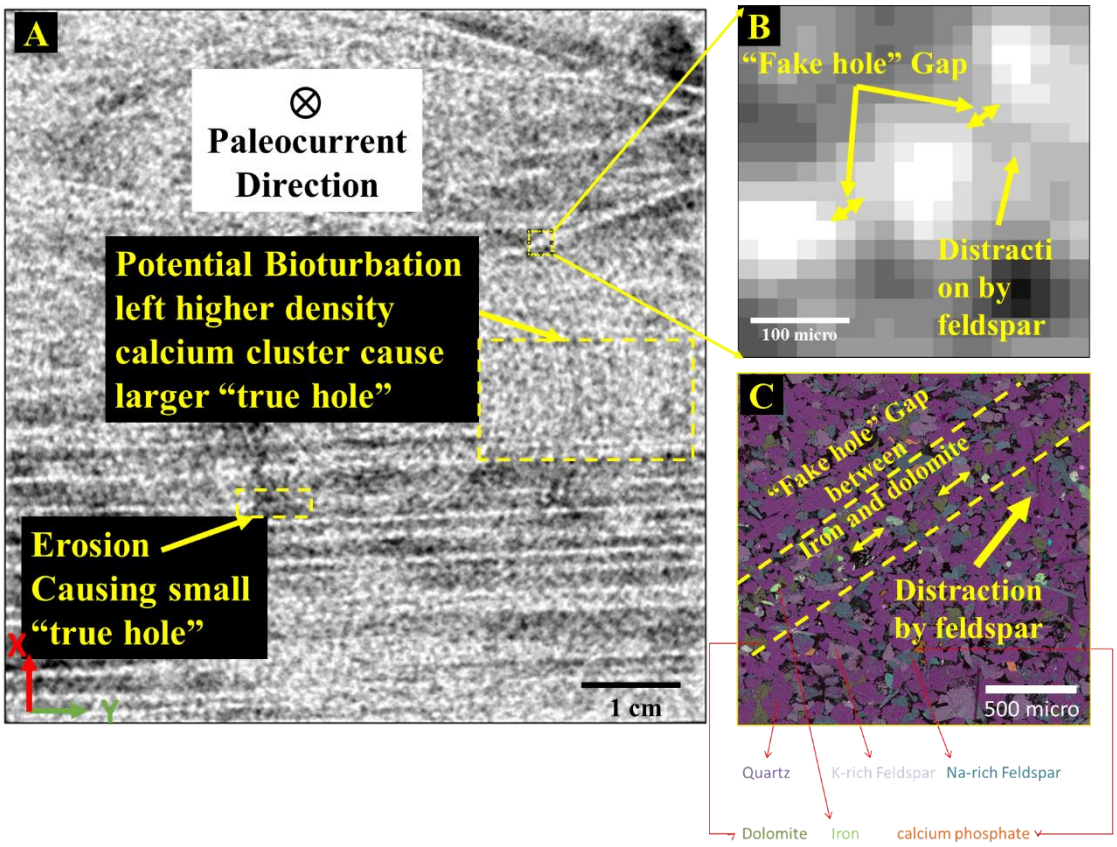

Figure 4.1 (A) 1st of 525 slices of the pre-processed MXRT image of L1 at xy face (550x562 pixels^2 at 100x100 μm2/pixel resolution); (B) Zoomed-in view of part of the curved bounding surface, whose overall thickness is about 4 pixels wide but the thinnest part could be as thin as 1-2 pixels thick; (C) Manually registered EDS of B at 1x1 μm2/pixel resolution.

It is, thus, challenging to segment the thin, piece-wise, unconnected and distracted bounding surface from low-quality MXRT images. This is consistent with what has been pointed out by Bultreys et al. (2016), that the low quantity of iron in the cement of laminated sandstone failed to provide enough contrast in the XRT image to segment the layer using the threshold method; however, they did not discuss the fundamental reason for this. A typical global thresholding approach, like that carried out by Otsu (1975), segments the image by an overall pixel intensity histograms and looking for intensity bands with a distinctive frequency distribution. There is, however, no universal standard threshold for a heterogeneous sample, because the indistinguishable physical bounding surface may present as different local average intensities, as a result of complex mineral

distribution and the hardening effect. A local thresholding method like the watershed approach, looking for pixels with distinctive intensity above the local average, has been claimed by Beucher and Meyer (1992) to be superior to a global approach in dealing with local intensity variations. However, this approach may still not work, because it does not look at the spatial relationship between pixels and would be unable to capture the continuous pattern of bounding surfaces hidden behind disconnected bright spots and distractions with similar intensity.

Figure 4.2 further demonstrates the challenge on one slice out of 525-slice stacked MXRT image, as shown in Figure 4.2(A). The greyscale image has its pixel intensity histogram normalized by stretching "minimum to maximum" to "0-255". Two-line Regions of Interest (ROIs) (two yellow dashed lines labelled as "1" and "2") in the zoomed-in grey image shown in Figure 4.2(B) are selected. Both ROIs are actually crossing inter-LBSs, as shown in Figure 4.2(B), but have different local intensity distribution. The pixel intensity plots along both ROIs, as given above and below the grey image in Figure 4.2(B), containing bounding surfaces as central intensity peaks, labelled in both intensity plots. The dashed line "1" includes pixels with similar intensity to the central peak bounding surface intensity (labelled as distractions), which are considered as noise. According to both intensity plots in Figure 4.2(B), the dashed line "1" includes much more noise than "2". When Otsu's well known-global thresholding method (Otsu, 1975) is applied, a threshold of the intensity value, 169, is determined, highlighted as a red dashed line in the overall image intensity histogram in Figure 4.2(C). The threshold segments pixels with intensity greater than 169 into the bounding surface from those below segment into matrix, thus segmenting the grey image in Figure 4.2(A) into black and white binary images respectively, as shown in Figure 4.2(C). The threshold of 169 is also labelled as red dashed line in the intensity plots of the two dashed line ROIs in Figure 4.2(B), to explain the result, which demonstrates that the global threshold segment works perfectly for the region of interest (ROI) "1", in which pixel intensities above 169 are segmented as the bounding surface. For ROI "2", using the same threshold of 169, noise distractions that have similar intensity to that of the bounding surface are segmented into the same white class in the binary image. Therefore, it can be seen that the segmentation of the bounding surface in Figure 4.2(C) is significantly distracted by local brighter patches (due to either bioturbation or feldspar). Moreover, even when the local intensity is taken into account, local distractions are hard to avoid, because the intensity

of the local distractions are very close to that of the bounding surface. Together with the issue of the unconnected gaps caused by scattered cementation, erosion and the thin nature of the bounding surface, all these conditions together lead to the low level of identification on the continuous pattern of bounding surfaces. Therefore, a local thresholding by the watershed method of segmentation, as shown in Figure 4.2(D), was still full of noise and failed to segment the connected bounding surfaces.

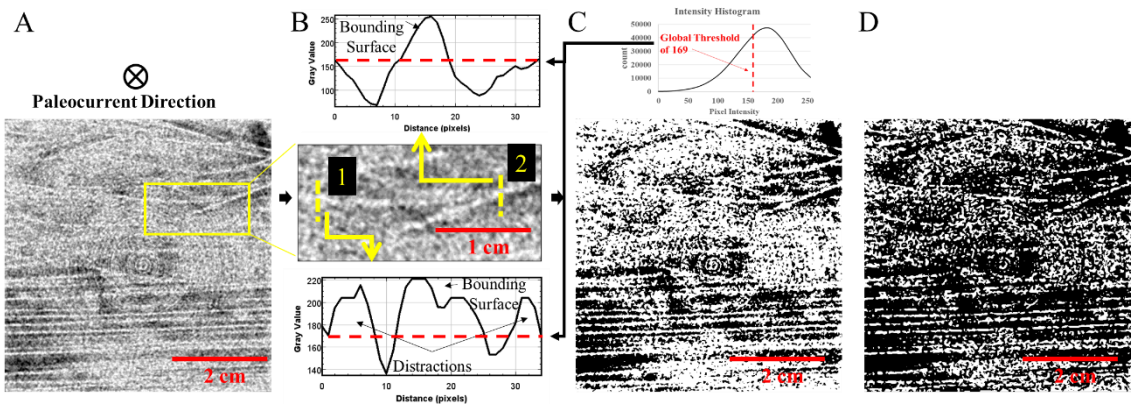

Figure 4.2 Illustration of the challenges in segmenting lamina bounding surface from XRT images; (A) a processed 2D slice (1/525) of a 3D MXRT rock image of cross-lamina core where brighter colour represents lamina bounding surface pixels and/or noises, excluding the marker line; (B) histograms of pixel intensity along dashed lines in the zoomed-in parts highlighted in yellow box of (A); (C) a segmented black and white image, white for lamina and noises, of the slice in (A) by the global thresholding method of Otsu (1975), at a threshold of 169/255. (D) a watershed-based segmented binary image of the slice in (A), white for lamina and noises.

For bounding surfaces that appear to be discontinuous in MXRT due to 'noises', as illustrated in Figure 4.2(A), most of them can still be easily picked out visually by a human observer. Human recognition makes use of not only intensity similarity, but also the spatial relationships of hidden patterns, based on experience. This suggests the need for a method that takes both intensity and local patterns into account and provides empirical examples of the patterns of interest. Given the challenge of natural discontinuity, a method needs to be developed with the following features: 1) identify local linear pattern; 2) bridge small "fake holes" of diameter less than a certain value; 3) avoid distraction by feldspar within a certain distance (because it does not have distinguishable intensity); 4) leave larger "true holes" of bioturbation with a size over a certain diameter. The combination of human recognition principle and the natural challenges of discontinuity, therefore, defines a method which is based on using given examples, and not only learning to recognize local linear patterns but also robustly bridging gaps, based on length, and excluding distractions, based on distance.

4.2 Extracting hidden features from MXRT – Connectivity-enhanced bounding surface segmentation

A technique for segmenting bounding surfaces from MXRT has been developed in this research to overcome the issues discussed above. This technique is developed to work on any 2D image and can robustly recognise local linear patterns "hidden" behind potential distractions, and override small "fake" gaps but retain large "true" gaps. The literature review in Chapter 2 suggested the promising method of a filter-based supervised segmentation, which captures the patterns and discontinuities of objects to be segmented in example images, referred to as training images, and to train and construct an classifier, using existing advanced machine-learning algorithms (see a review in Mohri et al. (2012)). In what follows, a brief summary of the development of this technique is presented, followed by key aspects of applying it to MXRT segmentation, which bridges the gap from noisy images, as described previously.

4.2.1 Summary of development of the technique

The suggestion discussed above led to a class of methods, as introduced previously in section 2.3.2.3 and named filter-bank based supervised segmentation, in this work. Given an image I(x), $x \in R^d$ and d = 2 or 3, the filter-bank based supervised segmentation for piece-wise linear structures can be considered as performing the following generic tasks:

1) The method starts by using an image filter at certain size, for example, a square window of 3×3 pixels, as illustrated in Figure 4.3(A), and with a mathematical operation to describe the local pattern (piece-wise linear structures in this study) around a pixel;
2) A set of suitable filters is found with different mathematical operations combined together to describe different aspects, referred to as features, of the local pattern. The set of filters is often referred to as a filter bank, and includes n filters. Each filter in the filter bank is applied to each pixel of the image to encapsulate image I(x) in a vector of filtered images $\boldsymbol{f}_n(x, I)$. Figure 4.3(B) illustrates an example of filtered images with n=2.
3) Each pixel after filtering can be considered as a data point distributed within the n-dimensional feature field, referred to as a feature vector, as illustrated in Figure 4.3(C) with n=2;

4) A suitable and representative training dataset $\boldsymbol{t}$ (a subset of I(x) or a separate image) is constructed, and for each pixel of $\boldsymbol{t}$ it is labelled as yes or no, as for example the green and blue coloured pixels shown in Figure 4.3(D), as binary ground truths $g(x, I_{\boldsymbol{t}})$;
5) A classifier is learned from the labelled training dataset, denoted by r () by a machine learning algorithm from the training dataset in the n-dimensional feature field, so that $g(x, I_{\boldsymbol{t}}) = r(\boldsymbol{f}_n(x, I_{\boldsymbol{t}}))$, as shown in Figure 4.3(E).
6) The learnt classifier r() is then applied to the rest of the un-labelled data, often referred to as the testing dataset $\boldsymbol{s}$ (black dots in Figure 4.3(E)), to predict whether or not a pixel belongs to a structure of interest (in this work a piece-wise linear structure) by $r(\boldsymbol{f}_{\boldsymbol{n}}(x, I_{\boldsymbol{s}}))$, shown as black dots in Figure 4.3(E) and labelled in green or blue in Figure 4.3(F);
7) The predicted results are assigned to each corresponding pixel location so as to presented a segmented image, as shown in Figure 4.3(G).

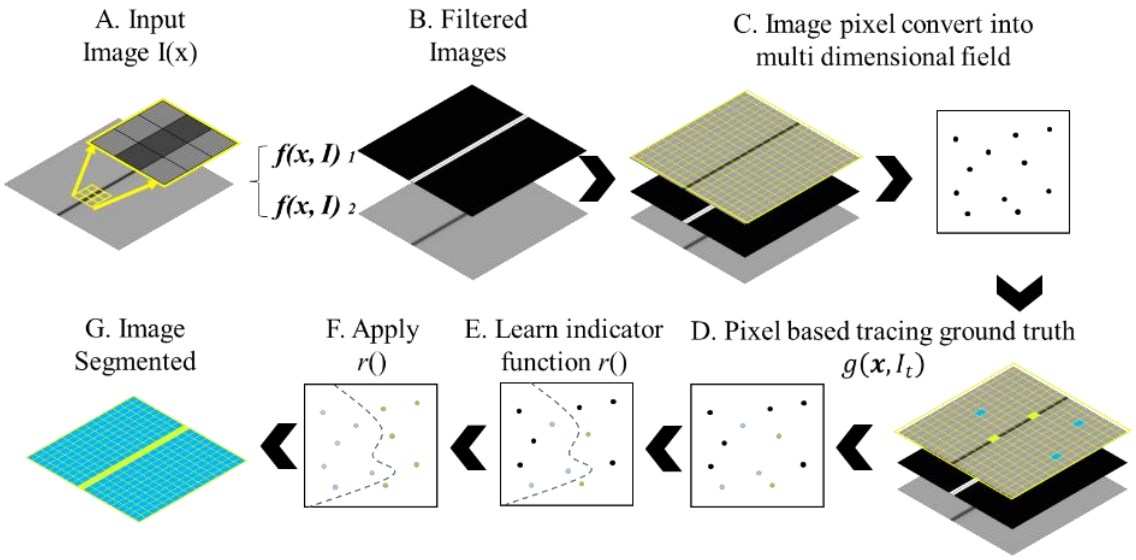

Figure 4.3 Illustration of typical process of filter-bank based supervised segmentation: (A) input image I(x) with darker single-pixel wide linear pattern in the middle; (B) illustration of (A) which has been filtered by two filters; (C) each pixel on the image can be seen as a data point (black dots) in a two-dimensional feature field; (D) a subset of image pixels have been labelled into two classes (green and blue colour dots) as ground truths and are treated as training data in the two dimensional feature field; (E) learning an classifier, denoted by r(), based on training data (feature vectors) in the multidimensional feature field by machine learning algorithm; (F) applying learnt classifier r() to the remaining unlabelled data points (black dots); (G) the segmented image.

The benefits of such an approach on segmenting a linear pattern from a noisy image are: 1) a set of filters could be applied to describe different aspects of linear patterns, so as to take into account complex local pattern information; 2) the vector of the filtered image

that describes the local pattern in a high-dimensional feature field could potentially more sufficiently describe the complex classifier; 3) by subjectively labelling the pixel ground truth, human expertise and knowledge could be incorporated; 4) a machine learning algorithm is typically good at learning complex non-linear classifiers, according to Mohri et al. (2012).

To override the unconnected gaps and distractions of the bounding surface in an MXRT image, as discussed above, the method should be developed with the following considerations: 1) How to configure the set of filters to maximise the characteristic differences, in a multidimensional feature field, between pixels which fall onto the linear bounding surface and "fake hole" gaps from pixels which fall onto "true hole" gaps and distractions? 2) How to configure training images/datasets and label them to reinforce expertise and knowledge to connect small gaps but retain large gaps? 3) How to select appropriate machine learning algorithms to learn the classifier effectively?

Factors have been proposed from both configuring the filter bank and the training image point of view to discuss their impact on connectivity enhanced segmentation of linear/planar structures in general. In the following subsections, key factors related to the specific challenges of bridging gaps and excluding noise on the segmented linear bounding surface are discussed as follows: section 4.2.2 summarises previous studies regarding the three aspects of configuration (filter bank, training image and machine learning algorithms) and key factors related to the specific challenge of a segmenting bounding surface, and their configuration to achieve best gap bridging and noise reduction are discussed in 4.2.3.

4.2.2 Previous studies on supervised classification

Filter banks for detecting features of piece-wise linear structures

A filter bank, according to Randen and Husoy (1999), can be regarded as a set of filters that characterizes one or more aspects of the local patterns and structures around a pixel in a multidimensional feature field, which collectively maximize characteristic differences of the structure of interest and the matrix, so that the classifier can be easily identified from the ground truth training dataset. The set of filters applied above is typically in the form of a mathematical operation matrix. The different mathematical operations designed within a filter determine the different features of the pattern to be characterised and can generally be classified as a direct or indirect mathematical approach

in this work. An example of directly mathematical approaches related to the interests of linear/planar pattern recognition is the Hessian filtering (Sato et al., 1997, Frangi et al., 1998, Voorn et al., 2013) and the use of eigenvalues or eigenvectors (Burgeth et al., 2009, Obara et al., 2012) that characterizes geometric aspects of thin planar structures in 3D, or linear structures in 2D, by the second-order partial derivatives matrix of the voxel/pixel intensity. It is one of the most popular approaches because it considers and makes use of linear geometric information (Lesage et al., 2009). The indirect mathematical operations describe the local pattern around a pixel by calculating convolutional similarity to the designed filters that contain different patterns. The convolutional similarity calculates the sum pixel product of the neighbouring patch around a central pixel to the designed filter of the same size and returns the sum to the central pixel, so a matched pattern would get the highest sum. One dedicated example is the LM filter bank designed by Leung and Malik (2001) that is composed of 48 filters, including a mix of filters containing edge bar patterns derived from a Gaussian derivative describing linear patterns and spot patterns derived by Laplacian of Gaussian and a Gaussian filter to describe cluster patterns with low or high intensity in the centre. The LM filters are also designed at multiple scales and orientations, to capture patterns at different orientation (for linear patterns) and sizes. By calculating convolutional similarity with each filter of the LM filter banks, local patterns of linear and spot features can be described.

The set of convolutional filters in a filter bank is designed, as explained above, or learned from example images with representative patterns of interest. It has been confirmed by Rigamonti et al. (2011a) that a learned filter bank is superior to a designed filter bank by having filters that more completely capture various features of patterns from example images. The learned filter bank approach was initialized by Olshausen and Field (1996), who proposed the Olshausen and Field's algorithm (OLS), to build a representation of images by iteratively optimising a set of filters containing various patterns with given filter size and set length to reconstruct the example image. The set of filters is initialized by randomly extracting a set of small image patches. The weighted sum of the set is compared with a randomly selected patch of the same size from the image by calculating the mean square difference of each pixel. The optimisation minimises the calculated mean square difference by iteratively optimising weighting factor. The approach has been extensively used for object recognition purposes and was proved to converge well on natural images, by Wright et al. (2010). However, it has also been pointed out that the

typical OLS filter bank learning approach is computationally expensive (Lee et al., 2009). Rigamonti et al. (2011b) modified the method of comparison from calculating the mean square difference to convolutional similarity and found improved efficiency in representing linear patterns.

Therefore, in this work, a learned convolutional filter bank is of interest and the applied approach is based on that of Rigamonti et al. (2011b). As discussed above, filter size and numbers of filters need to be configured before constructing a learning filter bank. The configuration is believed to impact on the classification result as follows: firstly, filter size is important because it controls the size of neighbouring features to be characterised. The filter size is therefore important in this study in determining the scope of the local gap length, and noises would be included in a local filter-based descriptor. It is also claimed by Hughes (1968) that the prediction power is closely related to the dimensions of the feature field (thus the number of filters in a filter bank). Therefore the number of filters applied needs to be discussed.

To simplify the classification procedure, this work assumes it is not necessary to learn a filter bank from the lamination MXRT image containing the bounding surface, but a learned filter bank from the general image containing a linear structure is enough. The assumption is based on Lee et al. (2009), who claimed the learned filter banks from different image datasets but containing a similar piece-wise linear structure would be similar. Therefore in this work, the configuration is based on existing filter banks learned from natural images that contain piece-wise linear structures (in the form of object edges).

Construction of training image datasets for supervised classification/segmentation

Practically, to classify a stack of image slices, the training image dataset typically contains one or more exemplary images that have similar patterns to the stack images to be classified, and on which a set of ground truths must be labelled, so as to learn classifier by the machine learning algorithm. Image artefacts like noise commonly affect the image signal-to-noise ratio, according to Huang and Aizawa (1993), thus making it challenging to trace ground truth from the image automatically. The trace is difficult, even with the best of practices among previously introduced pre-filtering approaches that combined Hessian filtering and mathematical morphology operations (Tankyevych et al., 2009, Dufour et al., 2013), as introduced in Chapter 2. For subjects requiring segmented piece-wise linear structures, manually tracing the binary (yes or no) ground truth of a linear structure with expert knowledge to overriding image artefacts on connectivity has proved

to overcome this challenge. For example, in medical image segmentation, the ground truth could be traced with expert knowledge of organs like blood vessels (Pujol et al., 2003), neurons (González et al., 2009) and tissue (Ughi et al., 2013)) and for satellite image segmentation, where roads could be traced by manual annotations (González et al., 2009). In this work, a similar approach is proposed to trace bounding surfaces, respecting the unconnected nature of bounding surfaces.

Many studies that address linear structure segmentation with supervised classification do not discuss the impact of training images, because the set of training images is usually selected and traced from the same dataset, which is assumed to be representative (Pujol et al., 2003, Rigamonti et al., 2011b, Becker et al., 2013, Ughi et al., 2013). This work chooses training images based on the same assumption, but three factors that potentially cause uncertainty to classification will be discussed comprehensively. When a subset of training images have a structure that is less representative, the three factors are the gap length, background intensity and orientation of the linear structure. These three factors matter for the segmented connectivity for following reasons: 1) It has been explained that this work aims to use supervised classification to bridge gaps selectively, based on expert knowledge on gap length. It is therefore important to discuss how efficiently gaps are bridged in the segmented image, with certain length gaps overridden in training images, and how much uncertainty would be caused when a given gap length from the training image did not cover the gap length expected to be bridged in the testing image; 2) The other factor is the background intensity, as summarised by Fraz et al. (2012), which is considered by most of the previous studies as the impact of artefacts during collecting images. Although this work does not expect a large impact from background intensity, because the training image would be taken from the same stack of images whose imaging condition is similar, nevertheless, the potential uncertainties introduced by varying backgrounds are discussed; 3) Lastly, the orientation of the linear structure given in the training image to specify the scope of the angle of the linear pattern should be recognized in the testing image. Therefore, the impact of orientation needs to be discussed. The importance of orientation is confirmed indirectly by Truc et al. (2009), who proved it was possible to avoid the impact of the orientation of linear structures by applying a set of directional filters to make the patterns' orientation invariant, prior to classification. In this work, orientation is based on linear structure traced from a training image. Similarly

to gap length, the uncertainty of the traced orientation in the training image, if not covered the expected orientation in the testing image, needs to be discussed.

Given that the thin, piece-wise bounding surface is challenging to segment, but requires to be accurately identified in this work, a distance transformation can be applied on the traced ground truth in the training image, to train the classifier to recognize the centreline of linear structure. This could be achieved based on the work of Sironi et al. (2014), who were the first to shrink given linear ground truth into single pixel-wide skeleton to represent the centreline, and secondly, applying a distance transform function so that the pixel had the highest values on the centreline, and those away from it decreasing monotonically, like a ridge. Note this approach was only applied on a fully traced training image, rather than a subset, as illustrated in Figure 4.3. Thus with the ground truth image $g(x, I_{\boldsymbol{t}})$, a distance map $d\big(x, g(x, I_{\boldsymbol{t}})\big)$ is obtained and normalized to $[0,1]$ for the training image **t**. For each pixel in the training image **t** it now has its feature vector $\boldsymbol{f}(x, I_t)$ and distance map $d\big(x, g(x, I_t)\big)$. A classifier *r*() of continuous value between 0 to 1 can then be trained so that $d\big(x, g(x, I_t)\big) = r(\boldsymbol{f}(x, I_t))$. For the testing image $I_s(x)$, the corresponding feature vector $\boldsymbol{f}(x, I_s)$ can be calculated. By applying the learned *r*(), the distance map $d\big(x, g(x, I_s)\big) = r(\boldsymbol{f}(x, I_s))$ for image $\boldsymbol{s}$ can be estimated (see the work of Sironi et al. (2014) for full details). To get the final binary centreline of the linear structure, Sironi et al. (2015) proposed applying a non-maximum suppression, where only pixels closest to the centreline of the estimated distance map are kept.

Machine learning algorithm

Supervised classification trains the classifier from the labelled training data and makes predictions on the remaining unlabelled testing data. The benefit of such an approach is to deal with the situation where data are classified under an unseen (nonlinear) manner (Buhmann et al., 1999, Mohri et al., 2012),. The set of filters in a filter bank not only improves the discrimination between classes but also increases the dimensionality of the feature field, thus increasing the difficulty of classification. This could be solved by either optimising the filter bank to increase the separation of data points of different classes in the multidimensional feature field or involving a machine learning algorithm which has proven strength in searching for a non-linear distributed "boundary" in the multidimensional feature field between classes (Randen and Husoy, 1999).

There are some successful machine learning algorithms for segmenting piece-wise linear structures by supervised classification, including those by Random forest (Ughi et al., 2013), AdaBoost (Pujol et al., 2003, Caballero et al., 2007, Rigamonti and Lepetit, 2012, Becker et al., 2013), SVM (González et al., 2009) or Bayesian (Xu et al., 2006). This research, however, is not interested in optimising the selection of machine learning algorithms but would prefer to focus on configuring previously proposed factors to reflect the nature of the challenge of segmenting a piece-wise bounding surface. Thus in this research only the most commonly used algorithm (AdaBoost) for segmenting linear structures (Pujol et al., 2003, Caballero et al., 2007, Rigamonti and Lepetit, 2012, Becker et al., 2013)) has been selected, for simplicity.

Summary of process

The application of the discussed supervised classification process for bridging gaps in segmenting a piece-wise linear structure is illustrated in Figure 4.4, in a top-down sequence. A synthetic grey-scale dashed line image with increasing gap length has been created to represent an unconnected thin linear structure with various discontinuities. A filter bank containing 8 convolutional filters of the same size but with different patterns has been applied for the purpose of illustration, to create a vector of filtered images in an 8-dimension feature field. The 8 convolutional filters yield different filtered intensities (by convolutional similarity) for a pixel, and therefore describe different types of neighbouring patterns. The ground truth has been traced with gaps overridden, and a skeletonized centreline has been obtained by shrinking ground truth, and distance transform is applied, as shown in the second row of Figure 4.4. Each pixel in the 8-dimensional feature field then corresponds to a distance value between 0-1, as given from the distance map for an AdaBoost algorithm, to learn the continuous classifier. A testing image has been created by rotating the training image by 180^{o} to illustrate the performance when training and testing images have different but similar structures. With same filter bank applied, 8 filtered images can be obtained. By applying the learned continuous classifier, the distance value of each pixel to the anticipated centreline in the testing image can be predicted. By applying non-maximum suppression, the centreline of the predicted result can be obtained. As shown in the last image of Figure 4.4, the single-pixel wide segmented centreline of the unconnected dashed line in the testing image is well connected. In this work, the segmentation bounding surface problem is

considered to be performed in a stack of 2D slices, following this procedure, which together would yield a segmented bounding surface in 3D.

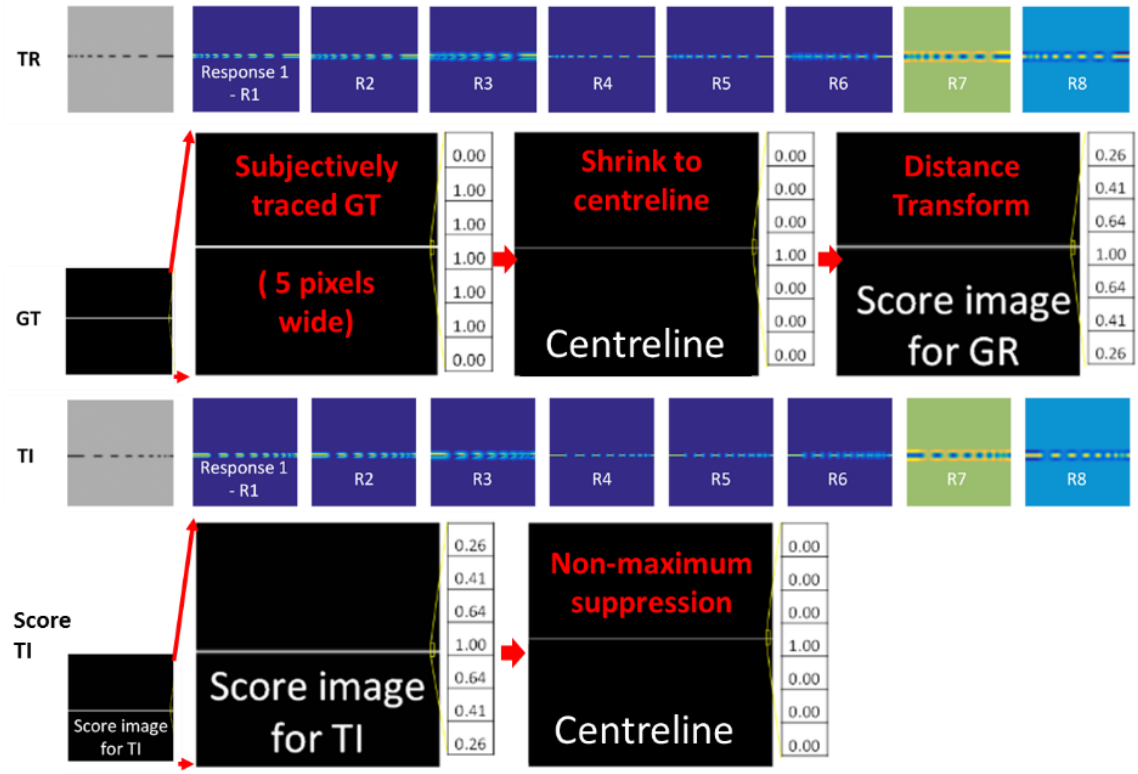

Figure 4.4 Illustration of supervised classification applied to segment a synthetic unconnected dashed line (13 pixels wide in, darker colour) presented on grey background: all images are the same size of 500x500 pixels^2: 1st row, a training image (TR) of 500x500 pixels^2 containing a13-pixel wide dashed line, with increasing gap from left to right (gap length ranging from 5-45 pixels) and filtered by 8 convolutional filters (43x43 pixel square) (Maximum Response 8 (MR8) filter bank based on Varma and Zisserman (2005)) to create an 8 feature map of TR; 2nd row: a ground truth (GT) 5-pixel wide straight line manually traced on TR with unconnected gaps bridged, followed by shrinking to centreline and calculating distance transform: the intensity values of a 7-pixel segment across centreline of each plot have been given on the side, from which can be seen 5-pixel wide ground truth with pixel value of "1", 1 pixel wide centreline with pixel value of "1" and a distance map whose intensity value decreases monotonically away from centreline, with pixel value decreasing from "1" to "0"; 3rd row, a synthetic testing image (TI) is created by rotating TR 180^o , along with the 8-feature map of TR by an 8-filter filter bank; 4th row: predicted distance map of TI and centreline after apply non-maximum suppression.

4.2.3 Configuration and discussion of supervised classification by five factors

Following the discussion in 4.2.2, five factors from both the filter bank and training image point of view (summarised in Table 4.1) have been proposed that are closely related to the nature of the challenges of a segmenting bounding surface. Each of the five proposed factors implies different aspects of the challenges, as discussed. Therefore, the understanding of the impact of these factors is essential in optimising configuring and evaluating the uncertainties for supervised classification of a bounding surface. The nature of the impacts of each of the five factors on enhanced-connectivity segmentation

of generic linear structures have been discussed in a separate work (draft paper). The discussion in the draft paper is based on same procedure as given in Figure 4.4, but with a set of different configurations to test each factor. In the following list, the key conclusions from the draft paper regarding the five factors are summarised and linked to the challenge of segmenting the bounding surface, from both the optimum configuration and uncertainty evaluation point of view. Based on the discussion, suggestions are given on configuring each of the five factors on the segmentation of the bounding surface from MXRT.

1) The filter window size determining the area of the neighbouring feature has been characterised. Taking the grey-scale dashed line image in Figure 4.4 for example, compare a pixel that falls into an unconnected gap and a pixel falls in the grey matrix, both in the grey colour, a small filter window that only includes pure grey tiles cannot differentiate both pixels. However, a relatively larger filter window for a pixel which falls into the grey gap would not only include the grey tile in the gap but also part of the darker linear pattern, and thus would be characterised differently from the pixel from the grey matrix. Taking the filtered image R6 of the dashed line in the first row of Figure 4.4 as an example, the filtered pixels falling into a small gap on the left has similar feature to pixels falling on the darker dashed line segment, whilst the pixels which fall into the large gap on the right has similar feature to pixels that fall into the matrix. This is because the filter size is just below the length of the largest gap on the right (a 43-pixel wide filter window compared to a 45-pixel wide gap) but is larger than most of the smaller gaps on the left. In Figure 4.4, however, the largest gap has still been bridged in the segmented image; this is because the filter width is just 2 pixels smaller than the largest gap length, thus creating a minor different feature between the pixels in the large gap and the matrix. However, in the separate work (draft paper) it has been shown that the larger the gap size compared to the filter window size, the worse the connectivity.

Therefore, the configuration of filter window size is suggested to cover the gap length anticipated for the bounding surface to be segmented. According to the measurements of the gap length caused by various holes, given in Table 3.2 of section 3.2.2.2, the filter size is expected to be larger than 2mm (20 pixels in MXRT) to bridge “fake holes” and smaller than 5mm (50 pixels in MXRT) to keep the “true holes”. Bridging the gap requires a large filter size to cover gap length, whilst excluding noise requires small filter size to reduce distraction, based on the same characterised neighbouring area principle.

Therefore, filter size is expected to be smaller than the average distance in which distraction would potentially occur, which can be estimated by the average distance between feldspar particles of 2.4 mm (24 pixels in MXRT) measured in Chapter 3. As a result, a filter size between 20-24 pixels in each dimension would theoretically bridge the small gaps of "fake holes", exclude the distractions of feldspar and keep the large gaps of "true holes".

Practically, the "fake holes'" gap length could be larger than the measured length, because the measurements are performed on a limited sub-dataset and uncertainty could be caused by subjective measurements. To implement the potential larger gap length features of the "fake holes", a second filter, with a larger size than the first small one (20-24 pixels), could be applied simultaneously. Although the second, larger, size may introduce distraction (because it exceeded average distraction distance), the simultaneous application of both filter sizes it kept the noise reduced linear pattern features captured by the small filter size. The second, larger, filter size should still be smaller than 50 pixels to keep "true holes".

As previously stated, in this work the configuration of the learnt filter bank is based on filter banks learnt from the general Berkeley BSDS500 benchmarked dataset, consisting of 200 natural images at a size of 481x321 (Arbelaez et al., 2011) which is similar to the MXRT image size of 562x550 in this work. Two learnt convolutional filter banks were selected, meeting the discussed filter size requirements, as in Figure 4.5, namely, Learnt89 and Learnt121, with 89 filters 21x21 pixels square in size and 121 43x43-pixel square filters respectively. Both filters include a set of linear as well as cluster patterns and are claimed by Rigamonti et al. (2011b) to well-represent linear edge structures in the training image. In the separate work, both filter banks proved successful in describing unconnected linear structures, and therefore are applied in this work on bounding surface segmentation.

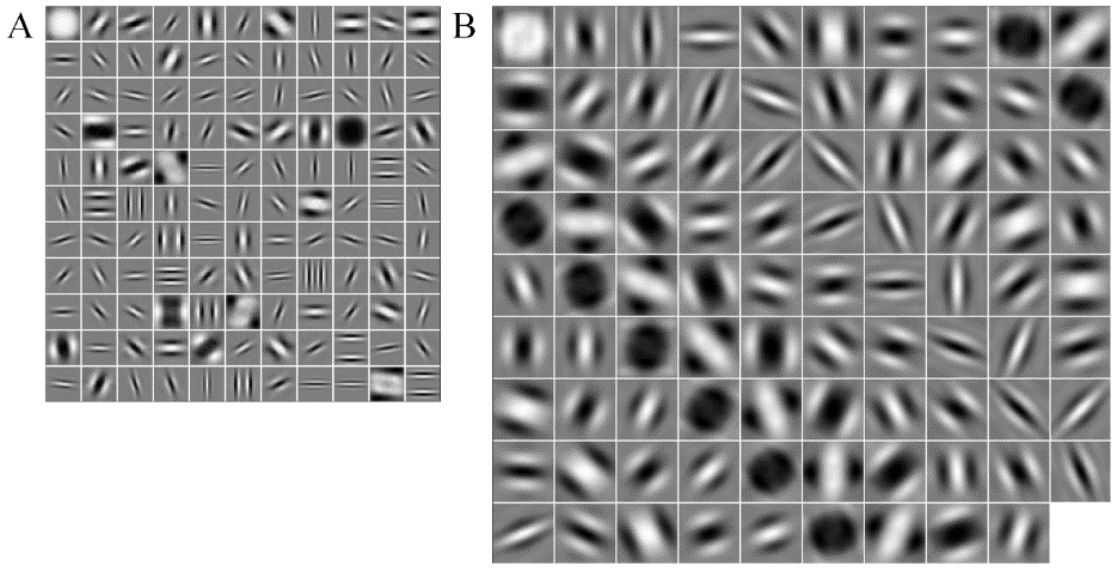

Figure 4.5 Filter banks: (A) Learnt filter bank Learnt121 with 121 filters each size of 21x21 pixels square Rigamonti et al. (2011b); (B) Learnt filter bank Learnt89 with 89 filters each with a size of 43x43 pixels square: Rigamonti et al. (2011b).

2) The numbers of filters indicate the diversity of features described; therefore, a greater number of filters implies a more subtle difference matrix could be detected between a linear pattern and the matrix. In the separate draft paper, filter banks yielding 8, 38 and 210 features are compared, and it was proved that for unconnected linear/planar structure segmentation the largest tested number of features improved segmented connectivity best. In this work, to ensure the bounding surface could be characterised under heavy noise, two sets of filter banks containing 89 and 121 filters are applied together to yield a 210-dimensional feature field for characterisation. The discussed configuration of filter banks is summarised in Table 4.1.

3) The general idea of configuring training image factors could be expressed as making sure given training information is as consistent as possible with a testing image. Therefore, in this work, one slice out of the 525-slice image stack was selected as a training image. However, the uncertainty exists that the selected slice has been less representative in covering anticipated patterns. In the separate work, the impact of lack representation on the segment connected piece-wise linear structure is discussed. Test cases were designed with the same procedure (with the same two learnt filter bank configurations, as discussed above) shown in Figure 4.4, but including different gap length, orientation and background intensity configuration on training and testing images. In the following paragraphs, the conclusions from the separate work are summarised, and the impact of proposed training image factors on segmenting bounding surfaces are discussed.

Gap length is the range of the disconnected gap length to be overridden in the traced ground truth of the linear structure in the given training example image. Gap length thus implies the range of gaps that should be picked up by the machine, following the "instruction" given by the training image and traced ground truth. Uncertainty would occur when a given gap length in the training image did not cover all the potential gap lengths in the testing. This could be tested on synthetic images, as shown in Figure 4.6, where only half of the gap lengths (in the range of 5-30 pixels) are provided and are overridden in the training image, to train the classifier, but applied on testing with the full range gap lengths (in the range of 5-45 pixels). The result showed that when the gap length is larger than what been provided in the training image, the predicted connectivity decreased (see Figure 4.6 for illustration, but the fully quantified discussion is available in the separate draft paper). However, one may also note that the relatively small gaps among the gaps in the right half of the testing without given training, for example, gap length 35, is also bridged in the predicted image. This implies that even though one training image from the full stack may provide a limited gap length example, the method would still pick up connectivity for gap lengths a bit larger than the given training, thus covering the uncertainty of lack of a representative training image. The full quantified discussion is available in the separate draft paper, where it is concluded that a gap 16% longer than given gap length would be bridged by 90% of its length, while a 50% longer gap will be bridged by 39.4% in length. Another uncertainty of concern is that a "true hole" been over-bridged by the above-discussed mechanism. In this work, the training image will be overridden based on measured knowledge of holes. Therefore "fake hole" gaps smaller than 2mm will be bridged. Given that "true holes" are measured as larger than 5mm, thus 250% longer than the bridged example gap in the training image, in this work it is considered that over-bridging of "true holes" can be ignored.

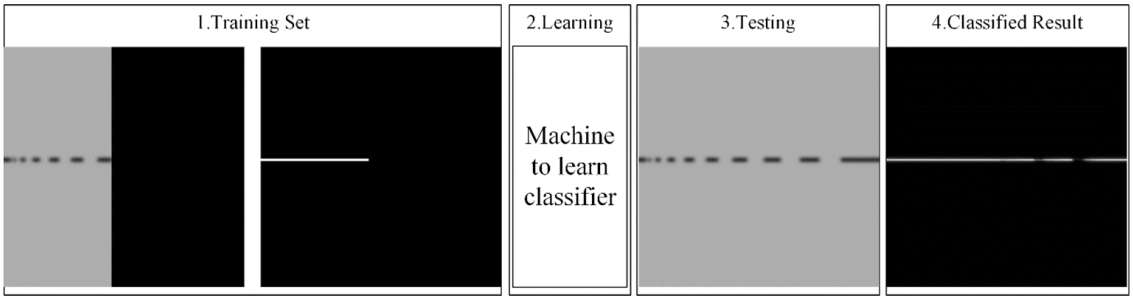

Figure 4.6 Gap length test: (1) training image with gap lengths of 5,10,15,20,25,30 pixels from left to right, along with gap bridged ground truth of 5 pixels wide; (2) training images are filtered by both learnt 89 and learnt 121 filter banks and together with ground truth image to pop into the machine to learn the classifier to follow same procedure as (Figure 4.4); (3) testing image with gap lengths 5,10,15,20,25,30,35,40,45 pixels; (4) predicted distance map of (3) (centreline is not presented, as it is too thin to illustrate);

4) Orientation describes the direction range of examples of connected/unconnected linear bounding surface patterns provided in the training image. The orientation enhances the distinguishability between pixels falling into the gap along the linear pattern direction and the noise pixels around the linear pattern. Orientation thus excludes the noise pixels with similar intensity and gap length to the thin bounding surface pixels but not following the direction of bounding surface. In this work again local orientations are believed to be represented by one 2D training slice, but the uncertainty regarding lack representation may exist. In the separate work, this has been examined by designing a synthetic testing dashed line with increasing orientation difference from the one given in training, as shown in Figure 4.7. The results showed that even for the largest tested orientation difference (16° deviation from given training image) the predicted distance map still enhanced the connectivity of 13.8% of the gaps in length (the fully quantified discussion is available in separate draft paper). In this study, inter-LBS has been believed to have similar geometry on the slices perpendicular to the paleocurrent direction, thus implying less orientation variation. Therefore, one training slice from a perpendicular cross-section is considered as representative.

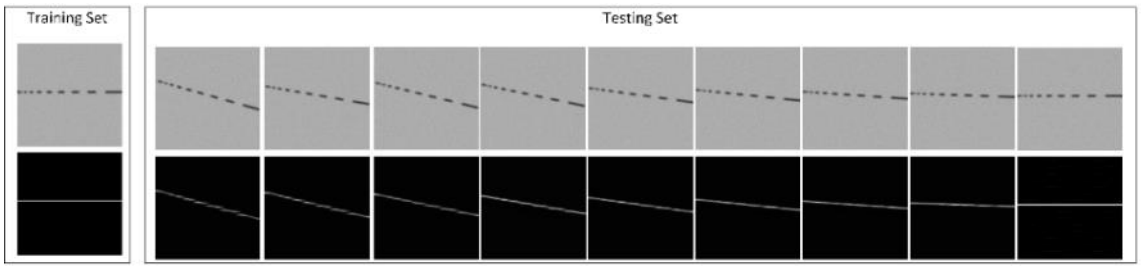

Figure 4.7 One horizontal dashed line and corresponding gap overriding ground truth as a training set to train the classifier and applied to a set rotated dashed line (2° incremental 8 times between 0°-16°) with corresponding predicted distance maps shown below (centreline is not presented as it is too thin to illustrate).

5) The background intensity of the training image determines the local background variations that could be picked up. Therefore, background intensity implies variations of background caused by local hardening and complex mineral distributions should be introduced in the example training image. One slice is also considered to include representative local intensity background variations, but the uncertainties regarding lack representation are discussed here. The impact of varying background intensity has been examined in the draft paper by designing testing cases, as shown Figure 4.8, in which classifiers trained from one image are applied to images containing the same dashed line but various background intensities. The results indicated that the largest background intensity difference (125%: 180 over 80) still bridged about 50% of the length of gaps (fully quantified discussions are available in the separate draft paper). Therefore, background, in this work, is believed not to have much impact, because slices from one MXRT stack are not expected to have large background variation. It should also be noted that it is not necessary to pre-process the MXRT image to remove hardening from the background, as mentioned in Chapter 2, because supervised classification recognizes patterns as long as the training and testing images are consistent. The discussed configuration of the training image is summarised in Table 4.1.

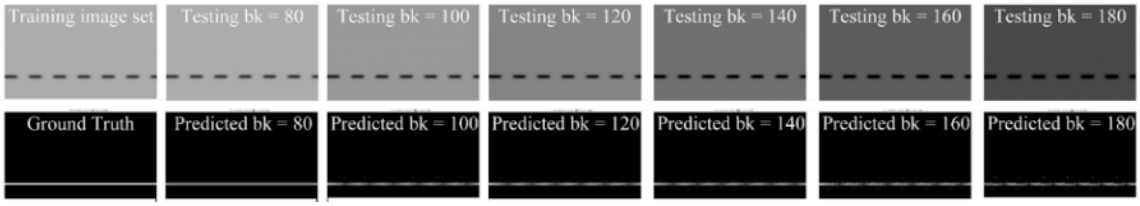

Figure 4.8 Testing of impact by varying background: training image with dashed line of same gap length over background intensity of 80, together with gap fully bridged ground truth to train the classifier and applied on the testing image, varying the background by adding a pixel value of 20 each time.

Table 4-1 Discussed factors impacting supervised classification on segmenting bounding surface

	Filter Bank			Training Image		
Factors	Filter window size	Number of Filters	Factors	Gap Length	Orientation	Background Intensity
Optimising configuration	Size Range Covered	Diversity of features covered	Tolerance/ uncertainty of largest measured deviation	50% longer gap bridged 39.4%	16° deviated orientation bridged 13.8%	125% background intensity difference bridged 50% gap
Configuration applied in this work	21x21 and 43x43 pixels^2	89 and 121	Configuration	Gap bridged < 2mm	Traced on one slice of stack	Traced on one slice of stack

4.2.4 Bounding surface extraction

The key procedure for applying supervised classification to segment bounding surfaces from MXRT with the discussed configuration is outlined as follows (illustrated in Figure 4.9):

1) Taking the claim made in the previous chapter that the sample has relatively similar inter-laminaset bonding surface geometry perpendicular to the paleoflow direction, one randomly selected slice (508/525) is taken as the training image (Figure 4.9(A)). Unconnected bounding surfaces on the training image are traced with additional connectivity knowledge to bridge the missing connectivity by overriding gaps and distractions (Figure 4.9(C)). The gaps are connected based on a measured range (< 2mm) to bridge "fake holes" and leave "true holes" over 5mm.
2) Both learnt89 and learnt121 filter banks are convolved to each pixel of the training image and yield a vector of filtered images (Figure 4.9(B)). The vector of filtered images together with the traced ground-truths (Figure 4.9(C)), with a distance transform, is put into an AdaBoost algorithm to learn a classifier to take into account the gap bridging.
3) The classifier is then applied to the remaining slices of the MXRT stack (with same filter bank applied) to predict the distance map. Figure 4.9(D) illustrates an example of the first of the 525 images in the stack, which returned the distance map shown in Figure 4.9(E).

4) Non-maximum suppression is performed on the distance map to keep only pixel values closest to the centreline on the distance map, and typical Otsu's segmentation can then be applied to segment the centreline of the bounding surface (Figure 4.9(E)).

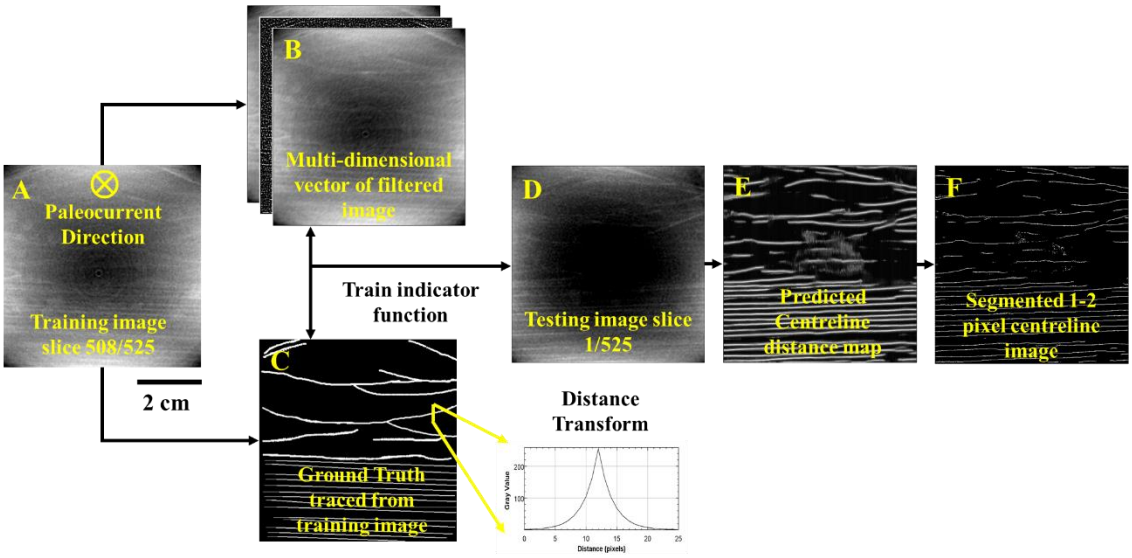

Figure 4.9 Process of enhancing connection with supervised classification over the unconnected bounding surface image (images did not apply background removal but colour balance is applied for better illustration): (A) slice 508/525 of the MXRT stack at perpendicular to paleoflow direction, with size 562x550 at 100um^2/pixel as training image, in which the bounding surface is presented as a brighter linear structure. Note the image has intensity normalized to 0-255; (B) The vector of the filtered image; (C) Connectivity-enforced ground truth image of A (white is bounding surface) together with distance transform example by intensity plots of one 25-pixel long segment across one traced bounding surface, shown as a "ridge"; (D) one example testing image slice 1/525; (E) predicted centreline distance map of bounding surface of D; (F) segmented centreline of bounding surface of E.

The segmentation is performed slice by slice over 525 slices of the MXRT image stack of L1, each of size 562x550 at 100um^2/pixel. As a result, the 3-dimensional bounding surface is segmented from the greyscale MXRT image stack, as illustrated in Figure 4.10(A-B). The procedure applied to each 2D cross section from one direction (e.g. xy cross section of Figure 4.10(A)) appears as lack of connectivity in another perpendicular direction (e.g. xz cross section of Figure 4.10(A)). Assuming that the 3D planar bounding surfaces are anticipated to present a linear structure in both perpendicular to and parallel to paleoflow 2D cross sections, the procedure is performed twice on each xy slice and xz slice to enhance the connectivity of the bounding surface in 3D. Lastly, post processing, which removes small spots (black in Figure 4.10(B-D)) less than 100 voxels in 3D, is performed to avoid small noises and artefacts. The results are verified by two methods. Firstly, a visual comparison to the same cross-sections with simple segmentation as applied in Chapter 3 is performed. Secondly, the results are compared with the watershed approach introduced in 4.1, by labelling each spatially separate but internally connected

surface in both results to examine connectivity enhancement and noise reduction. The results confirmed that the developed supervised classification approach segmented the thin 1-2-pixel wide centreline of the bounding surface with gaps bridged in the anticipated magnitude and reduced noise significantly.

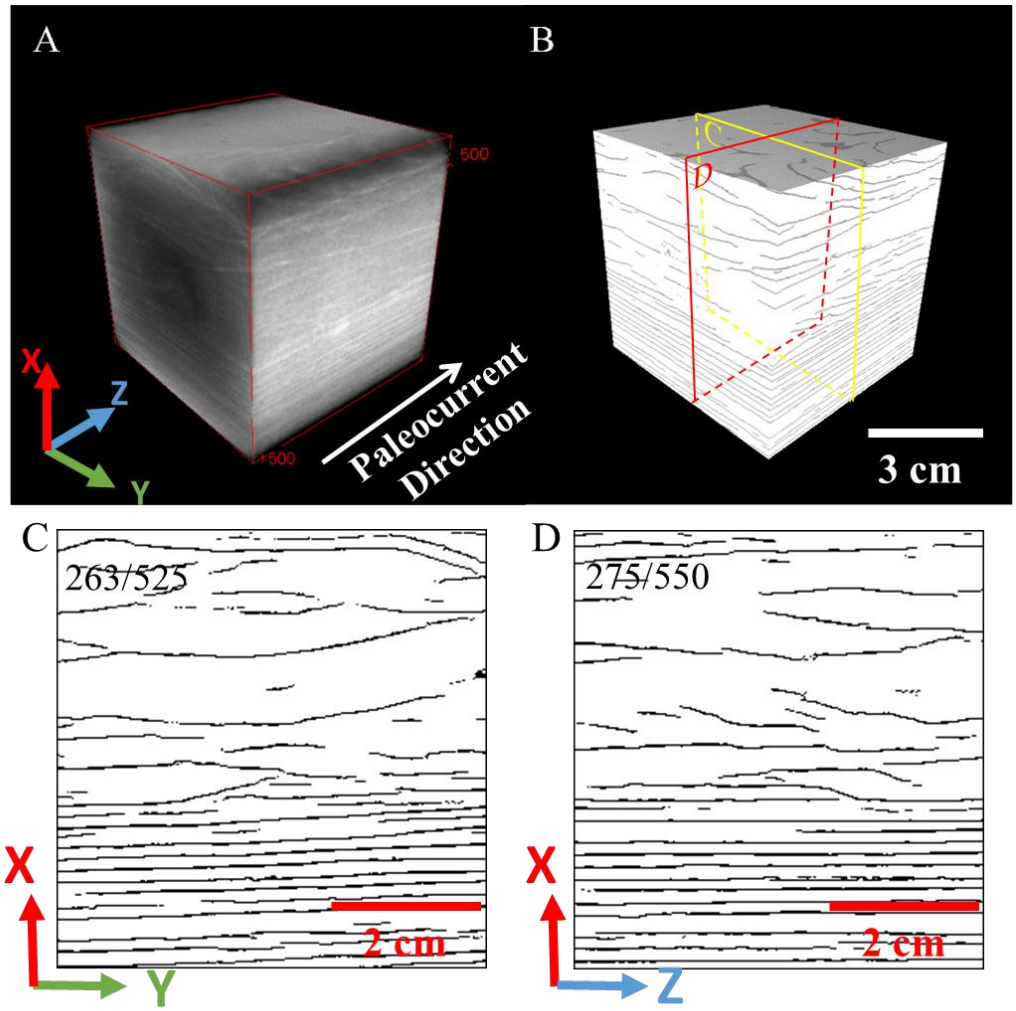

Figure 4.10 (A) 3D view of MXRT of L1 with size 562x550x525 at 100um^3/voxel (image intensity range normalized to 0-255 with bounding surface in brighter colour); (B) 3D view of supervised classification segmented bounding surface (in black colour); (C) xy slice 263/525 of segmented bounding surface (black); (D) xz slice 275/550 of segmented bounding surface (black).

Figure 4.10(C-D) gives the same two perpendicular cross-sections of the segmented bounding surface compared with the simple semi-automated segmentation in Figure 3.11 of section 3.2.1. The main advantages of supervised classification include: 1) Supervised classification identified the 100-200um thick finest bounding surface layer rather than the 1-2 mm transitional zone identified by the simple segmentation method; 2) The connectivity in the xz direction is clearly better than that obtained in the simple segmentation method based on visual observation; 3) much less labour and subjectivity

is introduced by supervised classification (trace one slice) than simple segmentation (trace 10 slices, evenly distributed over the 525 stack).

The result of the supervised classification segmentation of the bounding surface is also compared with watershed segmentation. Comparing Figure 4.2(D) with Figure 4.9(F) (both performed on the same slice), it can be seen that the supervised classification not only effectively avoided noises but also kept the connectivity based on manual identification. To better quantify the efficiency of noise removal and keep the connectivity, the 3D results of supervised classification in Figure 4.10 are compared with watershed segmentation (with the same setting as Figure 4.2(D) but performed on all 3D slices rather than on a single slice). Removal of small spots less than 100 voxels in 3D is also performed on the segmented watershed image, to be consistent with the supervised classification approach. Independent connected bodies are labelled in 3D by looking at connectivity in 26-neighbour voxels for both segmented results. Figure 4.11(A) shows that the supervised classification segmented bounding surface are labelled into 73 independent connected bodies in different colours. Figure 4.11(B) shows the watershed segmentation result labelled into 31 connected bodies and Figure 4.11(C) shows the 2^{nd}-30^{th} of the 31 independent connected bodies of watershed segmentation, by excluding the 1^{st} connected body. The main observations from comparing two approaches are: 1) the supervised classification segmented bounding surfaces have a geometry consistent with previous observations and well connected in the 3D domain. 73 connected bodies are reasonably consistent with the previous estimation in the preliminary study of Chapter 3. Small noises appear to have been removed in comparison to the watershed result, by visual observation. Bounding surfaces from the curved laminaset are intersecting with each other, therefore a limited number of independent connected bodies are identified; 2) the watershed segmentation also did not show a very large number of connected bodies because isolated small artefacts have been efficiently removed by removing the small spots. However, the first connected body appears to have all the bounding surfaces connected by the remaining artefacts and noises into one large connected body. Figure 4.11(B) suggests that there is still a significant amount of noise remaining. After removing the first connected body, only a few small connected bodies without the typical geometry of bounding surfaces are observed; 3) the connectivity of bounding surfaces by watershed segmentation is unidentifiable, because they could not be separated. However,

based on visual inspection the connectivity is still poor, considering the significant number of gaps observed at bounding surfaces.

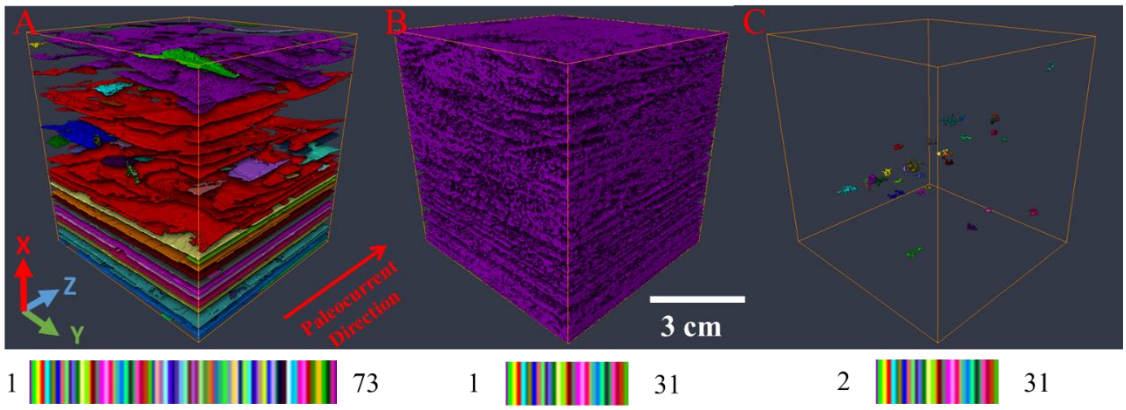

Figure 4.11 Labelling of independent connected bodies from: (A) supervised classification segmented bounding surface: 1-73 connected bounding surfaces are labelled based on the colour map given below; (B) watershed segmented (with small spots <100 voxels in 3D removed): 1-31 connected bodies are labelled, based on the colour map given below; (C) 2-31 connected bodies of B are labelled, based on the colour map given below.

To further illustrate the connectivity of supervised classification segmented bounding surface, the labelled surfaces in Figure 4.11(A) are visually analysed, one by one, and selected connected surfaces are illustrated in Figure 4.12. Horizontal planar bounding surfaces are mostly well connected, with no small unconnected holes, proving that small "fake holes" are fully bridged, Figure 4.12(A-B) illustrates two such examples. Only one horizontal bounding surface showed a large "true hole", as shown in Figure 4.12(C), which is considered to be a result of erosion or bioturbation, because the scale is over several centimetres long and about 1 cm wide. Curved LBSs appear as large connected bodies, as a result of the intersection. The two largest connected curved bounding surface bodies (labelled "1" and "5" in the 73 independent connected bodies) are shown in Figure 4.12(D and G), with top-down and bottom up views in Figure 4.12(E-F) and Figure 4.12(H-I) respectively. Both "1" and "5" appear well connected with no small "fake holes" and several large "true holes" with diameter from 1cm to 3cm. One zoomed-in view of Figure 4.12(G) is given in Figure 4.12(J), where several large "true holes" appear at similar locations that were potentially caused by bioturbation penetrating across several neighbouring bounding surfaces. Figure 4.12(K) traces the edge of holes and potential tracks across neighbouring bounding surface surfaces, which provides strong evidence of bioturbation activity that created holes of about 1.5-2 cm diameter and penetrated a set of neighbouring bounding surfaces. The traced bioturbation also has a location consistent with previously gained evidence from the EDS map of T2 and Tp. Figure 4.13 positions

the EDS of Tp and T2 at their roughly spatial collection locations relative to L1, with bioturbation traced on the labelled bounding surface in Figure 4.12(G). The calcite concentrated parts, as an indicator of bioturbation in the EDS image, are highlighted in Tp in the yellow square box and for T2 calcite is segmented out directly, with the concentrated part highlighted in the yellow square box. The relative locations of highlighted potential bioturbation in both EDSs of Tp and T2, together with the trend traced from the labelled surface, yield a consistent 3D spatial path of bioturbation.

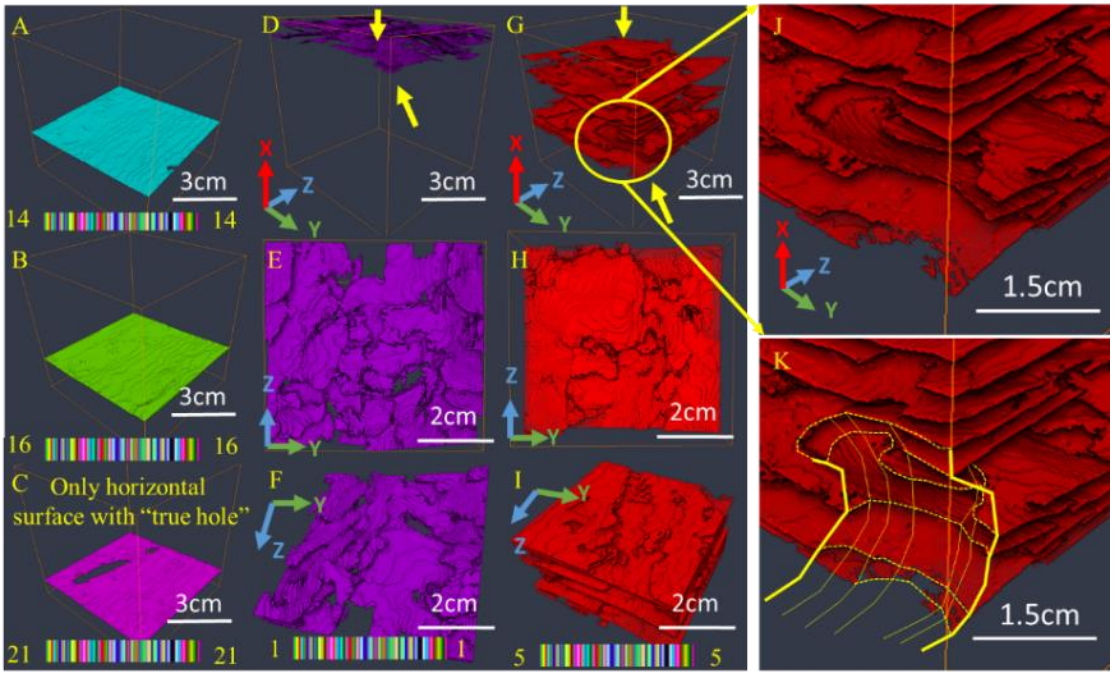

Figure 4.12 Illustration of segmentation for connectivity analysis and observation of bioturbation: (A-C): Three selected horizontal planar surfaces, numbered as 14, 16 and 21 respectively: A-B are well connected, and C presents one large "true hole"; (D): Top connected surface of curved laminaset numbered as 1; (E) top-down view of D and (F) bottom-up view of D: both top and bottom view present a few large holes, as a result of bioturbation, while the rest of the surface is well connected with no small holes appearing as artefacts; (G-I) shows a similar observation to D-F, but for another large intersecting connected curved LBS, numbered as 5, large holes appear at several locations but the rest of the surface is connected well, with no small holes appearing as artefacts; (J) shows a zoomed-in view of one potential bioturbation penetrating several curved bounding surfaces and (K) yellow dashed line traces the edge of a hole penetrating each bounding surface and the solid line tracing the track of the highlighted edge across the set of surfaces been penetrated, which clearly indicates bioturbation.

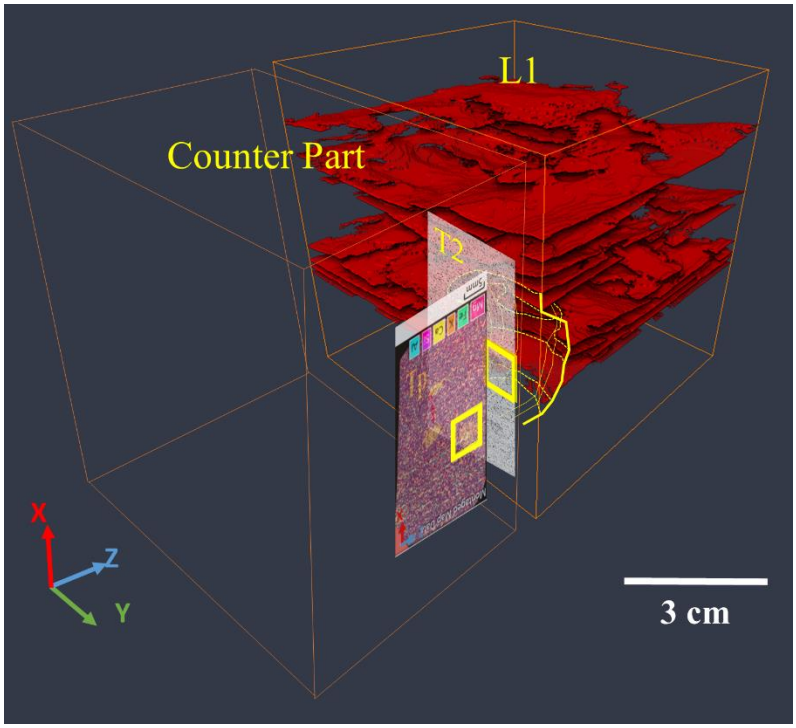

Figure 4.13 Illustration tracing bioturbation on segmented and labelled connected bounding surface body, together with EDS of Tp and calcite segmentation of EDS of T2, both roughly positioned at their spatial location of collection.

In this section, a filter-bank based supervised classification method has been developed to address the poor connectivity of the segmented bounding surface. Five factors have been proposed to impact the segmented connectivity respecting the challenges of identifying a bounding surface and bridging small "fake holes" but leaving large "true holes" as they are and excluding distractions. Among the five factors, filter size and traced gap length in the training image appear to have the most significant impact on bridging the gap, and the configuration of filter size and traced gap length in training image should be designed according to measured gap length and the distribution of distractions. The single training slice procedure applied in this work reduces labour and subjectivity, but may lead to uncertainties. The uncertainties are discussed from the point of view of three training image factors (gap length, orientation and background intensity), and the main conclusions are: 1) when the training image is less representative, an unconnected linear structure which has not been given in the training image could still be bridged to various degrees, according to different factors; 2) the bridging of an un-given unconnected linear structure would not lead to over-bridging "true hole" gaps. The predicted distance map may have the same maximum value at two discreet pixels closest to the centreline of the bounding surface. Therefore, the segmented bounding surface has a width of 1-2 pixels representing a thickness of 100-200 um. This thickness satisfies the

measurement from Chapter 3 to safely include the ~1-2 grains thick (average size between 100-200 μm) finest bounding layer. This work applies 2D classification twice, in two perpendicular directions, which appears to efficiently enhance connectivity of a segmented planar bounding surface in 3D. With supervised classification, inter-LBSs are clearly segmented, but the intra-laminaset surface is still unidentifiable. The extracted bounding surface image enables the 3D internal structure information of the bounding surface and will be used as a reference for multiscale registration and the characterisation in the following sections. The extracted bounding surface is also used to create the sub-domain constraints of the multiscale reconstruction in Chapter 5. The segmented bounding surface also provided strong evidence of bioturbation. Therefore, the disturbance of bioturbation on grading should be addressed during reconstruction.

4.3 Hidden features in SEM

This section discusses how hidden bounding surfaces can be revealed in SEM, in which they are presented less obviously than in MXRT, and thus present an obstacle to registration between SEM and MXRT. The nature of the challenge has been raised by the analysis of the literature in Chapter 2, and evidenced in Chapter 3 on a cross-laminated sandstone sample, that to register an XRT and SEM BSEM images, they must have similar resolution and retain the shared physical feature of inter-LBS similarly because: 1) the heavy minerals that highlight the bounding surface in MXRT are only represented as separate, brighter particles in a high resolution BSEM and it is hard to reassemble the topology of the bounding surface by simply connecting them; 2) As to be illustrated later in the following sections, the classical rescaling techniques by either linear or nonlinear (cubic) scaling on a BSEM image still fails to retain any information on a shared inter-LBS similar to MXRT. The different imaging principles between BSEM and MXRT will be discussed and proved responsible for the "missing" bounding surface feature in BSEM. This section begins by discussing the fundamental reasons of both these challenges and their impact on retaining of a bounding surface on a BSEM image. The discussion inspired the following development of a method to retain the bounding surface from a BSEM image, after upscaling, by taking composition into account with assistant of EDS image, to emphasis the role of heavy mineral in the similar way to that in a MXRT image. The method improves the presentation of the bounding surface on the BSEM image so as to assist in registration with MXRT. The registration will help further characterisation of

lamina thickness, which appeared to be hard to identify in the previous top-down characterisation performed in Chapter 3.

The nature of hidden bounding surfaces in BSEM beyond MXRT are:

1) The high-resolution BSEM image at 1x1 μm^2/pixel resolution image appears very different to the MXRT image at 100x100 μm^2/pixel, because of the large resolution difference (100 times). The latter has averaged the density of heavy particles presented in the former, together with the local hardening effect, to better reassemble the topology of heavy minerals concentrated on the bounding surface. Figure 4.14 gives an example of a partial view of both BSEM and MXRT images at a similar location containing three horizontal planar bounding surfaces to emphasise this challenge. The BSEM image shown in Figure 4.14(A) contains no obvious topology of the bounding surface, which is more observable in MXRT as brighter linear patterns. The heavier irons and dolomites expected to highlight the bounding surface are presented as separate, brighter particles with clear grain geometries, cemented in the fine bounding surface layer in BSEM as shown in Figure 4.14(A), which are hard to reassemble to represent the topology of the bounding surface. However, in the MXRT image shown in Figure 4.14(B), grain densities are averaged over the coarser pixels, without detailed grain geometries. The heavy mineral concentration on the bounding surface is therefore presented with the clear, brighter, linear pattern.

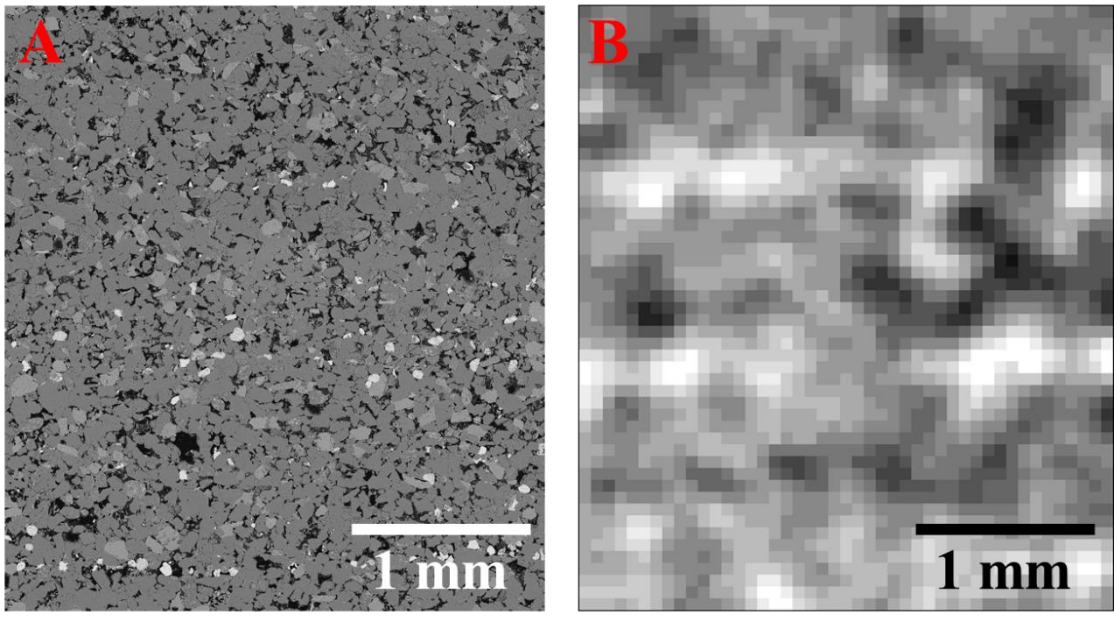

Figure 4.14 (A) Small FOV (2928x3294 pixels^2) of BSEM at 1x1 μm^2/pixel resolution compared with (B) MXRT at 100x100 μm^2/pixel at manually addressed similar FOV (45x51.)

2) The other reason bounding surface patterns are less obvious in BSEM is the different imaging principle. The image intensity I of BSEM (I_{BSE}) is expressed in equation (4.1), according to Müller (1954), and the intensity for MXRT (I_{CT}), is expressed in (4.2), according to Herman (2009). Apart from constants, I_{BSE} is determined by the BSE coefficient, η, and I_{CT} is determined by the attenuation coefficient, μ. Both BSE and the attenuation coefficients have a positive correlation with the atomic number of the element (e), but with different gradients as shown in Figure 4.15. The CT attenuation coefficient has a larger positive correlation gradient with increasing atomic number (thus density) and would result in a larger contrast between bounding surface and the matrix on the MXRT image than on the BSEM image.

   Figure 4.16 provides evidence of the impact of different imaging principles by comparing a low-resolution BSEM of T2 with an MXRT of L1, to exclude the resolution impact. Two low-resolution BSEM images are generated by either upscaling the high-resolution BSEM to the low resolution of 100x100 μm^2/pixel or directly imaging at low resolution (53x53 μm^2/pixel), similar to that of MXRT (100x100 μm^2/pixel), as shown in Figure 4.16 (A and B). The upscaling approach calculates the arithmetic average pixel intensity of every 100x100 fine pixel (1x1 μm^2/pixel) in a BSEM of T2 to one coarse pixel, thus yielding 100x100 μm^2/pixel resolution. Neither upscaled nor directly imaged low-resolution BSEM of T2

revealed obvious brighter bounding surface patterns similar to those in the MXRT image in Figure 4.16 (C).

$$I_{BSE} = \eta C + B \tag{4.1}$$

where I_{BSE} is determined by BSE coefficient, η, and constant value B, C.

$$I_{CT} = 1000 \times \frac{\mu - \mu_{water}}{\mu_{water} - \mu_{air}} \tag{4.2}$$

where I_{CT} is determined by the attenuation coefficient, μ, and normalized by the attenuation coefficient of water (μ_{water}) and air (μ_{air}).

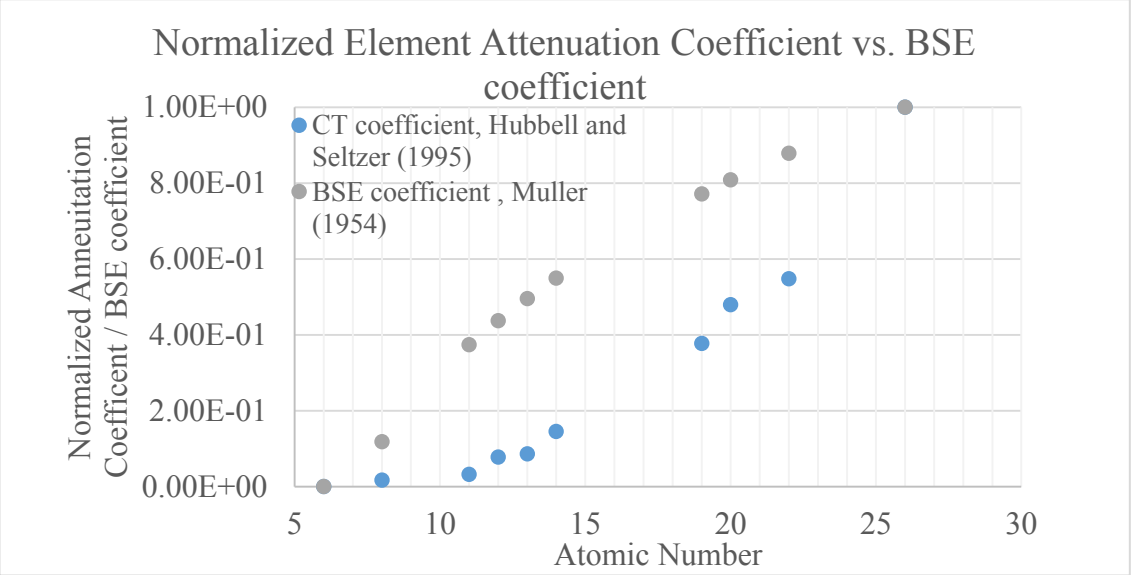

Figure 4.15 Relationship of normalized attenuation coefficient (CT coefficient) and BSE coefficient, with atomic number of element e ranging between 5-26, covering the major elements making up 98.5% of the crust. CT coefficients at 0.1MeV are given by Hubbell and Seltzer (1995) and BSE coefficients are calculated by atomic related function given by Müller (1954).

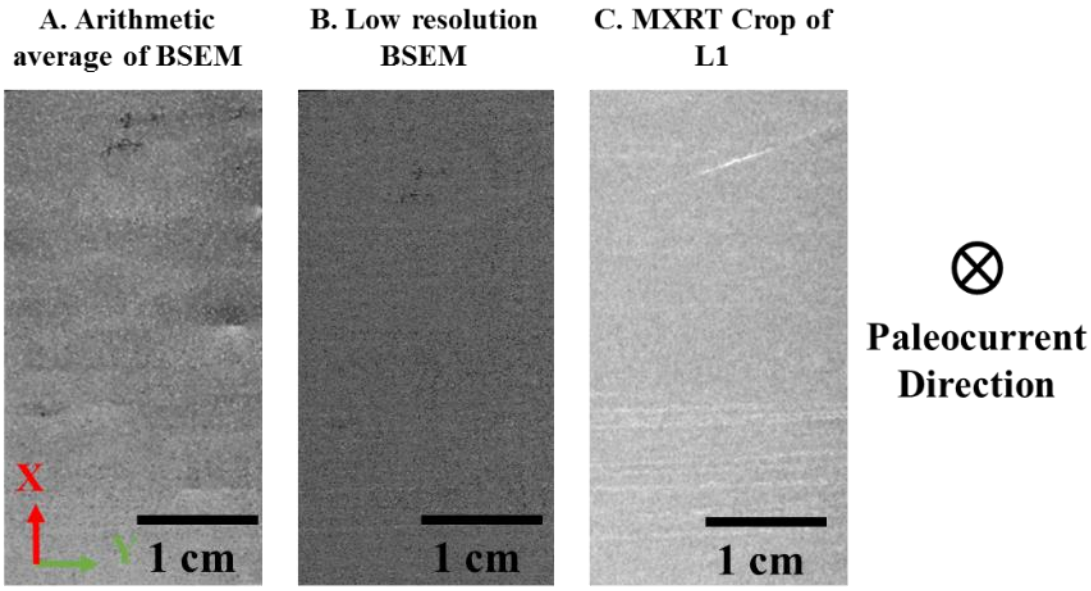

Figure 4.16 Comparison of low-resolution BSEM and MXRT images at similar location: (A) T2 BSEM image rescaled by arithmetic average to have resolution of 100x100 μm^2/pixel; (B) T2 imaged under low-resolution BSEM at 53x53 μm^2/pixel and (C) MXRT imaged at 100x100 μm^2/pixel at same area of T2

This section now develops a method to reveal a brighter bounding surface, as observed in MXRT, from high-resolution BSEM, by upscaling and simulating the MXRT imaging principle.

4.3.1 Extracting hidden features from BSEM- an upscaling using compositions

To address the two discussed inherent reasons "hiding" the bounding surface on BSEM images, a mechanism needs to be developed to retain key minerals identified previously that highlighting bounding surface, based on EDS map and simulate the MXRT imaging principle at the appropriate resolution. The analysis of the MXRT image in Chapter 3 concludes that heavy metal and high X-ray attenuation components along bounding surfaces are responsible for the observed high intensity in XMRT. Since the intensity of each voxel reflects the overall X-ray attenuation of all chemical elements within the volume of that voxel, one could mimic this on the EDS image that provides the element distribution map at the identical area of the BSEM images, to explore hidden bounding surface features.

Proposed method

The method can be summarised as follows: given a fine-scale EDS image of a thin section, a coarse-scale image overlapping the EDS image can be generated, following the scheme in Figure 4.17. On each coarse pixel, a weighting factor is firstly calculated, as in equation

(4.3), then an average of mass X-ray attenuation, as in equation (4.4), and, finally, the new image intensity, as in equation (4.5). For each chemical element, a weighting factor is determined from atomic mass values from EDS values on all corresponding fine pixels in each coarse cell. For each coarse cell, its mass X-ray attenuation is computed as the average of all the mass X-ray attenuations of all elements in the EDS, using the weighting factors.

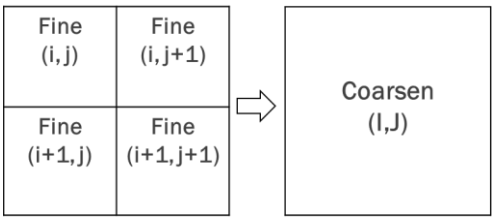

Figure 4.17 Coarsening scheme, illustrated by nϵ[1,4] fine pixels with coordination labelled with i, j upscaled into one coarse pixel with coordination I,J;

$$\mathrm{w}'(e) = \frac{\sum_{n} \mathrm{m}_{i,j}(e)}{\sum_{e}(\sum_{n} \mathrm{m}_{i,j}(e))} \tag{4.3}$$

where the weighting factor is calculated the by mass (*m*) fraction of each element *e* in the compound.

$$\frac{\mu}{\rho} = \sum_{e} \mathrm{w}'(e)(\frac{\mu_e}{\rho_e}) \tag{4.4}$$

where the calculation of average mass X-ray attenuation coefficient of the compound, $\frac{\mu}{\rho}$, consists different elements *e* with the corresponding mass X-ray attenuation coefficient of the element, $\frac{\mu_e}{\rho_e}$.

$$I_{(CT)} = 1000 \times \frac{\mu - \mu_{water}}{\mu_{water} - \mu_{air}} \tag{4.5}$$

where the MXRT image intensity $I(\mathrm{CT})$ is calculated by normalizing the calculated attenuation coefficient of the compound μ in (4.4) with attenuation coefficients of water μ_{water} and air μ_{air}.

Factors impacting on the proposed method

The reason different minerals (compounds) present different intensities in MXRT is that their constitutional elements have different mass attenuation coefficients. The mass attenuation coefficients, apart from varying across elements, also vary with energy, as shown in Figure 4.18. According to Figure 4.18, the applied imaging energy determines the contrast of heavy minerals concentrated on the bounding surfaces with the matrix in an MXRT image. In this work, however, the same energy as that in the real MXRT imaging of L1 has been applied in the simulation, given the purpose is to simulate a similar MXRT image for registration. The energy for acquiring the MXRT image is with a peak energy of 0.2Mev has been taken. According to Ketcham and Carlson (2001) "The energy spectrum generated is usually described in terms of the peak X-ray energy (keV or MeV) but actually consists of a continuum, in which the level of maximum intensity is typically less than half of the peak". Therefore, in this work, for the purpose of estimating the attenuation coefficient the decision has been made to use half the peak energy, i.e. 0.1 MeV (as highlighted in Figure 4.18) for calculation.

To evaluate and explain the energy configuration used for imaging the MXRT of L1, Figure 4.18 highlights the energy range that has a larger difference of attenuation coefficient across elements in the red dashed box. The half peak energy of 0.1Mev does not provide the largest contrast in the highlighted rectangular area, because the imaging of MXRT was compromised to apply higher energy to penetrate the large 6cm cubic L1. During MXRT imaging, the energy is designed to be high enough to penetrate the sample; however, according to Figure 4.18, the larger the energy the lesser the contrast of attenuation between different elements. For a smaller sample, lower energy could be applied to achieve higher contrast. However, according to the zoomed-in view of the attenuation coefficient band close to 0.1 MeV, as seen in Figure 4.18, Fe still stands out from the rest of the elements; this explains why iron highlights the bounding surface. The following three heavy minerals (Ti, Ca and K) can be classified as a second group with high attenuation coefficient. This explains why dolomite (ideally CaMg(CO3)2) is coherent with the iron-enhanced bounding surface. In addition, Ca, as an indicator of bioturbation, and K, as a potential indicator of K-feldspar, also create high-intensity

pixels, therefore leaving large gaps and distractions on the presented bounding surface in the MXRT image.

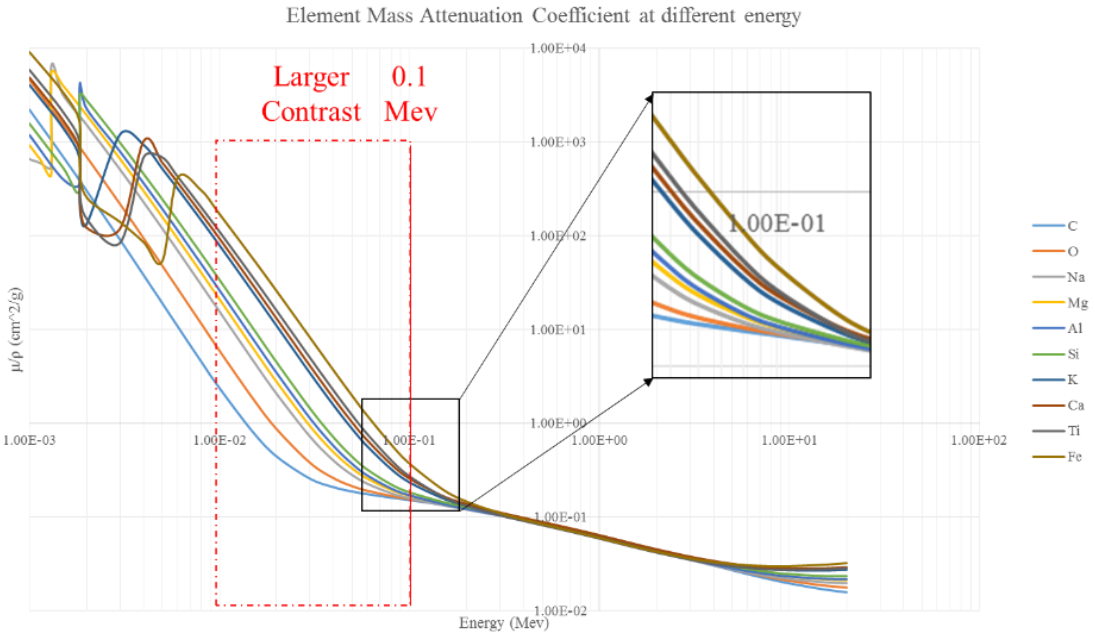

Figure 4.18 The 10 main elements' Mass Attenuation Coefficient at different energies

Apart from energy, the impact of coarser image resolution is also discussed, in the sense of the ratio between resolutions and average grain size. The reason behind this is that a resolution too low would average the thin ~1-2 grains layer of heavy minerals concentrated at the bounding surface with neighbouring lower density grains and reduce contrast. However, a high resolution will give too many details on the grain geometry and weaken the contrast between the heavy mineral highlighted bounding surface and the rest matrix. In this work, again, a decision has been made to simulate the coarser MXRT image with a resolution of 100x100 μm^2/pixel. The 100x100 μm^2/pixel resolution is slightly below the average grain size (measured between 100-200um in long axes diameter); thus, it reveals the thinnest bounding surface of 1 grain thick but avoids too much averaging with neighbouring grains. Each coarse pixel is therefore 100 times scaled up from the fine 1x1 μm^2/pixel, to exclude the geometry details of grains. The 100x100 μm^2/pixel is also the same resolution as the MXRT image taken on L1, and therefore appropriate for registration purposes.

Performing the proposed method on T2

The proposed method upscale BSEM by averaging X-ray attenuation coefficient of key elements that highlight bounding surface to retain its feature similarly with MXRT.

Therefore, the method has advantage of retain features related to the selected key elements. In this work, bounding surfaces are identified highlighted mainly by Fe element, and the 0.1MeV energy is discussed distinguish Fe to the rest elements. Therefore, in this work no specific elements selecting is required, and eight main constitutional element maps yielded by the EDS of T2 are used for calculating the MXRT image. Figure 4.19 illustrates the simulation procedure from eight fine-scale element maps imaged from T2 of 19845x38074 pixels^2 at a resolution of 1 μm^2/pixel. The element maps are applied to estimate atomic mass and calculate the weighting factor and with corresponding attenuation coefficient to the simulated MXRT value in a coarsened image. The procedure yields a simulated MXRT of 198x380 pixels^2 at 100 μm^2/pixel.

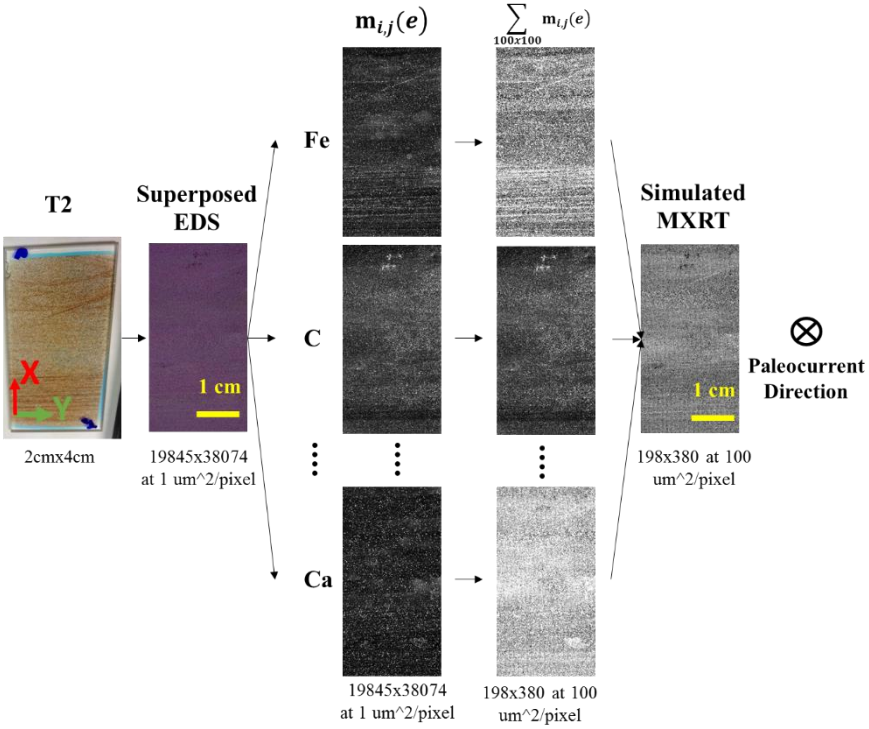

Figure 4.19 Illustration of proposed method simulating an MXRT image from EDS image of T2

A typical arithmetic average BSEM, low-resolution BSEM scanning and the crop of a slice of MXRT of L1 as shown in Figure 4.16 are put together with the simulated MXRT as the top row of Figure 4.20, to evaluate the effectiveness of the proposed method. To avoid the effect of different image intensity ranges, each image has been normalized by simply rescaling the original intensity range to 0-255 to normalize it, as shown in the bottom row of Figure 4.20. By visual observation, the simulated MXRT presents the most similar bounding surface pattern to the MXRT image, indicating that the proposed

method is superior to the other two in preserving the bounding surface. The remaining differences includes the following observations: 1) The simulated MXRT appears to have a thinner bounding surface than the real MXRT; this is because proposed method only simulates averaging the density by the MXRT principle, but not the hardening effect explicitly. The hardening effect is expected to increase thevpixel intensity value of neighbouring pixels around heavier minerals concentrated at the bounding surface thus make the bounding surface appear thicker; 2) The brighter patch area in the middle of the simulated MXRT is not observed in the real MXRT image. The potential reason is that the real MXRT imaging is reflecting a full range of element distribution, whilst in simulated MXRT only 8 main constituent elements are applied, therefore misleadingly emphasising different patterns. However, in this work as the purpose is to reveal the bounding surface to help registration, the simulated MXRT is believed sufficient for this purpose.

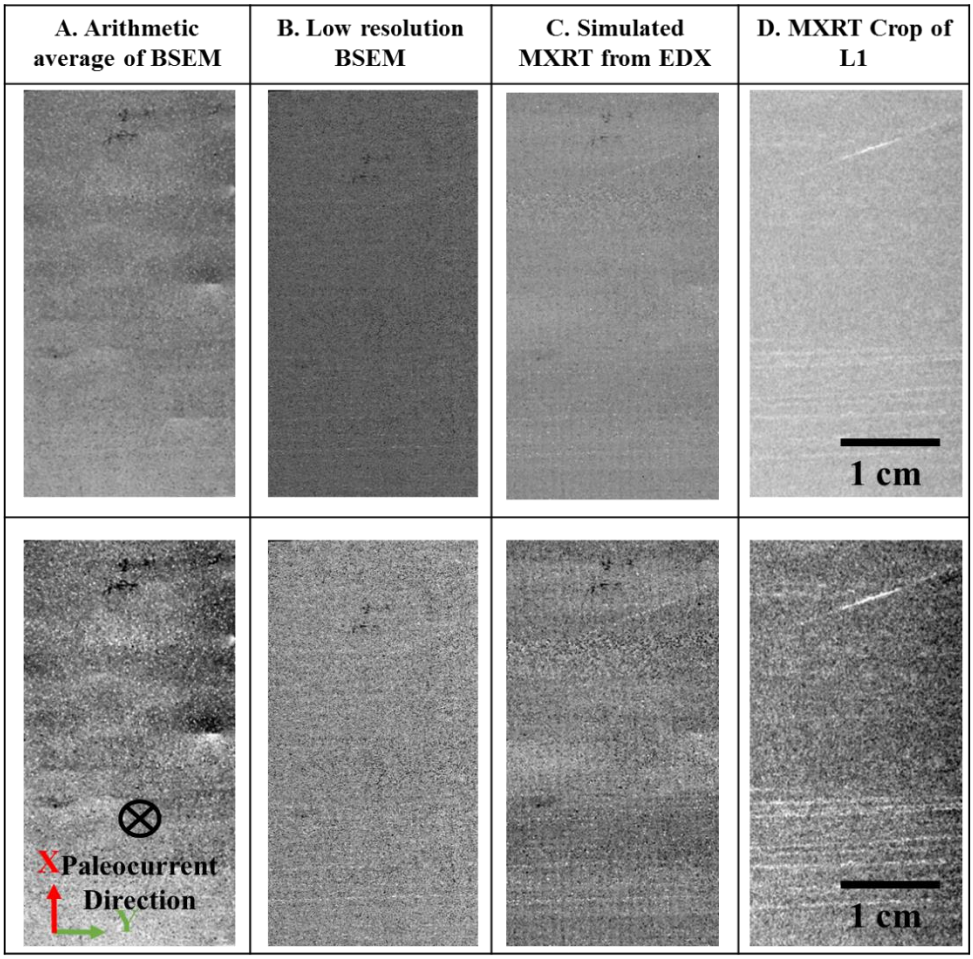

Figure 4.20 Top row before and bottom row after normalizing images of: (A) arithmetic average of SEM BSE of 198x380 at 100 μm^2/pixel; (B) SEM BSE image taken of 374x718 at 53 μm^2/pixel; (C) Simulated MXRT image of 198x380 at 100 μm^2/pixel, using the method developed in this work; (D) 2D MXRT image of 198x380 at 100 μm^2/pixel.

Quantitative evaluation

To objectively and quantitatively evaluate the four images in Figure 4.20, a convolutional filter bank approach is performed which has been proved to successfully characterize the linear features of bounding surfaces. Patterns around each pixel in an image are characterised by convolving the neighbouring area with each filter from one of the filter banks (learnt 121, in Figure 4.5(A), applied for segmenting the bounding surface from MXRT of L1). The frequency with which one pattern (described by a filter) occurs in one image can be estimated by calculating the average convolutional value of the filter over every pixel of the image. One image could, therefore, be characterised by the histogram of patterns described by filters in the bank. Taking the histogram of MXRT of L1 as a reference, the average differences of the histogram of the arithmetic averages of BSEM, low-resolution BSEM scanning and simulated MXRT to MXRT of L1 are 3.81, 3.64 and 1.02 respectively (where 1 stands for a 100% identical histogram with MXRT of L1: a detailed discussion is given in Appendix C.1). The simulated MXRT is therefore robust in revealing the bounding surface features presented in the real MXRT image.

4.3.2 Characterisation with registration

It has been explained that the missing information of hierarchical characterisation is intra-LBS, which is not directly observable from the obtained images. An alternative approach is to 1) statistically measure grading on a pore-scale subsample and indirectly estimate lamina thickness to reflect the distance between intra-LBSs; 2) register the subsample to the full domain to infer the spatial distribution of intra-LBSs. The grading measurement was performed on the μ-XRT image in the work reported in Chapter 3, but was less representative because of small FoVs. In this section, the similar grading measurements are performed on the BSEM image. The grading measurements require a dedicated designed sampling window based on the bounding surface to achieve two advantages: 1) the sampling window has the same geometry as the bounding surface, which represents the geometry of the conceptual grading layer within the lamina; 2) identifying the grading direction, which is expected to be perpendicular to the bounding surface plane direction. In this section, the BSEM image is registered to the MXRT image, referring to shared bounding surface features revealed in the simulated MXRT image. Therefore, the segmented connectivity which is preserved on the bounding surface from the MXRT image of L1 in 4.2 could be masked on registering BSEM image to design sampling

window. A set characterisation of lamina grading could be performed on the BSEM image with a known spatial location in the domain of L1, to assist in inferring missing intra-LBSs.

4.3.2.1 Registering MXRT and BSEM

In this work, a dedicated registration method proposed by De Boever et al. (2015), as reviewed in section 2.7.4, is not required. The reason is that one of the two advantages of a dedicated, designed sampling window that suggesting grading direction, has been rendered less important by the assumption of a vertical grading direction in Chapter 3. Therefore, the benefit of registration is only to provide the geometry of the bounding surface at a relatively correct location, while the grading direction has been previously determined. In this work, with prior knowledge of the sampling location of T2, T2 is registered with the MXRT image, based on the two intersecting curved bounding surfaces occurring in both simulated MXRT images (Figure 4.20 (C)) and the MXRT image of L1 (Figure 4.20 (D)) as the reference. By rotating and scaling the simulated MXRT image, the shared bounding surfaces are matched with those observed in the MXRT image of L1 and can be overlapped, as in Figure 4.21 (A). Figure 4.21 (B) also illustrates the BSEM image which has replaced the simulated MXRT image at the registered location on the MXRT image of L1. As a result, the segmented bounding surface of the MXRT image of L1 could be masked on the BSEM image, to design the sampling window according to both horizontal and curved bounding surfaces.

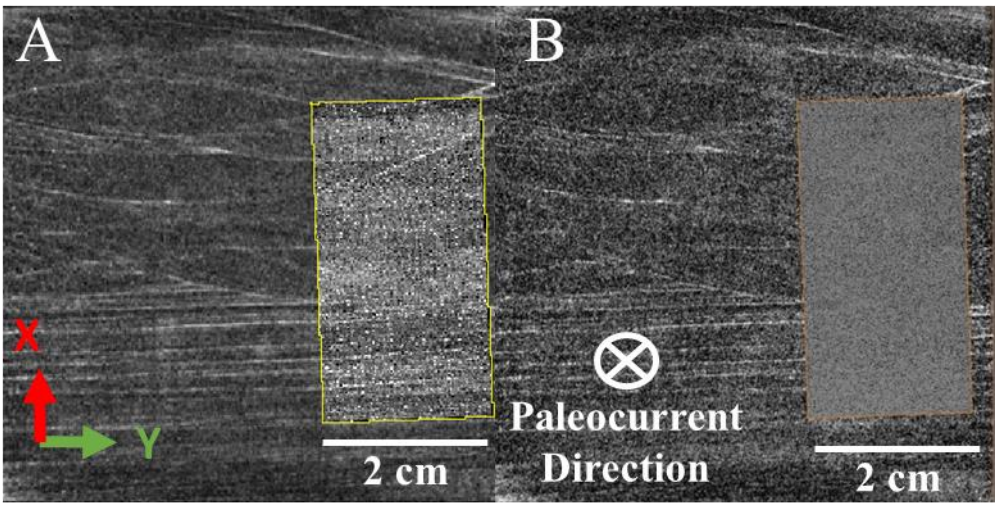

Figure 4.21 Registering simulated MXRT image to 1/525 slice of MXRT image of L1 (with hardening background removed): (A) registered simulated MXRT masked onto MXRT of L1 with the enhanced intersection of curved bounding surface as the reference; (B) Swamp 1x1 μm^2/pixel BSEM with registered simulated MXRT (scaled to the same resolution as BSEM).

4.3.2.2 Sampling window based characterisation

Designing the sampling window

To design sampling windows that have the same geometry as the bounding surface, the MXRT image is replaced by the segmented inter-LBS image, with the registered T2 area masked, as shown in Figure 4.22 (A). Sampling windows can be designed by tracing the segmented bounding surface and masking it onto the BSEM to measure grading. One horizontal rectangular sampling window has been designed as a red box, shown at the bottom of Figure 4.22 (B). The horizontal sampling window is parallel to all the bounding surfaces of the horizontal planar laminaset. Two curved sampling windows, referred to as cross1 and cross2, are traced in the upper curved laminaset region, following the two most distinct curved bounding surfaces, as labelled in Figure 4.22 (B).

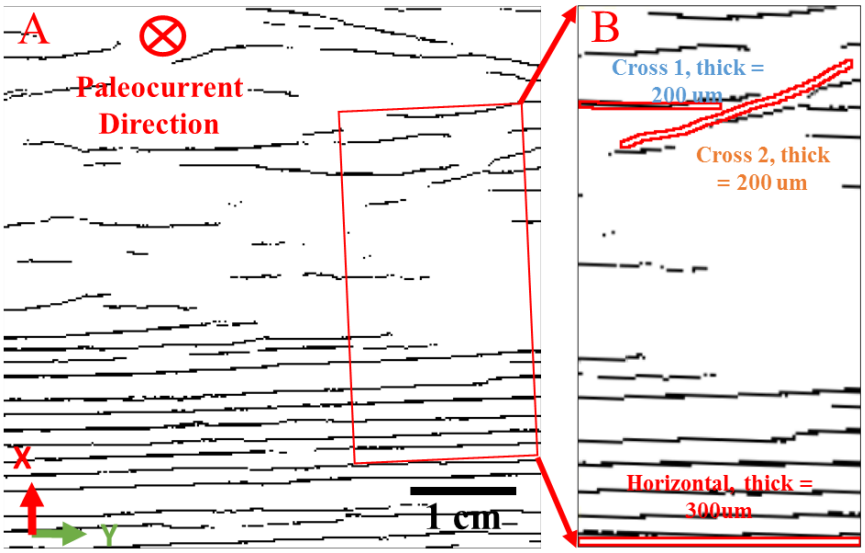

Figure 4.22 (A) Registered T2 area is masked onto the 1/525 slice of segmented bounding surface from MXRT of L1; (B) crop of the registered T2 area from (A) and three sampling windows are designed and labelled in a red box, based on segmentation of inter-LBS.

Sampling window and log measurement parameters

For a log type grading measurement as done for the μ-XRT image, the sampling window size, direction of movement, interval and distance need to be identified to reflect the nature of the layered grading. 1) Sampling window size: With the geometries of the sampling windows traced, the cross1 and cross2 sampling windows have been designed with a thickness of 200um and horizontal sampling windows with a thickness of 300um. The thickness is thicker than average grain size (<200um based on the measured long axes, presented in Table 3.4) but also thin enough to capture the variation over thin ~1-2

grains thick conceptual layers within the lamina. The sampling window also included the representative grains and pores, whose total quantity appears stable within the window of designed size at the randomly selected location. A detailed quantitative discussion based on Coefficient of Variation (CV) plot is given in Appendix C.2 . The sampling windows are then masked on the BSEM image to measure the variation of grain characters, as done for μ-XRT. Figure 4.23 shows the sampling window masked onto the BSEM (rotated 90 ^{o} right for better presenting the later log measurement). 2) Direction of movement: Each of the three sampling windows is moved along the +X (vertical direction on L1 that is assumed equal to sedimentation direction), as shown in Figure 4.23. Measurements can be performed within each moved sampling window to capture circulating grain pore variation by grading over a sedimentary layer parallel to the bounding surfaces and characterised by log plots. 3) Interval of movement: all three cases are non-overlapping sampling, whose interval of movement equals their corresponding thickness of window. For cross1 and cross2 the moving interval is 200um per move, and for the horizontal direction it is 300 μm per move. This thickness and sampling interval also ensure that even a single grain thin layer variation can be detected. 4) Distance moved: the total distance of movement needs to be larger than the maximum thickness estimated previously in Chapter 3 for laminae, thus covering the thickness of grading. For curved sampling windows cross1 and cross 2, 5mm have been moved by 25 moves that are greater than the estimated lamina thickness of 1-4mm, as in Table 3.4. The first and last moved sampling window are highlighted in yellow boxes in Figure 4.23. For the horizontal sampling window, as laminae and laminasets are all parallel to each other, the window has been moved from the bottom 38074 μm on the labelled depth axis up to 20000um on the labelled depth axis in Figure 4.23. The horizontal moving distance is designed to safely cover all observed horizontal bounding surfaces in Figure 4.22 (B), in which the last horizontal bounding surface before the curved laminaset is about 13000um from the bottom. Again, the first and last moved sampling window is highlighted in the yellow boxes in Figure 4.23.

Quantitative measurement of circulation of grain size

Quantitative measurements of average grain size are performed for each moved sampling window. Three log plots are masked in Figure 4.23, corresponding to each sampling window location and the presented circulated variation potentially represents grading. Based on the inverse grading system discussed in relation to the μ-XRT measurements in

Chapter 3, the starting layer of grading in one lamina could be potentially identified by valley points in grain size log plots. The starting layers representing potential intra-LBSs are labelled in the square in the log plots. The grading gradient within one lamina could, therefore, be measured between the square labelled starting layer and the following peak grain size on the log plots, as labelled in the triangle. Note that the labelled lamina between 24000um to 20000um in the horizontal log included multiple peaks but is still identified as one lamina because it follows a fluctuating rise trend and the small decreases in the middle are considered as disturbances. This lamina is classified as the curve1 lamina of curved the laminaset according to its performance distinguished on the log plot.

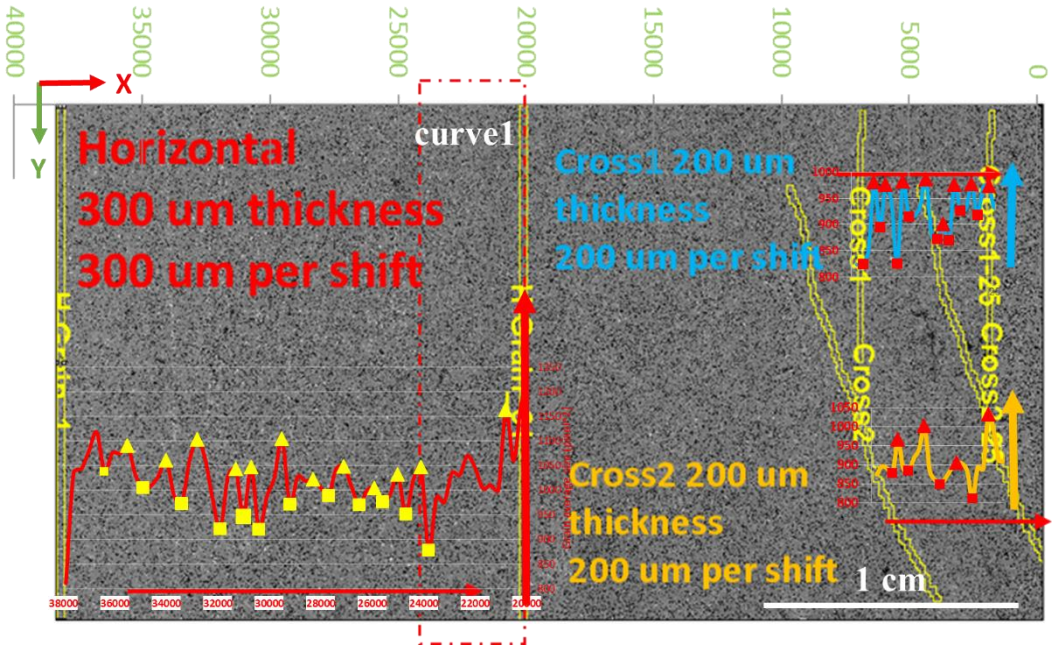

Figure 4.23 measured log plots of average grain size in the pixel area by three sampling windows and masked onto a BSEM of T2 (rotated 90 right from Figure 4.22 (B), for better illustration of log plots), x-axis of BSEM image is labelled from top of T2 (right) down to bottom (left) in μm units; horizontal log plot is given in red colour and masked between 39845 to 20000 μm on x-axis; the potential starting layer of laminae is labelled in yellow square and ending layer in yellow triangle on log plots; Cross1 are plotted in blue and Cross2 in orange; the potential starting layers are labelled in red square and ending layers in red triangle.

Numbers of measured laminae and lamina thickness are measured based on identified starting and ending points on log plots. The average grain size grading gradient SF_{rate} is calculated by same method as μ-XRT, for each lamina. The results are summarised in Table 4.2 (detailed calculation and measurement table are given in Appendix C.3) and the main observations includes: 1) 10 horizontal laminae and 13 curved laminae are measured, which are more representative than the 2 laminae measured for either S1 or S4; 2) the lamina thickness, typically between several hundred micrometres, agree with

previous measurements in Chapter 3. The histogram of lamina thickness of the horizontal part is plotted in Figure 4-17 (A), in which lamina thicknesses are typically 600-900um. Consider the 600-900um lamina thicknesses overlapped with the range of laminaset thicknesses measured in Chapter 3 (between 0-3mm for the horizontal part), it is suggested that it is not necessary to distinguish laminae and laminasets for the horizontal part, because both have shared thickness and geometry. Curved laminasets have thicknesses more distributed between 200-600 μm, as in Figure 4-17 (B). Thus, considering the identified curve1 lamina has an apparently large thickness of 3.9mm, it is suggested to define laminae with thickness covering the largest measured thickness. To keep the initial model simple, a single large thickness (>4mm) is suggested to be applied; 3) the grading gradient of both horizontal laminasets appears smaller than the 3D measurements (SF_{rate1D} per 200um thickness of 0.023 for S4) but curved cross 1 and 2 appear larger than the 3D measurements (SF_{rate1D} per 200um thickness of 0.021 for S1). In this work the 2D measurements are considered not representative to characterize 3D grain particles, because the 2D image only captures one cross-section of the grains.

Table 4-2 Summary of laminae measured by log plots

Location	Number of laminae measured	Circulation length	SF_{rate} per 200um thick layer	SF_{rate1D} per 200um thick layer
Horizontal Planar	10	682 μm	0.029	0.014
Curve1	1	3900 μm	0.013	0.006
Cross 1	8	325 μm	0.076	0.038
Cross 2	4	550 μm	0.063	0.031

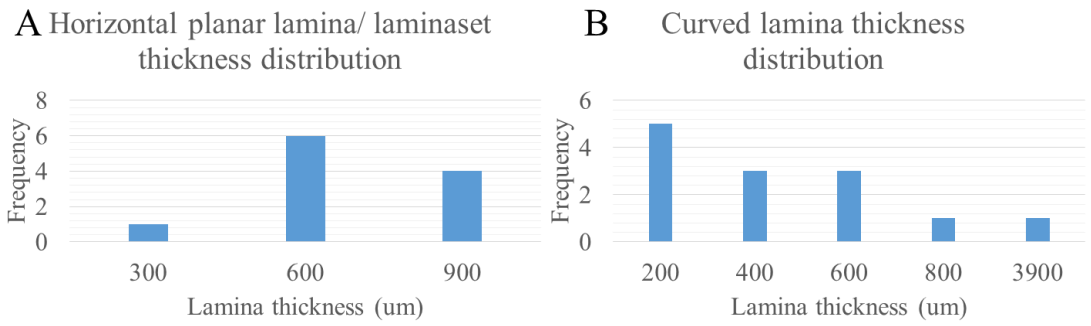

Figure 4.24 (A) Horizontal planar lamina/ laminaset thickness distribution; (B) Curved lamina thickness distribution.

Discussion of grain size at bounding surface

From the reconstruction point of view, it is useful to know the degree of variation of grain size occurring at different bounding surfaces. If grain size did not vary much over different bounding surfaces, the modelling could be simplified by using the same grain example across different bounding surfaces of different laminae and laminasets and applying the measured grading gradient to each grading layer. Investigation of grain size occurring at inter- and intra-LBS are performed by collecting grain sizes measured in the labelled valley layers representing bounding surfaces. The average measured grain size for 10 horizontal, 8 cross1 and 4 cross2 bounding surfaces are plotted in Figure 4.25, with the 95% confidence intervals plotted together (with standard score Z=1.96). The main observations are: 1) Firstly, the horizontal part has clearly larger bounding surface grain size than the curved part, where cross 1 and 2 have similar grain size; 2) Secondly, the 95% confidence interval of the horizontal part appears within a relatively narrow range of 60 pixels^2; thus about 8 μm at each axis. The narrow range of grain size in the horizontal part supports the previous claim by implying that inter- and intra-LBSs are not distinguishable in terms of their grain size; 3) Thirdly, for the curved part, the inter-LBS is directly identifiable. Therefore grain sizes from inter- and intra-LBSs could be compared. In Figure 4.25 grain sizes measured at identified in an inter-laminaset curved bounding surface (cross1, cross2 and curve1) are plotted. Cross1 has grain sizes out of the range of the 95% confidence interval of bounding surface average grain sizes measured at identified bounding surfaces of the cross1 log, but still falling in the range for cross2, while cross2 and curve1 have grain size falling into the 95% confidence intervals measured in both cross1 and cross2 logs. Therefore, in this work the decision have been made that grain size is non-distinguishable between inter- and intra-LBSs, within either the curved or horizontal parts.

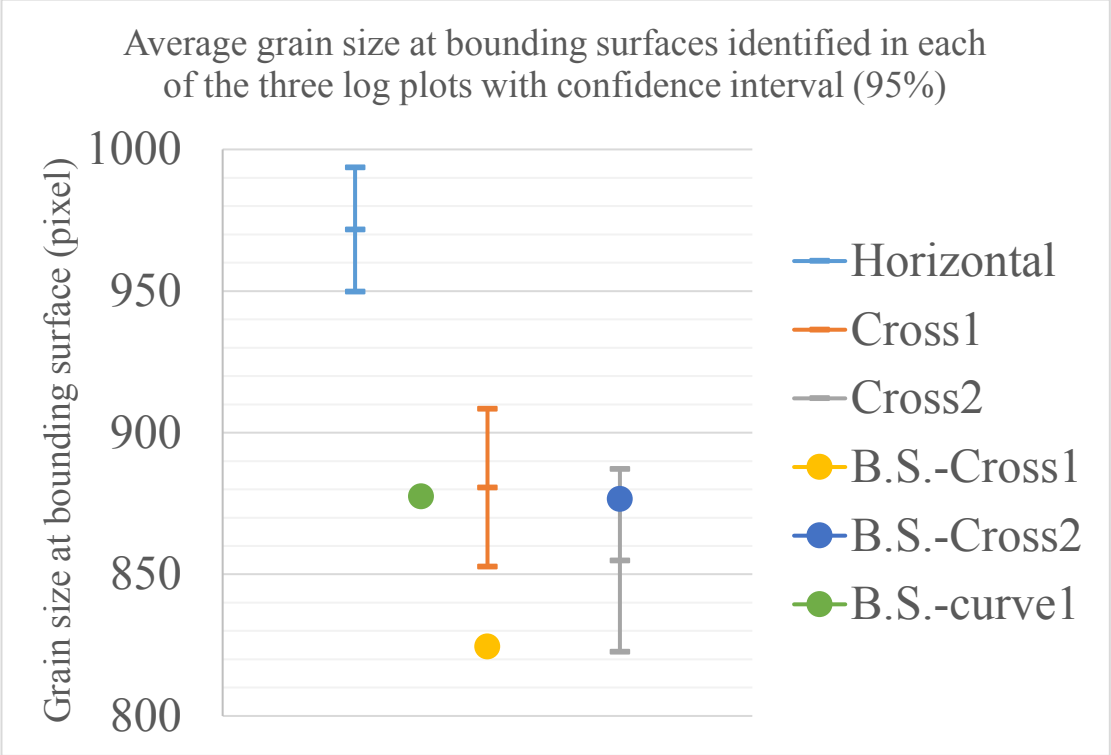

Figure 4.25 95% confidence interval of average grain size measured from 10, 8 and 4 labelled valley bounding surfaces (inter- and intra-laminasets for horizontal, cross1 and cross2, respectively). Grain sizes at identified inter-LBS cross 1, cross2 and curve1 layers are also labelled.

Discussion of results correlated with L1

Figure 4-15 masks the log plot over BSEM onto the segment of the bounding surface of L1 to correlate measured grain grading with the spatial distribution of inter-LBSs. The main conclusions are: 1) The labelled curve1 lamina from the horizontal log is confirmed to have entered into the curved laminaset region; 2) the labelled valleys on the grain size log plot of the horizontal part (as candidates of intra- or inter- LBS) are mostly spatially consistent with segmented inter-LBSs, which again suggests it is not necessary to distinguish inter- and intra-LBSs for the horizontal part. However, for the curved part, the labelled valley points are within the laminaset between segmented inter-LBSs. It is therefore suggested to consider hidden laminae exist within curved laminasets; 3) the average grain sizes at inter-LBS are not distinctively different to those from the potential intra-LBSs within either the horizontal or curved laminasets. Therefore this work suggests that during the reconstruction in Chapter 5 it is not necessary to distinguish the grain size at inter- and intra-LBS layers.

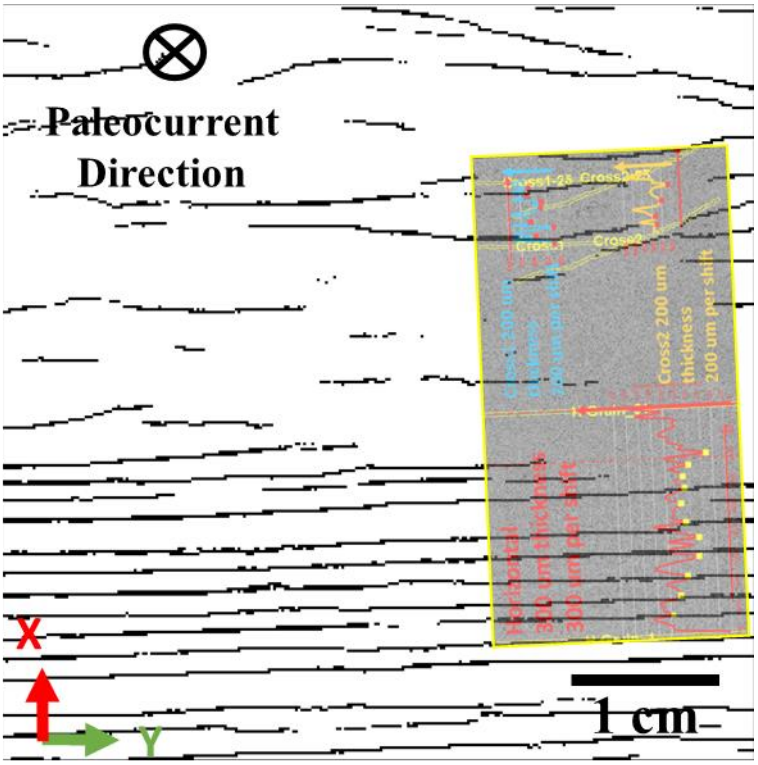

Figure 4.26 Figure 4.23 masked onto segmented bounding surface of MXRT of L1 at registered area

Discussion of uncertainty

The procedure discussed for measuring grading has uncertainty arising mainly from the following aspects: 1) Although cross2 is dedicatedly designed based on a segmented bounding surface, the moved measurements intersect with cross1 after several moves. From a sedimentation point of view, sedimentary layers above cross1 are "newer", which are parallel to cross1 and erode "old" sedimented layers parallel to cross2. Therefore the cross2 log measurements may not represent the true grading layer corresponding to the curved laminaset starting from cross2, but a mix with cross1. 2) The assumed vertical grading direction in the +X direction is not in the same direction as anticipated for the laminaset starting from cross2 (perpendicular to cross2). Both these two uncertainties suggest the log measurements starting with cross2 are not accurate. Additional measurements have been performed, to move the lower half of the sampling window of cross2 upward, perpendicular to the cross2, until it reaches cross1, referred to as cross2_half. With same thickness and moving interval to cross2 (200um), 6 moves of cross2_half have been made before reaching cross1. The 1st and 6th move are highlighted in Figure 4.27(A) and the measured average grain size log is plotted in Figure 4.27 (B), in which cross2 log measurements are also plotted for comparison. According to the log measurements, apart from the 1st measure of cross2_half, the remaining 5 measurements

give a "perfect" inverse grading lamina that has monotonically increased average grain size within each sampling window and with no fluctuation. Grading gradients are also measured for laminae identified between the square highlighted valley and triangle highlighted peak of cross2_half log plot and are summarised in Table 4.3 which gives SF_{rate1D} of 0.022. The SF_{rate1D} obtained for cross2_half is closer to the 3D measurements from μ-XRT S1 and S4, which are 0.021 and 0.023 respectively.

Therefore, it can be concluded that 3D measurements from μ-XRT are more accurate in grading gradient measurements. In this work, the two uncertainties for BSEM cross2 discussed above are considered not important in 3D μ-XRT measurements, for the following reasons. Firstly, S4 does not have either type of uncertainty, because the laminae are horizontal parallel to each other; thus there is no intersection and the sedimentary direction is in the vertical direction. For S1, firstly the sampling windows did not cross over each other after movement. Therefore, the first type of uncertainty of intersection could be excluded. The uncertainty caused by a vertical grading direction assumption for μ-XRT measurements can be neglected in this work, because a sampling window moving perpendicular to the bounding surface direction does not make a difference in the vertical direction. The reasons behind this can be illustrated by the labelled S1 location in Figure 4.27 (B) and summarised as: 1) the measured curved bounding surface typically has an inclined angle smaller than 30° to the horizontal direction; 2) μ-XRT sample is small and 3) the sampling window is naturally limited by the discrete square shape of a pixel.

Considering the consistency between cross2_half measurement and μ-XRT 3D, in this work the decision has been made to use the grading gradient SF_{rate1D} of 3D measurements on S1 and S4 for further grain-pore space reconstruction. However, given the thickness of laminae measured in 2D are more representative in terms of sampling area and obtained significantly larger maximum thickness for curved laminae, it was decided to base the lamina thickness information on 2D BSEM measurements.

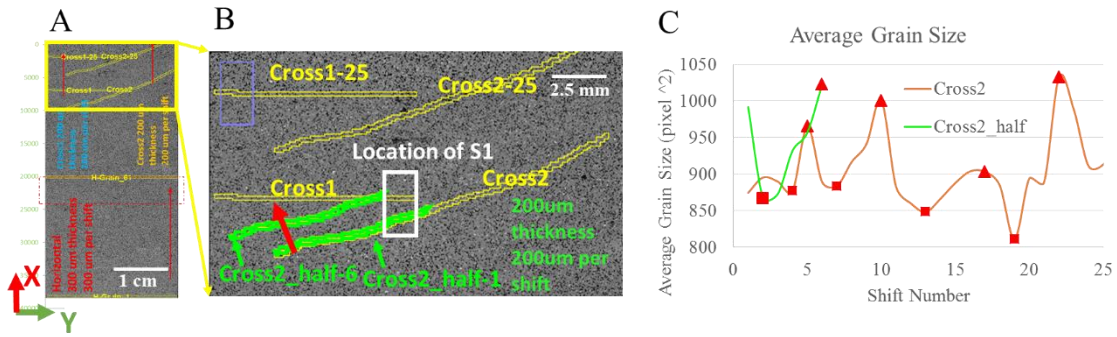

Figure 4.27 Uncertainty measurement of cross2_half, which is half of cross2 sampling window and moving perpendicular to the cross2 direction: (A) previously applied sampling window on the same BSEM as in Figure 4.23 but without rotating the BSEM, as a reference to display the location of cross2_half; (B) illustration of cross2_half-1 as lower half of cross2 and moved 5 times until cross2_half-6 is perpendicular to the cross2 direction; (C) measured grain size log of 6 moves of cross2_half sampling windows in comparison with cross2 log.

Table 4-3 Summary of laminae measured by log plots of cross2_hal between labelled square valley and triangle peak

Location	Numbers of laminae measured	Circulation length	SF_{rate} per 200um thick layer	SF_{rate1D} per 200um thick layer
Cross2_half	4	800 μm	0.045	0.022

Conclusion

This section described how the thickness of laminae from both horizontal and curved laminasets were measured by log measurements. The thickness of the horizontal part confirmed it was not distinguishable from laminaset thickness. Therefore, no intra-LBSs and laminae are required to be defined in addition to the segmented bounding surfaces. The thickness of curved laminae ranged from 200um to about 4mm. The range covered previous measurements in Chapter 3 and is thinner than the measured laminaset thickness of 1-2 cm. Therefore, intra-LBS separate laminae are suggested to be defined within segmented inter-LBSs from curved laminasets. It is suggested to define the distance between the intra-LBSs at 5 mm perpendicular to the paleoflow direction, because: 1) to simplify the initial model, the single thickness is suggested; 2) the measurements from single BSEM of T2 may lack representation; thus to cover the potential thickest lamina, a thickness greater than the largest measured lamina, 3.9 mm is required. However, one needs to bear in mind that the single 5mm thickness may differ from reality, because the measured distribution given in Figure 4.24(B) shows that thickness is typically less than 1mm, although the uncertainty of inaccurate measurement exists. Apart from thickness, inter- and intra-LBSs do not have distinctive different grain sizes, according to the

measurements. Therefore the same grain-pore configuration could be applied to bounding surface layers within either inter- and intra-laminasets.

4.4 Conclusions

This chapter has illustrated that the fundamental challenge in segmenting bounding surface from MXRT is to recognise and correct distractions to the geometry and connectivity of a thin piece-wise planar bounding surface. A filter bank based supervised classification approach has been developed and proved superior to others by: 1) a set of filters applied to the image to capture a set of characters in a multi-dimensional feature field reflecting different aspects of piece-wise planar structure and connectivity; 2) using a manually traced training image to clarify the classification of unresolved connectivity and unconnected parts, according to expertise and knowledge; 3) employing robust machine learning to learn the complex nonlinear classifier in a high-dimensional feature field. With a supervised classification segmentation method developed, thin piece-wise planar bounding surfaces were segmented from grey-scale MXRT images with appropriate preservation of connectivity. The segmentation highlighted the thin ~1-2 grains thick finest inter-LBS layer and could be applied as an index map to control grain-pore reconstruction. It could also be used as a basic index map for missing intra-LBSs and laminae to be defined on, to extend the index map. The segmented bounding surfaces also provided strong evidence of bioturbation which has a spatial track consistent with the EDS analysis observation on Tp and T2. The occurrence of bioturbation penetrates the bounding surface, and disturbs grading and, therefore, should be considered specially during reconstruction.

The missing thickness parameters to define the not directly observable intra-LBSs and laminae are measured by identitying the circulation of grain size on the log plot from BSEM of T2. The successful measure of log plot is based on the sampling window designed based on the bounding surface, which is not apparent on the BSEM image, but readily available from the segmented MXRT, and therefore calls for registration. The successfulness of registration is based on same physical structure presented in both image as a reference, but appears to be a challenge because of the large difference of imaging conditions and principles between BSEM and MXRT images. A method has been developed and reported in this chapter to reveal “missing” bounding surface features on BSEM, after upscaling and based on key elements provided by EDS images, and simulating X-ray attenuation of MXRT. The method revealed the heavy minerals highlighted bounding surface at the comparable condition to those presented in the MXRT of L1. The shared bounding surface could be taken as a reference for registration.

With the BSEM and MXRT of L1 registered, a sampling window could be designed based on segmented bounding surfaces, and log measurements could be performed on the BSEM. The log measurements established that, for the horizontal part laminasets and laminae have the same range of thickness. Therefore, the decision has been made not to define additional intra-LBSs for the horizontal part. For the curved part, intra-LBSs could be defined with a thickness of 5mm to cover the largest measured thickness. For grain-pore reconstruction purposes, the range of grain size occurring at inter- and intra-LBS was also compared with log measurements and were concluded to have similar grain size. Therefore, the decision was made not to distinguish grain size in inter- and intra-LBS during reconstruction.

The main uncertainties identified in this chapter include: 1) supervised classification enforcedly bridges "fake hole" gaps, but may also over-bridge "true hole" gaps. However, according to the measurements and discussion in this chapter, this effect can be ignored; 2) the assumed vertical direction gradings have been confirmed to introduce uncertainty during 2D BSEM measurement but it was decided they could be ignored for small μ-XRT measurement. Therefore, the decision was made that the grain gradient information from 3D μ-XRT measurement is considered as accurate. However, given that 2D measurement has more representative sampling size and, apparently, larger lamina thickness, the thickness information for reconstruction is decided to be based on 2D measurement.

The information obtained above would implement the reconstruction workflow proposed in Figure 3.23 of section 3.3.1. Apart from the segmented inter-LBS as an index map, the remaining uncertainties of unseen intra-LBSs and spatial distribution of grading will be addressed in Chapter 5, based on the obtained information. Based on the previous discussion, it was established that the samples of the study have relative constant laminaset and lamina geometries within each bedform and a narrow range of grading properties. Therefore, the decision has been made to deterministically define the hierarchical lamination structures and the grain-pore spaces within them with one set of parameters, based on measurements, as one realisation of among many possibilities. More specifically, with segmented inter-LBSs from MXRT in this chapter as the basic index map, missing intra-LBSs and laminae with conceptual layered index maps can be defined with the measured intersecting angle from Chapter 3 and thickness from BSEM in this chapter. With the full set of index maps representing the hierarchical structure of

the laminated sample, grain-pore geometries from μ-XRT could be taken as training exemplary images to stochastically reconstruct pore space, along with measured grading characteristics from μ-XRT, as non-stationary parameter controls, to reconstruct the non-stationary grain-pore structure. In addition, bioturbation needs to be addressed, especially during reconstruction, to represent the disturbance of grading, based on the quantitative observation provided in Chapter 3.

CHAPTER 5 - 3D FULL PORE-SPACE RECONSTRUCTION

5.1 Introduction:

The previous chapters have demonstrated that gradual and transitional non-stationary grain-pore variation across multiple-length scales in a sample must be identified by recursive top-down sampling and characterisation. To use the obtained hierarchical information to reconstruct multiscale structures at pore scale, a multiscale integration and reconstruction procedure is needed. This chapter reports the development and verification of a stochastic procedure for reconstructing a cross-laminated sample at grain and pore scales, based on a non-stationary index map developed and evaluates the procedure using the hierarchical information obtained on the same cross-laminated sample that has been described, analysed and characterised in Chapters 3 and 4.

Based on the procedures discussed in Chapters 3 and 4, the following hierarchical information on the sample has been obtained (also summarised in Table 5.1): 1) the inter-LBSs that separate adjacent laminasets from horizontal planar and curved laminasets, and also their geometries and distribution, from the MXRT image; 2) 2D geometrical distributions of pores and grains on the selected sample surface, from SEM images, including grain sorting, from which lamina distributions can be inferred; 3) from the μ-XRT image, 3D geometrical distribution of pores and grains on small volumes at specifically selected locations. Note that information becomes increasingly uncertain toward lower hierarchies; therefore, the defined hierarchical structures for the index map in the following sections represent just one realisation of many possibilities to simplify the illustration of developed process.

Table 5-1 Hierarchical information obtained on the sample by previous chapters

Image datasets	**Sample/ Sub-sample**	**Structural features**	**Method of Identification**	**Scope of interest in hierarchical model**
MXRT (3D)	L1 (Chapter 4)	Inter-LBS	Segmentation	Laminasets (spatial distribution)
SEM (2D)	Tp (Chapter 3)	Intra-LBS, intra-lamina grain-pore 2D	Visual interpretation	Laminae (orientation), grading direction
	T2 (Chapter 4)	Intra-LBS, intra-lamina grain-pore 2D	Indirectly estimated by measuring grading	Laminae (thickness)
μ-XRT (3D)	S1 and S4 (Chapter 3)	Grains and Pores 3D texture	Segmentation	Grading Gradient

Based on the obtained information summarised in Table 5.1, this chapter reports the development of a stochastic reconstruction procedure to generate pore and grain models for the centimetre-scale laminated sample, and an application of this procedure to the sample analysed in previous chapters. Note that the procedure is generic and could be applied to any cross-laminated sandstone sample from which the same classes of information have been obtained.

The procedure includes the following steps:

Step 1: defining a non-stationary index map of grain-pore variation associated with the structure hierarchy on the whole domain for reconstruction, based on the obtained information for the sample. The map can be thought to define spatial distribution of the 'mean sizes' of spatial-varying pores and grains at each hierarchical level and across two adjacent levels of the hierarchy;

Step 2: decompose the domain and the map onto subdomains to perform stochastic reconstruction in parallel in an ordering scheme, to minimise the latency of synchronisation;

Step 3: perform stochastic reconstruction on each subdomain, and integrate them back into a single model using one or more selected stochastic modelling techniques.

In what follows, tasks at each step are discussed in detail for the sample.

5.2 Step 1: Define an index map of the structure hierarchy

The procedure starts with integrating the obtained information in Chapter 3 and 4 for multiscale pore-structure reconstruction, as shown in Figure 5.1 where the three datasets above are registered in the same domain in the centre and useful measurements performed in previous chapters contribute to the reconstruction, highlighted by boxed images around:

1) Segmented inter-LBSs from MXRT, considering its relatively high certainty, are taken as a realisation of the fixed 1st part (big feature) of the index map in order to provide a regional constraint of pore structure reconstruction, as shown in the middle of Figure 5.1.

2) Intra-LBSs within each laminaset that separate the adjacent laminae cannot be identified with any certainty from M/μ-XRT images, and therefore need to be defined as the 2nd part of the hierarchical structure, in addition to the segmented inter-LBSs based on estimated lamina features (i.e. intersection angle and lamina thickness). The definition should follow the generic concept of the lamina model summarised in section 3.3.2 of Chapter 3. The inter-LBSs of horizontal laminasets are assumed to represent intra-LBS, because both have the same parallel planar structure observed from MXRT, as shown in Figure 5.1(B), and non-distinguishable thickness of horizontal planar laminae and laminasets, observed through all previous measurements (Figure 5.1(B-G)). Therefore, no additional intra-LBS is required to be defined for the horizontal part. However, in curved laminasets intra-LBSs appear to intersect with the inter-LBSs, based on manual observations from Tp (Figure 5.1(D-E)). Therefore, intra-LBSs in curved laminasets can be modelled at best as conceptual proxies, by generating the 2nd part of the hierarchical structure that demarcates intra-laminaset lithology variations between laminae. As the sample can be taken to be representative, and as the geometry of laminae within a curved laminaset appears similar, the assumption has been made that intra-LBSs in curved laminasets have a single orientation and thickness. The reasons are that 1) curved laminasets have wavelengths measured as over twice the sample size, as seen in Figure 5.1(A). Thus, within the same laminaset, laminae are expected to have the same features and 2) examining the internal structure of MXRT found all curved laminasets following the same paleocurrent direction (Figure 5.1(B)); therefore all laminae are assumed to have same features down to grain-pore scale. The angle is decided based on measurements from the sample surface (Figure 5.1(C)) and Tp parallel to the paleocurrent face, as observed in Figure 5.1(D) by manual observation. The thickness perpendicular to the

paleocurrent cross-section between intra-LBSs is decided to be consistent with maximum log type grading measurements from T2 (Figure 5.1(F)). The intra-LBSs are defined with relatively lower certainty than inter-LBSs, because, because they contain a set of assumption and decisions, as discussed previously.

3) Based on the inverse grading geometry observed from Tp and T2, the 3rd part of the index map requires to be generated as conceptual layers stacking on inter- and intra-LBSs (segmented in the1st part of the hierarchical structure and defined in the 2nd respectively) according to the generic conceptual lamina model summarised in section 3.3.2 of Chapter 3. The stacking is assumed in the vertical direction (X direction in Figure 5.1) which is assumed as the sedimentary direction, based on the geometry of the laminaset and paleocurrent direction obtained from the preliminary study (Figure 5.1(A-C)). As decided based on the previous discussion, the conceptual layers have the same thickness as used during measurements in SEM and μ-XRT (to cover at least one-grain size represent the finest bounding surface layer of ~1-~2 grains thick but less than the thinnest lamina of 1mm, to capture the variation of grading) across Figure 5.1(E-H). The layers are defined as stacking over a thickness twice that of the measured maximum lamina thickness, to cover the uncertainty introduced by limited measurement and ensure that most spaces between previously created bounding surfaces are filled. The rest would be especially defined to represent "true holes" caused by erosion and bioturbation. Together, they construct the full hierarchical structure, within which grain-pores are reconstructed in respect to an index map by populating grain-pore variation based on measured properties corresponding to each hierarchical structure. The decision needs to be made to separate horizontal and curved laminasets by defining the thickness of the horizontal laminasets. The separation could be based on geometry, identifying separation by segmented inter-LBSs (Figure 5.1 middle) in combination with Tp (Figure 5.1(E)) and T2 measurements (Figure 5.1(F)), where there is a transitional zone where the characteristics of both bedforms are observed.

4) It has been decided to use a small sub-volume of the horizontal bounding surface of S1 and S4, but with a representative quantitiy of grains, as a representative training image of local stationary grain-pore distribution, for the curved and horizontal part respectively (Figure 5.1.G-H). The stationarity is assumed because the sub-volumes have very thin physical thickness (~1-2 grains thick). This decision is based on the representativeness of the sample, and relatively narrow range of grain size occurring at bounding surfaces

measured from T2 (Figure 5.1(F)). The training image provides basic geometries of finest grain-pore without preferred orientation, and thus could be stochastically repeated with transformation of scaling and rotation according to the full index maps, defined by populating measured properties into the defined hierarchical structure. Such properties include the inverse grading gradient, SF_{rate1D}, from μ-XRT (Figure 5.1.G-H) and the identified preferred orientation on the curved part intra-LBSs, as observed from Tp (Figure 5.1(D)). Within each defined conceptual layer, and those with the same index, for grain-pore properties (including porosity, average grain size and orientation) are assumed to be stationary, because of the thin ~1-2 grains thickness of conceptual layer based on previous discussion. The model therefore has non-stationarity, first by spatial distribution of the index maps with respect to the geological structure of lamination, and secondly by grain size and orientation variation within index maps, to fully respect the non-stationarity of grain-pore distribution within a cross-laminated sandstone sample.

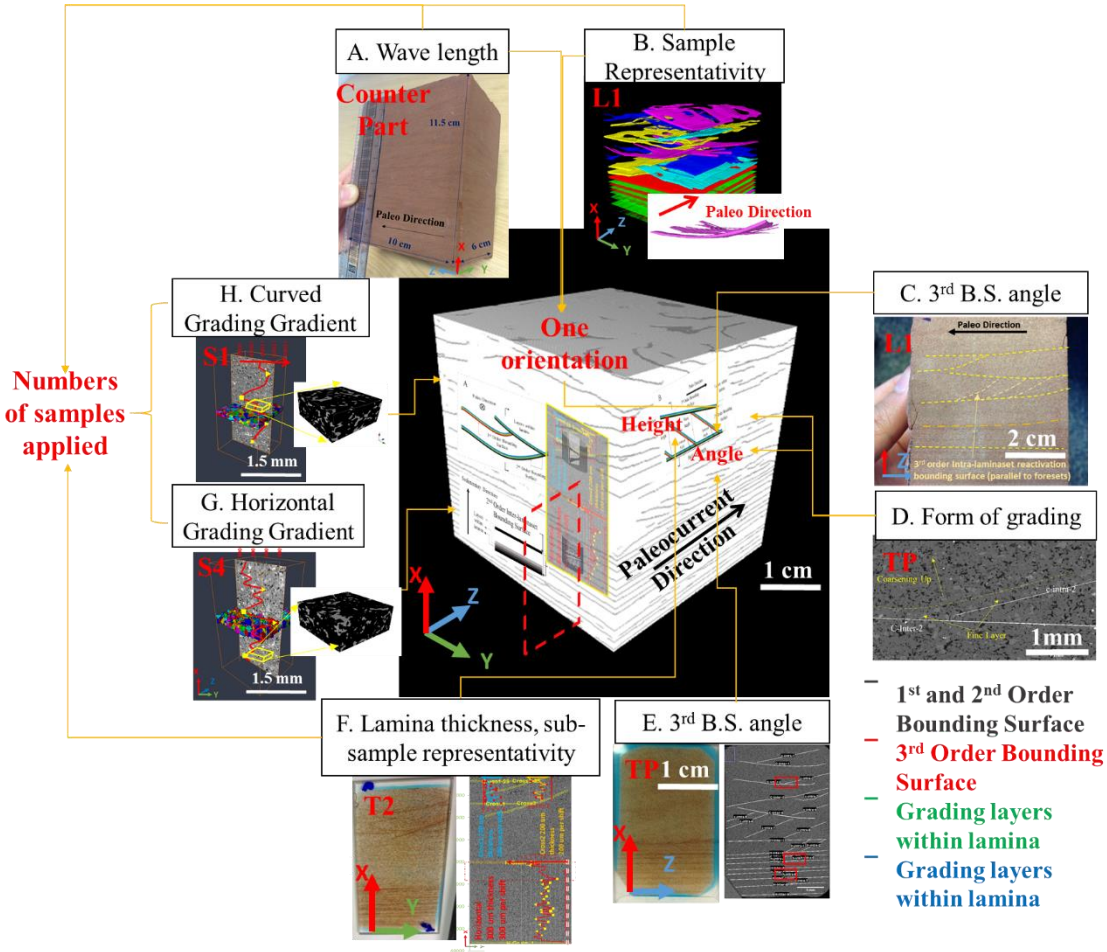

Figure 5.1 Integration of previously measured information for bottom up 3D pore space reconstruction of cross-lamination

The next part of this section defines the conceptual proxies, generically, to represent missing intra-LBS within each of the respective horizontal planar and curved laminasets and intra-lamina variation by conceptual layered grading between a pair of the intra-LBSs. Algorithm implementation of the proposed procedure is given.

5.2.1 Defining inter- and intra-laminaset variations

Defining inter- and intra-laminaset variations needs to be done separately in the upper region of curved laminasets and the lower region of horizontal planar laminasets, because of the hierarchical structure characteristics distinguished in Chapter 3. For a horizontal planar laminaset, laminae and conceptual grading layers are defined in the form of a horizontal planar plane and stacking parallel to the segmented inter-LBSs. For a curved laminaset, a set of parallel laminae are assumed, intersecting at an acute angle with inter-LBSs and separated by intra-LBSs. Conceptual grading layers within laminae are stacked parallel to the intersection of intra- and inter-LBSs in the assumed sedimentary direction (vertical direction) (Figure 5.1 middle). With intra-LBS and conceptual layers defined, the observed grading variations can be used to define the index for each individual conceptual layer.

5.2.2 Conceptual illustration for each horizontal planar laminaset

Defining the locations of the intra-LBS in each horizontal planar laminaset is difficult, because the laminaset is already very thin and the cyclic grading variation (see Figure 4-17 and Figure 5.1(F)) does not suggest the need to distinguish the intra-LBS. Therefore, the decision has been made to define the conceptual grading layers of the lamina stack directly on the segmented inter-laminaset horizontal planar bounding surface, without defining additional intra-LBSs.

The conceptual parallel layered regions within laminae can be defined with three parameters identified: the thickness of each layer, the thickness of the laminae and grading layer stack thickness. 1) Layer thickness can be determined to cover largest observed grain size to represent a layer of grain safely, but to be also thinner than the thinnest lamina thickness measured in BSEM characterisation in section 4.3.2, thus giving a layered region fine enough to reflect the grain-pore variation associated with grading. 2) The thickness of laminae for the horizontal part is pre-determined by segmented inter-LBSs, based on the decision that the laminaset and laminae are not distinguishable. 3)

The grading layer stack thickness is a conceptual thickness to be defined as larger than the thickness of the laminae, to ensure the defined grading layer fills over the laminae.

Based on the 2D-slice conceptual model given in Figure 5.2, starting with segmented inter-LBS from MXRT as black layers, horizontal planar layered regions are defined parallel to the extracted inter-LBS as grey coloured layers. The process defines one layered region on top of another along the sedimentary direction until reaching another segmented inter-LBS. To ensure the defined layers fill all empty regions between segmented inter-LBSs within a horizontal planar laminaset, a maximum layer stack thickness twice the measured maximum thickness of the horizontal lamina/laminaset will be defined and the stacking will stop when it reaches the next inter-LBS. Defined layered regions are assigned with a sequentially increasing indices (*Ln*), starting from the bounding surface labelled with pixel value "1" to "*Ln_h_max*" (*Ln_h_max* *layer thickness equal to the defined maximum layer stack thickness), which are later used for pore-space reconstruction to assign measured scaling factors to reflect grading.

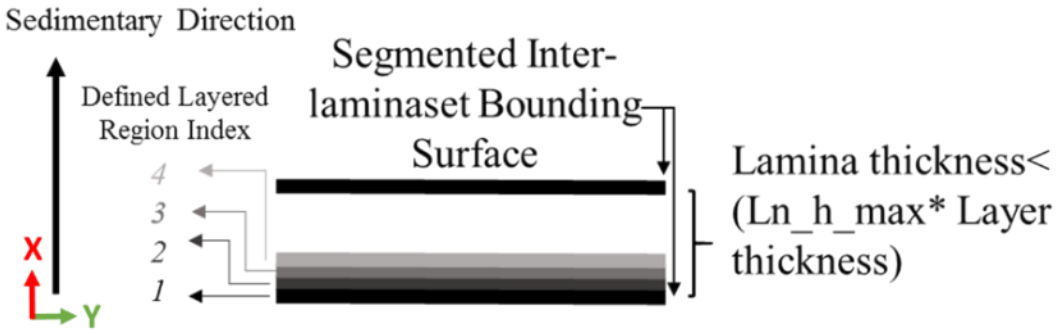

Figure 5.2 Illustrating defined layered regions parallel to segmented inter-LBS for horizontal planar laminaset.

5.2.3 Conceptual illustration for curved lamination

For a curved laminaset, intra-LBS needs to be defined first, followed by defining conceptual grading layers. For the three parameters: 1) conceptual layer thickness is based on the same principle as with the horizontal part; 2) lamina thickness is defined as the distance between curved intra-LBSs on the cross-section perpendicular to the paleocurrent direction; therefore, it is based on the maximum lamina thickness measured in T2 (by log plot) in Chapter 4, 4.3). The grading layer stack thickness is again designed to be larger than the thickness of the lamina, for the same principle as for the horizontal part.

Two perpendicular 2D slices are used to illustrate the 3D reconstruction of layered regions for the curved laminaset in Figure 5.3, because the intra-LBS is expected to be parallel to and intersect with the segmented inter-LBS perpendicular to and parallel to the paleocurrent direction, respectively. Starting with the segmented inter-LBS as black layers, shown in Figure 5.3, missing intra-LBSs are first defined as red layers with index (*Ln*), starting with "*Ln_h_max*+1" to distinguish them from inter-LBS. Intra-LBSs are defined as intersecting with extracted inter-LBS at an angle as measured in Tp on the downwind side of paleocurrent direction (Figure 5.3(B)). A set of parallel intra-LBSs is plotted with the distance along horizontal (paleocurrent) direction of half a wavelength, where half wavelength*tan (intersect angle) =lamina thickness measured in T2. Conceptual layers parallel to the intersection of black inter- and red intra-LBSs can be defined by the same method as for the horizontal planar laminaset (green and blue coloured layers stacking in the vertical direction, for illustration, in Figure 5.3). A different set of the index (*Ln*) for layers of the curved laminaset are applied to distinguish it from the horizontal laminaset. The index of the curved part starts from "*Ln_h_max*+1" and up to "*Ln_c_max*" where *Ln_c_max* *layer thickness is equal to a defined maximum layer stack thickness, which is again defined as twice the thickness of the curved lamina, to cover uncertainty caused by limited measurement and ensure most spaces between bounding surfaces are filled.

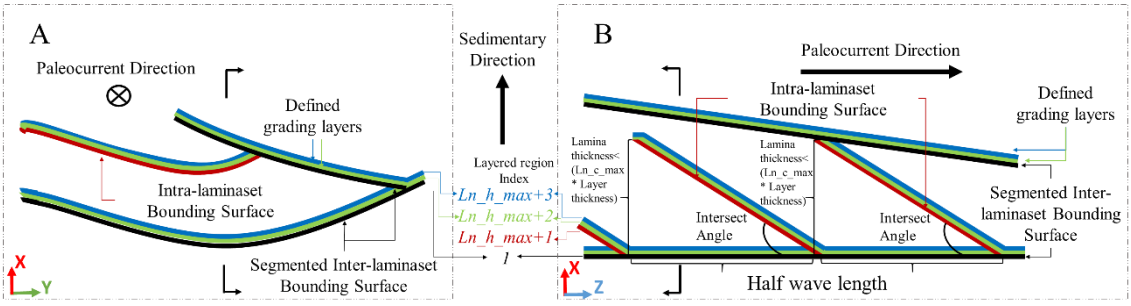

Figure 5.3 Illustration of defining layered grading on a white canvas and assigning it with the index for curved laminaset geometry structure at a cross-section (A) perpendicular or (B) parallel to the paleocurrent direction. Inter-LBS is plotted in black, intra-laminaset in red and layers within lamina are in green and blue.

5.2.4 Algorithm implementation

The definition of the layered region starts with the segmented binary inter-LBS image and follows the conceptual model proposed above to define layered regions labelled with a sequentially increasing index (*Ln*) to indicate different layers. The defining process for a horizontal planar laminaset is illustrated in Figure 5.4. Figure 5.4(A) represents discrete

pixel grids of one 2D xy slice of the segmented binary (pixel values "1" and "255") inter-LBS, which is shown as horizontal black layers ("1") and the matrix is shown as white ("255"). Assuming one pixel has a thickness the same as a defined conceptual layer of grading, as shown in Figure 5.4(B), Figure 5.4(A) is copied by moving the entire slice one pixel along the vertical X+ direction and adding "1" to the original pixel values (index (Ln)) to define a new layer parallel to the original bounding surface. This process would be repeated to create set of copied images (Figure 5.4(A-C)). The set of images are superimposed but keeping only the smallest value for each pixel. In this way, layers are defined as single-pixel-thick layered regions with an increasing index (*Ln*), starting from original bounding surface. The defined regions representing the grading of the horizontal laminaset, as illustrated in Figure 5.2. The decision needs to be made to repeat the process *Ln_h_max* times (thus $Ln \in [1, Ln\_h\_max]$ for a horizontal laminaset) to create a stack thickness larger than largest distance between the segmented inter-LBSs (lamina/laminaset thickness), to ensure the graded layers reach the neighbouring bounding surface. The grading will end at the next extracted bounding surface, if the distance between two original bounding surfaces is less than the defined stack thickness. For the horizontal part, the procedure is performed on whole 3D volume, in which the xy and xz slices would have the same result as illustrated, because a horizontal planar feature has same geometry in both directions.

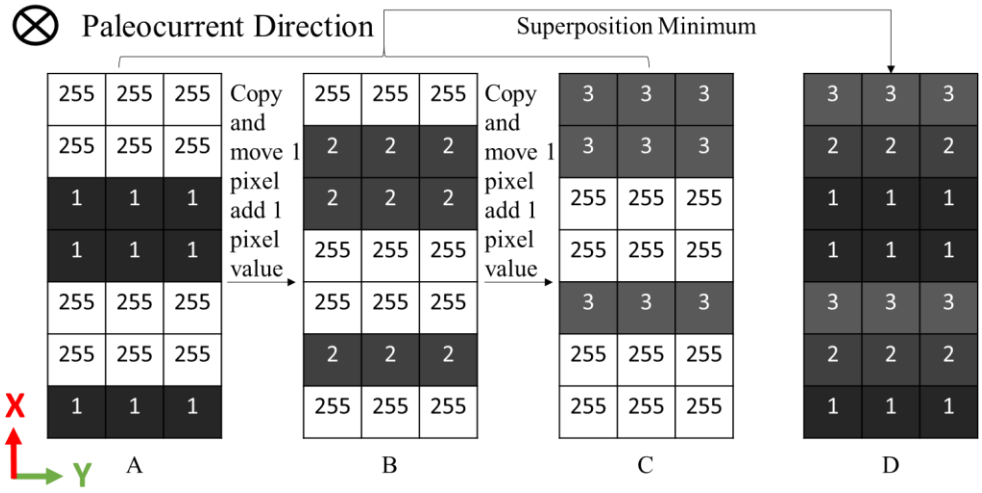

Figure 5.4 Illustration of defining layered regions for horizontal planar laminaset based on binary extracted inter-LBS: each grid represents one pixel of an MXRT image with size equal to a layer thickness: A) one 2D slice of the segmented binary inter-LBS. Bounding surface are assigned with pixel value "1" of black colour and "255" of white colour for matrix; B) Copy and move A upward one pixel and add pixel value 1 for all pixels (255 is maximum therefore do not change); C) repeat copy-move-add procedure on B; D) superposition of A-C and keep minimum value for each pixel.

For a curved laminaset, considering its different geometry in the directions perpendicular and parallel to the paleocurrent, the definition of grading could be illustrated by one xz slice (parallel to the paleocurrent direction), as in Figure 5.5(A). The procedure first defines the inclined intra-LBS inverse to the paleocurrent direction with toe side on the higher end of the Z axes. Starting from the xy slice (one column on the xz slice) with slice number *ZS* at end of Z axis (*ZS =Z_max)*; each xy slice *Nz* away from *ZS* with slice number *ZS-Nz* is copied to perform this procedure: 1) add pixel value "*Ln_h_max*" to existing bounding surface index (*Ln*) value to define intra-LBS (to differ from the horizontal part index with Ln ∈ [1, *Ln_h_max*]) and 2) move the xy slice *Nx* pixels along the vertical X+ direction, to plot an intra-LBS inclined to the inter-LBS. *Nx* is a function of *Nz*. In this case *Nx = tan (angle)*Nz*, which requires a reduction to a lower integer. So taking angle=*26.6*° as an example, each xy slice is copied with an added index value and moved one more pixel in the X+ direction every two slices on the Z- direction. Thus an intra-LBS intersecting at 26.6° with a segmented inter-LBS can be plotted. By performing the intra-LBS plotting process for *Nd* slices, intra-LBSs will have a distance in between them along the z-axis of *Nd* *resolution, and thickness at x-axis of *Nd**resolution*tan (*angle*), which is equal to the defined lamina thickness (measured maximum curved lamina thickness from T2). The intra-LBS defining procedure is therefore performed repeatedly for each *Nd* number of slices (thus *Nz ∈ [1, Nd])* starting with xy slices, with slice number *ZS=Z_max-n* Nd (n ∈ [0, Z_max/ Nd])*. All copy-added value-moved xy slices are superposed with the minimum kept, thus a set of parallel intra-LBS can be plotted. Number "*Ln_h_max*+1" is therefore defined as the index (*Ln*) of intra-LBS, as shown in Figure 5.5(B). The same layer stacking procedure is applied in the vertical direction as that for the horizontal planar part to define conceptual layers parallel to the intersection of the intra-LBS (voxel value = "*Ln_h_max*+1") with the inter-LBS (voxel value = "1" but treated as "*Ln_h_max*+1" during calculation). For the curved laminaset layered regions, the index (*Ln*) starts from "*Ln_h_max*+2" and repeats *Ln_c_max*=2**Nd*tan(angle)* to create a stack layer thickness twice that of the curved lamina to ensure covering the space between defined intra-LBS. Therefore, the curved laminaset has an index *Ln* ∈ [*Ln_h_max*+1, *Ln_h_max*+ *Ln_c_max*] to differentiate it from the horizontal planar laminaset. Figure 5.5(A-C) illustrates an example of the proposed procedure with angle= 26.6°, Ln_h_max=30 and Ln_c_max=50.

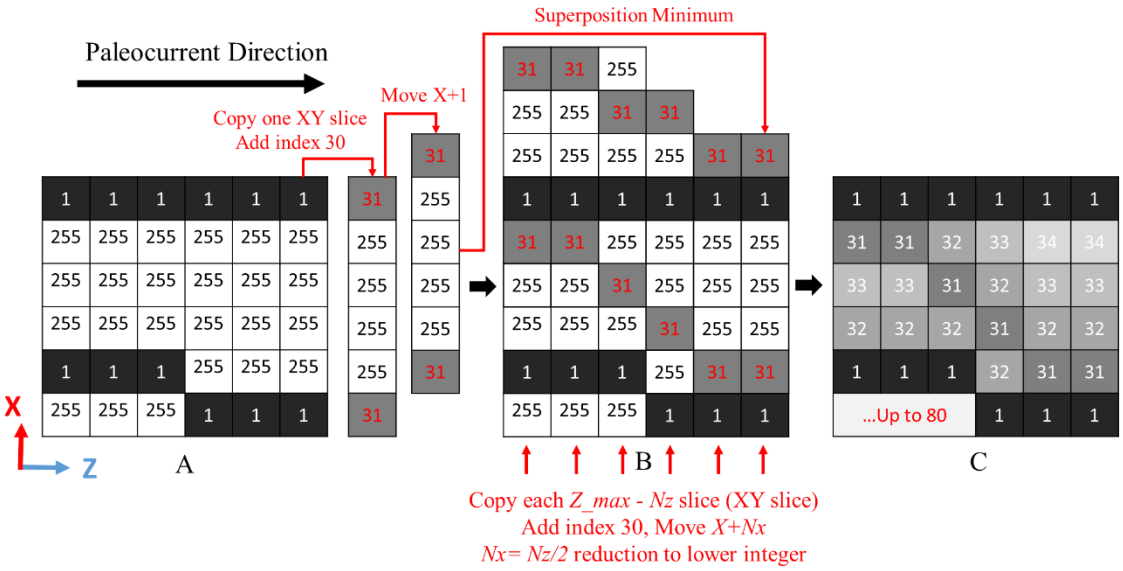

Figure 5.5 Illustration defining layered regions for a curved laminaset based on binary extracted inter-LBSs: each grid represents one pixel of MXRT image with size equal to a layer thickness: (A) one 2D slice of the segmented binary inter-LBS at xz parallel to paleocurrent direction. Bounding surfaces are assigned with pixel value "1" of black colour and "255" of white colour for matrix; (B) Copy each ZS - Nz slice (ZS=Z_max) (xy slice thus one column of A), add index Ln_h_max=30, Move Nx on X+ direction, Nx= Nz/2, reduction to lower integer and superposition with minimum value kept for each pixel; (C) repeat horizontal layer generation procedure in Figure 5.4 on (B).

Note that, for a curved lamina, circumstances would occur when the laminaset thickness between a segmented inter-LBS is larger than the defined stack thickness; a set of stacked grading layers over the intersected intra-LBS and intra-LBS would still not reach the next segmented inter-LBS, and therefore leave blank areas/ volumes. An abnormally large distance between inter-LBSs is potentially a result of bioturbation which has penetrated the bounding surface and disturbed grading. The remaining pixels that have not been assigned an index (*Ln*) would, therefore, be assigned to a specific index (*Ln_bio*) to be treated specially during grain-pore reconstruction to reproduce the bioturbation character as measured. Table 5.2 summarises key parameters to be determined in the implementation of the proposed algorithm, along with their physical implications for the hierarchical structure. Figure 5.6 illustrates an example to perform the proposed procedure on a segmented bounding surface from MXRT of L1 by assuming pixel size equal to layer thickness, with angle= 26.6°, Ln_h_max=30, Nd=50, Ln_c_max=50 and Ln_bio=100. A set of macro scripts has been written based on FIJI (www.Fiji.sc (Schindelin et al., 2012)) to automatically manipulate the segmented inter-LBS image to achieve the discussed definition of the layered region. The defined regions could then be

taken as regional index map constraints to insert into various pore-space structures according to the measured grading character.

Table 5-2 Summary of key parameters to be determined in implementing the algorithm and their physical implication of hierarchical structures

Key Parameters	Ln_h_max	Angle	Nd	Ln_c_max	Ln_bio
Physical implication of hierarchical structures	Ln_h_max *resolution equal horizontal grading layer stack thickness	Intersection angle of intra- to inter-LBS	Nd*resolution equal lamina thickness perpendicular to paleocurrent direction	Ln_c_max *resolution equal curved grading layer stack thickness	Specific index assigned representing occurrence of bioturbation

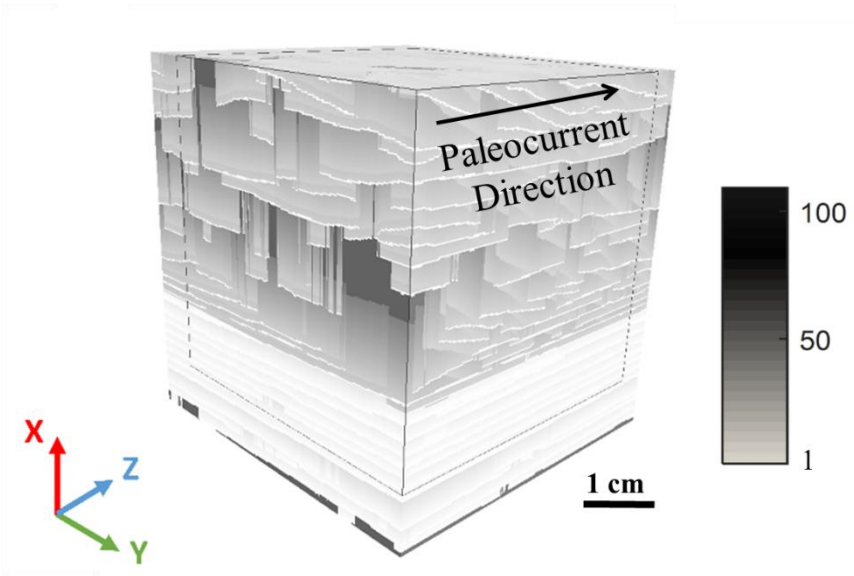

Figure 5.6 3D illustration of reconstructed layered regions respecting grading of L1, assuming voxel size has a thickness equal to the layer thickness: a colour map from white to black for Ln ϵ [1,100].

5.3 Step 2: Decomposing the domain for parallel simulations

It is estimated that reconstructing a full 3D pore-scale model, with the defined index map as a regional constraint, for a sample of over a 5x5x5 cm^3 cube would take more than 50000 hours of CPU time on a PC with a Xeon(R) CPU-E5-1603 at 2.8GHz. To make the simulation faster, a domain decomposition in an ordering scheme was applied to partition the defined index map domain into subdomains falling into four categories (see the next section), and then MPS simulations were carried out on the subdomains independently, in parallel. In this work, 80 subdomains were simulated in parallel on 40

stand-alone computers, each processing 2 simulations a time, which reduces the reconstruction time down to about 20 days.

To enable parallel simulation for decomposed subdomains, the key idea is that the subdomains are not connected with each other so they can be simulated independently (thus in parallel). The reason behind this is that connected subdomains need to be simulated in sequence to allow the boundary of the simulated volume to be considered as hard data of the next neighbouring subdomain (by extending the simulation domain) to keep connectivity. Such separated subdomains can be achieved by decomposing the full domain into four categories of, where the subdomains of each category are not spatially connected but the four categories' subdomains together would connect full domain. Figure 5.7(A-B) illustrates part of the domain partitioned into A, B, C, and D, four ordering categories of subdomains with representative volumes of grain-pore textures, which are not connected with each other within the same category but connected by combining different categories. Unconnected subdomains from first order category (e.g. eight cuboids A category subdomains) could be simulated independently, and thus in parallel. Connected neighbouring sub-grids from the second order category are simulated by extending the domain to take the pre-simulated neighbouring subdomains as hard data (e.g. 16 cuboid B category sub-grids could be simulated with the extended domain to take neighbouring pre-simulated A subdomains into account as hard data). In this way, each ordering category of subdomains is simulated sequentially, depending on each other, i.e. D depending on C which depends on B which depends on A, so that connectivity between subdomains is preserved. One may note the thinking behind four categories rather than two is to ensure neighbouring categories sub-domains at each edge including the corner of the A category are conditioned. The design of the dimension of these subdomains is based on simulation time. Each sub-grid should be large enough to include as much representative volume as possible but be small enough to make sure the simulation time is sensible. Within each subdomain, a set of previously defined layered regional index maps will be included, as shown in Figure 5.7(C). 3D stochastic stationary reconstruction will be applied to each layered region based on a given training image, but will include non-stationary variation according to the index (*Ln*) across layers to reflect grading character (Figure 5.7(C-D)).

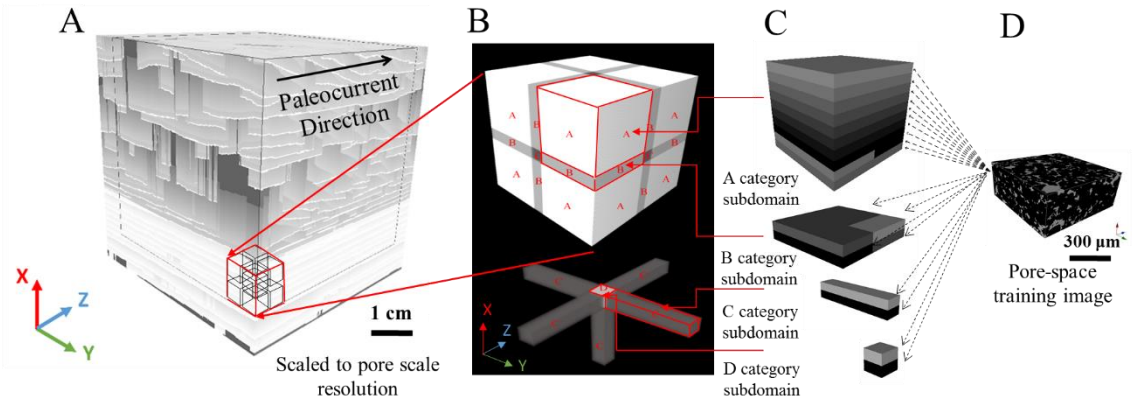

Figure 5.7 Domain partitioning in an ordering scheme for multiscale pore-space reconstruction: A) Full domain with layered region index map defined as regional index map constraint; B) illustration of an ordering partition into four ordering categories, A-B-C-D, here gives an example of space including eight cuboids A level, with 16 cuboid B level, six cuboids C level and one cuboid D level subdomains; C) illustration of one subdomain of each level containing layered region; D) illustration of stochastic regional reconstruction of pore-space into each region.

5.4 Step 3: Full 3D stochastic pore-space reconstruction

Assuming that grading can be represented by gradual variation of grain-pore size and orientation across layered regional index maps, pore-space reconstruction needs to respect the defined layered regional index maps as a constraint and include non-stationary variation based on stationary μ-XRT data as training. Based on the basic mechanism of MPS introduced in Chapter 2 and with emphasis on those requirements, the key features to reconstruct a layered grading system are identifying the training image, assigning scaling and rotation factors based on the index map and with the appropriate configuration on the template size. The configuration is summarised as three steps in Figure 5.8 and is explained as follows:

1) Selection of training image: It has been suggested previously that only one partial subvolume of each of the S1 and S4 grain-pore images is applied as a training image for all defined regional index maps, for curved and horizontal planar laminasets respectively. To have a representative stationary grain-pore space training example as the basis of grading, the finest layer of grain-pore space, which is expected to have no preferred orientation, is preferred. Figure 5.8(A) illustrates a sub-volume cropped from S1 and S4 close to one measured "valley" layer from log measurements to represent the finest bounding surface layer, which is assumed to have stationary homogeneous grain-pore structure. The representativeness of the selected sub-volume needs to be quantitatively verified. To avoid inclined grains, the sub-volume from S1 is taken from one horizontal bounding surface layer rather than an inclined curved. Both sub-volumes only crop the

centre volume of the identified horizontal layer, to minimise the potential intersection with another bounding surface potentially close to the edge area, based on geometrical observation from the segmented heavy mineral image (Figure 3.19 and Figure 3.20) that highlights the bounding surface. A training template size could be designed to cover grain and pore size as measured.

2) Configuring the regional non-stationary parameter: With the training image, the scaling and rotation factor within each regional index map reflecting the measured grading character need to be configured for MPS reconstruction. The configuration is correlated to the defined region index, *Ln*, directly and derived differently for horizontal laminasets (1<*Ln*<= *Ln_h_max*), curved laminasets (*Ln_h_max* <*Ln*<= *Ln_h_max*+ *Ln_c_max*) and bioturbation (*Ln* = *Ln_bio*). Scaling is achieved by the affinity function in MPS simulation, which is determined by a scaling factor on each axis. The scaling factor for each layered region, $SF_{Ln\,1D}$, can be estimated as the equation given in the centre red box of Figure 5.8(B). The calculation is based on the previously measured grading gradient, $SF_{rate\,1D}$, (reflecting the rate of increasing of grain size over the finest base bounding surface layer) and grain orientation from μ-XRT, measured as summarised in Table 3.4. In the equation given in Figure 5.8(B), *l* is related differently to *Ln* to distinguish the horizontal and curved laminaset. Regions with *Ln*=*Ln_bio* are treated specially according to measurements in terms of grain size and orientation representing bioturbation.

3) The discussed reconstruction process is performed for each defined layered regional index map sequentially, following the sequence of increasing index *Ln*. The reconstruction also extends each index-mapped region in each direction, equal to half of the template diameter, to take grain-pore structures reconstructed within the neighbouring index-mapped region as hard data. As a result, the grain-pore space is transitioned naturally at the boundary between index-mapped regions; therefore, connectivity is preserved.

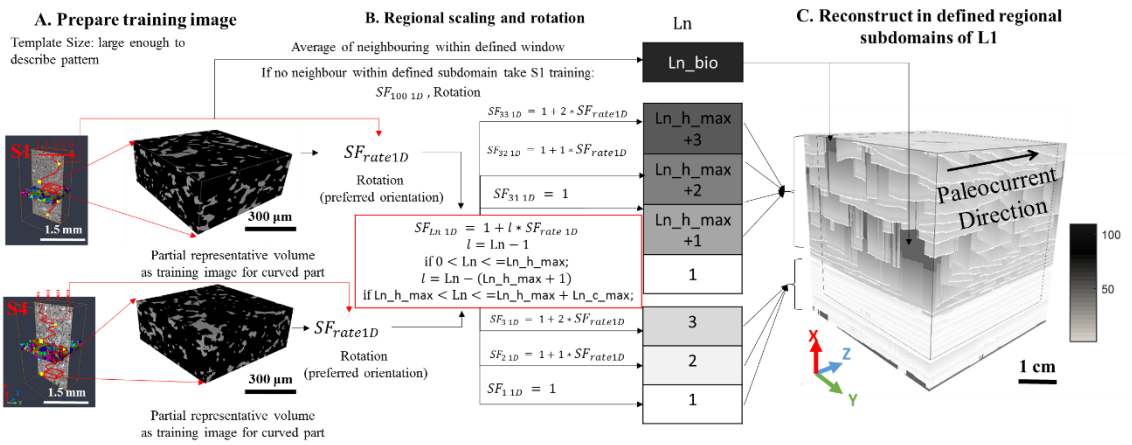

Figure 5.8 MPS setting and inputs for defined index maps of L1

A set of python scripts has been written to perform domain partition and MPS reconstruction automatically.

5.5 Applying three-step procedure on L1

This section summarises the configuration parameters and demonstrates the process based on the decisions made which are specific to the sample of study, for each of three proposed steps.

5.5.1 Defining inter- and intra-laminaset index maps on L1

Configuration parameters which are determined to define the hierarchical inter- and intra-laminaset structures are summarised in Table 5.3. The angle is decided as 26.6° to define a curved intra-LBS on a discrete pixel image that falls in the measured range between 20-30° from the surface, as shown in Figure 5.1(C) and Tp on the face parallel to the paleocurrent as Figure 5.1(D). A conceptual layer thickness of 200um (the same as that used during measurements in SEM and µ-XRT across Figure 5.1(E-H) is applied because 1) each layer represents the grain stack over the previous layer. The thickness of the layer, therefore, needs to contain the largest observed grain size (100-200 µm in diameter as measured across µ-XRT and BSEM) to represent a layer of grain safely and 2) 200um is well below the thinnest lamina thickness of 1mm, as measured in BSEM characterisation in section 4.3.2, so gives a layered region fine enough to reflect grading.

No additional intra-LBS has been defined for the horizontal laminaset. Therefore, the layered grading stack thickness is defined to cover a distance twice that of the measured maximum laminaset thickness (thus, 6mm over 0.5-3mm measured for the horizontal part). For the curved laminaset, a set of parallel intra-LBSs are plotted 10mm apart along

the paleocurrent direction and thus 5mm (tan (26.6°)*10mm) lamina thickness perpendicular to the paleocurrent direction to cover what been measured in T2 in section 3.2.2. Based on the segmented inter- and defined intra- LBS, the maximum grading thickness of 10mm in the vertical direction has been defined as twice the 5mm measured curved lamina thickness perpendicular to the paleocurrent direction, to ensure spaces between bounding surfaces are filled.

To simplify the algorithm's implementation, the decision has been made to coarsen the original segmented MXRT with volume of 562x550x525 at 100x100x100 $um^3/pixel^3$ resolution to volume of 293x287x274 at 200x200x200 $um^3/pixel^3$ resolution. Thus one pixel thick has the physical size of 200um, which is consistent with the anticipated thickness of the conceptual layer. Based on the coarsened resolution, the corresponding algorithm index (*Ln*) range for horizontal and curved laminasets related to each physical hierarchical structure are summarised in the last two columns in Table 5.3. The proposed procedure is performed on the central 281x275x262 volume cropped from the discussed coarsened 293x287x274 volume at 200x200x200 $um^3/pixel^3$. The decision has been made that the separation between applications of the horizontal and curved method is 1.9 cm on the planar yz surface from the bottom of the X axis, rather than the first continuous curved surface. This is because previous observation (from Tp) found the changes from horizontal to curved laminasets are transitional, as potentially inclined intra-laminaset surfaces are observed between some horizontal laminasets close to curved laminasets. Figure 5.9 and Figure 5.10 show two 2D cross-section views of the sample volume containing segmented inter-LBS images from the MXRT in section 4.2 and the same slice after the index maps defined are shown on the right. Figure 5.9 shows a cross-section perpendicular to the paleocurrent direction and Figure 5.10 a cross-section parallel to paleocurrent direction. The defined layered regions are labelled in grey, where the colour varies from dark to bright as the region's index (*Ln*) number increases. Therefore, the segmented inter-LBS with index number "1" has the darkest colour (black), while the defined intra-LBS with index number "31" has a dark grey colour. Defined layers further away from the corresponding starting bounding surface have a brighter colour. Empty regions are considered as bioturbation or erosion and are assigned as "100" and presented in white.

Table 5-3 Summary of decisions on hierarchical structure and corresponding symbol in algorithm implementation

Hierarchical Structure of lamina and grading	Physical scale	Symbol in algorithm	Index Number
Angle	26.6° (defined)	N/A	
Layer thickness	200um (defined)		
Horizontal lamina thickness between inter- or intra-LBS	0.5-3mm (observed)		
Horizontal grading layer stack thickness	6mm (defined)	Ln_h_max	30
Curved lamina thickness between intra-LBS	5mm (defined)	Nd	25
Curved grading layer stack thickness	10mm (defined)	Ln_c_max	50
Bioturbation and erosion "True hole"	N/A	Ln_bio	100

To analyse the geometry of the defined index map for hierarchical structures, Figure 5.9(A) gives one 2D slice of binary MXRT perpendicular to the paleocurrent direction. Figure 5.9(B-C) gives a zoomed-in view of Figure 5.9(A) at curved and horizontal planar laminasets respectively. The defined layered region index map is presented in Figure 5.9(D-F) correspondingly, for comparison. It can be seen from Figure 5.9(D) that intra-LBSs are defined parallel to inter-LBSs perpendicular to the paleocurrent xy surfaces. Defined layers with increasing index (*Ln*) (thus increasing brightness) are parallel to the bounding surfaces for both curved and horizontal planar laminasets, as shown in Figure 5.9(D-E) at the xy surface. One may note that the remaining unconnected gap in Figure 5.9(D) has created a "hole" and created a non-continuous distribution of region index numbers. It may create a channel having different fluid flow performance and reflect the randomly occurring bioturbation observed in the previous analysis.

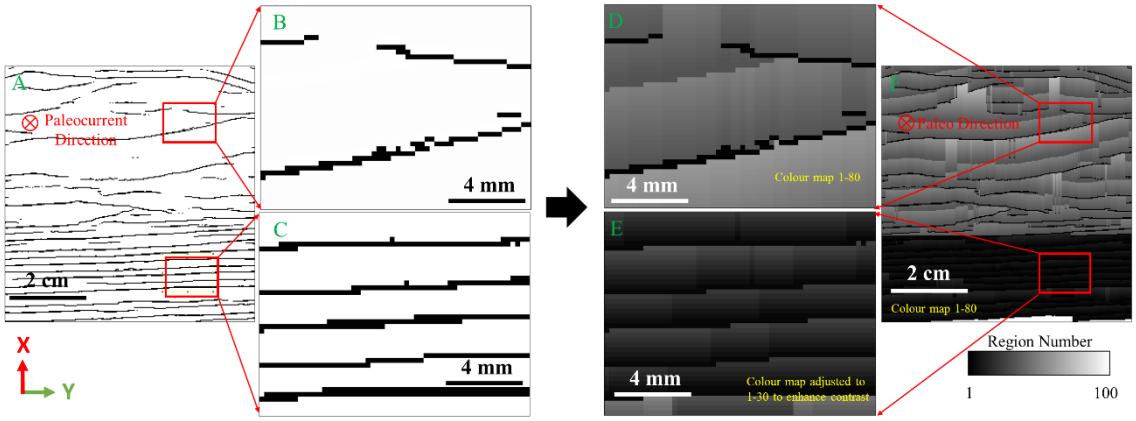

Figure 5.9 Illustrating defined layered regions (200um thick) perpendicular to the paleocurrent direction based on: A) one 2D slice (275x281 pixels^2 at 200um/pixel^2 for A and F) binary extracted inter-LBS which is assigned with pixel value "1" of black colour and "0" of white colour for matrix; B) zoomed-in view (58x42 pixels^2 at 200um/pixel^2 for B-E) of bounding surface in curved laminaset; C) zoomed-in view of bounding surface at horizontal planar laminaset; D) zoomed-in view of defined layered index map of B, colour map adjusted to the range of overall assigned regions' indexes (1-80); E) zoomed-in view of defined layered regions of C; colour map adjusted to the range of horizontal planar laminasets' assigned regions' indexes (1-30), for better contrast to illustrate the layered index map ; F) defined layered index map of A.

Figure 5.10(A) gives one 2D slice of binary MXRT parallel to the paleocurrent direction xz face. As in Figure 5.9, two zoomed-in views for the curved and horizontal planar laminaset respectively are given in Figure 5.10(B-C), together with their corresponding defined layer index map, given in Figure 5.10(D-F). Figure 5.10(D) shows intra-LBS, as dark grey colour, has been plotted with the intersecting angle and lamina thickness agreed with the designed configuration. Layers with increasing brightness parallel to the inter- and intra-LBS are defined for both the curved and horizontal planar laminaset. Figure 5.10(E) is similar to Figure 5.9(E) because the horizontal planar layers have the same features in both directions. With maximum 50 layer stacks (10mm) defined on top of the curved bounding surface, circumstances could occur where the added layers still do not reach the next bounding surface, like the empty white regions in the bottom-left corner of Figure 5.10(D) and Figure 5.10(F), as a reflection of bioturbation.

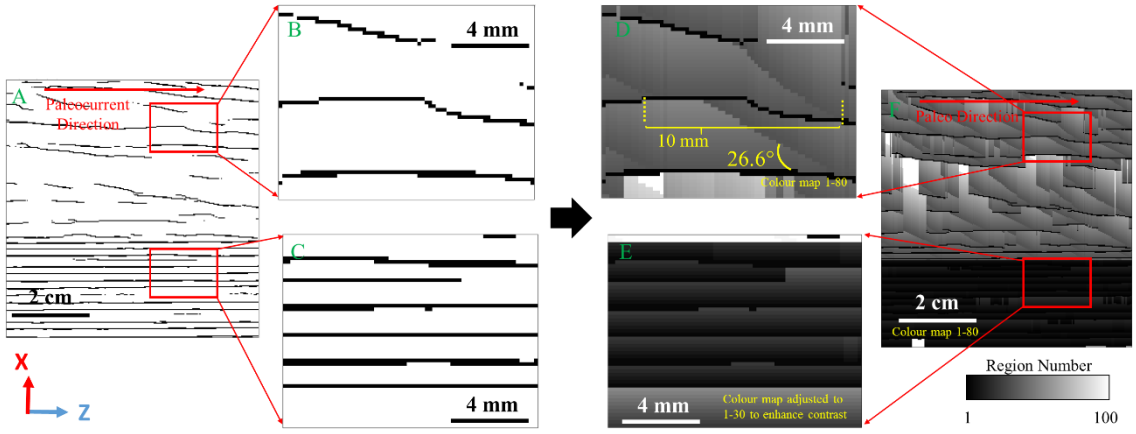

Figure 5.10 Illustrating defined layered regions (200um thick) parallel tp the paleocurrent direction based on: A) one 2D slice (262x281 pixels^2 at 200um/pixel^2 for A and F) a slice of a binary extracted inter-LBS which is assigned with pixel value "1" of black colour and "0" of white colour for matrix; B) zoomed-in view (70x53 pixels^2 at 200um/pixel^2 for B-E) of bounding surface at curved laminaset; C) zoomed-in view of bounding surface at horizontal planar laminaset; D) zoomed-in view of defined layered regions of B; colour map adjusted to the range of overall assigned regions' numbers (1-80); E) zoomed-in view of defined layered regions of C; colour map adjusted to the range of horizontal planar laminaset's assigned region numbers (1-30), for better contrast to illustrate layered regions; F) defined layered regions of A.

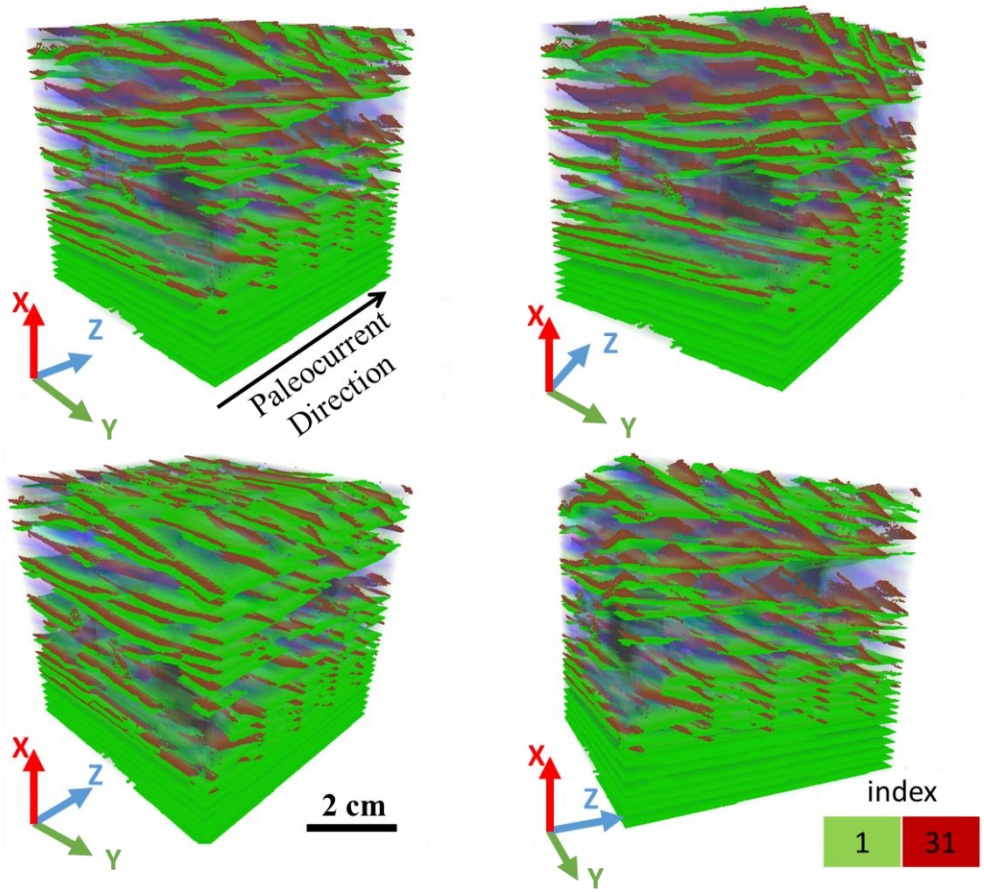

Figure 5.11 3D views of defined intra-LBS (with index "31" rendered in red) over segmented inter-LBS (with index "1" rendered in green).

Figure 5.11 plots a 3D view of intra-LBS (with index "31" rendered in red) defined over a segmented inter-LBS (with index "1" rendered in green) from four different directions. The 3D internal structure of the defined intra-LBS follows the curved surface of the segmented inter-LBS with the defined intersecting angle and distance in between them. Figure 5.12(A-D) plots a 3D view of the defined full index map of the bounding surface and conceptual layers, with the colour map given in Figure 5.12(F), which provide a clearer illustration of the sets of layers defined parallel to three orders of bounding surfaces. In Figure 5.12(B) the top view illustrates the nature of the lunar shaped cross-section of lamina grading in a parallel sedimentary cross-section which is consistent with curved crest trough cross-lamina geometry given from the literature in Chapter 2. Apart from the successfully defined grading index maps agreeing with both the discussed and observed nature of the features, Figure 5.12(C) highlights two significant abnormal observations: 1) an unconnected surface which was supposed to be solved by the supervised classification method developed in Chapter 4 and 2) a large empty volume assigned with index (Ln) "100" and displayed in black. The two are explained in Figure 5.12(E) by illustrating the same location of the previously analysed labelled connected bounding surface. Figure 5.12(E) highlights the zig-zag edge of the connected bounding surface in 3D which is responsible for the 2D presentation of the connected bounding surface. Figure 5.12(E) shows that although the dis-connectivity has been solved by supervised classification, it may leave some imperfect artefact at the edge of the 3D surface and leads to the unconnected presentation in 2D. However, such a circumstance is only expected to occur in 2D slices at the sample surface but not in the internal cross-sections in 3D. Figure 5.12(E) also highlights bioturbation, as previously analysed, which is consistent with the location where special index (*Ln*) "100" was assigned, that anticipated special treatment for the presence of bioturbation.

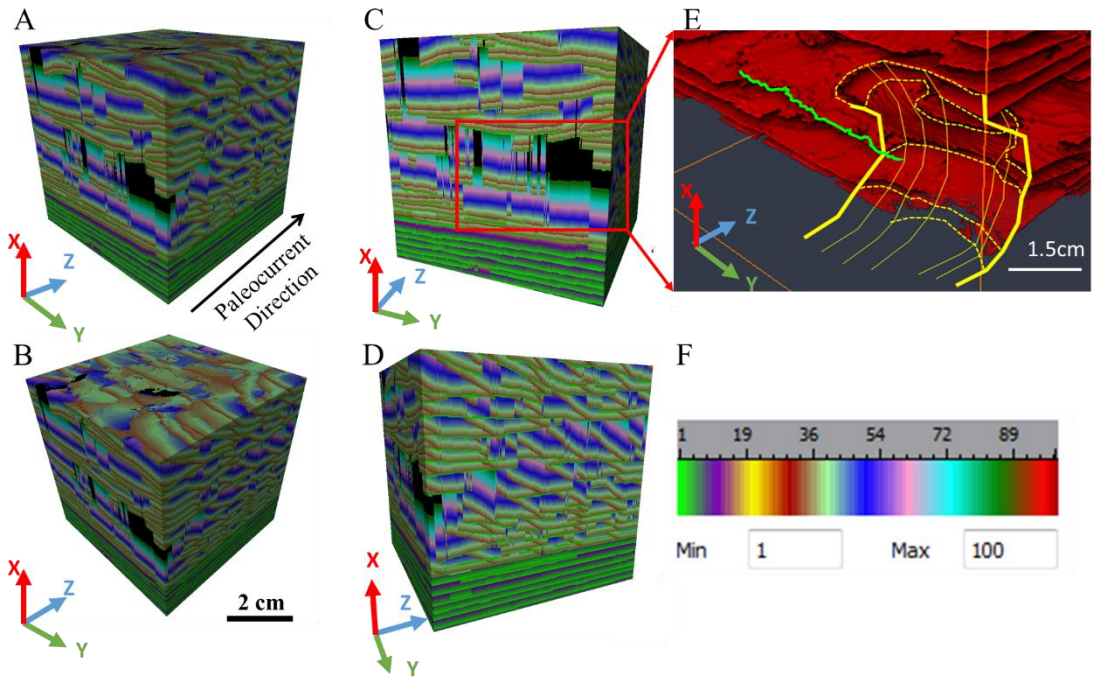

Figure 5.12 (A-D) 3D illustration of defined full index maps representing three orders of bounding surface and conceptual layers within laminae by a colour map, as in (F); (E) illustrating previously labelled connected bounding surface image of red box highlighted volume of C, with identified bioturbation highlighted in yellow and zig-zag edge on one bounding surface highlighted in green.

Figure 5.13 gives the final plots in the grey-scale colour map of the defined layered regions' index map, reflecting the grading of L1, including both the curved and horizontal planar system. The colour map is inverse, as discussed in the methodology with white for "1" and black for "100", for the purpose of better illustration. Based on Figure 5.13, the definition successfully: 1) defined missing intra-LBS with inclined character which were the same as measured in SEM and preliminary L1 observation; 2) defined conceptual layers within laminae with layer thickness that respected measured grain size; 3) the lamina thickness based on the log plot measurement of SEM and grading stack thickness covered most lamina thicknesses. A different range of index (*Ln*) numbers were assigned to horizontal planar (1-30) and curved (31-80) laminasets; therefore, different pore-space characters could be assigned respecting the different nature in either bedform. Table 5.4 summarised key parameters used for layered region definition to be referred for later pore-space reconstruction. For grain-pore reconstruction in the next step, L1 needs to have the same resolution as the grain-pore space to be reconstructed. 4x4x4 um^3/voxel is decided and the solid black line boxed 238x238x238 volume at 200 4x4x4 um^3/voxel of Figure 5.13 are scaled up 50 times to 11900x11900x11900 at 4 μm^3/ voxel.

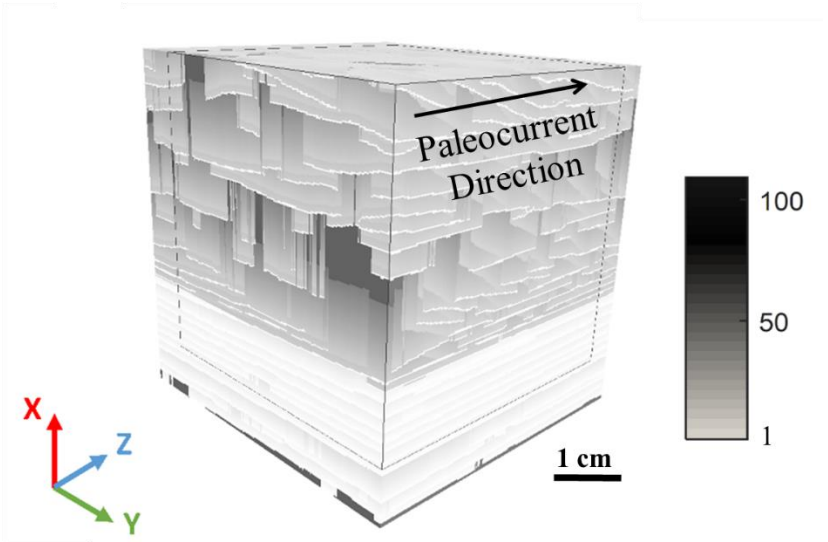

Figure 5.13 3D illustrations of defined layered regions respecting grading of L1, with dimension 281x275x262 at 200x200x200 um^3/voxel resolution; a colour map from white to black for region numbers between 1-100. Black solid line boxed 238x238x238 volume at 200 4x4x4 um^3/voxel is scaled up 50 times to 11900x11900x11900 at 4x4x4 um3/ Voxel for grain-pore reconstruction.

Table 5-4 Key parameters of defined layered region model

	Layer thickness	Lamina thickness	Intersect angle	Layered region number
Horizontal Planar	200 µm	1-3 mm (max 6mm)	0°	1-30
Curved	200 µm	5 mm (perpendicular to paleocurrent direction) between 3rd surface but 10mm if not reaching neighbour surface	26.6°	31-80 (100 for bioturbation)

5.5.2 Decomposing the domain for parallel simulations on L1

The dimension and resolution for ordering the partition and multiscale reconstruction applied for decomposition are labelled in Figure 5.14. The specific dimension and numbers of sub-grids for each ordering category's subdomains are summarised in Table 5.5. A 500x500x500 (4 µm resolution) cubic sub-grid takes an average of 2.5 CPU hrs for MPS regional reconstruction and is determined to be suitable for A category subdomains. The neighbouring volumes between A subdomains are designed to have thickness of 100 pixels, thus giving B of dimension of 500x500x100 (or 500x100x500 or 100x500x500), C of 100x100x500 (or 100x500x100 or 500x100x100) and D of 100x100x100 $voxels^3$ (details see Table 5.5). The physical thickness of each category subdomain is thicker than 400 µm, thus containing at least two previously defined layers, and therefore containing a representative volume of grain-pore textures. Therefore, the 11900x11900x11900 at 4 μm^3/ voxel layered region L1 could be partitioned by the

20x20x20 A category of grids, with corresponding B, C and D neighbours (for details see Table 5.5). The full 3D pore-space model of size 11900x11900x11900 voxels^3 has been reconstructed in parallel processing, with 80 simulations performed at a time on 40 stand-alone computers, by a 20-day simulation.

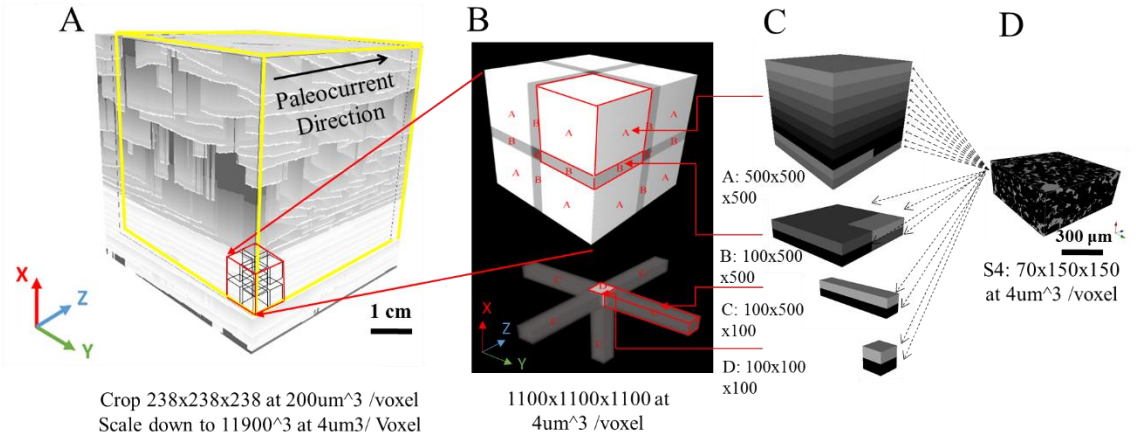

Figure 5.14 Ordering domain partitioning strategy, together with MPS reconstruction: A) yellow box highlighted 238x238x238 at 200 µm^3/ voxel of layered region index map defined for L1, scaled 50 times down to 11900x11900x11900 at 4 µm^3/ voxel to meet pore-space resolution to be reconstructed; B) illustration of a 1100x1100x1100 voxel of A partitioned into four ordered categories, A-B-C-D: here gives an example of space including 8 cuboids A level, with 16-cuboid B level, 6-cuboid C level and 1 cuboid D level subdomains; C) illustrating one subdomain of each level containing layered regions, each at 50 voxel thick (200um); D) illustrating MPS regional reconstruction of pore-space into each region.

Table 5-5 Details of four ordered grids for final simulation

Ordered categories	A	B	C	D
Dimension	500x500x500	500x500x100/ 500x100x500/ 100x500x500	100x100x500/ 100x500x100/ 500x100x100	100x100x100
Number of grids	20x20x20	3x(19x20x20)	3x(19x19x20)	19x19x19
Resolution	4um			

5.5.3 Full 3D stochastic pore-space reconstruction on L1

The configuration of stochastic pore-space reconstruction is summarised in Figure 5.15 and explained as follows:

1) S1 and S4 are scaled into the same resolution of 4x4x4 um^3/voxel for reconstruction of a grain-pore space model with the same resolution. Figure 5.15(A) illustrates a sub-volume of 150x150x70 voxels cropped from S1 and S4 in the central part close to one measured "valley" layer from log measurements, representing the finest bounding surface layer. The cropped volume is representative by including more than 200 grains, as measured after excluding small distraction particles with the same method as used in

previous μ-XRT grain-pore measurements (see Table 5.6). The measurements in Table 5.6 also confirmed quantitatively that the cropped volume represented a fine layer by having similar average size and porosities to those measured for the full sample in Table 3.4 of Chapter 3. The orientation measured for cropped volume is close to full volume measurements, proving there is no preferred orientation. A training template size of 30 voxels in each direction has been designed with a volume of 120x120x120 um^3 to cover grain and pore size, as measured.

Table 5-6 Grain-pore measurements performed on cropped training image (150x150x70) from S1 and S4

Sample	Measurement	Count	Average Size in volume (mm^3)	%Area	Long axis (3D) μm	Short axis (3D) μm	Angle	Shape_VA3d (3D)
S1 (4.30μ m^3)	Grain	207	4.50E-04	74.4	145.2	71.4	67.5	4.8
	Pore	402	4.52E-05	14.5	58.8	28.2	N/A	N/A
S4 (3.07μ m^3)	Grain	216	1.62E-04	77.0	99.6	49.3	64.9	4.2
	Pore	872	7.41E-06	14.2	22.7	12.1	N/A	N/A

2) With the training image, the scaling and rotation factor within each regional index map, reflecting the measured grading character, need to be configured. The configuration is correlated to the defined region number, Ln, directly and derived differently for horizontal laminasets (1<Ln<=30), curved laminasets (30<*Ln*<=80) and bioturbation (*Ln* = 100). For the horizontal part, with the cropped part from S4 taken as the training image, $SF_{rate\ 1D} = 0.02$ is decided, which is within the range of smaller measurements of 0.014 from T2 to 0.023 as measured from the full volume of S4. Based on the given equation, the inter-LBS layer would have no scaling with $SF_{1\ 1D} = 1$ and the following layers have scaling factors which increase by 0.02 over the previous layer each time. No rotation is applied for layers from the horizontal laminaset. For the curved part, with the cropped part from S1 taken as the training image, $SF_{rate\ 1D} = 0.021$ is applied, which is the same as that measured from the full volume of S1, because the average of the measured curved grading gradient (of curve1, cross1 and cross2) from BSEM of T2 is 0.025, thus roughly agreeing with the S1 measurement. With the given equation, the layer (Ln=31) as defined for intra-LBS has been treated same as the segmented inter-LBS (Ln=1), in that no scaling is performed. The following layers start from Ln=32: each layer has a scaling factor increase of 0.021 over the previous layer. Rotation of 30^o is applied around y-axis for

layers with Ln between 31-80, to represent the measured preferred orientation. The rotated angle, 30^{o}, is slightly larger but reasonably close to the inclined angle of 26.6^{o}. The explicit scaling factors assigned for each region can be referred to in Appendix D.1 .

Regions with *Ln*=100 are treated specially, to represent bioturbation. Taking into account that bioturbations are quantitatively measured to have smaller grain-pore size on the Tp SEM image than in the neighbouring area, a scaling factor the same as for *Ln*=30 is applied to represent a smaller grain size. Although *Ln*=30 did not represent smallest grain size in defined index map, they are still smaller than the neighbouring index maps, because the bioturbation regions defined in the index map only occur after *Ln*=80. Given that bioturbation under such definition only occurs in curved laminasets, a rotation of 30 ^{o} is also applied. The edging areas of bioturbation index maps are also treated specially to take into account the transitional variation: if a bioturbation index map has neighbouring index maps with $Ln \neq 100$ within each defined 500 voxels^3 decomposed subdomain, its scaling factor would be the average of the other index maps within the 500 voxels^3 window.

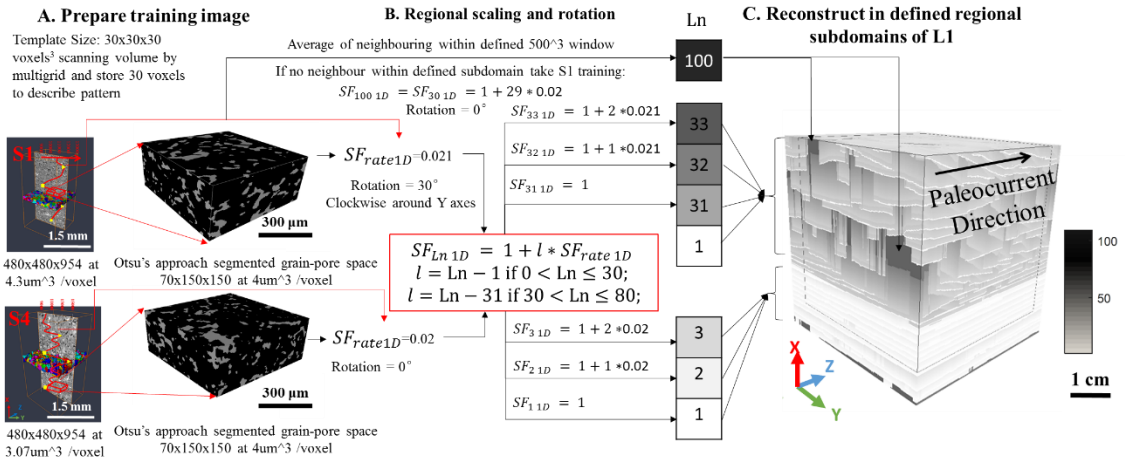

Figure 5.15 MPS setting and inputs for defined index maps of L1

5.6 Verification of results

The reconstructed pore-space model (11900x11900x11900 voxels^3) is hard to visualise fully in 3D. To examine the effectiveness of the proposed regional index map based MPS and ordering of the domain partition scheme, this section applies a set of visual verifications, including 1) a partial illustration of the result, to visually examine the technical efficiency of the reconstructed connectivity between the regional index map and

partitioned subdomains; 2) producing a 2D surface illustration of the reconstructed grain-pore space and correlating it with the defined regional index map on L1 and comparing it with the registered T2, to visually examine its effectiveness in revealing grading features associated with laminae and laminasets; 3) to further enhance visualization of (2), a synthesised set of grading factors with larger grain size and increasing gradient are applied to a small sub-set of sub-grids (the sub-grids are from the surface of L1, with 500 voxels thickness in the Z direction, including a set of A, B and C category partitioned subdomains) to generate larger grain-pore contrast to correlate with lamina and laminaset structures; 4) one partial block (500x500x500 voxel^3) containing a cross of two curved bounding surfaces is selected to illustrated its correlation with reconstructed grain-pore space variation, also based on a synthetic larger grading gradient; 5) with the 3D pore-space model fully reconstructed over the 5x5x5 cm^3 space (with the true measured grading gradient) the model size is over 10000 voxels in each of the three dimensions and hard to verified in full directly. A method is proposed to decompose the full model into 57x57x57 of 200^3 sub-models, and apply network approximation to characterise average grain and pore properties within each sub-model (yield in total 1.27E+09 pore elements and 2.03E+09 throat elements, as summarised in Table 5-7). The 3D spatial distribution of measured average properties would be plotted in space and correlate to the characterised grain-pore distribution associated with hierarchical structures, to verify the correctness of the model.

Table 5-7 Summary of the numbers of pores and throats in reconstructed pore space model (11900x11900x11900 voxels^3)

Numbers of pores	Numbers of throats
1.27E+09	2.03E+09

5.6.1 Technical verification

Figure 5.16 gives technique for verification of the reconstructed connectivity between subdomains by the four-category partition scheme in Figure 5.16(A), the same as that given in Figure 5.14(B). Four A, four B and one C category partitioned subdomains, as highlighted in the red box in Figure 5.16(A), are shown in Figure 5.16(B). The subdomains are parts of a horizontal planar laminaset with defined regional index maps reflecting layered grading. Figure 5.16(C) illustrates the reconstructed grain-pore distribution in 3D, in which grains are black, and pores are white. To better visualise grain-pore distribution, Figure 5.16(D) gives the 2D xy surface view, in which grains and

pores appear to be well connected across the index mapped regions in Figure 5.16(B). Apart from connectivity, reconstructed pores appear larger on the upper regions, which is consistent with the index map, in which larger grain size is expected in regions with larger indexes (darker colour in Figure 5.16(B)).

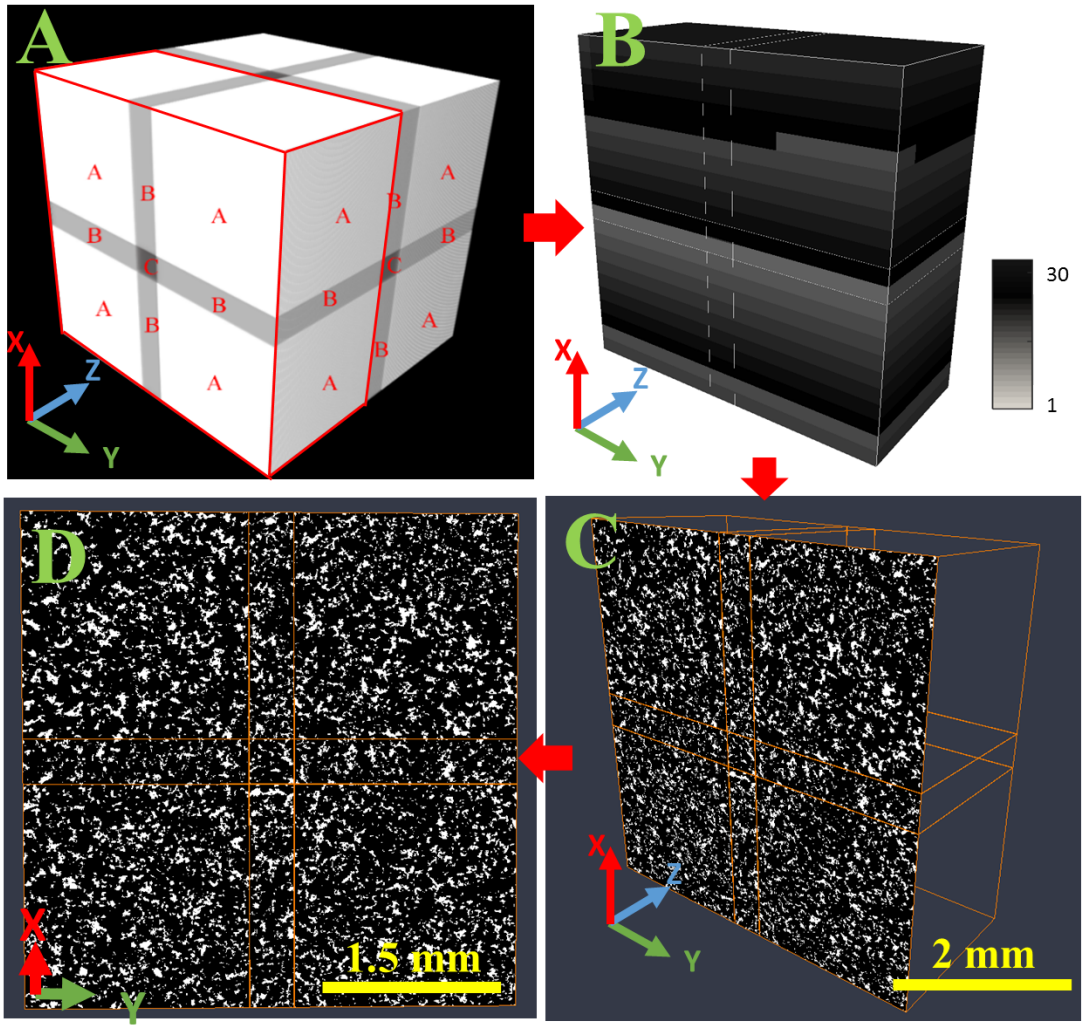

Figure 5.16- Illustration of partitioned subdomain reconstruction :(A) The four-category partition scheme, with highlighted part shown in B; (B) four A, four B and one C category partitioned subdomains from horizontal planar laminaset with defined regional index maps reflecting layered grading displayed (defined regional indexes between 1-30 are coloured from grey to black); (C) 3D view of 1st slice of reconstructed grain (black) and pore (white) spaces; (D) 2D xy view of reconstructed grain pore space.

5.6.2 2D surface verification

Figure 5.17(C) illustrates the partial 2D xy slice of reconstructed grain-pore (white-black) space which has shared the area with T2, whose segmented grain-pore space is given in Figure 5.17(D) for comparison. To correlate with the lamina and laminaset structure, Figure 5.17(A-B) also gives a defined region map in which the corresponding areas of

the reconstructed 2D image and T2 are highlighted. The reconstructed image of Figure 5.17(C) has visually similar grain-pore size to Figure 5.17(D); however, they are too small to display on a centimetre scale section for the human eye to recognise different patterns and distributions, because of the large 1 to 2 orders of scale difference between the millimetre to centimetre scale lamina structure compared with grains and pores with a diameter less than 100 micrometres. Therefore, two zoomed-in FOVs of the highlighted black box shown in Figure 5.17(C), and Figure 5.17(D) are displayed in Figure 5.18(A and B respectively). A relatively coarse grain-pore band is observed in the middle of both Figure 5.18(A and B). Besides the visual consistency, Figure 5.18(A) also has a relatively distinctive finer grain-pore space in the upper right corner above the coarse grain-pore band. By looking back at the defined index map in Figure 5.17(A-B), it can be seen that this is a reflection of the black square area which is a result of bioturbation, based on the previous analysis. The finer grain-pore space reconstructed in this area proves the effectiveness of the special setting dealing with bioturbation.

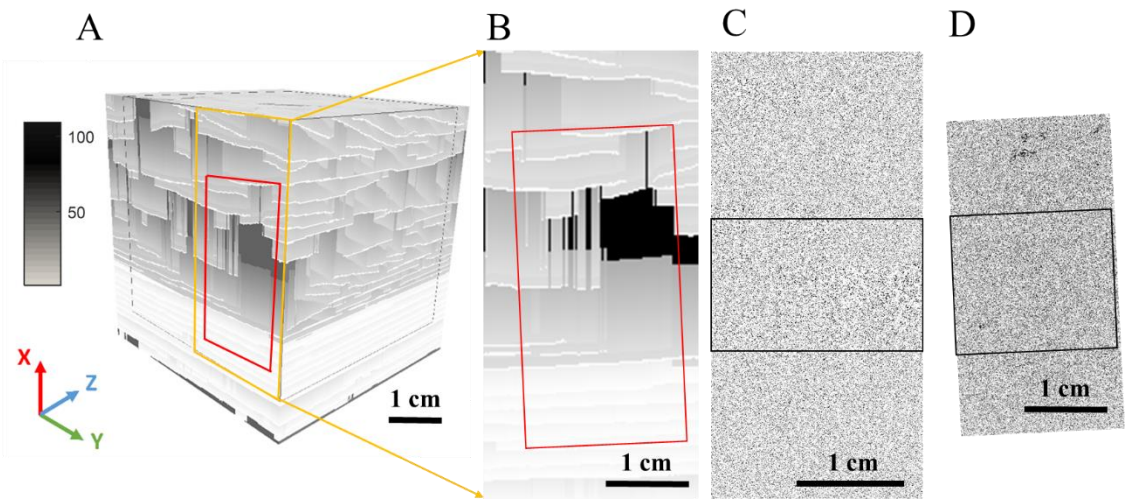

Figure 5.17- One 2D surface of reconstructed grain (white)-pore(black) space of 5400x11400 at 4um^2/pixel resolution, illustrated in (C) and correlated with defined regional distribution of L1 in (A); the 2D defined region of (C) is given in (B),which is highlighted in yellow in (A); as a comparison, the segmented pore space of registered T2 of 19845x38074 at 1um^2/pixel that has a shared area with (C) is given in (D), whose corresponding location in the defined regional map is highlighted in the red box in (A) and (B).

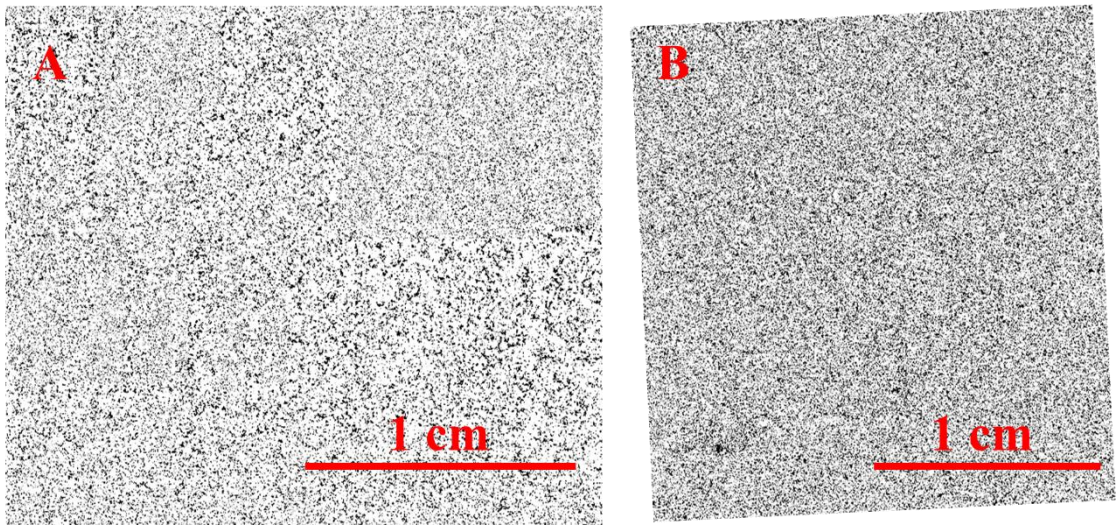

Figure 5.18 the zoomed-in view of black box highlighted FOV in Figure 5.17(C) and Figure 5.17(D)

5.6.3 Synthesis grading factor verification

The main limitation of the previous reconstructed result is the small contrast of grain-pore variation, which could not be visually observed on a centimetre-scale image by the human eye. The purpose of verification is mainly to 1) verify that reconstructed grain-pore size variation has same spatial distribution as the layered index map and 2) the simulated results in neighbouring regions are connected. The main obstacle for such a verification is that the contrasts of grain-pore size between index map defined regions are too minor to be observed with the same FoV that the 1-2 orders larger lamina structure needs in order to be observed. Therefore, a synthetic set of parameters for reconstruction has been developed to have larger grading gradient and, therefore, create a larger contrast in grain-pore size. The scaling factors setting to defined regions (with index *Ln*) are given in Figure 5.19, in which the red line is a result of synthetic parameters with larger gradient, referred to as large contrast, with scaling factor SF_{rate}=0.2, and thus 10 times that of the actual measurement of 0.02, which is shown in blue and referred to as normal contrast (the specific calculated scaling factors are given in Appendix D.1).

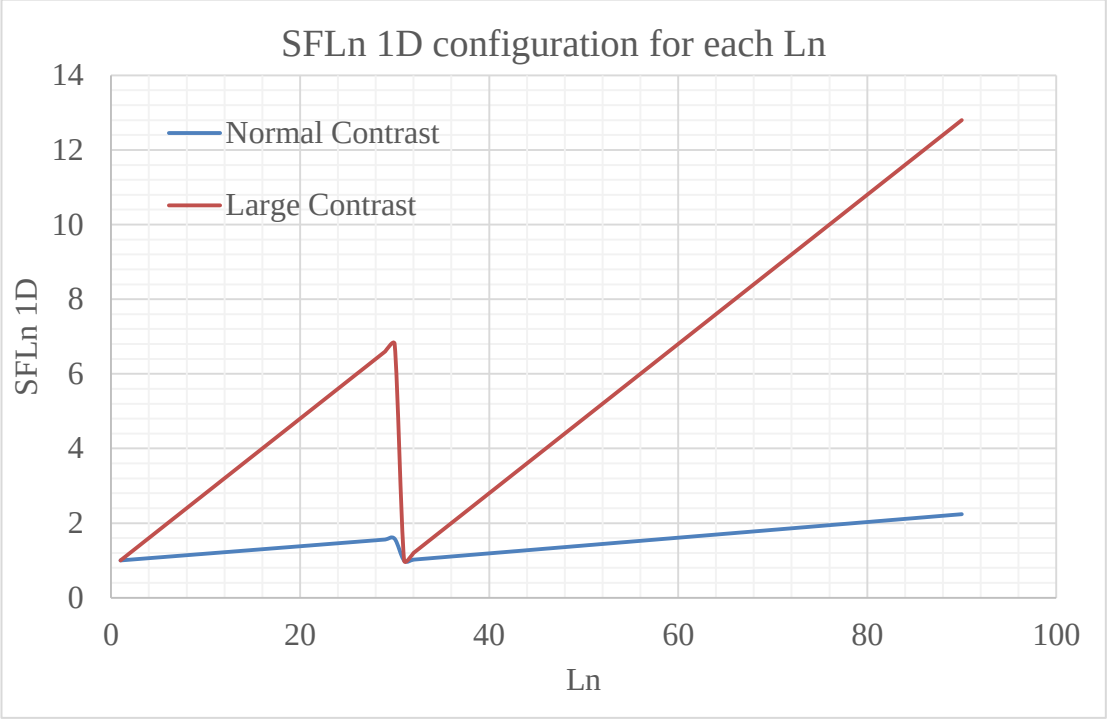

Figure 5.19 Synthetic scaling factors (SFLn 1D) with large contrast, arranged for each regional region with index Ln compared with normal contrast setting

With large contrast, the visual verification of part of the surface xz slice is compared with the index map, in Figure 5.20. Coarser pores are distributed at regions with larger scaling factor (larger index numbers corresponding to darker coloured regions). For a better illustration of more detailed pore variation along inverse grading regions, Figure 5.20 also gives two zoomed-in regions. The square bounded by the red line gives a zoomed-in simulated pore image of regions where two curved laminae are crossing. The square bounded by the yellow line gives zoomed-in pore structure over several parallel horizontal planar laminae. The zoomed-in views of Figure 5.20 verified that: 1) pore size is increasing gradually with the proposed inverse grading MPS simulation strategy,

according to the given layered index map; 2) the connectivity between regions is well kept.

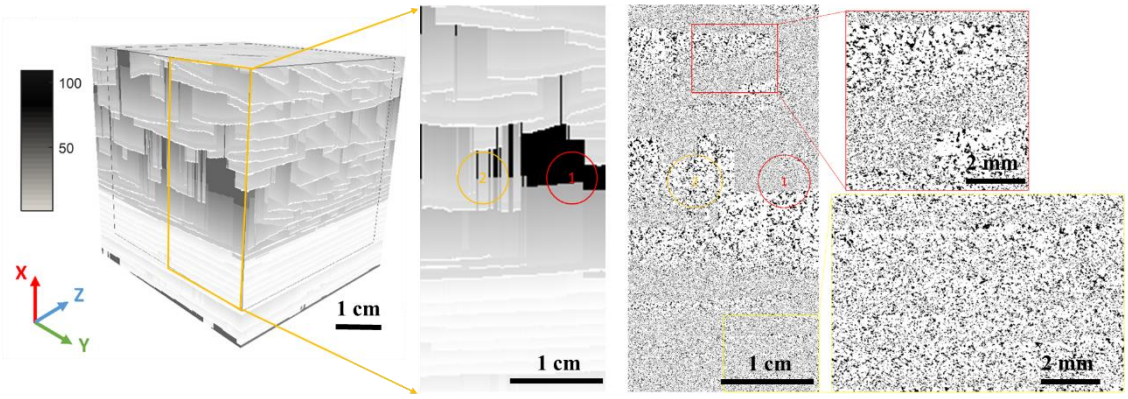

Figure 5.20 Surface slice 2D area bounded with yellow line simulates result verification; 2D view of the layered region and corresponding reconstructed pore-space are compared (black are pores and white are grains). Two regions are zoomed in for a better illustration: a red bounding square of two curved laminae with inverse grading and the yellow bounding square of several horizontal planar laminae with inverse grading. Round circled areas mark two areas with abrupt variation

Besides assigned grading and connectivity, a small amount of abrupt variation has been observed caused by holes/gaps from the region plot, as marked with circles 1 and 2 in Figure 5.20. Among them, position 1 corresponds to bioturbation (black regions in defined regions) and looks abrupt because of the unrealistic scaling factor (10 times that measured) applied, which leads to apparent smaller grain-pore size within bioturbation regions, which is consistent with the trend being measured in Chapter 3. Position 2 has dis-connectivity, which has been explained previously in Figure 5.12(E) as a result of edge artefacts, and in this work it is considered that such abrupt variations would not affect the final result because: 1) such artefacts only occur at limited edging places; 2) in the real model, the parameters for those areas are close to the mean value, e.g. scaling factor ranging between 1-2.13 for the whole model, and those in the holes/gaps are around 1.5, so would not actually introduce abrupt variations, thus not affecting the real simulated result significantly.

5.6.4 Partial block verification with synthetic grading parameter

A 500x500x500 partial block containing an intersection of two curved lamina bounding surfaces has been cropped for 3D verification. Figure 5.21 illustrates the location in both regional index map (Figure 5.21(A-B)) and the segmented inter-LBS structure of the intersection (Figure 5.21(C-D)). Figure 5.21(B) gives the rainbow coloured mapped layered regions of the cropped block to enhance visualisation of defined layered regions,

where colder colours represent the finer layer with smaller region index and warmer colours the reverse. The block contains a cross of two curved laminae, with bounding surfaces (one triangular above one planar) intersecting in the middle of the cropped block Figure 5.21(C-D).

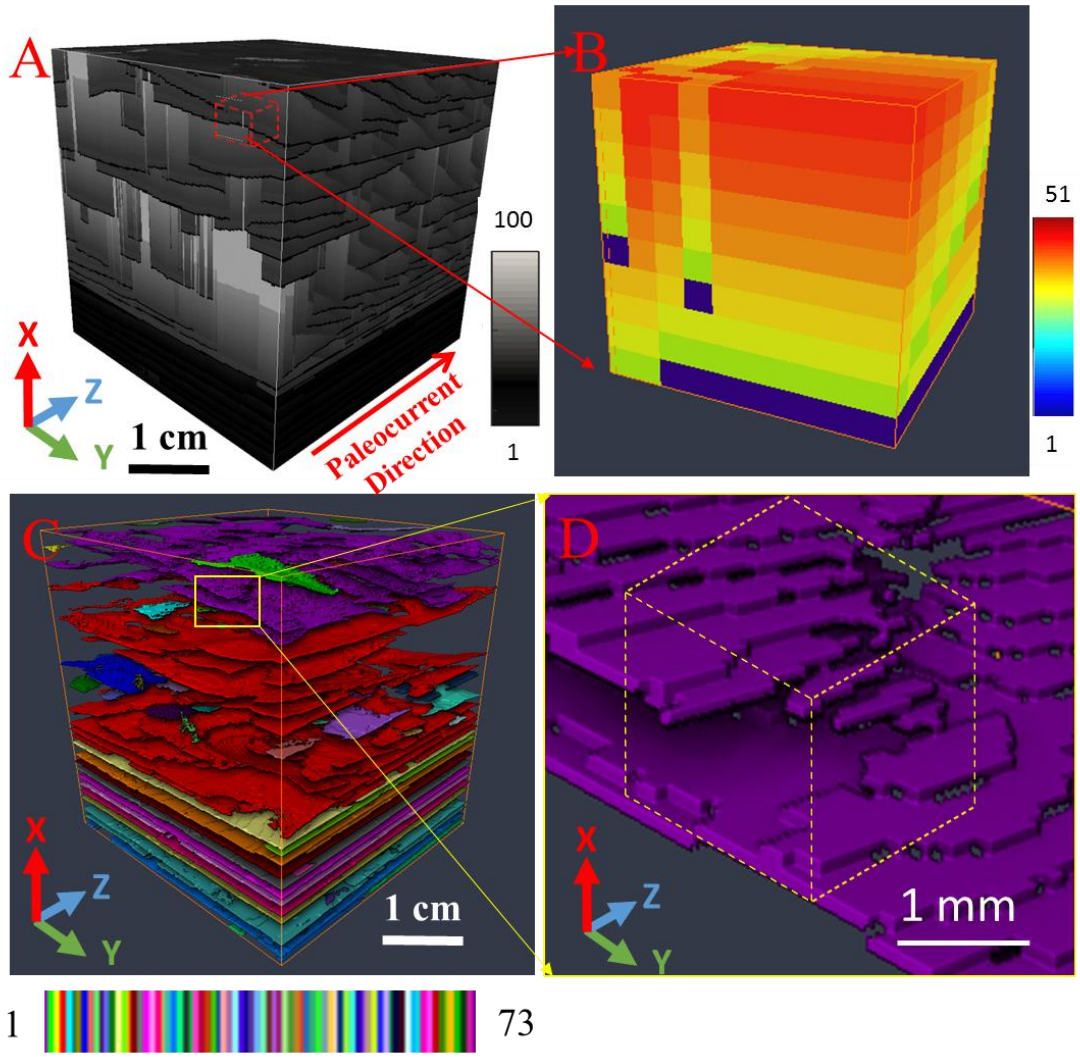

Figure 5.21 Illustrations of location and lamina structure of 3D partial 500x500x500 block of layered region for 3D verification: A) 11900x11900x11900 layered region (black to white for region number 1-100); B) Zoomed-in view of layered region where the partial cubic sample (highlighted in A) was taken, in rainbow colour map for regional index between 1-51; C) overall labelled bounding surface of L1; D) zoomed-in view of bounding surface structure at cropped partial location.

Regional MPS reconstruction is performed using a large contrast grading gradient configuration to enhance contrast. For the purpose of better illustration the pore-spaces of the large-contrast model are coloured by their radius in 3D, as in Figure 5.22 (based on Avizo's skeletonlisation function www.Avizo.com), where the green colour stands for smaller radius and the red colour the reverse. It is clear that the regions at and beside bounding surfaces (blue regions in index map given in left plot of Figure 5.22) reflected

significantly smaller pore size (in volume). The fine pore-space region is also consistent with the spatial distribution of the layered region.

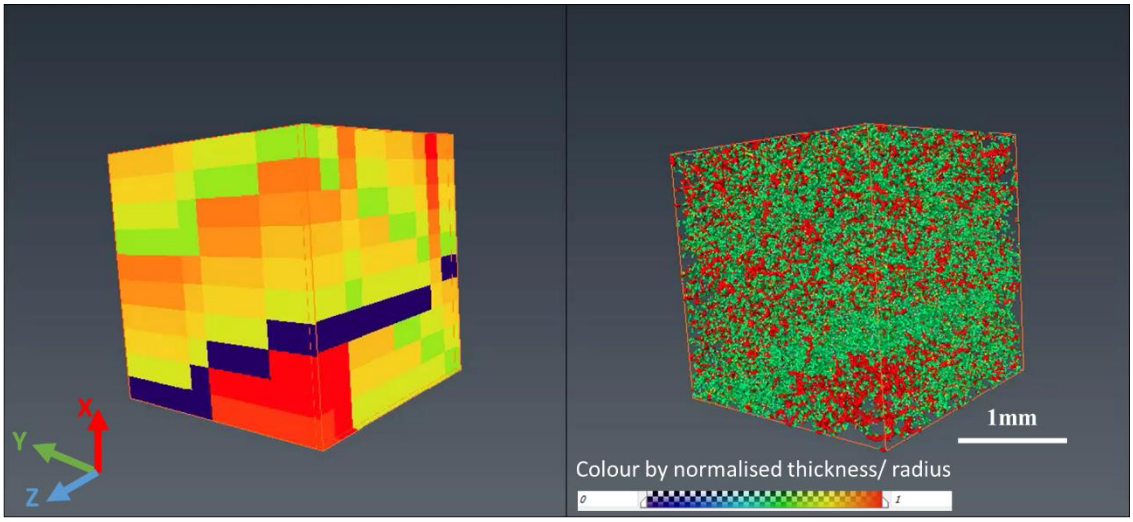

Figure 5.22 3D views of 500x500x500 layered region (left) and reconstructed pore-space of large contrast model (right) with colour map labelled by the normalised radius of pore elements, the cold colour is for smaller radius and warm colours the reverse.

For better understanding of the reconstructed pore-space associated with the internal structure of the intersected lamina, three cross-sections along the Z direction are illustrated in Figure 5.23. To present the 3D structure, 50 xy slices are shown each time along different parts of the Z axes. The intersection is revealed differently at different parts, because, as previously described in Figure 5.21, the bounding surface consists of one triangular bounding plane with one corner obliquely insert into the horizontal one. The complex intersecting structure implies the 3D structure of lamination needs to be

considered, as 2D will not cover the full anisotropy of fluid flow caused by the complex structure.

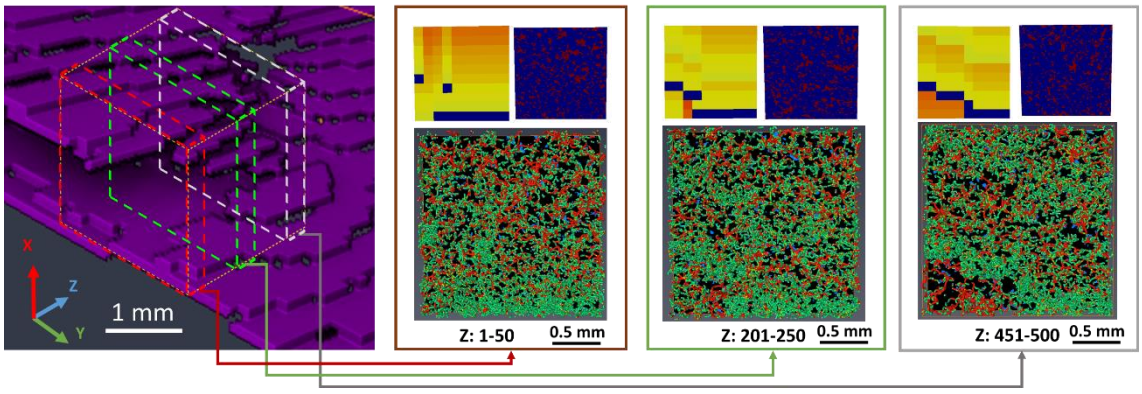

Figure 5.23 Thick section view for different cross-sections along Y direction

5.6.5 Quantitative verification by decomposition

The visual verification only provides qualitative analysis. Further quantitative verification on grain-pore distribution is required to be performed on the full model to verify the reconstructed grain-pore distribution, based on normal grading gradient contrast as measured, over the whole domain of hierarchical lamination. A decomposition and network characterisation approach is proposed in this section, and in the following sections the basic background of network approximation is firstly introduced, followed by quantitative characterisation on the reconstructed model.

5.6.5.1 Network approximation

The key of a network-based approach represents the binary (reconstructed) pore space by networks constituting the skeleton of pore space with simplified nodes and bonds with regular shapes, to represent pores and throats along the skeleton respectively. A set of effective properties like volume, inscribed radius and shape factors can be calculated and assigned to each of the bond and node elements. The spatial location and connectivity of the elements with each other are also recorded, to represent the full pore-space.

Various approaches have been proposed to derive the network structure from analysis of 3-D pore geometries. For example Lindquist and Venkatarangan (1999) found the skeleton of pore space by erosion-dilation and then defined the topologies. However, according to Blunt et al. (2013) “this method suffers from ambiguities given images of finite resolution and has difficulty uniquely identifying pores and their connections”.

Another method by Dong (2007) identified pore elements by filling balls maximizing occupation of the pore spaces; however, according to Jiang et al. (2007), it may oversimplify the topology. Jiang et al. (2007) proposed a middle axis based network extraction approach to extract a simplified network model which represents the corresponding complicated pore space model as well as respecting the geometric and topological information. These simplified models are constructed by nodes (representing pores) and bonds (representing throats), by identifying the media axis of pore space first, followed by partition of the pore space into nodes and bonds, and describing the effect of the shape of pores and throats by a set dedicated descriptions based on shape factors (Jiang et al., 2007). Although other methods like the watershed transform method, which merges regions to identify the skeleton were developed later by Sheppard et al. (2006), Ngom et al. (2011) compared different approaches and concluded there were relatively insignificant differences compared to the media axis approach. In this work, the media axis approach is employed for illustration and verification purposes.

5.6.5.2 Network based characterisation by decomposition

Full pore-space models of 11900x11900x11900 voxels at resolution of 4x4x4 um^3 are reconstructed as shown in Figure 5.24(A). The model is ideally quantified and simulated as whole to verify the model and study the combinational impact of micro-scale pore-space associated with centimetre scale. However, none of the currently available pore-space characterisation tools and fluid flow simulators are capable of performing simulation on a model of such size directly. A compromised decomposition approach has been applied in this work, to allow some preliminary study and verification. The full reconstructed model is partitioned into 57x57x57 numbers 200x200x200 sub-models (a set of scripts has been written in Python for automatic partition, converting format and compression to save output data). For each sub-model, network extraction is performed to obtain statistical characterisations of pore-space within each sub-model in around 5 mins. In this work, a media axis based network extraction approach based on Jiang et al. (2007) is applied, which claims to be more accurate and retain low computation cost (see configuration in Appendix D.2).

A parallel simulation could then be performed for the model to be simulated within a practical length of time. A set of scripts have been written to perform this task automatically and parallel with Windows batch. With 57x57x57 sub-models simulated, a set of parameters for each model could be collected and plotted in Cartesian grids for

the whole volume, to visualize the distribution and evaluate the impact of laminae (performed automatically by a set of Matlab scripts written in this work). Figure 5.24(B-C) gives an example of numbers of pore elements and throats within each of the 200x200x200 sub-models respectively. The distribution of sub-models with larger numbers of pore/throat elements, shown in yellow, reflects the geometry of the defined inter- and intra-LBS. This is because there is smaller grain pore space within those sub-grids at bounding surfaces and this results in a larger number of pores and throats. The gradually decreasing numbers of pores along the sedimentary direction (vertical +X direction) from inter- and intra- LBS also reflected the anticipated inverse grading.

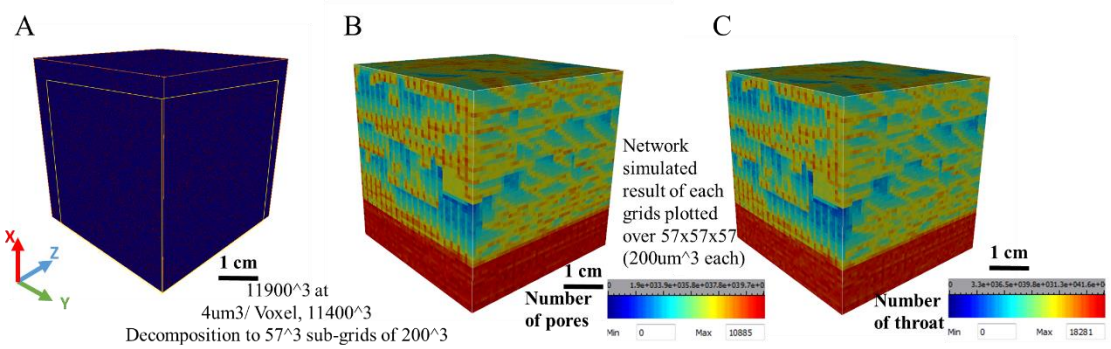

Figure 5.24 Results verification by decomposition and quantitative verification by network extraction: (A) reconstructed full 3D pore space model; (B) network extracted number of pores within each decomposed 57x57x57 sub-grid; (C) network extracted number of throats within each decomposed 57x57x57 sub-grid.

5.7 Discussion

In this work, hierarchical structures have been defined as a set of index maps based on either direct observation or inference. The model has a general representation of cross-lamination while only reflecting one realisation, with a set of deterministic decisions on parameters. The decisions introduce a different level of uncertainty, as summarised in Table 5.7. In the model, those structures with high certainty are the inter-LBSs segmented from the MXRT image and those hierarchical structures for the horizontal bedform, whose geometry is simple. For the more complicated, curved part, more uncertainty is introduced by a strong deterministic assumption on the vertical grading direction and single lamina character, mainly because of: 1) the limited subsample available: the single assumed intersection angle at the toe side of the lamina and lamina thickness may have underestimated the heterogeneity of the lamina properties; 2) the limited method of measurement: although this work tried hard to improve the accuracy of measurement for the more complicated curved lamina by identifying intra-LBSs from a different dataset, the measure could still be uncertain because the measurements potentially deviated from

the true grading direction with assumed vertical sedimentary direction. Grain pore geometry and grading were measured from 3D sub-sample directly, but the deterministic decision to apply one sample as representative and stationary for each bedform limited the certainty.

Table 5-8 Summary of decision on key characters of hierarchical structure model and evaluation of uncertainty

Hierarchical Structures	Bedform	Key Character	Certainty	Reason
Laminaset	Both curved and horizontal	Thin horizontal planar or curved inter-LBS	High	Robust supervised segmentation
Laminae	Horizontal planar	Laminae parallel to inter-LBS	High	Observation and quantitative measurement
		Lamina thickness non-distinguishable with laminaset	High	Observation and quantitative measure
	Curved	Lamina intersect to inter-LBS at 26.6°	Medium	Deterministic mean based on limited measures
		Lamina thickness between intra-LBS of 5mm	Medium	Deterministic mean based on limited measures
Grading	Horizontal planar	Conceptual layered grading parallel to intra-LBS	High	Quantitatively observed and quantitatively verified grading
		Grading distance covered segmented bounding surface distance	High	Ultimately determined by directly segmented bounding surfaces
	Curved	Conceptual layered grading parallel to intersection of inter- and intra-LBS at vertical direction	Low	Visually observed with strong assumption: quantitative measurement only partially agreed.
		Grading distance twice of measured maximum	Medium	Deterministic mean based on limited measures
Grain and pore	Both	Geometry directly trained from image	Medium	A limited number of samples (one for each bedform)
		Gradient measured from image	Medium	Deterministic mean based on limited measures

5.8 Conclusion

This chapter has integrated the obtained multiscale information regarding the hierarchical structures of lamination. Based on this integration, a three-step generic reconstruction procedure has been proposed to reconstruct the full 3D pore-space of the pore-space in a hierarchical lamination structure. The three steps include: 1) defining the full hierarchical structure according to the integrated information as spatial constraints of pore-space reconstruction and populating them with the measured non-stationary grain-pore variation of grading to yield an index map; 2) decomposing the hierarchical structure domain in an ordering scheme to ease the computational cost; 3) multiscale reconstruction respecting both the defined regional index maps and decomposed subdomains simultaneously. In this work, a set of parameters have been determined deterministically on the sample under study to yield one realisation of hierarchical lamination, according to the measurements, for the purpose of illustrating the workflow. Both visual and quantitative verification proved the robustness of the proposed workflow in revealing grain-pore variation associated with the hierarchical structure of lamination.

CHAPTER 6 - CONCLUSION

6.1 Summary of contribution

This work developed a multiscale characterisation and reconstruction workflow to address the recent critical shortfall of multiscale DCA on the characterisation of a representative sample of sedimentary rock which has non-stationary grain-pore variation associated with spatially non-separable hierarchical structures.

Because the spatial relationship of non-separable structures is hard to identify, the key to develop a characterisation procedure is a highly correlated understanding between their geological nature and the nature of imaging. Such an understanding should be built on a generic understanding from literature as well as a combination of exploratory analysis and quantitative analysis, so that features of interests can be mapped with appropriate imaging and characterisation techniques.

As the non-separable geological structures are formed in a hierarchy, it is essential to investigate a sample in a top-down sequence, because a larger structural feature at a higher level in the hierarchy controls smaller structural features in the lower level in the hierarchy. Such a top-down characterisation will construct a correlative understanding of the nature of hierarchical geological structures.

To enable an accurate reconstruction at grain-pore scale, top-down sampled datasets need to be spatially registered. The registration is challenging when there is a lack of separable shared features as references across datasets obtained by different means (i.e. imaging technique and conditions). Therefore, methods for improving the ability to identify shared features have been developed, respecting the geological and imaging natures of different types of datasets.

A typical reconstruction approach assumes stationary grain-pore variation, which is, however, in conflict with the geological nature, which means that the smallest stationary unit could be only several grains thick and vary gradually across hierarchical structures from mm to cm scales. In this work an index map has been developed which respects the characterised geological nature of hierarchical structures, to instruct non-stationary transformation of grain-pore properties during reconstruction.

This work takes a piece of aeolian sandstone sample which includes hierarchical cross-lamination structures as an example to emphasise the above-mentioned challenges. The

contributions of each chapter and conclusions drawn are summarised in the following subsections.

6.1.1 The contributions of Chapter 2

The key to multiscale characterisation and reconstruction is a data-driven statistical parameter collection process to estimate the stationary and non-stationary grain-pore texture distribution associated with hierarchical structures and to yield a non-stationary index map to stochastically instruct grain-pore reconstruction. Chapter 2 presented a literature review into the background to address key issues by developing a highly correlated understanding between the geological nature, the imaging principles, and characterisation and reconstruction methods to instruct multiscale characterisation as follows:

- The review established that an aeolian cross-laminated sandstone is an appropriate example to emphasise the challenges arising from generic non-separable structures and multiscale non-stationary texture variations in performing multiscale DCA. It contains a set of hierarchical structures from laminasets on a scale of tens of centimetres to centimetre-scale laminae, but these may hard to distinguish from one to another because they are formed by stacking grains with gradual textural and compositional variation;
- Inter- and intra-LBSs with sudden grain-pore texture variation are identified as the mark of hierarchical structures and the best candidates of reference for registration. Among them, intra-LBSs appear less identifiable than inter-LBSs, which are subject to more significant compositional change, due to the preferred cementation of heavy haematite and dolomite minerals. Moreover, potential challenges to identification highlighted include unconnected cementation of heavy minerals, distractions arising from complex composition and randomly located erosion and bioturbation creating “holes” of different sizes;
- A set of digital imaging methods was reviewed and proved capable of characterising a set geological features to describe hierarchical structures at different scales. The characterisation included direct estimation and inferring, which correspond to higher or lower certainty, respectively. However, it was also established that none of the available DCA techniques is capable of simultaneously

capturing grain-pore scale features as well as a laminaset structure with a scale of tens of centimetre and this, therefore, calls for multiscale DCA;

- However, based on the review of the nature of imaging and characterisation techniques, it was established that a typical multiscale DCA process is limited in the following aspects: 1) Designing a multi-scale spatial sampling and characterisation scheme appears to be a challenge because the spatial relationship is hard to define for non-separable structures; 2) Identifying shared features to register individual datasets is challenging because LBSs are presented differently as a result of different imaging principles; 3) Developing a stochastic reconstruction procedure that honours spatial non-stationary grain-pore variation appears challenging because the typical reconstruction methods reviewed only work under a stationary assumption.

6.1.2 The contributions of Chapter 3

Based on the review, a recursive top-down a sampling and characterisation procedure based on the "geo-pseudo" concept was proposed and verified in Chapter 3. It started with an exploratory study to confirm the anticipated hierarchical structures of interest and representativeness of a sample, and proved able to estimate a large number of valuable features at low cost and suggested further top-down subsampling. The preliminary compositional analysis also confirmed cross-scale linkage (in this case inter-LBSs) which should be involved in all scales of subsampling as cross-scale references. The top-down procedure was then designed and confirmed the efficiency of a recursive top-down sampling approach in improving the spatial correlation. The efficiency of the reviewed DCA imaging and characterisation techniques in estimating or inferring the non-separable hierarchical structures of lamination can be summarised as follows.

- MXRT has been proved efficient in capturing internal structures with its density-sensitive nature. The heavy minerals preferentially cemented in inter-LBSs are therefore identifiable in MXRT and act as markers of laminaset structures;
- Thin section images have been proven effective in providing large FoVs in 2D, capturing a set of textural and compositional features from centimetre scale laminasets to micrometre scale grain-pore geometry, as well as mineral distribution. These are therefore suggested as an ideal cross-scale link between MXRT and μ-XRT;

- μ-XRT has been proved essential in revealing a 3D complex structure, but only for features under a millimetre in scale, because of the small FoV.

With top-down sampling, a conceptual model describing the hierarchical structure can be summarised based on characterisation and calls for techniques to be developed to estimate missing features. The potential challenges of identifying shared features and obstacles to multiscale registration were verified. The challenges identified as specific to the aeolian cross-lamination sandstone sample were as follows:

- It was confirmed that most intra-LBSs cannot be identified with great confidence, although they may be inferred from measurable parameters, including thickness and intersection angle.
- Segmenting a continuous bounding surface from MXRT was confirmed as a challenge because a set of discontinuities and distractions exist in the MXRT including:
    - Scattered distributed haematite and dolomite minerals only highlight the unconnected part of a continuous inter-LBS and leave gaps at the smallest length scale;
    - The thin 1-2-grains thick bounding surface present as a 1-2 pixel-thin linear/planar structure in MXRT are easily obscured by another heavy mineral like feldspar, which masks out connectivity by presenting as clusters with relatively large size and brighter intensities similar to bounding surface;
    - Erosion and bioturbation occasionally occur at random locations on the surface, creating holes and leaving large gaps.
- Bounding surfaces appear as "hidden" features in SEM, in contrast to MXRT, due to the different imaging conditions and principle:
    - A BSEM image has resolution much finer than grain size, and emphasises the high grain lithology variation rather than the overall trend of inter-LBSs;
    - The imaged pixel intensity value of BSEM has a more gradual positive correlation with density than in MXRT.

6.1.3 The contributions of Chapter 4

The accurate segmentation of continuous thin planar inter-LBSs from MXRT and SEM is essential as cross-scale shared references for registration. For an MXRT image, an advanced supervised segmentation method that characterises linear LBS features by a set of image filters and encapsulates connectivity knowledge into an exemplary training image was found to be capable of improving segmented connectivity. The method was further developed to bridge smaller "fake" gaps caused by scatter distribution of haematite/dolomite and the distraction from feldspar but leave larger "real" gaps caused by erosion and bioturbation. This is achieved by:

- Describing a variety of linear patterns from a highly noisy image by means of a large number of convolutional image filters to construct a multidimensional feature field;
- Utilising small filters to avoid distractions outside of the small local neighbouring area;
- Utilising training examples with gaps overlaid to bridge those small "fake gaps";
- Keeping those larger "true gaps" caused by erosion and bioturbation by designing a corresponding upper limit of filter size;
- Using training examples to constrain orientation and background intensity, which, however, also proved to have good tolerance when the uncertainty of the training image is less representative.

For an SEM image, a method to upscale the image to similar resolution of MXRT and retain feature of interests similar to MXRT is required to assist registration. In the BSEM image, the finer pixel, without weighted average density and without the hardening effect, makes the bounding surface pattern unobservable. The study found the typical arithmetic average would not reveal the pattern as well, because it ignores density. A low-resolution BSEM averaged density thus enhanced a little the contrast of the bounding surface but still not obviously as MXRT, as a result of the different imaging principle. A low-resolution MXRT simulator was therefore developed, based on composition map provided by EDS, and demonstrated that it could retain some inter-LBSs at the same resolution as MXRT by:

- Treating an EDS image as a sample, where each pixel possesses the mass of elements;
- For each coarse pixel, calculating a weighting factor for each element from the sum of its atomic mass overall, the underlying fine pixels weighting factors are normalised by summing them over all elements;
- Calculate an effective mass attenuation coefficient for each coarse grid pixel using a weighted average of elemental X-ray mass attenuation coefficients and therefore estimate the MXRT image intensity for the coarse pixel.

Considering intra-LBSs are potentially not directly observable, a more representative indirect measure of lamina thickness and grading gradient by circulation of grain size is anticipated from SEM. The measurement is based on a sampling window that has geometry and moving direction designed based on an inter-LBS, which is not directly available on BSEM. With BSEM registered with MXRT, based on the partially revealed inter-LBS after upscaling, the segmented inter-LBS from MXRT could be masked to design the sampling window. The measurements showed, together with BSEM measurements in previous top-down characterisation, that lamina and grain-pore features are similar within each bedform, but different across the bedforms.

6.1.4 The contributions of Chapter 5

Multiscale imaging only provides characterisation for a limited domain. Combining the summarised conceptual model, using both the directly obtained and indirectly inferred structure features obtained through Chapters 3 and 4, a generic index map of hierarchical structures on cross-laminated sandstone has been proposed, as follows, to instruct non-stationary grain-pore reconstruction.

- Take a realisation of inter-LBSs segmented from MXRT to define the inter-laminasets;
- Distribute intra-LBSs with respect to inter-LBSs, according to estimated parameters, to define the laminae in each laminaset;
- Define conceptual grading layers within laminae and populate the grain grading gradient and orientation for each and every conceptual layer within a lamina, as a non-stationary index.

To improve computational efficiency, a strategy has been developed to decompose the domain of the index map into sub-domains in an ordering scheme to perform stochastic reconstruction in parallel. The concept is generally applicable and could be summarised as follows:

- The domain is decomposed into subdomains of ordered categories, such that sub-domains of each category do not spatially connect to each other; therefore, the internal part can be reconstructed independently, and thus in parallel;
- Sub-domains are spatially connected when combining different ordered categories, and therefore, each sub-domain can be reconstructed in an ordering scheme to include neighbouring pre-simulated results as conditional hard data, and therefore retain connectivity of the reconstructed pore-space at the boundaries of sub-domains.

A stochastic reconstruction strategy has been developed to perform the simulation for each sub-domain, and a sample of the study was reconstructed based on selected MPS modelling techniques as follows:

- A representative sub-volume of μXRT was chosen to serve as a training dataset of the local stationary grain-pore distribution for each bedform;
- The defined index map of structures was applied as a regional sub-domain of MPS to constrain simulation;
- Indices representing the grading gradient and preferred orientation were converted into affinity and rotation in MPS, to include non-stationary regional parameters;
- Regions were reconstructed in sequential order, with each region conditioned to pre-simulated data in the neighbouring regions as hard data to keep connectivity.

The procedure was applied on the cross-laminated sandstone sample studied in this work and validated that the reconstructed grain-pore space had variation associated with the hierarchical structure, as anticipated.

6.2 Summary of uncertainty and limitation

This work proposed the top-down characterisation approach to define spatially non-separable hierarchical structures across multiple scales of a cross-laminated sample.

- As fully discussed in Chapter 5, the main limitation is the different levels of uncertainty in estimating or inferring structural features, as a result of the limited number of subsamples;
- Besides, although the work tried hard to improve measurement accuracy, uncertainty still exists because some small-scale structures are hard to define as a result of gradual grain-pore variation without distinctive signature like compositional variation;
- Fluid flow simulation is anticipated on the result of this work but is limited by current simulation technique and computation power.

6.3 Summary of future work

- This work developed the workflow to study the hierarchal structures of lamination from centimetre scale down to micrometre scale. One of the keys to designing such a workflow is to identify the most appropriate imaging technique corresponding to each geological feature of interest, based on the nature of the imaging principle and the geology. Generally, imaging is a process of collecting and plotting signals corresponding to each spatial physical point. The relationship between a signal and the physical property at a point depends on different imaging techniques and deciding what physical feature can be captured. Therefore, if the physical property of one geological feature "matches" one imaging principle, that imaging technique would be the best candidate. For example, in this work density-sensitive XRT images captured the heavier minerals concentrated at a bounding surface. In this work, the imaging techniques discussed are mainly sensitive to density or composition, and would be applicable to identify geological features with such variations. However, for those geological features not having specific physical property variations that "match" an imaging technique, user intervention is required. For example, a gradual geometrical variation of grain-pore space could be hard to directly identify from the image; thus, a more sophisticated method is required to extract such less obvious characteristics from the image in order to help geological feature identification.
- A crucial function of the developed workflow in this thesis is measuring and identifying the features of lamination, bounding surface and grading. The bounding surface determines the spatial heterogeneity of the lamination structure and grading determines the local heterogeneity of grain-pore texture. Through the developed

workflow, the bounding surface and grading are spatially correlated, thus determining the spatial distribution of the grain-pore texture. In other words, this distribution determines the heterogeneity of the physical property in a sample, which is of critical scientific interests in terms of studying and predicting a set of physical and chemical behaviours (e.g. fracturing, wave transforming and fluid flow transport), which are worth exploring in future work.

- The current reconstructed model could not be simulated to predict or study fluid flow behaviour with the current techniques and computational powers. However, computational power is increasing at an extraordinarily fast rate, with speed double every two years, according to Moore's law (Moore, 1998). Therefore, it is expected that the model could be useful for studying fluid flow and other physical-chemical behaviours in the near future.

- Because heterogeneity exists at every scale, from molecules to the universe, it is always of scientific interest to study the combination of the smaller scale property variations associated with larger scale structures. Although imaging techniques are advancing, the natural trade-off between imaging resolution and field of view will always exist, and therefore always be the critical challenge for the multiscale study of the natural world. Therefore, the developed workflow which is capable of performing a multiscale study of heterogeneity under large scale range is also important in more general scientific research areas such as geoscience and materials science.

- In the oil industry, the exploration is usually studied at kilometre scale (field scale). The centimetre scale sample studied in this work, even if successfully simulated with petro-physical fluid flow properties, could still not be used directly to help to make predictions at field scale. Upscaling is required to populate the obtained properties into the field scale model. Such upscaling is more likely not to be straightforward, and would require repeating several times at different scale lengths in a hierarchy to respect the nature of multiscale heterogeneity. The model built in this work that introduces grain-pore scale heterogeneity into a centimetre scale model would, however, potentially provide an avenue, to studying and verifying methods of performing upscaling, thus contributing indirectly to field scale exploration.

- Specific to this work, to improve accuracy, more subsampling could be carried out, which would improve not only the representativeness of measures but also provide

hard data for reconstruction. The key idea of reconstruction is based on developing an index map and would address the issues of non-stationary reconstruction that typical approaches cannot resolve. It is currently embedded into an MPS-based algorithm, while the generic concept is expected to be compatible with other stochastic methods. The developed approach proved to robustly characterise and reconstruct the non-stationary grain-pore structures of lamination, which is purposely selected as a special challenge case considering its non-separable hierarchical structures. Therefore, the developed approach is expected to work robustly on most heterogeneous samples with more distinctive hierarchical structures.

APPENDIX A -Chapter2

A.1 Compare Multiple Point Statistics (MPS) with Markov Chain Monte-Carlo (MCMC)

In this section MPS (SNESIM, by Strebelle (2002)) is compared with MCMC ((Wu et al., 2004)), which both use templates to scan a training image to collect soft pattern and reconstruct based on hard neighbouring data. Major differences of typical MCMC over MPS including: 1) template size are typically small limited by computation power and do not apply multigrid method to increasing template scanned area; 2) during reconstruction MCMC visit pixels sequentialy by row and column rather than randomly as MPS; 3) MCMC typically applied without regional reconstruction feature to personalize scaling and rotation.

The test in this section compares the reconstructed 2D pore-space of a heterogeneous breccia sandstone sample. A 2D optical microscope image with size 456x342 pixels^2 is provided as training in which pores are impregnated with blue-stained epoxy resin as in Figure A.1. Large pores upto 100 pixels in diameter are observed on the left between breccia sands parked whiles around 10 pixels thin and up to 150 pixels long ranged pores observed on the right. The thin section image is first segmented by simple colour threshold method to construct training image. A first approach applies the MPS (SNESIM as function of SGeMS (Remy et al., 2009) software package) specific regions for training image and reconstruction to address two types of distinctive pore system. 176x176 pixels^2 template searching area have been set to capture large and long range pore patterns. The reconstruction also set rotation at both regions to illustrate the rubustness on controlling orientation required for layered gradiing reconstruction. The second approach apply MCMC without specify regions for training and reconstruction in which whole segmented image are trained to reconstruct a pore-space image. The last approach apply MCMC with separate training image subsampled from two distinctive pore system and reconstructed into two neighboured region but without taken results of each other as hard data at boundary. The configuration with more detailed parameter for three approaches are given in Figure A.1.

The reconstructed result in Figure A.1 shown 1) large template size of MPS is essential on capturing large pore-grain pattern who reconstructed large and long ranged pore with size consistent with training whiles other two only have scattered homogeneous pores with diameter no more than 50; 2) pre-reconstructed pattern at neighbouring region

boundary as hard data in MPS is essential on preserving connectivity between regions comparing with MCMC regional whose pore-space at region boundary are not naturally connected; 3) regional manipulation of MPS are again verified by 90^{o} rotation without defect on boundary connectivity.

This section proved the key advantage of MPS comes from its searching template nature to collect soft pattern possibility and reconstruct based on hard data. Although MCMC shared similar feature, however typical MCMC did not apply multigrid to increase template searching area thus limited the reconstruction of large heterogeneous pattern. Besides typical MCMC also do not apply regional reconstruction with respecting neighbouring region as hard data. The regional reconstruction advantage of MPS on the other hand makes it naturally fit layered grading whose grain-pore size and orientation vary gradually across layered regions. In this work MPS are recruited for full 3D pore-space reconstruction. The key factors concluded here limit MCMC are also suggested to be addressed to improve its performance.

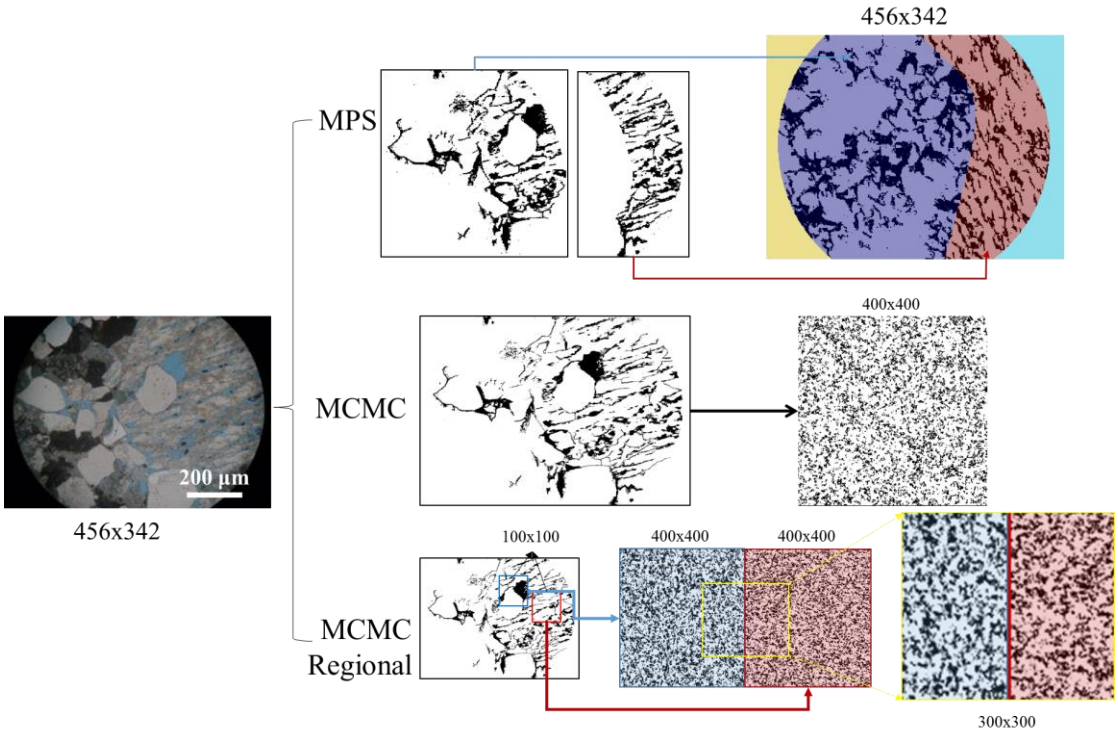

Figure A.1 Reconstruction of optical microscope image (456x342 pixels2) of breccia rock sample, blue are pores grey and black for grain matrix; First row illustrates two types of binary pore space images (black is pore) which are given as training image to reconstruct pore space for purple and red regions separately with MPS

Table A.1 Key feature configuration for MPS and MCMC

Feature	Template size scan through training image	Hard data honoured reconstruction	Regional scaling	Regional rotation
MPS	176x176 pixels^2 scanning area by multigrid and store 121 pixels to describe pattern	Neighbouring reconstructed result as hard data	1	90° (clockwise)
MCMC	4x4 pixels^2	No region boundary constraint	N/A	N/A
MCMC Regional	4x4 pixels^2	No region boundary constraint	1	N/A

A.2 Multiple Point Statistics (MPS): detailed mechanism

The MPS reconstruction process could be illustrated as Figure A.2 which a binary sand channel image is reconstructed as Figure A.2(E) from the training image of Figure A.2(A). Figure A.2(A) illustrates a 3x3 pixel^2 template scan through each pixel over a training image to collect potential patterns as Figure A.2(B). The 3x3 pixel^2 template is large enough to capture the potential pattern of interests which is a 1-2 pixel wide in Figure A.2. The probability of central pixel as black or white for one pattern is calculated as Figure A.2(C) and the central pixel probability for all potential patterns are stored as a probability histogram in Figure A.2(D). On a new canvas, stochastic reconstruction search probability at each randomly localtioned pixel and assign pixel value by match existing neighbouring pattern to probability histogram. The existing neighbouring pattern could either from existing or previously simulated hard data. Figure A.2(E) illustrated a reconstructed image with similar patterns to training image Figure A.2(A). (Guardiano and Srivastava, 1993) initialised the idea of MPS, but it was limited by requiring the training image to be scanned at each un-sampled data point, thus resulting in low efficiency. (Strebelle, 2002) extended the traditional MPS by building a search tree, thus the training image only needed to be scanned once, which improved efficiency significantly. A multiple grid simulation feature (Gomez-Hernandez, 1992) is also typically applied on MPS to increase template searched area without increasing numbers of pixels of the template to be stored. It collects pattern with size increased template but only pixels separated at fixed interval are saved.

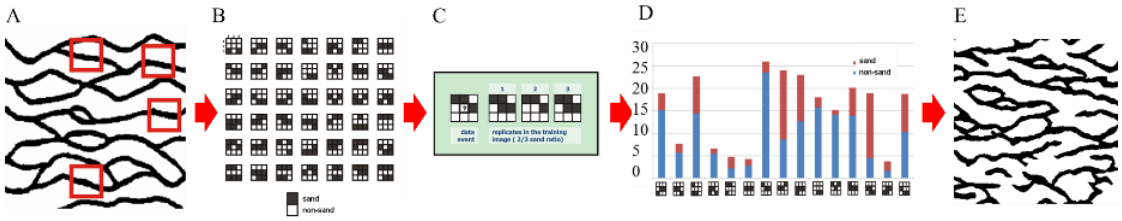

Figure A.2 Mechanism illustration of MPS: A) pattern collection from training image by 3x3 pixels^2 template (sand channel as black coloured and the rest white coloured); B) Collected pattern illustration with 3x3 pixels^2 template; C) probability of centre pixel to be "1" or "0" for one pattern; D) histogram of collected patterns contain probability of centre pixel to be "1" or "0" for each pattern; E) reconstructed image with similar pattern with A. Figure modify and extended based on Strebelle (2002).

APPENDIX B -Chapter3

B.1 Geological background

Sedimentation

Sedimentation creates sedimentary structures by processes including transportation and deposition. The transportation could be done by either fluid flow or gravity flow. With the former particles picked up (eroded) and transport by moving fluids such as: air (wind), water (river currents, waves and oceanic currents), and ice (glaciers). Whiles the later particles transported down a slope by gravity action. Deposition occur after either fluid or gravity flow, when force moving grains become less than force of gravity and leading grains to settle.

Fluid flow sedimentation is commonly a successive process, because there are always grains deposit and others lifted into the current. The successive deposition as a result produce a stack of successive sediments. Such successive sediments are called beddings.

Geological History of sample

Geological background has been researched by the author from related literature aiming to explain the occurrence of red/brown lamination and corresponding mineral distribution character of our sample. The precise position of the sample is yet not available in this case, however the overall geological information around the corresponding area are: North-West England or South West Scotland, Permian- Triassic geological sequence, red bed sandstone from sand dunes in hot, arid desert environment (Shotton, 1956, Walker, 1967, Thompson, 1969, Waugh, 1970).

Depending on (Shotton, 1956, Walker, 1967, Thompson, 1969, Waugh, 1970), the red bed sandstone from sand dunes in hot, arid desert environment is caused by red coloured haematite. The occurrence of red/ brown coloured iron also consistent with what been observed by Huang et al. (1995) whose sample been taken at similar location and claimed from Permian period too. From the literatures the occurrence of this behaviour could be categorized as two: 1) pure Aeolian system with ground water level change effect on diagenesis (McKee, 1966, Walker, 1967, Stokes, 1968, Waugh, 1970, Walker, 1976, Waugh, 1978) or 2) Aeolian system with alluvial fan/ wadi-fan breccias inclination (Wills, 1951, Waugh, 1970). Yet as there is no clear source of water around at the period of sedimentation and the sample is quite clean (mainly quartz and rarely clay from

lithology lab study) so The author would take the ground water theory as the most possible case to discuss.

A low permeability bounding surface would first form in the dried desert system. Due to dehydration or "aging" process and Gibbs Free Energy theory, detrital ferric hydroxides including goethite and ferrihydrite will spontaneously transform into red coloured haematite pigment with time (Van Houten, 1961, Berner, 1969). Further diagenetic came along with the changing of ground water table, the processes of weathering, which had been largely inhibited in the arid environment of the desert surface, took place in the humid environment below the water table, thereby releasing a variety of ions for incorporation into new minerals. (Walker, 1967, Walker and Waugh, 1973, Walker, 1976) claimed the key to this mechanism is the intrastratal alteration of ferromagnesian silicates by oxygenated ground waters during burial. As a result, a hardening layer composed of finer detrital with haematite coated or cemented has been built.

During the process of ground water level change, Glennie and Evans (1976) analogized with modern deserts, pointed out that because of the high Mg++/Ca++ ratio of the interstitial waters caused by gypsum precipitation, any early calcite cement in this facies was rapidly dolomitized, and based on Glennie et al. (1978) those authigenic dolomites are preferentially cemented in the finely laminated layer.

A bound surface concentrated could occur in either cases as a result of capillarity; solutions enriched with dissolved silica drawn towards the desert surface, by evaporation precipitated the silica. Result the dune a silicified first producing a crustal hardening layer (Waugh, 1970). It is also pointed out that Bounding surfaces of differing magnitude have been described from both recent and ancient Aeolian deposits and often attributed to changes in wind character, deflation, dune migration and changes in groundwater level (McKee, 1966, Stokes, 1968). As a result, a small scale (cm scale) linear lamination system separated by those bounding surface are expected in the corresponding area.

As a conclusion of geological background study: 1) Lithological features as an important product of laminae which potentially impact fluid flow need to be captured during analysis to assist future modelling; 2) The characterisation of inter-laminaset could be based on bounding surface identified with cementation of antigenic dolomite along with iron and fine fabrics and registered through images at different scales; 3) One might also expect preferred orientation been observed along inter-laminaset bounding surface and

intra-laminaset foresets. Those conclusions would instruct our analysis in the following sectors.

B.2 BSEM measurement on Tp

BSEM image have been taken over the whole sample at highest resolution available for the author at about 0.6x0.6 μm^2/ pixel with dimension 33098x49119 pixels^2 (Figure B.1(B)) for prior analysis which is capable retain grain-pore size down to 6 um^2 (it is typically believed 10 pixels long structure could be well observed). The resolution therefore well covered the average grain size with diameter of 100um from electrical microscope study. Taking high resolution scanning are time consuming, for prior analysis low resolution EDS image are firstly taken with resolution of 124x124 μm^2/ pixel over the whole sample yield 154x277 pixels^2 image (Figure B.1(C)). Partial of it have been scanned with higher resolution 0.6x0.6 μm^2/ pixel for 4090x14392 pixels^2 (Figure B.1(D)).

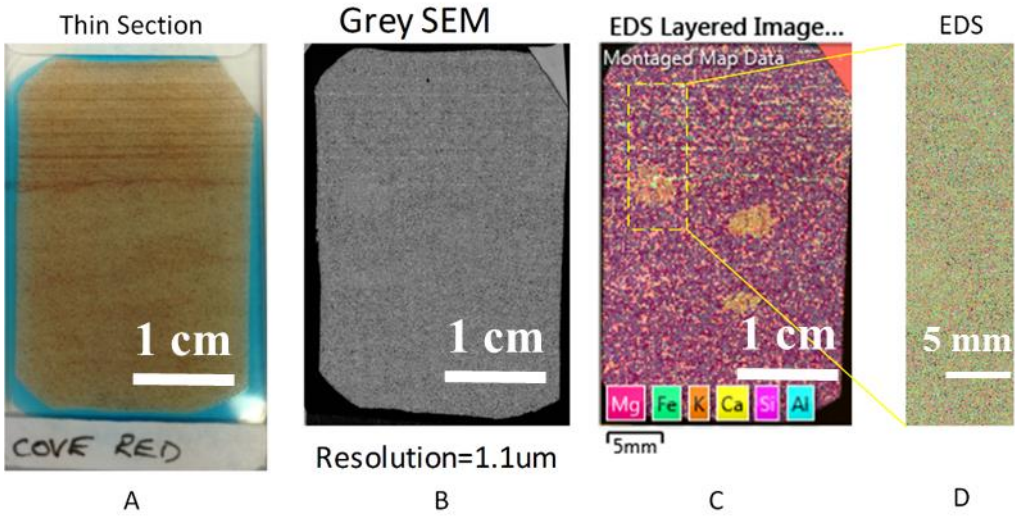

Figure B.1 Thin section for prior analysis introduced in chapter 1; (C) Coarse EDS overall scanning with resolution ~ 124x124 μm^2/ pixel for 154x277 pixels^2; (D) Fine EDS scanning at selected field of view in C, with resolution of 1.1x1.1 μm^2/ pixel for 4090x14392 pixels^2. (images are phtted upside down)

Pre-processing and Segmentation

For grains separation purpose, the segmentation would base on the Reference segmentation (VSG) to keep boundary between grains. But additionally to solve the afore-mentioned problem in literature review, the author used four markers instead of typically two, to determine four phases separately: pore (black), feldspar (light grey), quartz mainly minerals (darker grey) and iron or titanium rich particles (white) as in Figure B.2 -left, based on different grey scale intensity identified respecting correspond

EDS image as in Figure B.2 -right. Four phases will be marked Figure B.3 (C) and will be segment out by applying corresponding thresholds.

On our sample, the following four phases marked in Figure B.3 (C), are each segmented out. In this article, the author used a procedure based on the first approach, cycles of erosion and dilations operations would first be applied, then the watershed lines of a binary image will be computed. But it is further implemented a high-level combination of watershed, distance transform and numerical reconstruction algorithms. A contrast level which is used to adjust the number of seeds for the watershed is user-determined. At last, interior holes of the objects are removed to reduce inaccuracy of measurements on small objects, for details please refer Avizo object separation build-in and (Russ, 1990). Cycles of erosion and dilations operations would be applied for "minority" phase (feldspar and iron or titanium rich particles) then images of all four phases are stacked Figure B.3 (D). As The author can see contacted grains of different phase are now separated. To separate grains under the same phase, aforementioned procedure would be applied and finally interior holes are filled Figure B.3 (E). Although there are probably still un-separated grains, the author considers the amount is minor and could be ignored. The pore segmentation is illustrated by Figure B.3 (F). By comparing Figure B.3 (A, D and F) The author could see the Stanford approach without grain separation is more accurate for pores segmentation.

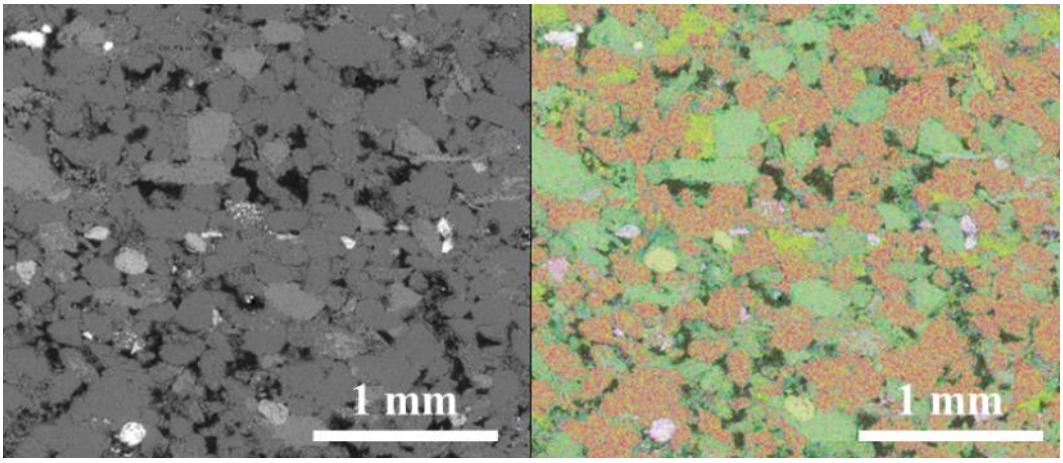

Figure B.2 Comparison between BSEM (left) and EDS(right) image on same region. Red = quartz porosity (dark grey in BSEM), greenish blue = feldspar (light grey in BSEM), Yellow = calcite porosity (dark grey in BSEM), Pinkish = iron or titanium rich particles (white in BSEM), Black = pores porosity (black in SEM)

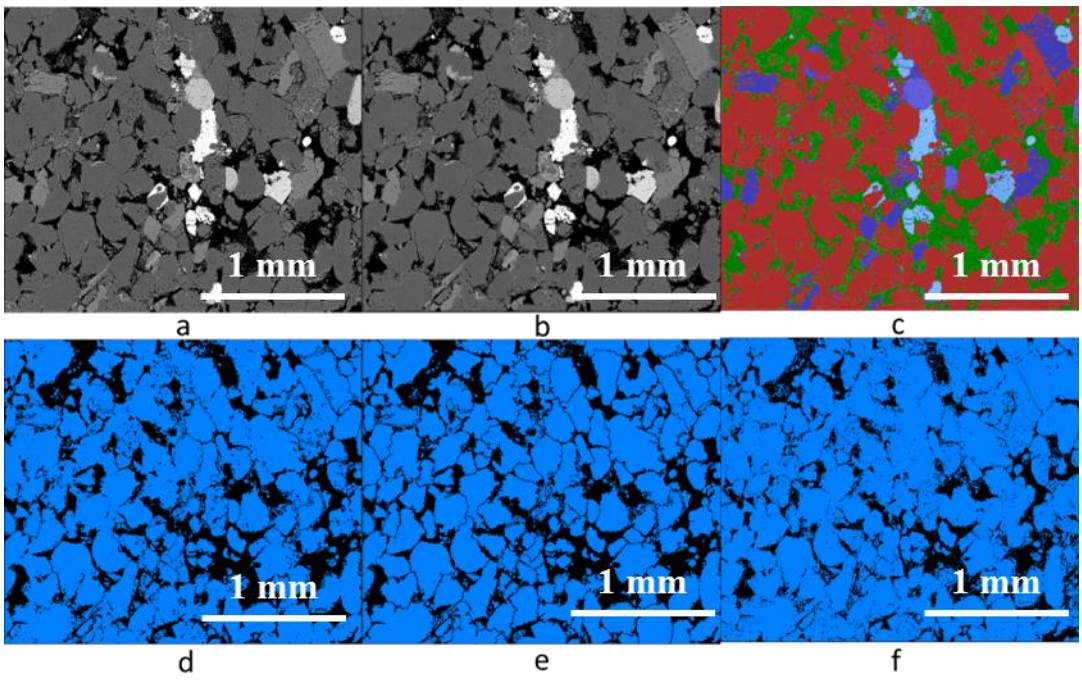

Figure B.3 (A)Zooming in on a grey scale BSEM image (b)Anisotropic diffusion and un-sharp mask filter applied (c)Four phases marked by marked-based watershed algorithm (d) four phases segmented post processing applied (e) segmented grains separated by (f) the Stanford approach based on Otsu (1979)

Quantitative measurement

A first quantitative measurement is performed to investigate the spatial distribution of grain size in relation with lamina structure to verify visually plotted bounding surfaces. 26 sub-regions representing lamina has been manually plotted in Figure B.4 (A) separated by the manually determined bounding surfaces in Figure 3.4(B). Average grain sizes are measured simply in the area rather than more complex long and short axes because the purpose is to investigate the relative variation across laminae. Average grain size of each region is plotted in Figure B.4 (B). According to Figure B.4 (B), average grain size in the area vary from 2500 to 3300 um^2. Generally, regions from horizontal planar part have smaller grain size than the curved part. Grain size across manually labelled regions appears similar within curved and horizontal laminaset suggested either lamina feature is homogeneous within each type of laminaset or inaccuracy of manually labelled regions. Four laminae (R17-R20) belong to one same laminaset have a relatively large variation of grain size. The potential reasons include the existence of intra-laminaset lamina separated by intra-laminaset bounding surfaces or bioturbation, but not certain which is true.

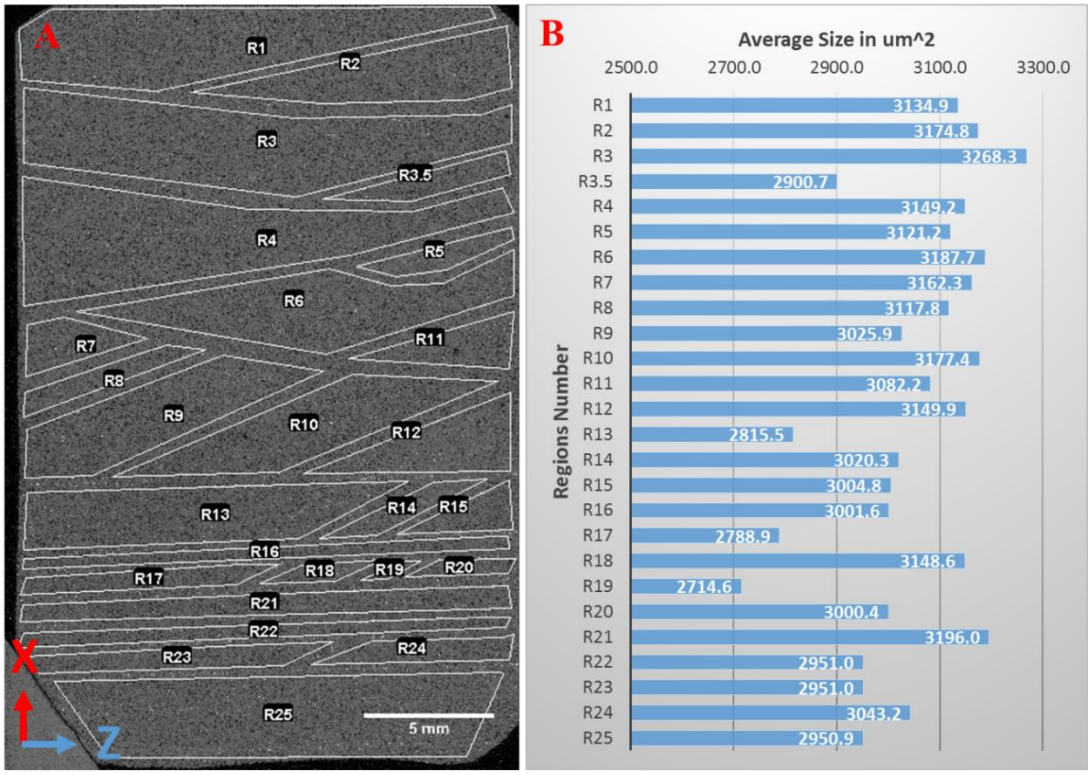

Figure B.4 （A) manually plotted 26 regions named as R1-25 according to manually determined bounding surfaces; B) Average grain size measured for each region.

A second quantitative grain orientation measurement is performed to investigate potential preferred alignment of grains along lamina bounding surface. Grain orientations are measured within lamina regions separated by visually identified bounding surface at small FoVs (three selected FoVs illustrated in Figure 3.4(B)). The reason not applying quantitative measurements to the large FoVs is to avoid potential distraction by unidentified laminae. The measurement on large FoVs containing two or more unidentified laminae would potentially mix grains aligned at different orientations. Because the orientation could vary more abruptly by aligning to and only close to bounding surface, therefore, the average over different laminae would obstacle the true preferred orientation more significantly than grain size who vary relatively gradually over laminae. The regions defined in smaller FoV is less likely introduce unseen lamina, at least manually, therefore is safer to perform quantitative grain orientation measurement.

The three selected FoVs illustrated in Figure 3.4(B) and analysed in Figure 3.5 are employed here again and divided into regions separated by bounding surface as in the first column of Figure B.5 . With grain long axes orientation calculated, for each region, the grains are filtered by orientations of the selected range, and area fraction of filtered

grains occupying each corresponding region are calculated and labelled as in 2-4 columns of Figure B.5 . By comparing the grain area fraction for each orientation range over different lamina regions the existence of preferred orientation could be verified.

For view-1 grains with orientation between 0°-30° are preferred occupied about 22% for the regions close to the nearly horizontal inter-laminaset bounding surface whiles 17% for the region above inclined intra-laminaset bounding surface. In contrast grains with orientation between 30°-60° are preferred occupied by 15% for the regions above inclined intra-laminaset bounding surface in comparison to around 10% for the regions close to the nearly horizontal surface. Similarly, grains with orientation between 60°-90° preferred occupied 13% for regions above inclined intra-laminaset bounding surface in comparison to less than 10% for regions close to the nearly horizontal surface. In View-2 and View-3, no strong preferred occupations in line with the inclination of bounding surface are observed for orientation between 0°-30°. For orientation between 30°-60° minor preferred occupations (about 1-2% higher area fraction) are observed for regions above inclined bounding surface than those close to the horizontal surface in both View-2 and View-3. For orientation between 60°-90° View-2 have no clear preferred occupation in line with bounding surface inclination whiles View-3 minor preferred orientation (0.5-1% higher area fraction) are observed for regions above inclined bounding surface than those above and below the horizontal surface.

The preferred occupation in line with bounding surface inclination provided evidence on the existence of preferred orientation. It suggested manually plotted regions, for View-1 from curved laminaset, reflected intra-laminaset lamina region with relatively high certainty because strong preferred orientation occurred close to the inclined bounding surface. The unclear preferred orientation in View-2 and View-3 suggested the manually labelled regions may not reflect the true intra-laminaset geometries for horizontal laminaset.

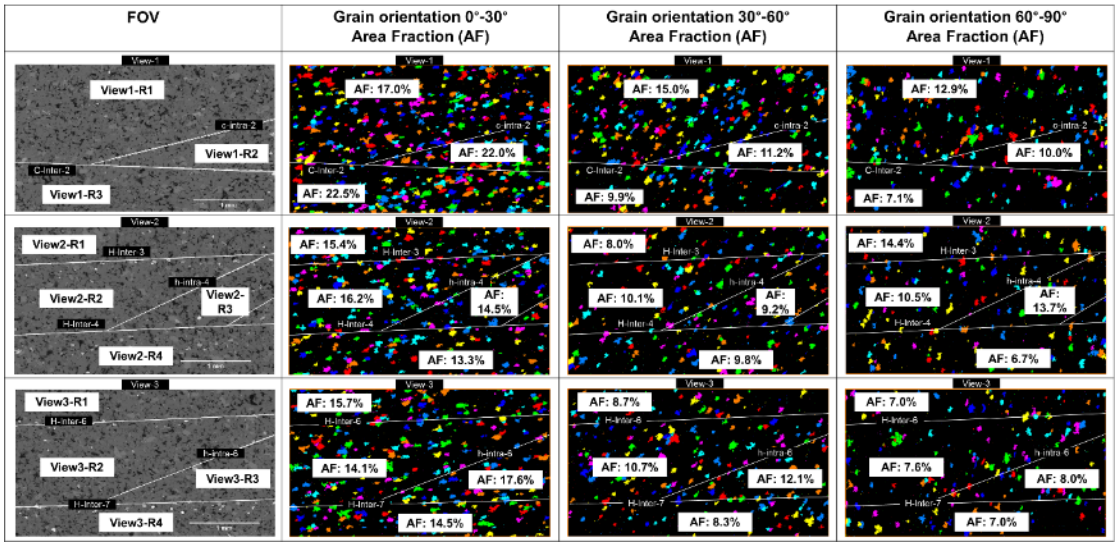

Figure B.5 Quantitative measurement of grain orientation for selected FoVs illustrated in Figure 3.5 (A) are illustrated in the first column, each FoV has been separated into regions by manually plotted bounding surfaces. Segmented and separated grains are labelled as regions in different colours. Grain long axes orientation are calculated in the range of -90° to 90°, from +Z direction to +X direction, for segmented and separated grains for three FoV. Taking identified bounding surfaces in selected FoVs are mainly between 0°-90°, grains with orientation fall into 0°-90° are investigated with a special focus. Column 2-4 plotted grains with orientation fall into three average split orientation range between 0°-90°. For each column, the area fraction (AF) of plotted grains within each region are measured and labelled.

Overall Characterisation

The main purpose of prior characterisation is grain and pore size, by which a reasonable lower resolution to enable simultaneous scan of BSEM and EDS image need to be figured out. This resolution should be as high to capture the smallest pores and grains need to be observed in this sample, but also low enough to enable simultaneous scanning. To this end, a pre-analysis on high resolution BSEM of T1 need to be carried out.

General information of grains and pores counted statistically on the BSEM image of T1 has been concluded in Table B.1 . Large numbers of samples ensured the representative of the result. The average size is the area of grains and pores in pixels, each pixel has an area of 0.6^2=0.36 um^2. The average grain size would be then 3102 um^2 and average pore size would be 71.8 um^2. With assumption of square shape, the diameter of 55um for grain and 8um for pore are estimated. One may notice that the sum of the percentage of area do not equal 100%, that is caused by two images are segmented by different procedure separately. And the grain separation would decrease the percentage area of grains to some extent.

As illustrated in Figure B.6 , histograms of the log of grains area and pores area have been plotted. To exclude noise generated by image, particles with area less than 10 pixels have

been excluded. Particles contacted with edge have also been excluded to avoid effect of uncompleted particles on edge.

To determine the appropriate resolution, the author treat the inversion point of 956 pixels (red point in Figure B.6 (b) as an important point because The author believes that: before this inversion point, particles with area below this point are secondary generated grains (compression, fracture, diagenesis etc.); after this inversion point, particles with area above this point are sediment grains originally deposited without other effects. Grains larger than this size would be more meaningful for studying the depositional environment.

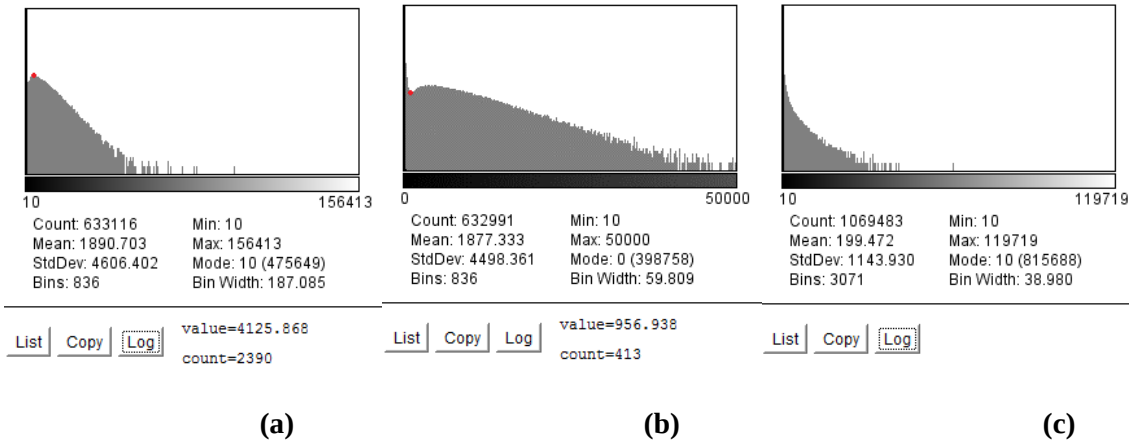

(a) **(b)** **(c)**

Figure B.6 Histograms of the log of the grains area and pores area: (a) full range of grain area (10-infinity), red spot points out the maximum value (b) part range of grain area (10-50000), red spot points out the inversion point (c) full range of pore area (10-infinity)

To estimate the resolution, for grain analysis, 956 pixels^2 in area have been chosen to be treated as the smallest grains the author needs to observe. By assuming a square shape and by resolution of 0.6um/ pixel, the smallest grain with diameter of 18.5um needed to be observed; by knowing that at least 10 pixels are needed to observe this smallest grain, a resolution of 1.85um is needed. For pore analysis, as there is not an inversion point, the mean value is needed to estimate the resolution needed, which was 199 pixels^2 in area; by same assumption, a resolution of 0.8um is needed.

Table B.1 Grains and Pores analysis result on BSEM (MASON and MORROW, 1991)

Count	Total Area	Average Size	%Area	Major	Minor	Angle	Circ.	Solidity
135975	1171788345	8617.675	72.077	128.121	77.26	92.795	0.246	0.762

B.3 X-ray L1 Processing

Hardening Effect

According to the literature, this effect could be effectively removed based on the concept of the 'rolling ball' algorithm described by Sternberg (1983). A ball of given radius is rolled over the bottom side of this surface; the hull of the volume reachable by the ball is the background to be subtracted. The radius of the ball should be at least as large as the radius of the largest object in the image that is not part of the background (Figure B.7(A). Assuming the bounding surfaces are typically 1-2 pixel thick as previously discussed, a ball with radius of 50 pixels would be definitely enough. After this correction, one could see the background been removed (Figure B.7(B, C)). Note in Figure 3.8-b the colour maps are also normalized to 0-255 for better human visual observation.

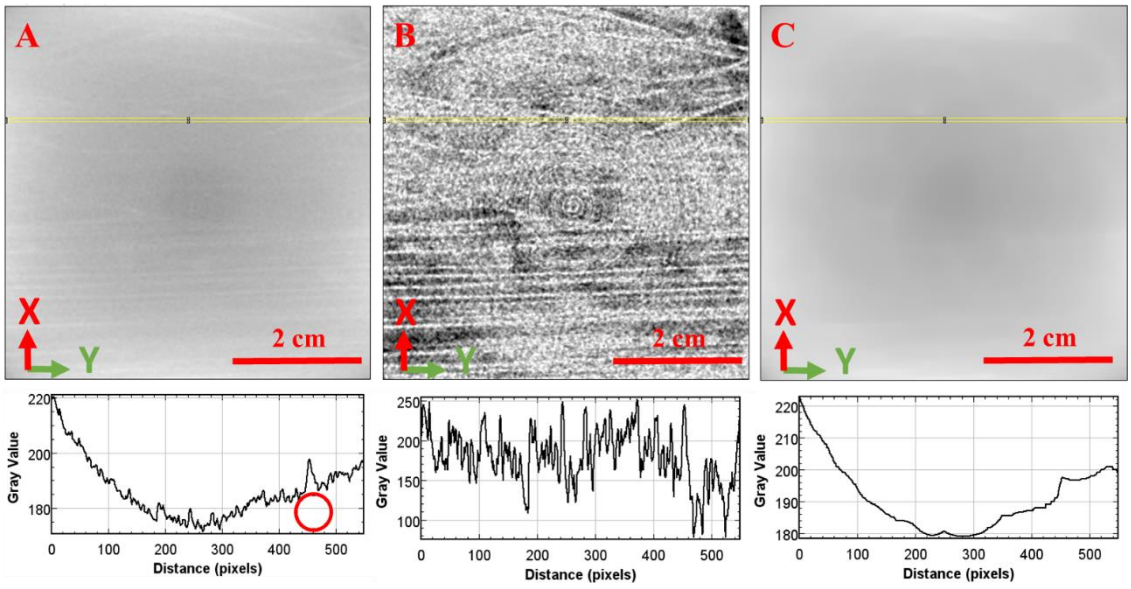

Figure B.7 2D images slices of (A) one raw CT slice image obtained by industrial CT; (b) hardening effect background removed image and (c) removed hardening effect background. Below each image are pixel intensities plots along the selected line as highlighted by yellow 1 pixel wide rectangular. The x-axis represents distance along the rectangular long axes and the y-axis is the pixel intensity. The red circle in intensity plot of A represents the ball with diameter of 50 pixels applied to remove background.

Simple Segmentation

A simple imaging analysis method ("segmentation editor" plugin in imageJ, see http://imagej.net/Segmentation_Editor) was applied to visually explore internal inter-laminaset structures. The method segment 3D bounding surface start with subjective traced bounding surface on 10 xy slices evenly distributed along Z axes and automatically connect missing bounding surface by propagation based on local intensity similarity. Figure B.8 illustrated three planar LBS been traced from one xy slice and labelled into different colours.

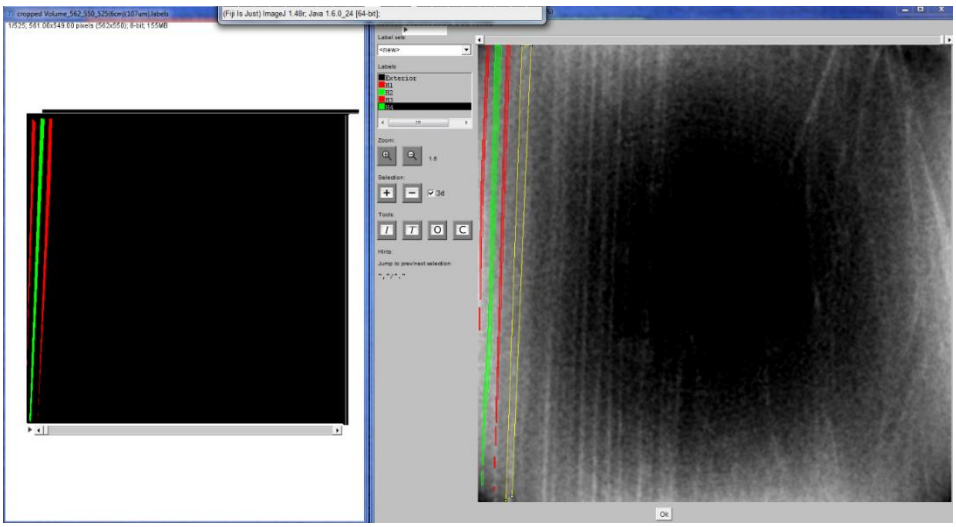

Figure B.8 illustration of simple segmentation by segmentation editor

Measurements

With segmented inter-LBS, thickness of laminasets between segmented inter-LBS could be quantitatively estimated at subjectively selected locations as Figure B.9. As an initial estimation, the measurements are selected at random locations in random slices. In Figure B.9, the locations of measurements are projected onto one slice for illustration. For the curved part, laminasets are measured on both a set randomly selected xy and xz slices.

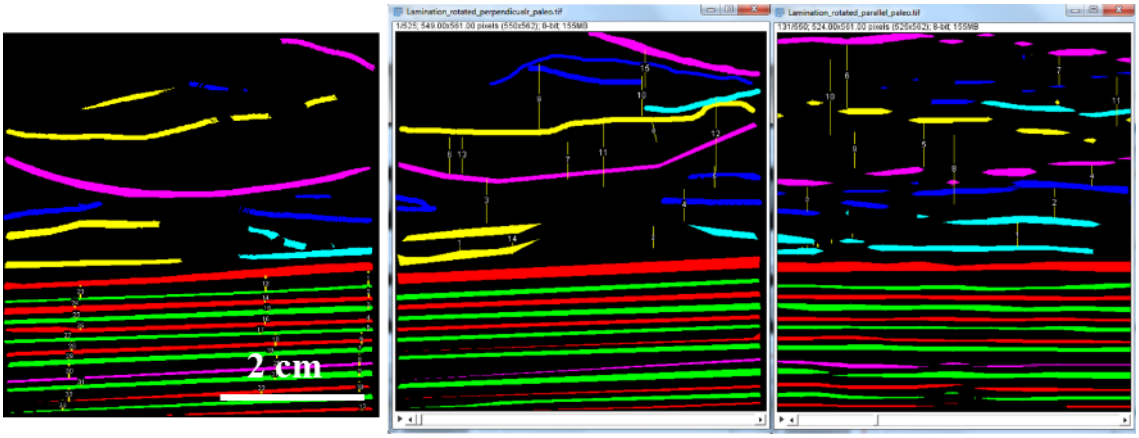

Figure B.9 subjective measure laminaset thickness between segmented inter-LBS at subjectively and randomly selected locations. Left shows planar laminaset thickness measurements at randomly selected locations; Middle shows curved laminaset thickness measurements at randomly selected locations in xy slices, and projected on one xy slice; Right shows curved laminaset thickness measurements at randomly selected locations in xz slices, and projected on one xz slice;

B.4 Intra-laminaset characterisation (T2)

Optical microscope analysis for compositional study

Among the four FoVs on T2, labelled as P1-P4 in Figure 3.12(B), P1 and P2 are located on the bounding surface of curved laminasets, while P3 and P4 on different bounding

surface in planar laminasets. Optical analysis using polarized light was performed at each of the four locations at three magnifications as in Figure B.10 . According to Figure 3.13, quartz and feldspar appear in light brown colour, while the dark brown indicates mainly heavy metal –iron and dolomite along with some calcium rich clay. Note that since the thin section has been impregnated with blue-stained epoxy resin before being polished, the pores appear in blue in the images.

Potential bounding surfaces are labelled manually, based on finer grain-pore and concentration of darker heavy minerals. According to 10X magnification images at four FoVs the bounding surface layer could be as thin as 2-3 grains thick for horizontal part. For curved laminaset, the bounding surface appears less concentrated and thicker up to 4-5 grains thick. Still the bounding surface appears to be a transitional band where a distinctive boundary is hard to be identified. Layered coarsening up, thus inverse grading, has been observed in 5X and 10X magnification images for four FoVs at vertical (+X) direction which is assumed to be the sedimentary direction based on previous laminaset geometry analysis. For both horizontal and curved laminasets, the layered inverse grading is parallel to manually-defined bounding surfaces. However, the intra-laminaset bounding surface is still hard to identify: the only one possibility is observed in P2 and yields a lamina about 6 grains thick. The estimations are implemented in Table 3.3.

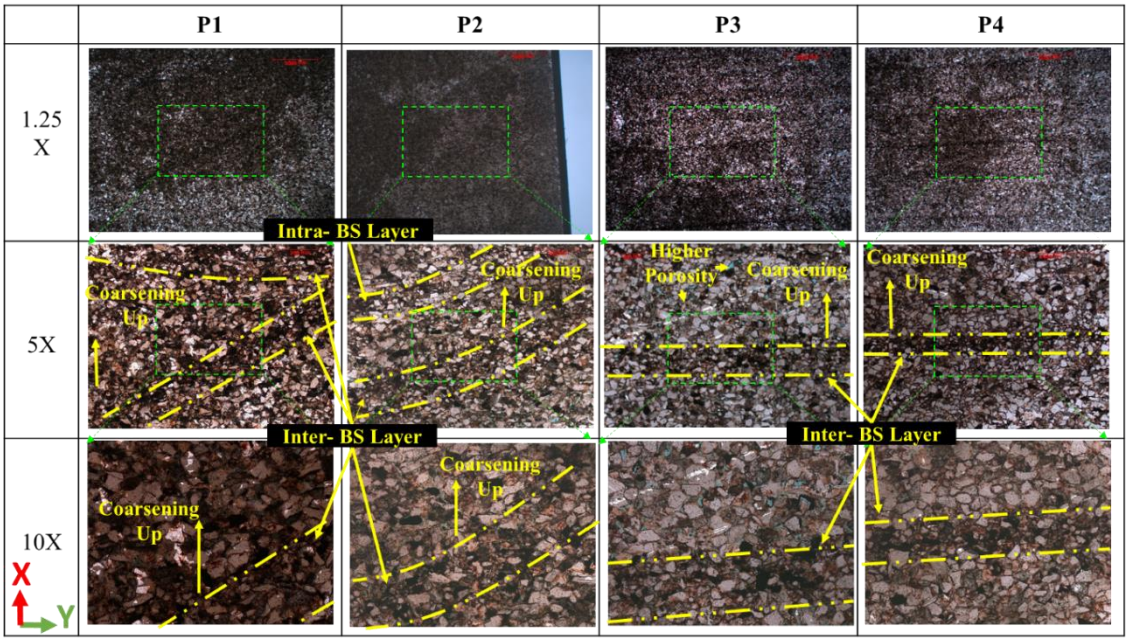

Figure B.10 Optical microscope images of 4 positions over three scales by polarized light.

EDS analysis

The “fake hole” and “true hole” analyses are performed on segmented EDS images of dolomite together with iron and calcite, in binary format, and scaled with arithmetic average to have similar average effect (without the Harding effect, though) to the same resolution to MXRT (100 micro square). The measurements are subjective and illustrated in Figure B.11 , where “fake holes” are identified by looking for regularly occurring small gaps with stable distances, following the trend of the bounding surface from Figure B.11 (A) and measured between 0.5-2mm, while “true holes” of erosion are also estimated on the same map, by searching for abnormal and randomly occurring gaps with larger distances and measured between 1.5-3mm. Gap length of the “true hole” of bioturbation could be estimated by measuring the diameter of clusters in the calcite map in Figure B.11 (B), where gap lengths are measured between 1-6mm. Considering those measurements are performed on a 2D cross-section, the measured gap length may not represent the longest axis of a hole in 3D. Only the largest measurements are used to be summarised in Table 3.2.

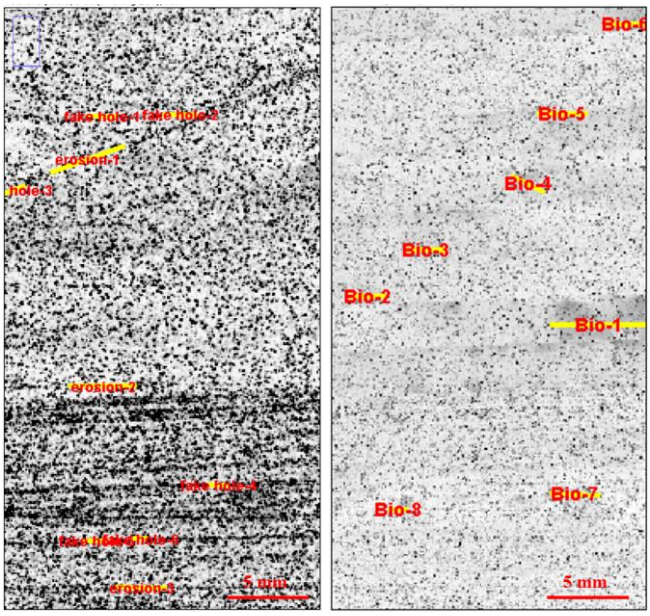

Figure B.11 segmented EDS images of dolomite together with iron (A) and Calcite(B), both scaled to 100-pixel micro resolution with dimension of 198x384.

Table B.2 Discontinuity of bounding surface

Discontinuity reason	"fake hole" of scattered iron and dolomite cementation	Distraction by feldspar	"true hole" of erosion	"true hole" of bioturbation
Length scale	< 2mm	<4mm	> 5mm	> 6mm

The measurement of distraction by feldspar is performed differently. It follows the logic by searching the average distance between small clusters of feldspar, because the distraction is caused by the Harding effect and would be more significant when it is closer to the bounding surface. Therefore, we want to know the average distance between the scatter distributed feldspar so as to have an idea within what size of neighbouring area of a bounding surface feldspar would be likely to occur thus as a distraction. Given the need to estimate grain-pore scale features, the measurements are performed on high resolution segmented EDS map of feldspar as Figure B.12 (A). Only the upper 19845x5000 part is measured, limited by computation power. The matrix between feldspars is separated loosely (by subjective judgement) as Figure B.12 (B-C) and labelled for measuring, as shown in Figure B.12 (D) (small particles are excluded by "4489" in pixel size, according to same inflection point method, but for long axes of grain measurements for T2. as shown in Figure B.12 (E). After excluding small distraction particles, an average long axis of 2.4 mm is calculated.

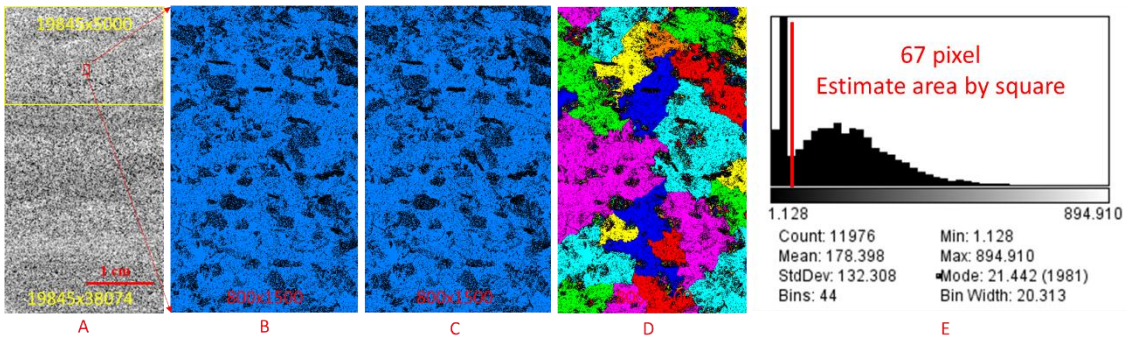

Figure B.12 (A) segmented feldspar with 1 micro pixel resolution and dimension of 19845x38074 pixels^2 (feldspar in black and the rest matrix in white); (B) zoomed in segmented area of 800x1500 for illustration of measurement (feldspar in black and rest matrix in blue); (C) separated rest matrix by separation object function in Avizo (with separation coefficient of 8); (D) labelled separated matrix; (E) distribution of long axes of segmented matrix..

B.5 Whole sample T2 measurement

An area distribution of grains and pores has been shown in Figure B.13, to give an overview of the T2 grain and pore distribution. As mentioned before, to avoid noise, particles below 10 pixels for grain and 4 pixels for pores are excluded. The inversion point for grains on T2 is 221 pixels; grains bigger than this value would be measured for parameters mentioned above.

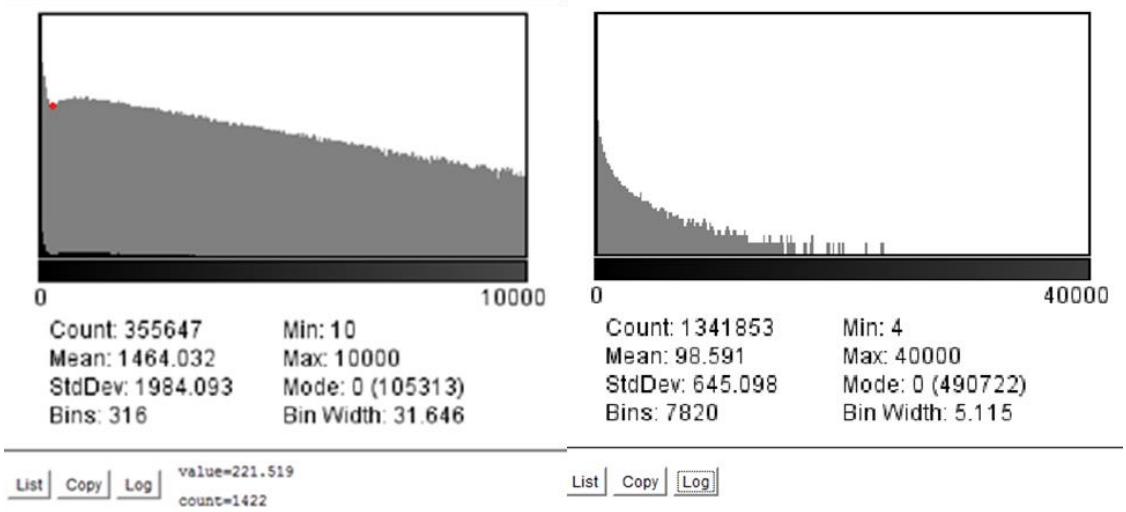

Figure B.13 Histograms of the log of the Left: full range of grain area (10-infinity), red spot points out the inversion point; Right: full range of pore area (4-infinity)

The summarise of measurements of grains in the range of 10-infinity and 221-infinity pixels in area are given in Table B.3 and Table B.4 , pores measurements in the range of 4-infinity are given in Table B.5 , the histograms of grains in the range of 221-infinity pixels in area of the measurements are given in Figure B.14 . Comparing Table B.3 and Table B.4 The author can see after The author remove small particles before the inversion point, total number of particles decreased about 1/3 and average size about doubled. However, the percentage of area only decreased 0.8%. So it is again proved that by remove particles smaller than the inversion point, it will effectively threshold out the interfere brought by small particles.

Table B.3 Summarize of measurements of grains in the range of 10-infinity pixels in area

Measurements	Count	Total Area	Average Size	%Area	Perim.	Circ.	Solidity
Sum/ Mean	359481	569355836	1583.827	75.354	189.572	0.48	0.771

Table B.4 Summarize of measurements of grains in the range of 221-infinity pixels in area

Measurements	Count	Average Size	%Area	Major	Minor	Angle	Circ.	Solidity
Sum/ Mean	198760	2803.698	73.753	70.204	43.776	89.825	0.347	0.771

Table B.5 Summarize of measurements of pores in the range of 4-infinity pixels in area

Measurements	Count	Average Size	%Area	Major	Minor	Angle	Circ.	Solidity
Sum/ Mean	1347635	91.794	16.372	8.472	3.841	79.842	0.633	0.715

Comparing Table B.3 -5 with Table B.1 , after converting the pixel size into physical size depending on different resolution, the average pore size is about same for both samples, the grains for the high resolution BSEM (0.6μm) is smaller than T2. This is because with T2 used lower resolution which excluded tiny fragments whose size below 1x1 μm^2, just as previously mentioned, small particles are removed during grain measurements. The porosity of both samples is also believed consistent considering the difference of resolution and position.

From Figure B.14 The author can see that by removing small particles, the distribution of area and perimeter changed from bimodal curves to unimodal curves. The overall circularity is inclined to 0 which stands for elongated shape. The aspect ratio, roundness and solidity distribution shown the overall grains have been relatively well rounded. Figure B.15 gives the rose diagrams for grain in the range of 221-infinity pixels in area. The overall mean orientation is 179.28, which means the majority are horizontal.

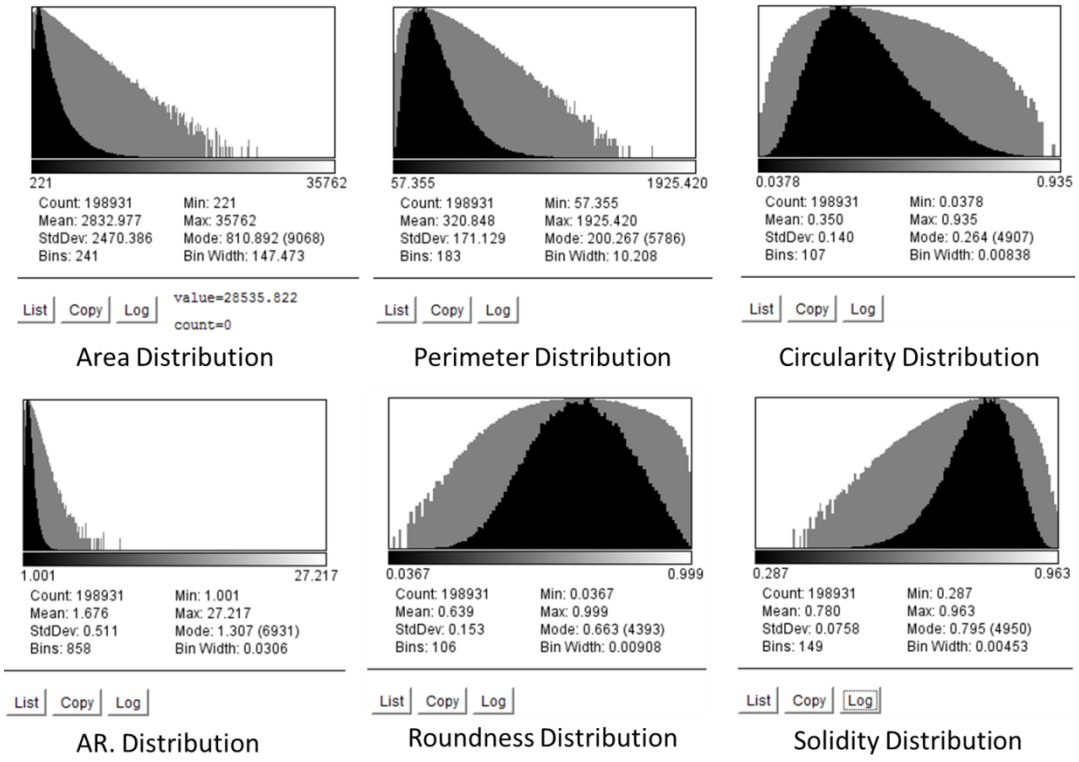

Figure B.14 Histograms of the overall measurements of grains in the range of 221-infinity pixels in area

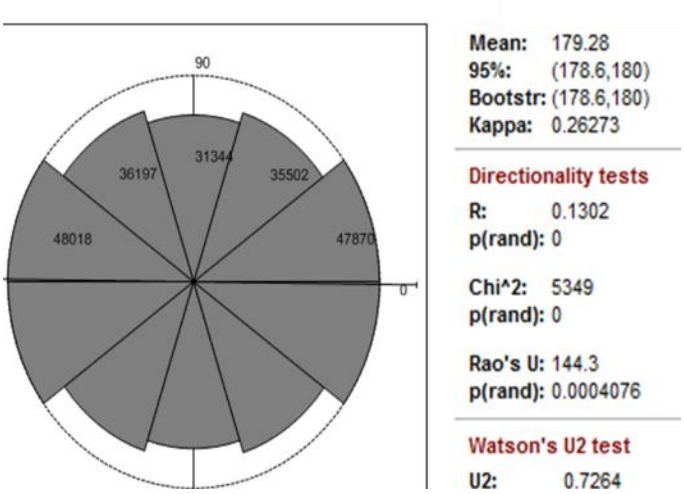

Figure B.15 Overall rose diagrams for grains in the range of 221-infinity pixels in area

B.6 S1 and S4 measurement

The measurements are performed on centre block of S1 and S4 low resolution images, with dimension of 480x480x954 voxels^3 as illustrated in Figure B.17 . Similarly, with

thin section BSEM images, anisotropic diffusion is applied to smooth and remove noise before segmentation.

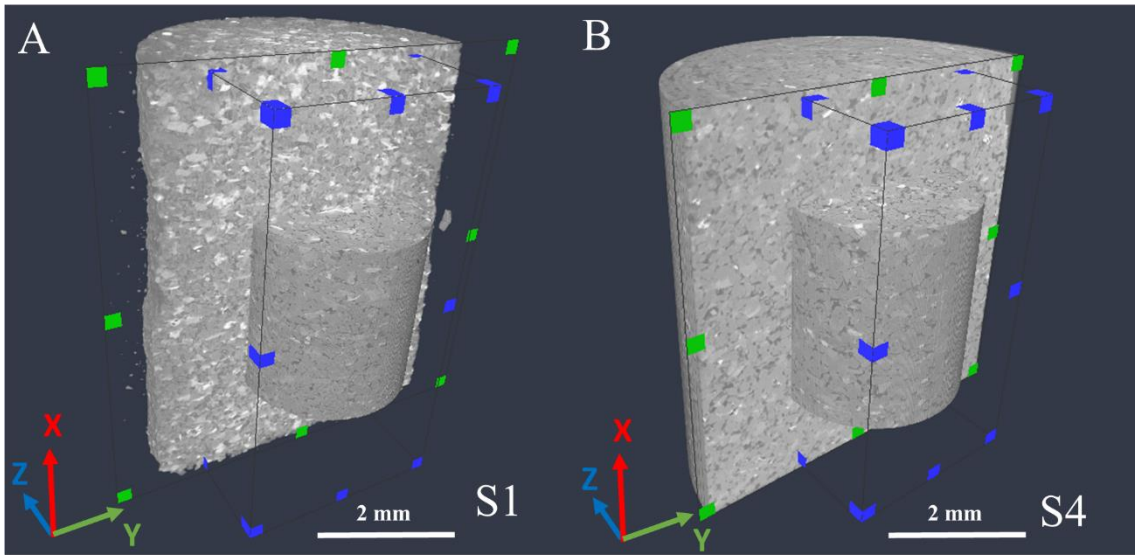

Figure B.16 (A) renders of S1 imaged at 4.3um and 1um FOV in the centre, blue boxed 480x480x954 voxels^3 volume are cropped for full quantification measurements; (B) renders of S4 imaged at 3.1 µm and 1um FOV in the centre, blue boxed 480x480x954 voxels^3 volume are cropped for full quantification measurements.

Segmentation

Same with 2D image, watershed based approach are applied for grain segmentation whiles Otsu thresholding approach applied for pore segmentation. Grain segmentation are performed on Avizo, gradient (55 for S1 and 45 for S4) are calculated to preserve edge and four phase are identified with intensity range of S1 (1:235-252, 2:207-235, 3:173-207, 4:0-173) and S4 (4, 45, 1:235-255, 2:158-235, 3:90-158, 4:0-90) for watershed segmentation. Erosion are applied on two "minority phases" on 1-bright and 2-light grey to separate particles. Finally, "separate object (1)" and "fill holes" are applied. Pore segmentation are performed on ImageJ, global intensity thresholding Otus approach applied.

Grain overall measurements

As discussed in section 2.2.2 small grain particles need to be excluded and an inflection point is decided as the threshold. Figure B.17 (A) and Figure B.17 (C) plotted grain histogram in the range of voxel volume between 0-3000 voxels^3 of S1 and S4 respectively. Inflection point are highlighted in yellow line therefore grains with volume less than 101 voxels^3 and 62 voxels^3 are removed during the grain measurements of

S1 and S4 respectively. Despite overall measurements summarised in Ch3. Table 3-3, overall grain orientations for S1 and S4 in rose map are given in Figure B.17 (B) and Figure B.17 (D). Note the grain orientation are measured as angle formed with the Z-axis in spherical coordinates as introduced in section 2.2.2. The coordinates are illustrated in Figure B.18 whiles the axes will not be shown in chapter 3 instead a consistent coordination through all subsamples are labelled.

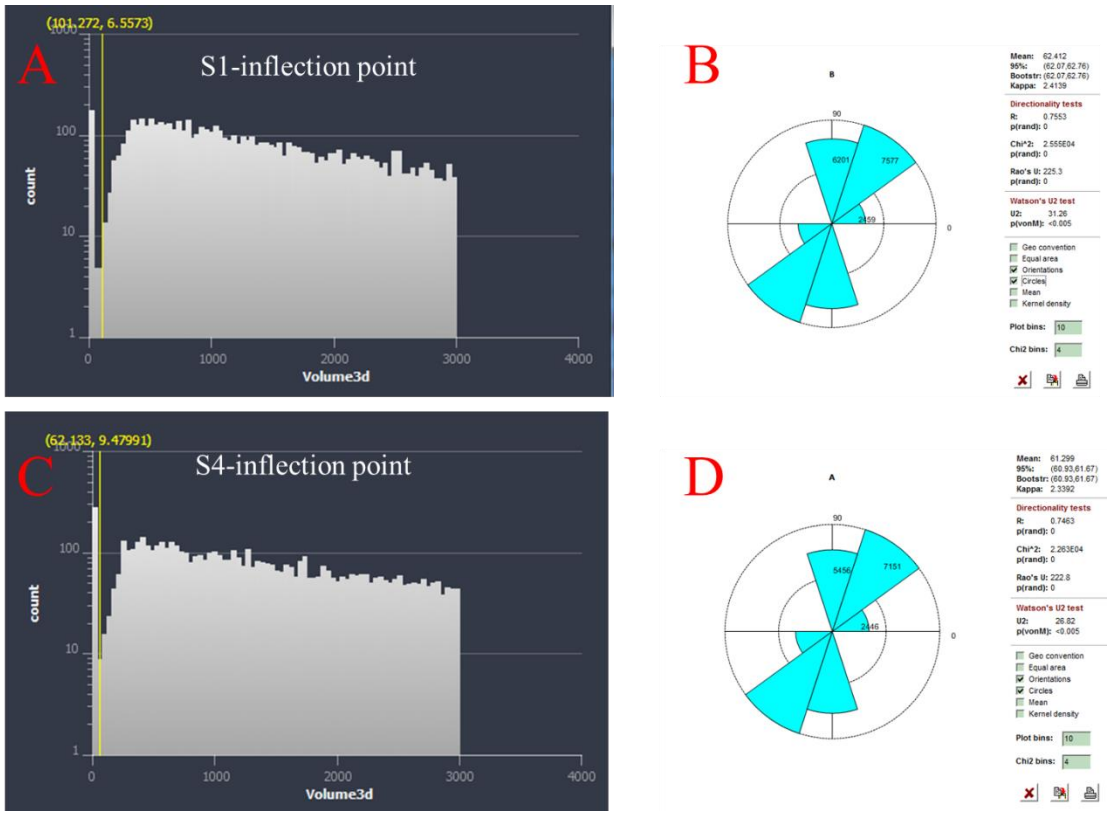

Figure B.17 Determination of inflection point on grain histogram (in the range of voxel volume between 0-3000 voxels^3) of S1 (A) and S4 (C); B and D gives grain orientation rose map plotted for S1 and S4 respectively after small grains removed.

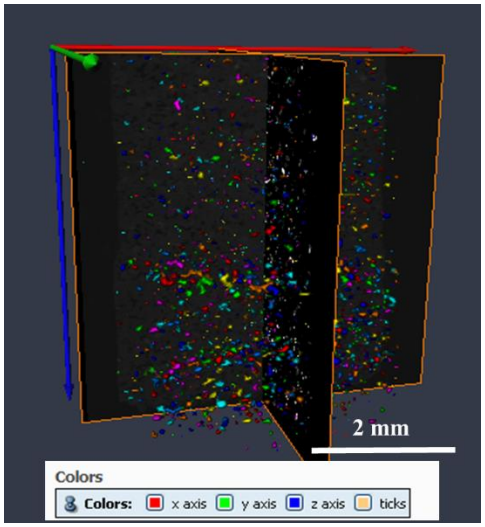

Figure B.18 Illustration of grain orientation measurement in labelled coordination

Brighter bounding surface segmentation and measurements

The segmentation of brighter heavy minerals is based on subjective thresholding as illustrated in A-B of Figure B.19 and Figure B.20 for S1 and S4 respectively. Segmented particles are labelled into different colours as in Figure B.19 (C) and Figure B.20 (C) for further character measurements.

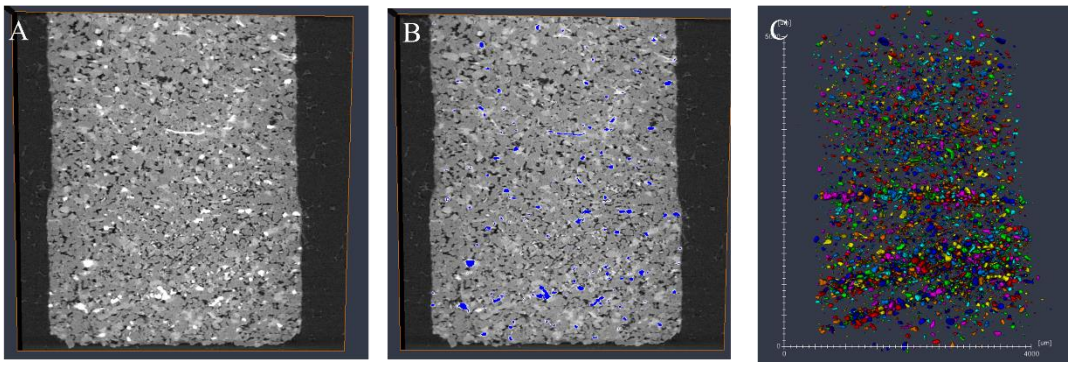

Figure B.19 Subjective thresholding of brighter heavy minerals of S1 in (A) and masked by blue in with thresholding setting of 9867/65535; (C) illustrated labelling of segmented heavy mineral particles in different colour to be measured.

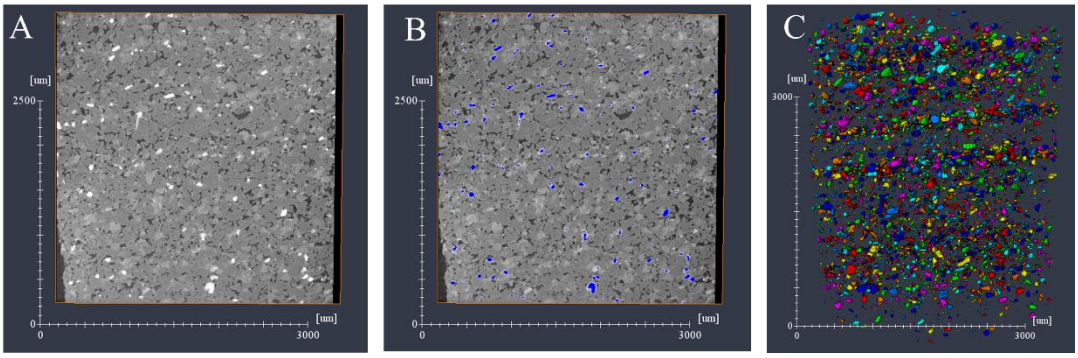

Figure B.20 Subjective thresholding of brighter heavy minerals of S4 in (A) and masked by blue in with thresholding setting of 12040/65535; (C) illustrated labelling of segmented heavy mineral particles in different colour to be measured.

Grading measurements

Horizontal planar S4

The measurement over horizontal planar sample S4 is rather straightforward because the bounding surfaces are horizontal (parallel with yz plane). As a result, the sampling box is parallel with bounding surface (Figure B.21 (A)) whose long axes along yz plane and short axes along sedimentation direction X are designed for S4 as illustrated in Figure B.21 (B). The thickness and sampling interval are designed with same principle as in 2D measurement. The thickness (short axes) along Z direction are kept same with the thickness discussed and designed in 2D measurement – 200um to include representative measurement and still as thin as possible to include even minor single layer (< 5 grains) variation. According to the resolution of 3D micro XRT image of 3.07x3.07x3.07 um^3/voxel, 50-pixel thickness has been designed (shown as blue endpoint box in Figure B.21 (A) and Figure B.21 (B)). Figure B.21 (C) illustrated grains measured within one sampling box labelled into different colours.

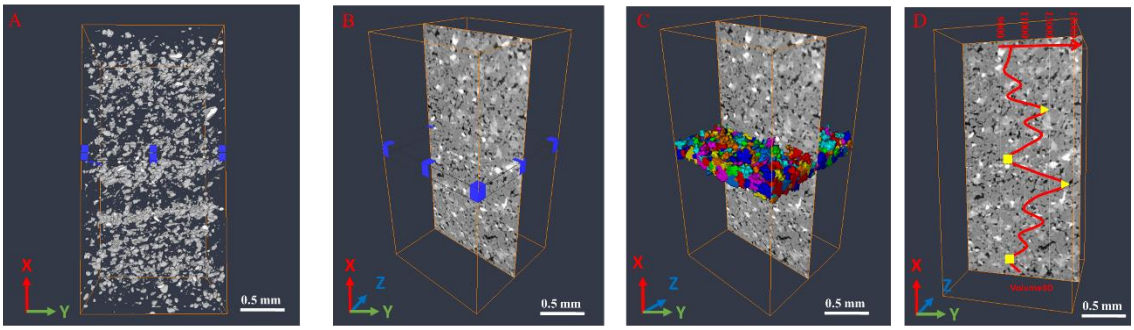

Figure B.21 Illustration of grading measurement on plug S4(3.07x3.07x3.07 um3/voxel) from horizontal part (cropped volume illustrated in Figure B.16 (A) and shown as orange colour bounding box): (A) illustrated segmented bright heavy mineral highlighted bounding surface and a designed 480x480x50 sampling box at 500 voxels depth parallel to the bounding surface with thickness about equal to one heavy mineral concentrated surface layer; (B) illustrated the sampling box on one xy slice are shown in

the middle for reference; (C) illustrated segmented grains fall into sampling box in B labelled in different colours for measurements; (D) measured grain volume in voxels versus depth plot and masked on one xy slice of cropped S4.

With sampling window designed, the measurements have been made by moving 50 voxels each time (with the same thickness) so there is no overlap between each other. The movement is along X direction, which is perpendicular to the paleocurrent direction (along yz plane) so the variation along the sedimentation direction can be captured. The measurement of each moved sampling window would represent one grading layer *l*. The measurement started from the bottom (S4_H15 in Table B.6) up to the top (S4_H-3) of S4 (Figure B.21 (A)). 19 movements (2.9mm thick) measurements were gained by moving at X+ direction as shown in

Table B.6 . The average grain volume is measured for each sampling box and plotted over depth and masked over on xy slice in the middle as reference in Figure B.21 (D).

For quantitative measurement, the average grain size increase rates are represented by a scaling factor (SF_l) and calculated for 2 monotonically grain size increasing interval for S4. The measured interval starting layer are highlighted in yellow square and end layer highlighted in yellow triangle in the log plot in Figure B.21 (D) and each interval is highlighted in yellow in

Table B.6 . The scaling factor's increasing gradient, defined as SF_{rate}, can be calculated as Equation B.1 to Equation B.2 and an arithmetic average of 3D volume scaling factor increasing gradient of 0.078 can be calculated. A 1D scaling factor of 0.025 at each axis can also be calculated based on Equation B.3. The two inverse grading intervals have an average thickness of 5 moves thus 767.5 μm.

$$SF_{rate\ (H2-6)} = \frac{\frac{12665}{9604.4}-1}{4} = 0.079 \qquad \text{Equation B.1}$$

$$SF_{rate\ (H6-8)} = \frac{\frac{14341}{9766.8}-1}{6} = 0.078 \qquad \text{Equation B.2}$$

$$SF_{rate\ 1D} = \sqrt[3]{1+0.078}-1 = 0.025 \qquad \text{Equation B.3}$$

Table B.6 Rectangular sampling box measurements with short axes and moving direction perpendicular to paleocurrent direction (so along sedimentation direction)

Depth	S4_H-3	S4_H-2	S4_H-1	S4_H0	S4_H1	S4_H2	S4_H3	S4_H4	S4_H5	S4_H6	S4_H7	S4_H8	S4_H9	S4_H10	S4_H11	S4_H12	S4_H13	S4_H14	S4_H15
GrainVolume 3D (voxels^3)	99133.16	96700.33	93820.8	107033.6	96666.67	12665.4	11016.8	12414.3	10970.3	9604.39	11866.1	14340.7	11949.1	10961.3	1527	10590.2	11168.4	9766.83	10585.4

Curved laminaset S1

Measurement over curved sample S1 is not as straightforward as for horizontal planar sample S4. The first thing to do before measurement is define the bounding surface so that the measurement sampling box could be designed representing the thin grading layer and moving along with sediment direction. Similarly to what was done on the industrial XRT image, the bounding surface was highlighted by the more brightly presented heavy mineral which needed to be extracted. Taking the µ-XRT image provided high resolution on identifying heavy minerals in this section the simple semi-automatic approach is applied to extract the bounding surface from µ-XRT image of S1. The approach is referred to as segmentation editor tool box in FIJI (Schindelin et al., 2012). The basic principle is to manually label the structure of interest from one slice over several slices from an image stack; the machine would then propagate voxels with similar intensity on those un-labelled slices in 3D. For this sample, 10 slices spread over a 480 slice-thick image stack of S1 are labelled to extract the rest of the 3D bounding surface. The extracted bounding surface as shown in Figure B.22 (A) captured the 3D surface structure but appeared to lack continuity in Z direction. An inclined sampling box and a horizontal sampling box are therefore traced with unconnected regions overlaid on the extracted slices (Figure B.22 (B-C)). \the same thickness (50 pixels thick) and moving distance (50 pixels) have been used. Figure B.22 (B-C) also illustrates grain particles falling into each sampling box, which have been labelled into different colours. For an inclined curved laminaset, measurement started with Sur1 in Table B.7 and three moves have been made (Sur1-1 to

Sur 1-3) along X+ direction. Horizontal planar measurement starts from H0 with the same sampling box with S4 and 6 movement has been made along X+ direction.

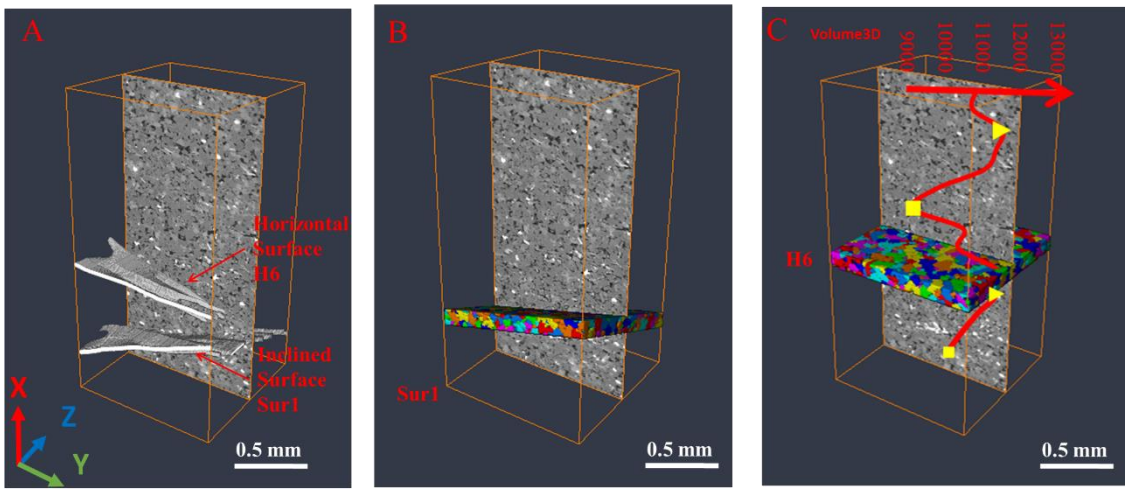

Figure B.22 Illustration of grading measurement on plug S1 (4.3x4.3x4.3 um^3/voxel) from curved part (cropped volume illustrated in Figure 3-19(A) and shown as orange colour bounding box), one xy slice are illustrated in the middle for reference: (A) illustrated one horizontal and one inclined surface traced with semi-automated method; (B) illustrated segmented grains fall into a sampling box Sur1 created for inclined surface in A are labelled in different colours for measurements; (C) illustrated segmented grains fall into a sampling box H0 created for horizontal surface in A are labelled in different colours for measurement, measured grain volume in voxels versus depth plot and masked on one xy slice of cropped S1.

Similar with S4, SF_{rate} are calculated for one monotonically grain size increasing interval in horizontal planar part and one for inclined part are calculated separately. The measured interval starting layer are highlighted in yellow box in log plot in Figure B.22 (C) and each interval are highlighted in yellow in Table B.7 . The scaling factor increasing gradient defined as SF_{rate} could be calculated as Equation B.4 and Equation B.5 and an arithmetic average of 3D volume scaling factor increasing gradient of 0.065 could be calculated. A 2D scaling factor of 0.021 at each axes could also be calculated based on Equation B.6. The two inverse grading interval has an average thickness of 3.5 moves thus 752.5 μm.

$$SF_{rate\ (H0-1-6)} = \frac{\frac{11533.7}{9152.96}-1}{4} = 0.065 \qquad \text{Equation B.4}$$

$$SF_{rate\ (S0-3)} = \frac{\frac{12003.79}{10056.57}-1}{3} = 0.065 \qquad \text{Equation B.5}$$

$$SF_{rate\ 2D} = \sqrt[3]{1+0.065}-1 = 0.021 \qquad \text{Equation B.6}$$

Table B.7 Sampling box measurements of inclined sample S1 with moving along sedimentation direction

Depth	H0-3	H0-2	H0-1	H0	H1	H2	H3	H4	H5	H6	Sur1-3	Sur1-2	Sur1-1	Sur1
GrainVolume3D (voxels^3)	1083 9.4	1075 7	1153 3.7	1137 7.8	1108 2	9783. 57	9152. 96	1048 7.4	1037 3.7	1134 2.6	12003. 79	11280. 86	10617. 92	10056. 57

APPENDIX C -Chapter4

C.1 Verification of simulated MXRT

Taking there is no binary ground truth of image, the verification here are compare arithmetic average BSEM, low resolution BSEM and simulated MXRT with real MXRT image at similar location. It is however challenge to compare those images because: 1) all those images are not exactly registered; 2) even registered, compare intensity values across those images are meaningless because different imaging principle would yield different contrast between structures of interests, referred to bounding surface in this work, over matrix even after normalization. Taking the work here is focus on verifying whether or not linear bounding surface structures are revealed, a convolutional filter based method is proposed to characterize frequency of patterns occurred within each image with same standard of measurement. It is achieved as follows: 1) define one filter bank (a set of filters) represent the linear structures occurred in target image to be characterized; 2) calculate convolutional similarity around each pixel with one image to each filters in the filter bank; 3) plot a histogram, for one image, the average response of each filter over each pixels in the image versus every filter in the filter bank; 4) assume average response represent the frequency a pattern described by one filter occurred in the image, thus the histogram gives a description the possibility of occur on interested patterns from given filter bank; 5) by apply such process to each image to be evaluated, images could be compared, in terms of pattern given by the filter bank.

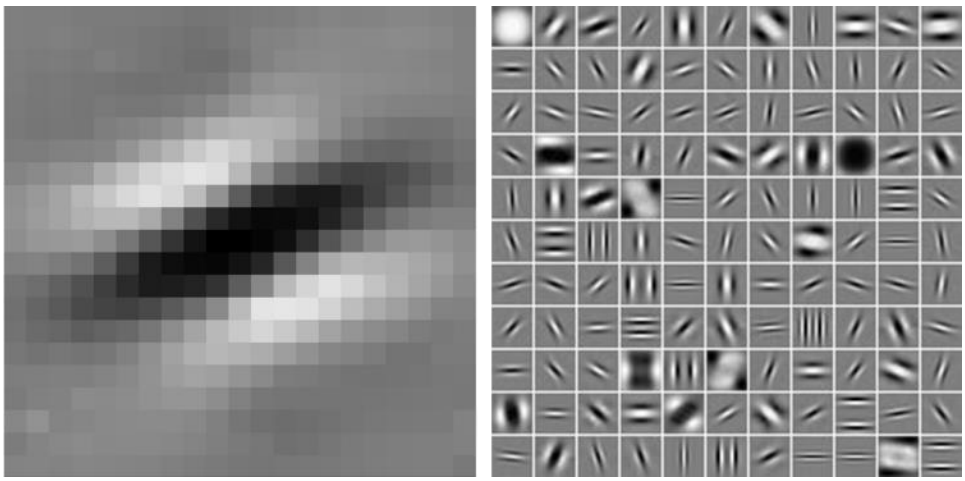

(A) (B)

Figure C.1 (A) one example of 21x21 filter and (B) learnt 121 filter bank contain 121 filters of size 21x21 pixels square which learnt from generic benchmark image (Rigamonti et al., 2011b)

In this work the filter bank of learnt 121 that has been used to segment the bounding surface from MXRT is used, given its variability on capturing bounding surface structure and size has been discussed. Learnt 121 are convolved to each pixel of arithmetic average BSEM, low resolution BSEM and simulated MXRT with real MXRT image, and the convolutional response of each 121 filters are plotted in histogram as described in Figure C.2 . Visually the histogram curves of simulated MXRT with real MXRT image matched well but clearly different with arithmetic average BSEM, low resolution BSEM (who are similar to each other). To better quantify the difference, the difference between average response of each filter in the histogram of each arithmetic average BSEM, low resolution BSEM and simulated MXRT are compared to real MXRT image, and the average difference over 121 filters are calculated in Table C.1 . Take the histogram of MXRT of L1 as reference, the relative difference of histogram of arithmetic average BSEM, low resolution BSEM scanning and simulated MXRT are 3.81, 3.64 and 1.02 respectively (where 1 stands for 100% same histogram with MXRT of L1).

Figure C.2 convolutional response of each 121 filters are plotted in histogram for arithmetic average BSEM (orange), low resolution BSEM (grey) and simulated MXRT (yellow) with real MXRT image (blue) with full histogram given in upper left of zoomed in view.

Table C.1 Average Difference over MXRT by 121 filters feature vector/ average of 121 filters feature vector (in convolution value)

	Average Difference over MXRT
AverageDownscale_BSEM_f_ver	3.81
BSE_20_kV_cropped	3.64
out_C_O_Na_Mg_Al_Si_K_Ca_Fe	1.02

C.2 Sampling window configuration

Size of sampling window

The REV of a rectangular windows is evaluated on segmented grains and pores images. The evaluations are based on the measurements of average grain size, average pore size and percentage of area of grains and pores correspondingly. For a rectangular sampling window, it starts with a rectangular window with its width equal to the width of the entire BSEM image, which equals to 19845 pixels. The height of it starts with 100 pixels then each incensement of 50 until it gets to 1000 pixels in height. The author randomly sampling 50 times in different height to make sure got enough and representative information. After sampling, the mean values of each sampling size by 50 times measure of abovementioned measurements have been gained. The corresponding standard deviation for each sampling size could also been calculated. The coefficient of variation (CV), defined as the ratio of the standard deviation to the mean, could then be calculated and plotted Figure C.3.

The plot of Coefficient of variation **(**CV**)** for all grains and pores measurements versus Rectangular sampling size in Figure C.3 did not shown converged well. This indirectly proved that heterogeneity exit between laminations. The reason is the shape of rectangular sampling window is more similar with the shape of the laminations, and the long axis of the rectangular window is parallel to the horizontal laminations. Percentage of pore area kept low CV who did not changed much whiles percentage of grains area converged quickly at the height around 200 pixels.

The measurement of average size, comparing with percentage area, showed a higher sensitivity. In this work the REV are decided depending on the convergence of percentage area curves only. It as a result gives a REV of 19845x200-19845x300 pixels^2 for rectangular window. This would also satisfy the previously mentioned principle, the height of sampling window is smaller than the thickness of the thinnest lamination, which is about 1 mm (1000 pixels). This section illustrates calculation REV of sampling window for two shape of sampling windows, rectangular and square, in 2D.

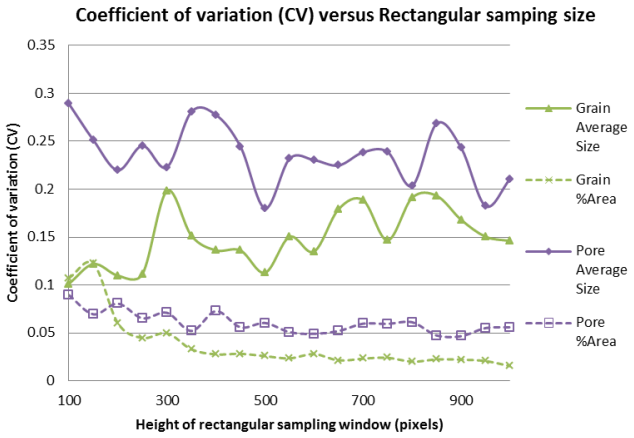

Figure C.3 Coefficient of variation (CV) versus Rectangular sampling size

C.3 Registered T2 characterisation

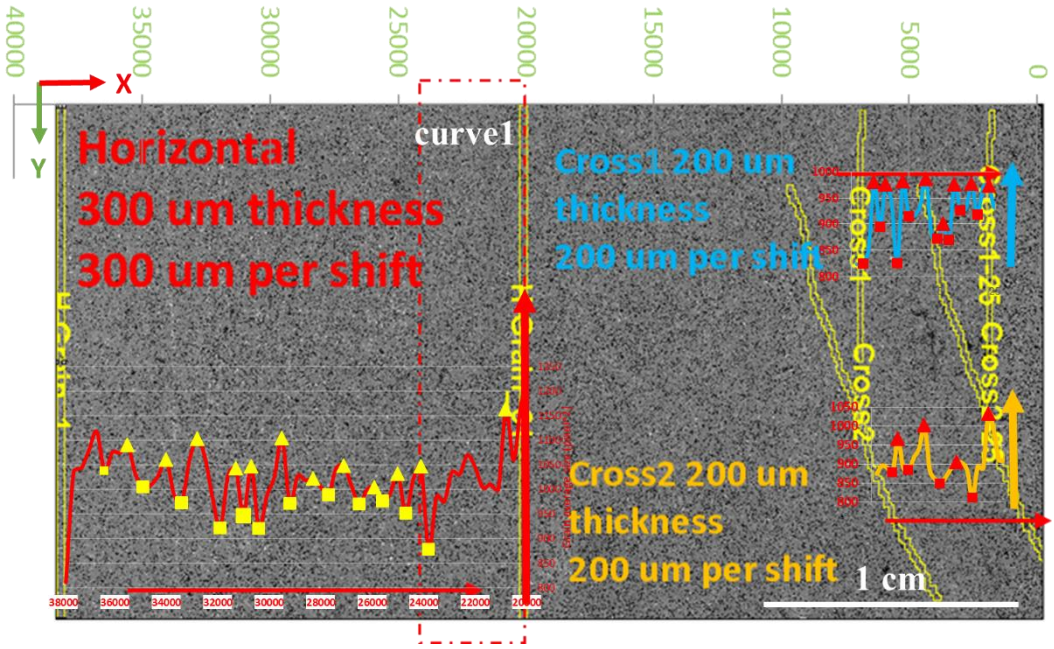

Figure C.4 measured log plots of measured average grain size in pixel area by three sampling window and masked onto BSEM of T2 (rotated 90 right from Figure 4-14(B) for better illustration of log plots), X axes are labelled from top of T2 (right) down to bottom (left) in µm units; horizontal log plot are given in red colour and masked between 39845 to 20000 µm on X axe, laminae start are labelled in yellow square and end in yellow triangle; Cross 1 are plotted in blue and Cross 2 in orange, laminae start are labelled in red square and end in red triangle.

Measurements of log plots are given in Table C.2 for horizontal planar, Table C.3 for curve 1 and Table C.4 for cross-1 and cross-2. The measurements of gradient following same equation as S1 and S4. Measured intervals are labelled in different colours. Measured length represent lamina thickness are count in number of moves, each move has an interval of 300um for horizontal part and 200 for cross 1 and 2.

Table C.2 Sampling window log measurements of horizontal planar laminaset

Horizontal Planar				
Y_coordination(pixels)	Grain Average Size	Circulation length	2D gradient	1D per 200um thick
average		2.273	0.029	0.014
37900	811.061			
37600	1035.526			
37300	1042.754			
37000	1080.16			
36700	1117.698			
36400	1037.648	3	0.016916	
36100	1075.501			
35800	1074.334			
35500	1090.307			
35200	1031.346			
34900	1005.212	3	0.018378	
34600	1008.81			
34300	1029.566			
34000	1060.632			
33700	989.646			
33400	973.032	2	0.066761	
33100	1058.954			
32800	1102.954			
32500	1066.107			
32200	983.151			
31900	922.146	2	0.065039	
31600	1028.825			
31300	1042.096			
31000	946.437	1	0.105487	
30700	1046.274			
30400	920.561	3	0.06643	
30100	985.668			
29800	1025.731			
29500	1104.019			
29200	971.167	3	0.017118	
28900	1026.985			
28600	1018.703			
28300	1021.039			
28000	1005.413			
27700	988.576	2	0.02982	
27400	1043.002			
27100	1047.535			
26800	1007.045			
26500	970.469	2	0.01738	
26200	999.579			

25900	1004.203			
25600	976.556	2	0.028263	
25300	991.86			
25000	1031.756			
24700	952.059	2	0.049381	
24400	1020.994			
24100	1046.087			

Table C.3 sampling window log measurements of curve 1

Curve1				
Y_coordination(pixels)	Grain Average Size	Circulation length	2D gradient	1D per 200um thick
average		13.000	0.013	0.006
23800	877.537	13	0.019056	0.009
23500	985.643			
23200	975.066			
22900	1035.145			
22600	1030.936			
22300	1069.832			
22000	1045.195			
21700	1003.668			
21400	1010.554			
21100	1000.459			
20800	1162.065			
20500	1059.752			
20200	1178.253			
19900	1203.628			

Table C.4 sampling window log measurements of curved laminaset

Cross 1 and 2				
Slice	Grain Average Size 4-infinity	Circulation length	2D gradient	1D per 200um thick
		2.000	0.072	0.035
Cross1-0	822.94			
Cross1-1	824.57	2	0.094457	
Cross1-2	850.724			
Cross1-3	980.342			
Cross1-4	894.813	1	0.090582	
Cross1-5	975.867			
Cross1-6	943.337			
Cross1-7	824.796	1	0.189345	
Cross1-8	980.967			

Cross1-9	914.815	3	0.025887	
Cross1-10	916.139			
Cross1-11	933.697			
Cross1-12	985.86			
Cross1-13	879.148			
Cross1-14	872.287	1	0.031748	
Cross1-15	899.98			
Cross1-16	869.345	1	0.12208	
Cross1-17	975.475			
Cross1-18	926.547	2	0.026746	
Cross1-19	930.953			
Cross1-20	976.109			
Cross1-21	917.856	2	0.030415	
Cross1-22	971.345			
Cross1-23	973.689			
Cross1-24	931.633			
Cross1-25	984.405			
Cross2-0	874.423			
Cross2-1	895.344			
Cross2-2	889.876			
Cross2-3	876.662	1	0.100895	
Cross2-4	965.113			
Cross2-5	889.175			
Cross2-6	883.645	3	0.044163	
Cross2-7	916.799			
Cross2-8	941.475			
Cross2-9	1000.718			
Cross2-10	882.354			
Cross2-11	859.834			
Cross2-12	848.254	4	0.016211	
Cross2-13	866.35			
Cross2-14	887.877			
Cross2-15	903.76			
Cross2-16	903.257			
Cross2-17	884.626			
Cross2-18	811.312	3	0.090867	
Cross2-19	894.111			
Cross2-20	888.909			
Cross2-21	1032.477			
Cross2-22	988.717			
Cross2-23	911.008			
Cross2-24	913.374			
Cross2-25	950.351			

APPENDIX D -Chapter5

D.1 MPS configuration

Detailed MPS parameters setting for regions based on measurements

Table D.1 Detailed parameter arrangement calculated for regions between 1-80 based on measurement result

Ln	1.00	2.00	3.00	4.00	5.00	6.00	7.00	8.00	9.00	10.00	11.00	12.00	13.00	14.00	15.00
ScalingFactor(X,Y,Z	1.00	1.02	1.04	1.06	1.08	1.10	1.12	1.14	1.16	1.18	1.20	1.22	1.24	1.26	1.28
Porosity	0.15	0.15	0.17	0.17	0.16	0.15	0.15	0.15	0.13	0.16	0.17	0.16	0.16	0.13	0.15
Matrix_P	0.85	0.85	0.83	0.83	0.84	0.85	0.85	0.85	0.87	0.84	0.83	0.84	0.84	0.87	0.85
Orientati	0	0	0	0	0	0	0	0	0	0	0	0	0	0	0
Ln	16.00	17.00	18.00	19.00	20.00	21.00	22.00	23.00	24.00	25.00	26.00	27.00	28.00	29.00	30.00
ScalingFactor(X,Y,Z	1.30	1.32	1.34	1.36	1.38	1.40	1.42	1.44	1.46	1.48	1.50	1.52	1.54	1.56	1.58
Porosity	0.13	0.15	0.13	0.14	0.16	0.17	0.17	0.17	0.17	0.13	0.13	0.15	0.17	0.17	0.13
Matrix_P	0.87	0.85	0.87	0.86	0.84	0.83	0.83	0.83	0.83	0.87	0.87	0.85	0.83	0.83	0.87
Orientati	0	0	0	0	0	0	0	0	0	0	0	0	0	0	0
Ln	31.00	32.00	33.00	34.00	35.00	36.00	37.00	38.00	39.00	40.00	41.00	42.00	43.00	44.00	45.00
ScalingFactor(X,Y,Z	1.00	1.02	1.04	1.06	1.08	1.11	1.13	1.15	1.17	1.19	1.21	1.23	1.25	1.27	1.29
Porosity	0.15	0.16	0.17	0.17	0.14	0.16	0.15	0.16	0.16	0.15	0.17	0.16	0.16	0.16	0.12
Matrix_P	0.85	0.84	0.83	0.83	0.86	0.84	0.85	0.84	0.84	0.85	0.83	0.84	0.84	0.84	0.88
Orientati	30.00	30.00	30.00	30.00	30.00	30.00	30.00	30.00	30.00	30.00	30.00	30.00	30.00	30.00	30.00
Ln	46.00	47.00	48.00	49.00	50.00	51.00	52.00	53.00	54.00	55.00	56.00	57.00	58.00	59.00	60.00
ScalingFactor(X,Y,Z	1.32	1.34	1.36	1.38	1.40	1.42	1.44	1.46	1.48	1.50	1.53	1.55	1.57	1.59	1.61
Porosity	0.13	0.12	0.13	0.13	0.12	0.16	0.16	0.15	0.13	0.16	0.16	0.15	0.16	0.15	0.15
Matrix_P	0.87	0.88	0.87	0.87	0.88	0.84	0.84	0.85	0.87	0.84	0.84	0.85	0.84	0.85	0.85
Orientati	30.00	30.00	30.00	30.00	30.00	30.00	30.00	30.00	30.00	30.00	30.00	30.00	30.00	30.00	30.00
Ln	61.00	62.00	63.00	64.00	65.00	66.00	67.00	68.00	69.00	70.00	71.00	72.00	73.00	74.00	75.00
ScalingFactor(X,Y,Z	1.63	1.65	1.67	1.69	1.71	1.74	1.76	1.78	1.80	1.82	1.84	1.86	1.88	1.90	1.92
Porosity	0.16	0.16	0.12	0.13	0.16	0.15	0.12	0.12	0.12	0.13	0.16	0.13	0.16	0.17	0.17
Matrix_P	0.84	0.84	0.88	0.87	0.84	0.85	0.88	0.88	0.88	0.87	0.84	0.87	0.84	0.83	0.83
Orientati	30.00	30.00	30.00	30.00	30.00	30.00	30.00	30.00	30.00	30.00	30.00	30.00	30.00	30.00	30.00
Ln	76.00	77.00	78.00	79.00	80.00										
ScalingFactor(X,Y,Z	1.95	1.97	1.99	2.01	2.03										
Porosity	0.16	0.16	0.17	0.14	0.17										
Matrix_P	0.84	0.84	0.83	0.86	0.83										
Orientati	30.00	30.00	30.00	30.00	30.00										

Detailed large contrast MPS parameters setting for regions

Table D.2 Detailed parameter arrangement calculated for regions between 1-80 based on large contrast assumption

Ln	1.00	2.00	3.00	4.00	5.00	6.00	7.00	8.00	9.00	10.00	11.00	12.00	13.00	14.00	15.00
ScalingFactor(X,Y,Z	1.00	1.20	1.40	1.60	1.80	2.00	2.20	2.40	2.60	2.80	3.00	3.20	3.40	3.60	3.80
Porosity	0.17	0.16	0.15	0.15	0.16	0.13	0.14	0.15	0.16	0.16	0.14	0.17	0.15	0.16	0.14
Matrix_P	0.83	0.84	0.85	0.85	0.84	0.87	0.86	0.85	0.84	0.84	0.86	0.83	0.85	0.84	0.86
Orientati	0.00	0.00	0.00	0.00	0.00	0.00	0.00	0.00	0.00	0.00	0.00	0.00	0.00	0.00	0.00
Ln	16.00	17.00	18.00	19.00	20.00	21.00	22.00	23.00	24.00	25.00	26.00	27.00	28.00	29.00	30.00
ScalingFactor(X,Y,Z	4.00	4.20	4.40	4.60	4.80	5.00	5.20	5.40	5.60	5.80	6.00	6.20	6.40	6.60	6.80
Porosity	0.14	0.13	0.14	0.15	0.14	0.14	0.15	0.16	0.13	0.15	0.16	0.16	0.16	0.14	0.13
Matrix_P	0.86	0.87	0.86	0.85	0.86	0.86	0.85	0.84	0.87	0.85	0.84	0.84	0.84	0.86	0.87
Orientati	0.00	0.00	0.00	0.00	0.00	0.00	0.00	0.00	0.00	0.00	0.00	0.00	0.00	0.00	0.00
Ln	31.00	32.00	33.00	34.00	35.00	36.00	37.00	38.00	39.00	40.00	41.00	42.00	43.00	44.00	45.00
ScalingFactor(X,Y,Z	1.00	1.20	1.40	1.60	1.80	2.00	2.20	2.40	2.60	2.80	3.00	3.20	3.40	3.60	3.80
Porosity	0.13	0.13	0.16	0.17	0.14	0.14	0.15	0.15	0.12	0.17	0.13	0.16	0.17	0.15	0.15
Matrix_P	0.87	0.87	0.84	0.83	0.86	0.86	0.85	0.85	0.88	0.83	0.87	0.84	0.83	0.85	0.85
Orientati	30.00	30.00	30.00	30.00	30.00	30.00	30.00	30.00	30.00	30.00	30.00	30.00	30.00	30.00	30.00
Ln	46.00	47.00	48.00	49.00	50.00	51.00	52.00	53.00	54.00	55.00	56.00	57.00	58.00	59.00	60.00
ScalingFactor(X,Y,Z	4.00	4.20	4.40	4.60	4.80	5.00	5.20	5.40	5.60	5.80	6.00	6.20	6.40	6.60	6.80
Porosity	0.15	0.17	0.16	0.13	0.16	0.16	0.14	0.17	0.15	0.15	0.16	0.16	0.17	0.16	0.12
Matrix_P	0.85	0.83	0.84	0.87	0.84	0.84	0.86	0.83	0.85	0.85	0.84	0.84	0.83	0.84	0.88
Orientati	30.00	30.00	30.00	30.00	30.00	30.00	30.00	30.00	30.00	30.00	30.00	30.00	30.00	30.00	30.00
Ln	61.00	62.00	63.00	64.00	65.00	66.00	67.00	68.00	69.00	70.00	71.00	72.00	73.00	74.00	75.00
ScalingFactor(X,Y,Z	7.00	7.20	7.40	7.60	7.80	8.00	8.20	8.40	8.60	8.80	9.00	9.20	9.40	9.60	9.80
Porosity	0.15	0.14	0.15	0.15	0.13	0.14	0.17	0.17	0.14	0.14	0.13	0.17	0.16	0.15	0.14
Matrix_P	0.85	0.86	0.85	0.85	0.87	0.86	0.83	0.83	0.86	0.86	0.87	0.83	0.84	0.85	0.86
Orientati	30.00	30.00	30.00	30.00	30.00	30.00	30.00	30.00	30.00	30.00	30.00	30.00	30.00	30.00	30.00
Ln	76.00	77.00	78.00	79.00	80.00										
ScalingFactor(X,Y,Z	10.00	10.20	10.40	10.60	10.80										
Porosity	0.15	0.16	0.15	0.17	0.16										
Matrix_P	0.85	0.84	0.85	0.83	0.84										
Orientati	30.00	30.00	30.00	30.00	30.00										

D.2 Network Extraction Configuration

```
&&&&&&&&&&&&&&&&&&&&&&&&&&&&&&&&&&&&&&&&&&&&&&&&&&&&&&&&&&&&&&&&&&&&&&&&
/* &&&&&&&&&&        12 June 2015        &&&&&&&&&&
/*
&&&&&&&&&&&&&&&&&&&&&&&&&&&&&&&&&&&&&&&&&&&&&&&&&&&&&&&&&&&&&&&&&&&&&&&&
```

```
/*
/*#Specify fullpath file name of 3D rock image (*.raw)
/*
/* &&& Only raw format with data type of UNSIGNED Byte !!!
/*
/*============================================
C:\extract\1-1-1\1-1-1.raw
/*============================================
/* (1) Specify x-dimension in voxels
/* (2) Specify y-dimension in voxels
/* (3) Specify z-dimension in voxels
/* (4) Specify voxel size of the image (micrometer)
/*============================================
200, 200, 200, 4.29
/*============================================
/* Specify the value range for pore voxels between 0 to 255
/* (1) bottom limit value (>=0),
/* (2) top limit value (<= 255)
/*============================================
255, 255
/*============================================
/* Remove pores of volume within the following specified range [SN, LN)
/* (1) SN: Smallest number of voxels (e.g. 1),
/* (2) LN: Largest number of voxels (e.g. 10)
/* (3) Using HYDRAULIC radius for HW code? otherwise this must be false!
/*============================================
1, 1, false
/*============================================
/*  MS: Medial surface for modelling fracture/plate pores
/*  MA: Medial axis for modelling normal pore system
/* (1) Using MA (true) or MS (false)?
/*  ###################################################################
/*  ### The following arguments (2 - 4) for previous algorithm ###
/*  ###################################################################
/* (2) Medial surface (MS) coefficient (0 ~ 1.0)
/* (3) MS valid value (VV = 0, 1, 2,...17),
/*     i.e. surface points will be removed
/*     if number of its 3x3x3 neighbours > 9+VV
/* (4) Create virtual nodes or not if necessary?
/*  ###################################################################
/*  ### The following arguments (5 - 7) for current algorithm  ###
/*  ###################################################################
/* (5) Surface coefficient (>= 2.0, OTHERWISE using previous algorithm)
/* (6) Density coefficient (>=1.0) for virtual network
/* (7) Using Euclidean distance map (true) or Boundary distance map (false)
/* (8) Is the pore structure complicated (not a simple model)?
/* (9) Parameter for determine dead-end node (1 ~ 99)
/*============================================
true,0.5,0, false,2.0,1.0, false,70
/*============================================
/* (1) Directional networks (1-X, 2-Y, 3-Z, 0 for all)
/* (2) Directly compute permeability (true or false)
/*============================================
0, true
```

LIST OF REFERENCES

Abdel-Qader, I., Abudayyeh, O. & Kelly, M. E. 2003. Analysis of edge-detection techniques for crack identification in bridges. *Journal of Computing in Civil Engineering,* 17**,** 255-263.

Achterhold, K., Bech, M., Schleede, S., Potdevin, G., Ruth, R., Loewen, R. & Pfeiffer, F. 2013. Monochromatic computed tomography with a compact laser-driven X-ray source. *Scientific reports,* 3.

Allen, J. R. L. 1973. A classification of climbing-ripple cross-lamination. *Journal of the Geological Society,* 129**,** 537-541.

Allen, J. R. L. 1982. *Sedimentary structures, their character and physical basis*, Elsevier.

Almarzooq, A., Alghamdi, T., Koronfol, S., Dernaika, M. & Walls, J. Shale Gas Characterization and Property Determination by Digital Rock Physics. SPE Saudi Arabia Section Technical Symposium and Exhibition, 2014. Society of Petroleum Engineers.

Andrä, H., Combaret, N., Dvorkin, J., Glatt, E., Han, J., Kabel, M., Keehm, Y., Krzikalla, F., Lee, M. & Madonna, C. 2013. Digital rock physics benchmarks—Part I: Imaging and segmentation. *Computers & Geosciences,* 50**,** 25-32.

Andriani, G. & Walsh, N. 2002. Physical properties and textural parameters of calcarenitic rocks: qualitative and quantitative evaluations. *Engineering Geology,* 67**,** 5-15.

Anguy, Y., Erlich, R., Prince, C., Riggert, V. & Bernard, D. 1994. The sample support problem for permeability assessment in sandstone reservoirs.

Arbelaez, P., Maire, M., Fowlkes, C. & Malik, J. 2011. Contour detection and hierarchical image segmentation. *IEEE transactions on pattern analysis and machine intelligence,* 33**,** 898-916.

Baas, J. H. 2000. EZ-ROSE: a computer program for equal-area circular histograms and statistical analysis of two-dimensional vectorial data. *Computers & Geosciences,* 26**,** 153-166.

Baas, J. H., Hailwood, E. A., Mccaffrey, W. D., Kay, M. & Jones, R. 2007. Directional petrological characterisation of deep-marine sandstones using grain fabric and permeability anisotropy: methodologies, theory, application and suggestions for integration. *Earth-Science Reviews,* 82**,** 101-142.

Balafar, M. A., Ramli, A. R., Saripan, M. I. & Mashohor, S. 2010. Review of brain MRI image segmentation methods. *Artificial Intelligence Review,* 33**,** 261-274.

Barnes, R., Lehman, C. & Mulla, D. 2014. Priority-flood: An optimal depression-filling and watershed-labeling algorithm for digital elevation models. *Computers & Geosciences,* 62**,** 117-127.

Beard, D. & Weyl, P. 1973. Influence of texture on porosity and permeability of unconsolidated sand. *AAPG bulletin,* 57**,** 349-369.

Becker, C., Rigamonti, R., Lepetit, V. & Fua, P. 2013. Supervised feature learning for curvilinear structure segmentation. *Medical Image Computing and Computer-Assisted Intervention–MICCAI 2013.* Springer.

Berner, R. A. 1969. Goethite stability and the origin of red beds. *Geochimica et Cosmochimica Acta,* 33**,** 267-273.

Beucher, S. & Meyer, F. 1992. The morphological approach to segmentation: the watershed transformation. *OPTICAL ENGINEERING-NEW YORK-MARCEL DEKKER INCORPORATED-*, 34**,** 433-433.

Blunt, M. J., Bijeljic, B., Dong, H., Gharbi, O., Iglauer, S., Mostaghimi, P., Paluszny, A. & Pentland, C. 2013. Pore-scale imaging and modelling. *Advances in Water Resources,* 51**,** 197-216.

Botha, P. W., Golab, A. N., Bhattad, P., Goodwin, C. & Sheppard, A. P. 2015. MULTI-SCALE IMAGING AND CROSS-PROPERTY CORRELATIONS IN HETEROGENOUS SANDSTONE. *International Symposium of the Society of Core*

Analysts.

Branney, M. J. & Kokelaar, B. P. Pyroclastic density currents and the sedimentation of ignimbrites. 2002. Geological Society of London.

Bryant, S. & Blunt, M. 1992. Prediction of relative permeability in simple porous media. *Physical Review A,* 46**,** 2004.

Bryant, S. L., King, P. R. & Mellor, D. W. 1993. Network model evaluation of permeability and spatial correlation in a real random sphere packing. *Transport in Porous Media,* 11**,** 53-70.

Buchter, B., Hinz, C. & Flühler, H. 1994. Sample size for determination of coarse fragment content in a stony soil. *Geoderma,* 63**,** 265-275.

Buhmann, J. M., Malik, J. & Perona, P. 1999. Image recognition: Visual grouping, recognition, and learning. *Proceedings of the National Academy of Sciences,* 96**,** 14203-14204.

Bultreys, T., De Boever, W. & Cnudde, V. 2016. Imaging and image-based fluid transport modeling at the pore scale in geological materials: A practical introduction to the current state-of-the-art. *Earth-Science Reviews,* 155**,** 93-128.

Burgeth, B., Didas, S. & Weickert, J. 2009. A general structure tensor concept and coherence-enhancing diffusion filtering for matrix fields. *Visualization and processing of tensor fields.* Springer.

Caballero, K. L., Barajas, J., Pujol, O., Rodriguez, O. & Radeva, P. Using reconstructed ivus images for coronary plaque classification. 2007 29th Annual International Conference of the IEEE Engineering in Medicine and Biology Society, 2007. IEEE, 2167-2170.

Campbell, C. V. 1967. Lamina, laminaset, bed and bedset. *Sedimentology,* 8**,** 7-26.

Chisholm, H. 1911. *The Encyclopædia britannica: a dictionary of arts, sciences, literature and general information*, Encyclopaedia Britannica.

Cnudde, V. & Boone, M. N. 2013. High-resolution X-ray computed tomography in geosciences: A review of the current technology and applications. *Earth-Science Reviews,* 123**,** 1-17.

Coles, M., Muegge, E. & Sprunt, E. 1991. Applications of CAT scanning for oil and gas production. *IEEE Transactions on nuclear science,* 38**,** 510-515.

Corbett, P., Couples, G., Cardiner, A. & Lever, H. 2005. *Petroleum Geoscience*, Edinburgh, United Kingdom, Heriot-Watt University.

Corbett, P., Ringrose, P., Jensen, J. & Sorbie, K. Laminated clastic reservoirs: The interplay of capillary pressure and sedimentary architecture. SPE Annual Technical Conference and Exhibition, 1992. Society of Petroleum Engineers.

Curcio, C. A., Sloan, K. R., Kalina, R. E. & Hendrickson, A. E. 1990. Human photoreceptor topography. *Journal of comparative neurology,* 292**,** 497-523.

Damcı, E. & Çağatay, M. N. 2016. An automated algorithm for dating annually laminated sediments using X-ray radiographic images, with applications to Lake Van (Turkey), Lake Nautajarvi (Finland) and Byfjorden (Sweden). *Quaternary International,* 401**,** 174-183.

De Boever, W., Derluyn, H., Van Loo, D., Van Hoorebeke, L. & Cnudde, V. 2015. Data-fusion of high resolution X-ray CT, SEM and EDS for 3D and pseudo-3D chemical and structural characterization of sandstone. *Micron,* 74**,** 15-21.

Descoteaux, M., Audette, M., Chinzei, K. & Siddiqi, K. 2006. Bone enhancement filtering: application to sinus bone segmentation and simulation of pituitary surgery. *Computer aided surgery,* 11**,** 247-255.

Deutsch, C. V. & Journel, A. G. 1998. Geostatistical software library and user's guide. *Oxford University Press, New York.*

Dong, H. 2007. *Micro-CT imaging and pore network extraction*.

Dufour, A., Tankyevych, O., Naegel, B., Talbot, H., Ronse, C., Baruthio, J., Dokládal, P. & Passat, N. 2013. Filtering and segmentation of 3D angiographic data: Advances based on mathematical morphology. *Medical Image Analysis,* 17**,** 147-164.

Dunsmuir, J. H., Ferguson, S., D'amico, K. & Stokes, J. X-ray microtomography: a new tool for the characterization of porous media. SPE annual technical conference and exhibition, 1991.

Francus, P. 1998. An image-analysis technique to measure grain-size variation in thin sections of soft clastic sediments. *Sedimentary Geology,* 121**,** 289-298.

Frangi, A. F., Niessen, W. J., Vincken, K. L. & Viergever, M. A. 1998. Multiscale vessel enhancement filtering. *Medical Image Computing and Computer-Assisted Interventation—MICCAI'98.* Springer.

Fraz, M. M., Remagnino, P., Hoppe, A., Uyyanonvara, B., Rudnicka, A. R., Owen, C. G. & Barman, S. A. 2012. Blood vessel segmentation methodologies in retinal images–a survey. *Computer methods and programs in biomedicine,* 108**,** 407-433.

Fujita, Y. & Hamamoto, Y. 2011. A robust automatic crack detection method from noisy concrete surfaces. *Machine Vision and Applications,* 22**,** 245-254.

Ghous, A., Bauget, F., Arns, C., Sakellariou, A., Senden, T., Sheppard, A., Sok, R., Pinczewski, W., Harris, R. & Beck, G. Resistivity and permeability anisotropy measured in laminated sands via digital core analysis. paper VVV, 46th SPWLA annual logging symposium, 2005.

Glennie, K. & Evans, G. 1976. A reconnaissance of the Recent sediments of the Ranns of Kutch, India. *Sedimentology,* 23**,** 625-647.

Glennie, K., Mudd, G. & Nagtegaal, P. 1978. Depositional environment and diagenesis of Permian Rotliegendes sandstones in Leman Bank and Sole Pit areas of the UK southern North Sea. *Journal of the Geological Society,* 135**,** 25-34.

Goldstein, J. 2003. *Scanning Electron Microscopy and X-ray Microanalysis: Third Edition*, Springer US.

Gomez-Hernandez, J. J. 1992. A stochastic approach to the simulation of block conductivity fields conditioned upon data measured at a smaller scale.

González, G., Fleurety, F. & Fua, P. Learning rotational features for filament detection. Computer Vision and Pattern Recognition, 2009. CVPR 2009. IEEE Conference on, 2009. IEEE, 1582-1589.

Guardiano, F. B. & Srivastava, R. M. 1993. Multivariate geostatistics: beyond bivariate moments. *Geostatistics Troia'92.* Springer.

Hajizadeh, A., Safekordi, A. & Farhadpour, F. A. 2011. A multiple-point statistics algorithm for 3D pore space reconstruction from 2D images. *Advances in water Resources*, 34**,** 1256-1267.

Hamblin, W. K. 1965. *Internal structures of" homogeneous" sandstones*, University of Kansas.

Harms, J. C., Southard, J. B. & Walker, R. G. 1982. Structures and sequences in clastic rocks.

Heintzmann, R. & Ficz, G. 2006. Breaking the resolution limit in light microscopy. *Briefings in Functional Genomics,* 5**,** 289-301.

Herman, G. T. 2009. *Fundamentals of computerized tomography: image reconstruction from projections*, Springer Science & Business Media.

Hounsfield, G. N. 1973. Computerized transverse axial scanning (tomography): Part 1. Description of system. *The British journal of radiology,* 46**,** 1016-1022.

Huang, T. S. & Aizawa, K. 1993. Image processing: some challenging problems. *Proceedings of the National Academy of Sciences*, 90**,** 9766-9769.

Huang, Y., Ringrose, P. & Sorbie, K. 1995. Capillary trapping mechanisms in water-wet laminated rocks. *SPE Reservoir Engineering,* 10.

Hubbell, J. H. & Seltzer, S. M. 1995. Tables of X-ray mass attenuation coefficients and mass energy-absorption coefficients 1 keV to 20 MeV for elements Z= 1 to 92 and 48 additional substances of dosimetric interest. National Inst. of Standards and Technology-PL, Gaithersburg, MD (United States). Ionizing Radiation Div.

Hughes, G. P. 1968. On the mean accuracy of statistical pattern recognizers. *Information Theory, IEEE Transactions on,* 14**,** 55-63.

Hunter, R. E. 1977. Basic types of stratification in small eolian dunes. *Sedimentology,* 24**,** 361-387.

Ismail, N. I., Latham, S. & Arns, C. H. Rock-typing Using The Complete Set Of Additive Morphological Descriptors. SPE Reservoir Characterization and Simulation Conference and Exhibition, 2013. Society of Petroleum Engineers.

Jiang, Z., Wu, K., Couples, G., Van Dijke, M. I. J., Sorbie, K. S. & Ma, J. 2007. Efficient extraction of networks from three-dimensional porous media. *Water Resources Research,* 43**,** n/a-n/a.

Johnson, D. L. 1990. Biomantle evolution and the redistribution of earth materials and artifacts. *Soil Science,* 149**,** 84-102.

Kang, Y., Engelke, K. & Kalender, W. A. 2003. A new accurate and precise 3-D segmentation method for skeletal structures in volumetric CT data. *IEEE transactions on medical imaging,* 22**,** 586-598.

Ketcham, R. A. & Carlson, W. D. 2001. Acquisition, optimization and interpretation of X-ray computed tomographic imagery: applications to the geosciences. *Computers & Geosciences,* 27**,** 381-400.

Latham, S., Varslot, T. & Sheppard, A. Image registration: Enhancing and calibrating X-ray micro-CT imaging. Proceedings of the International Symposium of the Society of Core Analysts. SCA2008-35. Abu Dhabi, United Arab Emirates, 2008.

Lawes, G. 1987. Scanning electron microscopy and X-ray microanalysis.

Lee, H., Grosse, R., Ranganath, R. & Ng, A. Y. Convolutional deep belief networks for scalable unsupervised learning of hierarchical representations. Proceedings of the 26th annual international conference on machine learning, 2009. ACM, 609-616.

Lesage, D., Angelini, E. D., Bloch, I. & Funka-Lea, G. 2009. A review of 3D vessel lumen segmentation techniques: Models, features and extraction schemes. *Medical image analysis,* 13**,** 819-845.

Leung, T. & Malik, J. 2001. Representing and recognizing the visual appearance of materials using three-dimensional textons. *International journal of computer vision,* 43**,** 29-44.

Liang, Z., Fernandes, C., Magnani, F. & Philippi, P. 1998. A reconstruction technique for three-dimensional porous media using image analysis and Fourier transforms. *Journal of Petroleum Science and Engineering,* 21**,** 273-283.

Lindquist, W. & Venkatarangan, A. 1999. Investigating 3D geometry of porous media from high resolution images. *Physics and Chemistry of the Earth, Part A: Solid Earth and Geodesy,* 24**,** 593-599.

Lloyd, G. E. 1987. Atomic number and crystallographic contrast images with the SEM: a review of backscattered electron techniques. *Mineralogical Magazine,* 51**,** 3-19.

Macqueen, J. Some methods for classification and analysis of multivariate observations. Proceedings of the fifth Berkeley symposium on mathematical statistics and probability, 1967. Oakland, CA, USA., 281-297.

Makse, H. A. 2000. Grain segregation mechanism in aeolian sand ripples. *The European Physical Journal E: Soft Matter and Biological Physics,* 1**,** 127-135.

Mason, G. & Morrow, N. 1991. CAPILLARY BEHAVIOR OF A PERFECTLY WETTING LIQUID IN IRREGULAR TRIANGULAR TUBES. *Journal of Colloid and Interface Science,* 141**,** 262-274.

Mcdougall, S. & Sorbie, K. The combined effect of capillary and viscous forces on waterflood displacement efficiency in finely laminated porous media. SPE

Annual Technical Conference and Exhibition, 1993. Society of Petroleum Engineers.

Mcdougall, S. R. & Sorbie, K. S. 1999. Estimation of critical gas saturation during pressure depletion in virgin and waterflooded reservoirs. *Petroleum Geoscience,* 5**,** 229-233.

Mckee, E. D. 1966. Structures of dunes at White Sands National Monument, New Mexico (and a comparison with structures of dunes from other selected areas) 1. *Sedimentology,* 7**,** 3-69.

Mohebi, A., Fieguth, P. & Ioannidis, M. A. 2009. Statistical fusion of two-scale images of porous media. *Advances in water resources,* 32**,** 1567-1579.

Mohri, M., Rostamizadeh, A. & Talwalkar, A. 2012. *Foundations of machine learning,* MIT press.

Moon, P. & Spencer, D. E. 2012. *Field theory handbook: including coordinate systems, differential equations and their solutions,* Springer.

Moore, G. E. 1998. Cramming more components onto integrated circuits. *Proceedings of the IEEE,* 86**,** 82-85.

Müller, R. H. 1954. Interaction of beta particles with matter. *Physical Review,* 93**,** 891.

Naruse, H. & Masuda, F. 2006. Visualization of the internal structure of the massive division in experimental sediment-gravity-flow deposits by mapping of grain fabric. *Journal of Sedimentary Research,* 76**,** 854-865.

Ngom, N. F., Garnier, P., Monga, O. & Peth, S. 2011. Extraction of three-dimensional soil pore space from microtomography images using a geometrical approach. *Geoderma,* 163**,** 127-134.

Nishiyama, T. & Kusuda, H. Identification of pore spaces and microcracks using fluorescent resins. International journal of rock mechanics and mining sciences & geomechanics abstracts, 1994. Elsevier, 369-375.

Obara, B., Fricker, M. & Grau, V. Coherence enhancing diffusion filtering based on the Phase Congruency Tensor. 2012 9th IEEE International Symposium on Biomedical Imaging (ISBI), 2012. IEEE, 202-205.

Okabe, H. & Blunt, M. J. 2004. Prediction of permeability for porous media reconstructed using multiple-point statistics. *Physical Review E,* 70**,** 066135.

Olea, R. A. 2012. *Geostatistics for engineers and earth scientists,* Springer Science & Business Media.

Olshausen, B. A. & Field, D. J. 1996. Emergence of simple-cell receptive field properties by learning a sparse code for natural images. *Nature,* 381**,** 607.

Øren, P.-E. & Bakke, S. 2002. Process based reconstruction of sandstones and prediction of transport properties. *Transport in Porous Media,* 46**,** 311-343.

Otsu, N. 1975. A threshold selection method from gray-level histograms. *Automatica,* 11**,** 23-27.

Otsu, N. 1979. An automatic threshold selection method based on discriminate and least squares criteria. *Denshi Tsushin Gakkai Ronbunshi,* 63**,** 349-356.

Pettijohn, F. J. 1987. *Sand and sandstone,* Springer Science & Business Media.

Pujol, O., Rosales, M., Radeva, P. & Nofrerias-Fernández, E. Intravascular ultrasound images vessel characterization using adaboost. International Workshop on Functional Imaging and Modeling of the Heart, 2003. Springer, 242-251.

Randen, T. & Husoy, J. H. 1999. Filtering for texture classification: A comparative study. *IEEE Transactions on pattern analysis and machine intelligence,* 21**,** 291-310.

Reading, H. G. 2009. *Sedimentary environments: processes, facies and stratigraphy*, John Wiley & Sons.

Reed, S. J. B. 2005. *Electron microprobe analysis and scanning electron microscopy in geology*, Cambridge University Press.

Rees, A. 1968. The production of preferred orientation in a concentrated dispersion of elongated and flattened grains. *The Journal of Geology***,** 457-465.

Remy, N., Boucher, A. & Wu, J. 2009. *Applied geostatistics with SGeMS: a user's guide*, Cambridge University Press.

Rigamonti, R., Brown, M. & Lepetit, V. Are sparse representations really relevant for image classification? Computer Vision and Pattern Recognition (CVPR), 2011 IEEE Conference on, 2011a. IEEE, 1545-1552.

Rigamonti, R. & Lepetit, V. 2012. Accurate and efficient linear structure segmentation by leveraging ad hoc features with learned filters. *Medical Image Computing and Computer-Assisted Intervention–MICCAI 2012.* Springer.

Rigamonti, R., Türetken, E., González Serrano, G., Fua, P. & Lepetit, V. 2011b. Filter learning for linear structure segmentation.

Ringrose, P., Sorbie, K., Corbett, P. & Jensen, J. 1993. Immiscible flow behaviour in laminated and cross-bedded sandstones. *Journal of Petroleum Science and Engineering,* 9**,** 103-124.

Robinson, B. W. & Nickel, E. H. 1979. A USEFUL NEW TECHNIQUE FOR MINERALOGY- THE BACKSCATTERED-ELECTRON/LOW VACUUM MODE OF SEM OPERATION. *American Mineralogist,* 64**,** 1322-8.

Rubin, D. M. & Carter, C. L. 1987. Cross-bedding, bedforms, and paleocurrents.

Russ, J. C. 1990. Computer-assisted microscopy.

Russ, J. C. & Woods, R. P. 1995. The image processing handbook. *Journal of Computer Assisted Tomography,* 19**,** 979-981.

Sato, Y., Nakajima, S., Atsumi, H., Koller, T., Gerig, G., Yoshida, S. & Kikinis, R. 3D multi-scale line filter for segmentation and visualization of curvilinear structures in medical images. CVRMed-MRCAS'97, 1997. Springer, 213-222.

Schindelin, J., Arganda-Carreras, I., Frise, E., Kaynig, V., Longair, M., Pietzsch, T., Preibisch, S., Rueden, C., Saalfeld, S. & Schmid, B. 2012. Fiji: an open-source platform for biological-image analysis. *Nature methods,* 9**,** 676-682.

Schnaar, G. & Brusseau, M. L. 2006. Characterizing pore-scale dissolution of organic immiscible liquid in natural porous media using synchrotron X-ray microtomography. *Environmental science & technology,* 40**,** 6622-6629.

Sheppard, A., Sok, R., Averdunk, H., Robins, V. & Ghous, A. Analysis of rock microstructure using high-resolution X-ray tomography. Proceedings of the International Symposium of the Society of Core Analysts, 2006. 1-12.

Shotton, F. 1956. Some aspects of the New Red desert in Britain. *Geological Journal,* 1**,** 450-465.

Sironi, A., Lepetit, V. & Fua, P. Multiscale Centerline Detection by Learning a Scale-Space Distance Transform. Computer Vision and Pattern Recognition (CVPR), 2014 IEEE Conference on, 2014. IEEE, 2697-2704.

Sironi, A., Tekin, B., Rigamonti, R., Lepetit, V. & Fua, P. 2015. Learning Separable Filters. *Pattern Analysis and Machine Intelligence, IEEE Transactions on,* 37**,** 94-106.

Sok, R. M., Knackstedt, M. A., Varslot, T., Ghous, A., Latham, S. & Sheppard, A. P. 2010. Pore scale characterization of carbonates at multiple scales: integration of Micro-CT, BSEM, and FIBSEM. *Petrophysics,* 51.

Sternberg, S. R. 1983. Biomedical Image Processing. *Computer,* 16**,** 22-34.

Stokes, W. L. 1968. Multiple parallel-truncation bedding planes--a feature of wind-deposited sandstone formations. *Journal of Sedimentary Research,* 38.

Strebelle, S. 2002. Conditional simulation of complex geological structures using multiple-point statistics. *Mathematical Geology,* 34**,** 1-21.

Taira, A. 1989. Magnetic fabrics and depositional processes. *Sedimentary Facies in the Active Plate Margin: Tokyo (Terra Sci. Publ.)***,** 43-77.

Tankyevych, O., Talbot, H., Dokládal, P. & Passat, N. Direction-adaptive grey-level morphology. Application to 3D vascular brain imaging. 2009 16th IEEE International Conference on Image Processing (ICIP), 2009. IEEE, 2261-2264.

Thompson, D. B. 1969. Dome-shaped aeolian dunes in the frodsham member of the so-called "keuper" sandstone formation (scythian-anisian: triassic) at Frodsham, Cheshire (England). *Sedimentary Geology,* 3**,** 263-289.

Torquato, S. 2002. Statistical description of microstructures. *Annual Review of Materials Research,* 32**,** 77-111.

Truc, P. T., Khan, M. A., Lee, Y.-K., Lee, S. & Kim, T.-S. 2009. Vessel enhancement filter using directional filter bank. *Computer Vision and Image Understanding,* 113**,** 101-112.

Turpeinen, T. 2015. Analysis of microtomographic images of porous heterogeneous materials. *Jyväskylä studies in computing 230.*

Ughi, G. J., Adriaenssens, T., Sinnaeve, P., Desmet, W. & D'hooge, J. 2013. Automated tissue characterization of in vivo atherosclerotic plaques by intravascular optical coherence tomography images. *Biomedical optics express,* 4**,** 1014-1030.

Van Den Berg, E. H., Bense, V. F. & Schlager, W. 2003. Assessing textural variation in laminated sands using digital image analysis of thin sections. *Journal of Sedimentary Research,* 73**,** 133-143.

Van Dijke, M. I. J., Piri, M., Helland, J. O., Sorbie, K. S., Blunt, M. J. & Skjaeveland, S. M. 2007. Criteria for three-fluid configurations including layers in a pore with nonuniform wettability. *Water Resources Research,* 43**,** n/a-n/a.

Van Houten, F. 1961. Climatic significance of red beds. *Descriptive paleoclimatology***,** 89-139.

Van dijke, M. I. J. & Sorbie, K. S. 2003. Three-phase capillary entry conditions in pores of noncircular cross-section. *Journal of Colloid and Interface Science,* 260**,** 385-397.

Varma, M. & Zisserman, A. 2005. A statistical approach to texture classification from single images. *International Journal of Computer Vision,* 62**,** 61-81.

Voorn, M., Exner, U. & Rath, A. 2013. Multiscale Hessian fracture filtering for the enhancement and segmentation of narrow fractures in 3D image data. *Computers & Geosciences,* 57**,** 44-53.

Walker, T. & Waugh, B. 1973. Intrastratal alteration of silicate minerals in late Tertiary fluvial arkose, Baja California, México. *Geological Society of America Bulletin,* 7**,** 853-854.

Walker, T. R. 1967. Formation of red beds in modern and ancient deserts. *Geological Society of America Bulletin,* 78**,** 353-368.

Walker, T. R. 1976. Diagenetic origin of continental red beds. *The Continental Permain in Central, West, and South Europe.* Springer.

Waugh, B. 1970. Petrology, provenance and silica diagenesis of the Penrith Sandstone (Lower Permian) of northwest England. *Journal of Sedimentary Research,* 40.

Waugh, B. 1978. Authigenic K-feldspar in British Permo-Triassic sandstones. *Journal of the Geological Society,* 135**,** 51-56.

Wildenschild, D. & Sheppard, A. P. 2013. X-ray imaging and analysis techniques for quantifying pore-scale structure and processes in subsurface porous medium systems. *Advances in Water Resources,* 51**,** 217-246.

Wills, L. J. 1951. *A palaeogeographical atlas of the British Isles and adjacent parts of Europe,* Blackie.

Wilson, I. G. 1972. Universal discontinuities in bedforms produced by the wind. *Journal of Sedimentary Research,* 42.

Wright, J., Ma, Y., Mairal, J., Sapiro, G., Huang, T. S. & Yan, S. 2010. Sparse representation for computer vision and pattern recognition. *Proceedings of the IEEE,* 98**,** 1031-1044.

Wu, K., Nunan, N., Crawford, J. W., Young, I. M. & Ritz, K. 2004. An efficient Markov chain model for the simulation of heterogeneous soil structure. *Soil Science Society of America Journal,* 68**,** 346-351.

Wu, K., Van Dijke, M. I. J., Couples, G. D., Jiang, Z., Ma, J., Sorbie, K. S., Crawford, J., Young, I. & Zhang, X. 2006. 3D Stochastic Modelling of Heterogeneous Porous Media – Applications to Reservoir Rocks. *Transport in Porous Media,* 65**,** 443-467.

Xu, Y., Sonka, M., Mclennan, G., Guo, J. & Hoffman, E. A. 2006. MDCT-based 3-D texture classification of emphysema and early smoking related lung pathologies. *IEEE transactions on medical imaging,* 25**,** 464-475.

Yeong, C. & Torquato, S. 1998. Reconstructing random media. *Physical Review E,* 57**,** 495.